The
University
Of
Sheffield.

Kinetic and biophysical approaches to the assembly of magnesium chelatase

By:

Luke John Taurino

A thesis submitted in partial fulfilment of the requirements for the degree of
Doctor of Philosophy

The University of Sheffield
Faculty of Science
Department of Chemistry

September 2016

Abstract

Magnesium chelatase catalyses the first committed step in chlorophyll biosynthesis, the insertion of Mg^{2+} into protoporphyrin-IX yielding magnesium protoporphyrin-IX; This enzyme stands at a branch-point in chlorophyll and heme biosynthesis. Mg^{2+} insertion is energetically unfavourable and is coupled with ATP hydrolysis. Magnesium chelatase from *Synechocystis* sp. PCC6803 contains three essential protein subunits ChlI, ChlD and ChlH. ChlI and ChlD belong to the AAA^+ family of ATPases and form motor complexes that catalyse ATP hydrolysis which drives the Mg^{2+} insertion reaction occurring on ChlH. The number and arrangement of these protein subunits that represent the active chelatase are poorly understood.

My work used a series of techniques to probe the complexes formed by the chelatase. Kinetic titrations show active complexes that catalyse either Mg^{2+} insertion or ATP hydrolysis occur at two widely different levels of subunits, either 1:1 levels or at much higher levels of ChlI over ChlD. ChlH influences these ChlID complexes, with high levels of ChlH appearing to cause a reorganisation of higher order ChlID complexes as well as causing a dramatic change in the ATPase activity of the system.

A I_6D_6 complex has been demonstrated previously within the *Rhodobacter capsulatus* chelatase and a similar complex could be expected within the *Synechocystis* system. Sedimentation velocity analytical ultra centrifugation performed on the *Synechocystis* chelatase gives no evidence for this complex. A smaller complex is observed, favoured at high levels of ChlI, or in the presence of ChlH, this complex was proposed to represent an I_5D complex or a similar arrangement. No ChlIDH complex was observed, although ChlH appears to influence the arrangement of smaller ChlID complexes.

Modelling of the reaction cycle provides evidence for an isomerisation of ChlH preceding D_{IX} substrate binding that may contribute to the observed lag phase prior to Mg^{2+} chelation.

To Bob

Acknowledgements

I would like to thank Dr Jim Reid for his invaluable help and input which made all this work possible.

Dr Nathan Adams for his help in the lab during the start of my PhD and for showing me how to make proteins and do kinetics; Dr Dawn Hesson for other general help and questions. Members of the Grasby group, in particular Dr David Finger and Dr Mark Thompson for letting me steal their AKTA.

The AUC work would not have been possible without the help of Dr Thomas Jowitt and the facilities at the University of Manchester.

The many members of E81, past and present, for providing much needed comic relief, and finally current members of the Reid group for keeping the lab in order whilst I ran that one last experiment.

I would like to thank my family for their patience and support whilst writing my thesis.

Contents

List of Figures

List of Tables

Abbreviations

AAA^+ - ATPases Associated with various cellular Activities
ALA - 5-Aminolevulinic acid
AUC - Analytical ultracentrifugation ATP - Adenosine triphosphate
DTT - Dithiothreitol
D_{IX} - Deuteroporphyrin-IX
ETC - Electron Transport Chain
FRET - Förster Resonance Energy Transfer
$MgATP^{2-}$ - Magnesium adenosine triphosphate
MgADP - Magnesium adenosine diphosphate
MgD_{IX} - Magnesium deuteroporphyrin-IX
MOPS - 3-(N-morpholino)propansulfonic acid
NADH - Nicotinamide adenine dinucleotide
NADPH - Nicotinamide adenine dinucleotide phosphate
PBG - Porphobilinogen
PC - Plastocyanin
PEP- Phosphoenolpyruvate
PK/LDH - Pyruvate kinase/ lactic dehydrogenase
PS I - Photosystem I
PS II - Photosystem II
PQ - Plastoquinone
SDS-PAGE - Sodium dodecyl sulfate polyacrylamide gel electrophoresis
SV-AUC - Sedimentation velocity analytical ultracentrifugation

1 Introduction

1.1 Photosynthesis and the photosynthetic aparatus

1.1.1 Solar energy has huge potential as a renewable energy source

The worlds annual energy consumption was approximately 13.5 terawatts (TW) in 2001 [1] and is projected to increase dramatically, at least by 50 % by 2040, as a result of the worlds ever increasing energy needs [2]. In comparison, the amount of solar energy striking the earths surface is enormous — with estimations in the region of 89000 TW [1] — and under such levels sufficient solar energy reaches the earths surface every 90 minutes adequate to meet annual worldwide energy needs [1].

Although the direct harvesting and utilisation of significant proportions of this energy is unfeasible for widespread reasons — such as the current technical limitations in harvesting technologies — it is still estimated that approximately 2500 TW of this solar energy has a direct technical potential for use as a renewable energy source [1], an amount strikingly greater than the worlds energy needs. Despite this huge potential, still only a relatively small proportion of the world energy needs are currently being met through solar energy generation (approximately 1% [3, 4]). However, this has increased substantially in recent years with a near 6-fold increase (from 0.04 - 0.2 TW) in worldwide energy generation through solar cells alone [4] observed between 2010 and 2015. Given the huge future technical potential of solar energy as a renewable energy source (2500 TW, over 10000x what is currently being generated [1]) solar energy generation is only expected to show further dramatic increase in the future to meet ever rising energy demands in favour of non renewable sources.

1.1.2 Photosynthesis

Photosynthesis is the 3.5 billion year old process [5] performed by plants, algae and cyanobacteria that utilises solar energy for energy generation through the conversion of carbon dioxide and water into more energy rich sources, such as glucose, in addition to oxygen. This energy produced as a result of photosynthesis is utilised by and essential for all life on earth.

$$\mathrm{CO_2 + H_2O \xrightarrow{\text{Solar Energy}} CH_2O + O_2}$$

Figure 1.1: Photosynthesis - the conversion of carbon dioxide and water into glucose and oxygen is essential for sustaining life.

Although extremly high levels of solar energy reaches the earth surface daily, only a small amount of this energy ultimately ends up being used in photosynthesis and biomass production (approximately 100 TW [6]). However, such levels are still significantly higher than those currently achieved by human energy generation through solar methods (approximately 0.2TW or 1% of worldwide energy generation [4, 3]) and indeed worldwide energy consumption in general (15 - 30 TW [2]). In addition to the energy gained and stored from the production of energy rich molecules, the resulting plant material, or biomass, as a result of photosynthesis also has huge potential as a renewable energy source [7]. Furthermore, it is estimated that the annual food intake by humans is only 0.4 percent of annual world wide biomass produced as a result of photosynthesis [8].

Given this ability of photosynthesis to generate much higher levels of energy than current artificial methods such as photovoltaic cells, further investigation into the natural processes and enzymes governing photosynthesis is of great interest in the field of future energy generation.

1.1.3 Chlorophyll - an essential light harvesting pigment within the photosynthetic aparatus

The capture of the solar energy required for photosynthesis is achieved through light absorbing organic pigments, specialised for the absorption of specific wavelengths of visible light. Chlorophylls are one type of these key light-absorbing pigments, contained in abundant levels within the large photosystem I and II thylakoid bound supercomplexes that make up the photosynthetic aparatus.

Numerous different chlorophylls have been isolated and identified, including chlorophyll *a*, the universal chlorophyll present in all photosynthetic organisms and chlorophyll *b* found within higher plants and green algae [8].

The particular wavelengths of light photosynthetic pigments such as chlorophyll are capable of absorbing varies widely. In relation to chlorophyll *a* and *b* such variations in their absorbance maximum can be seen, with chlorophyll *a* showing absorption maxima at 420nm and 660nm whilst chlorophyll *b* exhibits maxima at 435nm and 643nm in acetone [8]. As a result of the specialised light absorbing properties of such pigments, photosynthetic organisms usually contain a wide range of various different chlorophylls and/or other photosynthetic pigments allowing the efficient absorption of a broad spectrum of light to be utilised during photosynthesis.

Although the chemical structures of different types of chlorophylls show some variations, mostly variation in side chains, chlorophylls do exhibit many essential conserved structural features. The overall structure of chlorophyll constitutes a highly conjugated porphyrin head — responsible for giving chlorophylls their crucial light harvesting properties — containing a central magnesium ion, in addition to a long hydrophobic chain. These structural features can be observed in two of the most abundant chlorophylls, chlorophyll *a* and *b* (Figure 1.2).

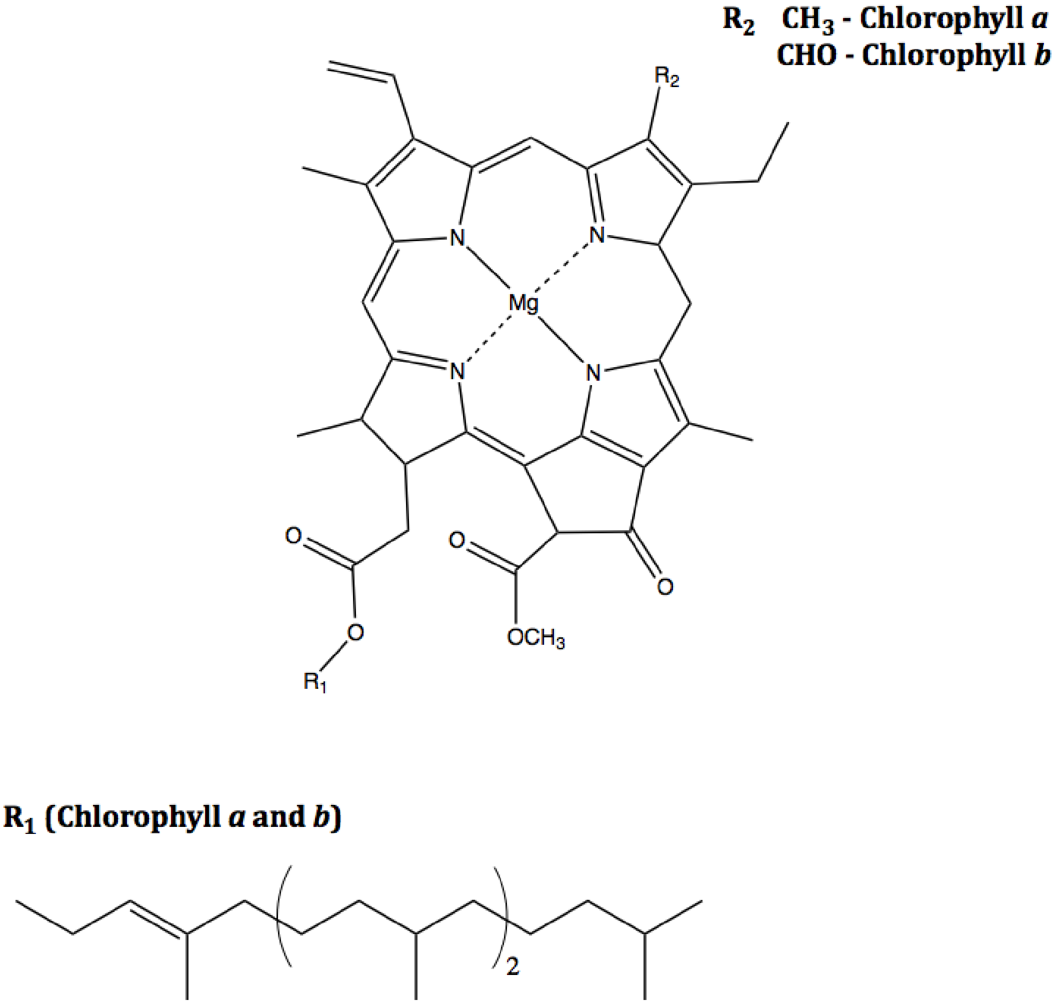

Figure 1.2: The structures of two abundant light absorbing pigments essential for photosynthesis, chlorophyll *a* and *b*.

1.1.4 Overview of the photosynthetic aparatus and photosystems I and II

The main processes of photosynthesis occur within the thylakoid bound photosystem I and II supercomplexes, which make up the larger photosynthetic aparatus (Figure 1.3).

Following the capture of protons by phycobilisome antenna complexes of photosystem II, photons are then transferred by chlorophyll *a* molecules of photosystem II towards two special pairs of chlorophyll *a* molecules within the core of photosystem II (the P680 special pair, named due to their respective absorption maximum at 680nm [9]). At these special chlorophylls, a key water splitting reaction is catalysed, in which the splitting of a water molecule generates 2 electrons, two protons (H^+) and an Oxygen atom [8].

The electrons generated from this water splitting reaction within photosystem II then pass along a series of steps of the electron transport chain (ETC) ending at photosystem I, the second of the key complexes involved in photosynthesis. Briefly, this involves firstly the transport of the electrons from pheophytin to plastoquinone (PQ) then subsequently to the cytochrome b_6f complex, which then transfers the electrons to the plastocyanin complex (PC). Finally, this plastocyanin complex then transfers the electrons to the next reaction center, photosystem I [8].

In addition to its involvement within the ETC the cytochrome b_6f complex also generates and pumps additional protons into the thylakoid space; this H^+ gradient drives ATP synthesis by ATP synthase [10].

At photosystem I, the special pairs of chlorophylls, in this case the p700 special pairs [11, 12], absorb two photons of solar energy, and uses this to excite two electrons to a higher energy state. These excited electrons are then transferred to a ferridoxin acceptor complex and then onto the enzyme ferredoxin-NADP$^+$ reductase which utilises these electrons, in addition to two protons, to reduce NADP$^+$ to NADPH. This NADPH ultimately goes on to provide the electrons that are used in the reduction of carbon dioxide to glucose [8].

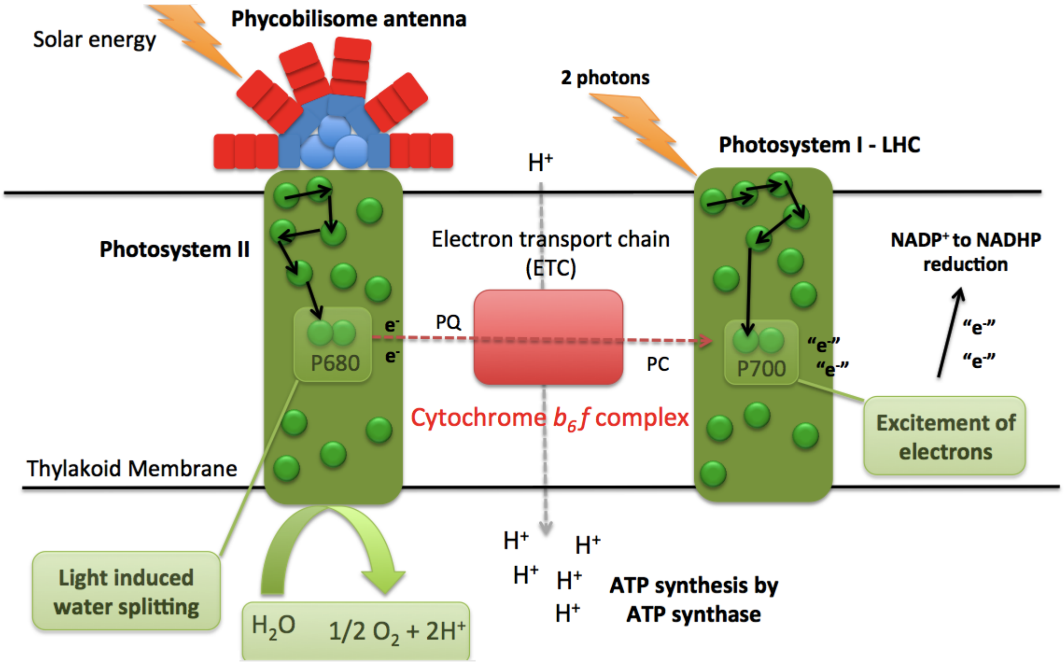

Figure 1.3: Overview of the photosynthetic reaction chain along the thylakoid membrane. The photosystem I and II complexes, the phycobilisome antenna and the electron transport chain (ETC) complexes plastocyanin (PC), cytochrome b_6f complex and plastoquinone (PQ) are shown.

1.1.5 Structural overview of Photosystems I and II

The crystal structures of PS I and PS II have been widely studied from a range of species, including the PSII from *Thermosynechococcus vulcanus* [13, 14] and *Thermosynechococcus elongatus* [15, 16]. Structural studies of PS 1 include that from *Synechococcus elongatus* [17, 18] and *Pisum sativum var. alaska* [19, 20].

The 1.9Å crystal structure of a PS II dimer from *T. vulcanus* [13] provides a model example of its overall structure (Figure 1.4). Structurally, each monomer contains 19 protein subunits (total weight 350kDa), 35 chlorophyll *a* molecules (shown in green in Figure 1.4), 11 β-carotenes, 2 plastoquinones, three irons (two belonging to haem), four manganese atoms, three calcium ions, three Cl^- ions, one bicarbonate ion, 15 detergents and 20 lipids. In addition PSII contains over 1300 water molecules, contained mainly within two distinct layers on the lumunal and stromal sides [13].

PS II contains the site of the water splitting reaction, responsible for the generation of the electrons utilised during photosynthesis. Of the 35 chlorophyll *a* molecules that are present within PSII, four specific chlorophyll *a* molecules (P680 chlorophylls) make up this reaction centre, buried within the core of PSII [9, 21].

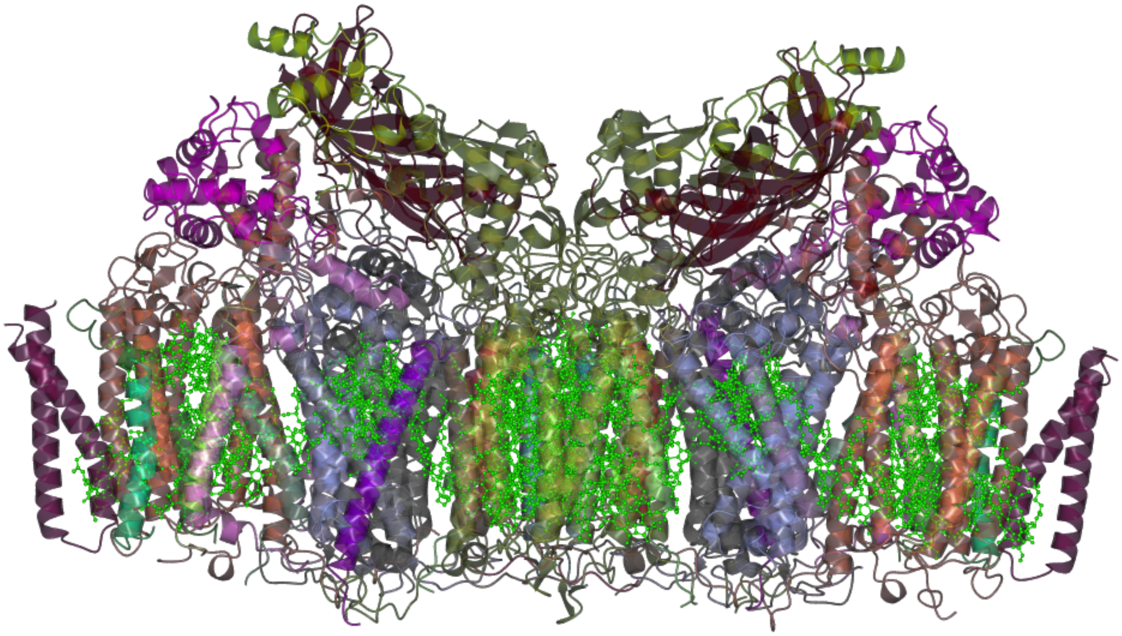

Figure 1.4: Overall structure of the photosystem II dimer from *T. vulcanus* at a 1.9Å resolution (PDBe ID 3WU2, [13]). The position of the 35 chlorophyll *a* molecules are shown in green. Other cofactors and water molecules are ommited for clarity. Coloured according to domain. Generated using CCP4 Molecular graphics program (University of York) [22].

PSI-LHCI, the second main reaction centre of the photosynthetic aparatus, is involved in the excitation of the electrons that are ultimately utilised during NADP$^+$ reduction, within PSI-LHCI, this occurs at special pair of chlorophyll *a* molecules, the p700 pair [11, 17].

The structure of PSI-LHCI from *Pisum sativum var. alaska* [20] provides a model example of PS I structure (Figure 1.5). Structurally the PSI (PSI-LHCI) supercomplex contains two components, the PSI 'core' and its chlorophyll abundent integral light-harvesting antenna, the light-harvesting complex I (LHCI).

Overall PS I contains 16 individual protein subunits and 240 individual ligands, much more than PS II, of which include 143 chlorophyll *a* molecules, 13 chlorophyll *b* molecules, 26 β-carotenes, 3 iron sulfur clusters, 2 phylloquinones, 10 detergents in addition to over 200 water molecules [20]. Within PS I, the p700 special pair lies at the dimer interface between the two main subunits of PS I, PsaA and PsaB [11].

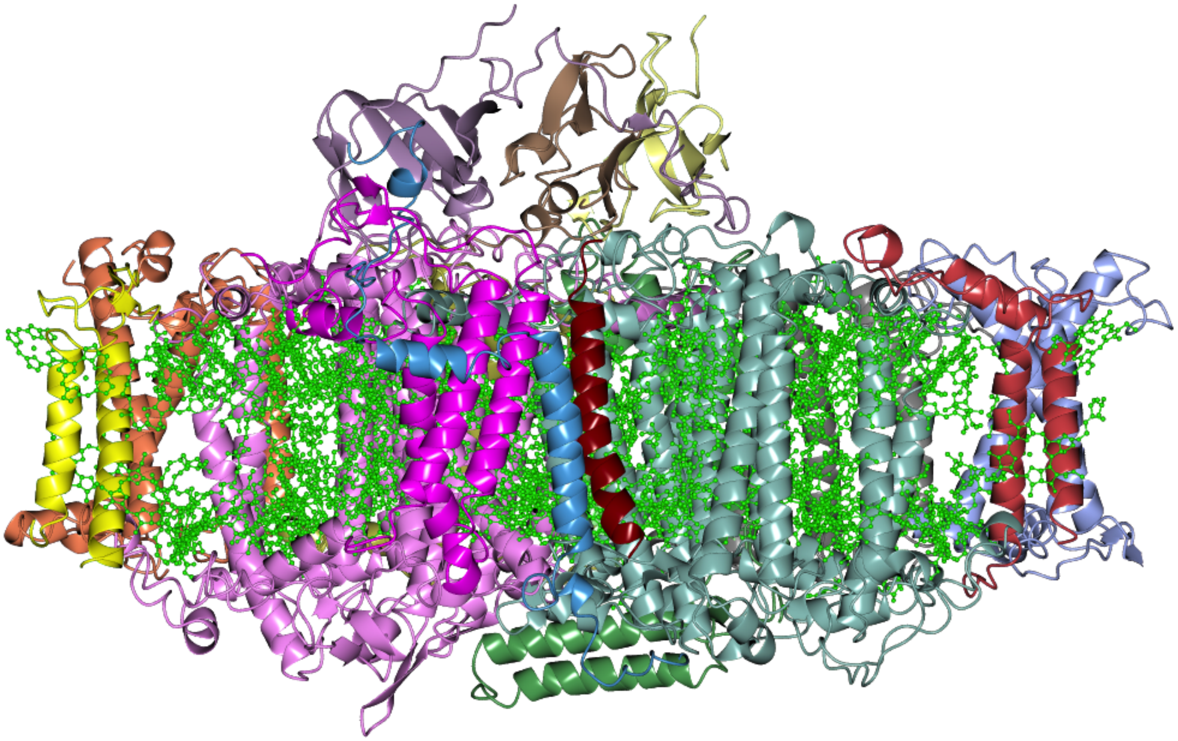

Figure 1.5: Overall structure of the PSI-LHCI from *Pisum sativum var. alaska* (PDBe ID 5L8R, [20]) at a 2.6Å resolution. The chlorophyll *a* and *b* molecules are shown in green. Other cofactors are ommited for clarity. Coloured according to domain. Generated using CCP4 Molecular graphics program (University of York) [22].

1.1.6 Phycobilisomes

Phycobilisomes are light harvesting antenna protein complexes of photosystem II, found in cyanobacteria and red algae, specilised in the efficient capture of subsequent transfer of photons to photosystem II to be utilised during photosynthesis [23, 24, 25]. Structurally (Figure 1.7), these phycobilisomes supercomplexes constitute numerous stack like arrangements of individual phycobiliproteins — homologous proteins containing α and β type subunits that are joined via linker polypeptides [24]. The 5 major classes of these phycobiliproteins which make up the larger phycobilisomes supercomplexes are outlined in Table 1.1.

The overall spectroscopic properties of a phycobiliprotein is governed by the type and chemical structure of the linear tetrapyrroles bilin prosthetic group it contains, in addition to the overall conformation orientation of the phycobiliprotein [24].

Table 1.1: The major classes of phycobiliprotiens. Adapted from Bryant *et. al* [26].

Phycobiliprotein class	Absorption maximum / nm	Fluorescence maximum / nm	Subunit structure
Allophycocyanin B	618 - 671	673	$(\alpha\beta)_3$
Allophycocyanin	650	660	$(\alpha\beta)_3$
Phycocyanin	610-620	637	$(\alpha\beta)_3$;$(\alpha\beta)_6$
Phycoerythrocyanin	568-590	607	$(\alpha\beta)_3$;$(\alpha\beta)_6$
Phycoerythrin	555-565	577	$(\alpha\beta)_3$

The overall tertiary structure of phycobiliproteins varies depending on the specific class (Table 1.1, far right column). Allophycocyanin B from *Synechocystis* PCC 6803 — one of the more structurally simpler phycobiliproteins (Figure 1.6) — exists as a trimer of dimers of $\alpha\beta$ subunits [27].

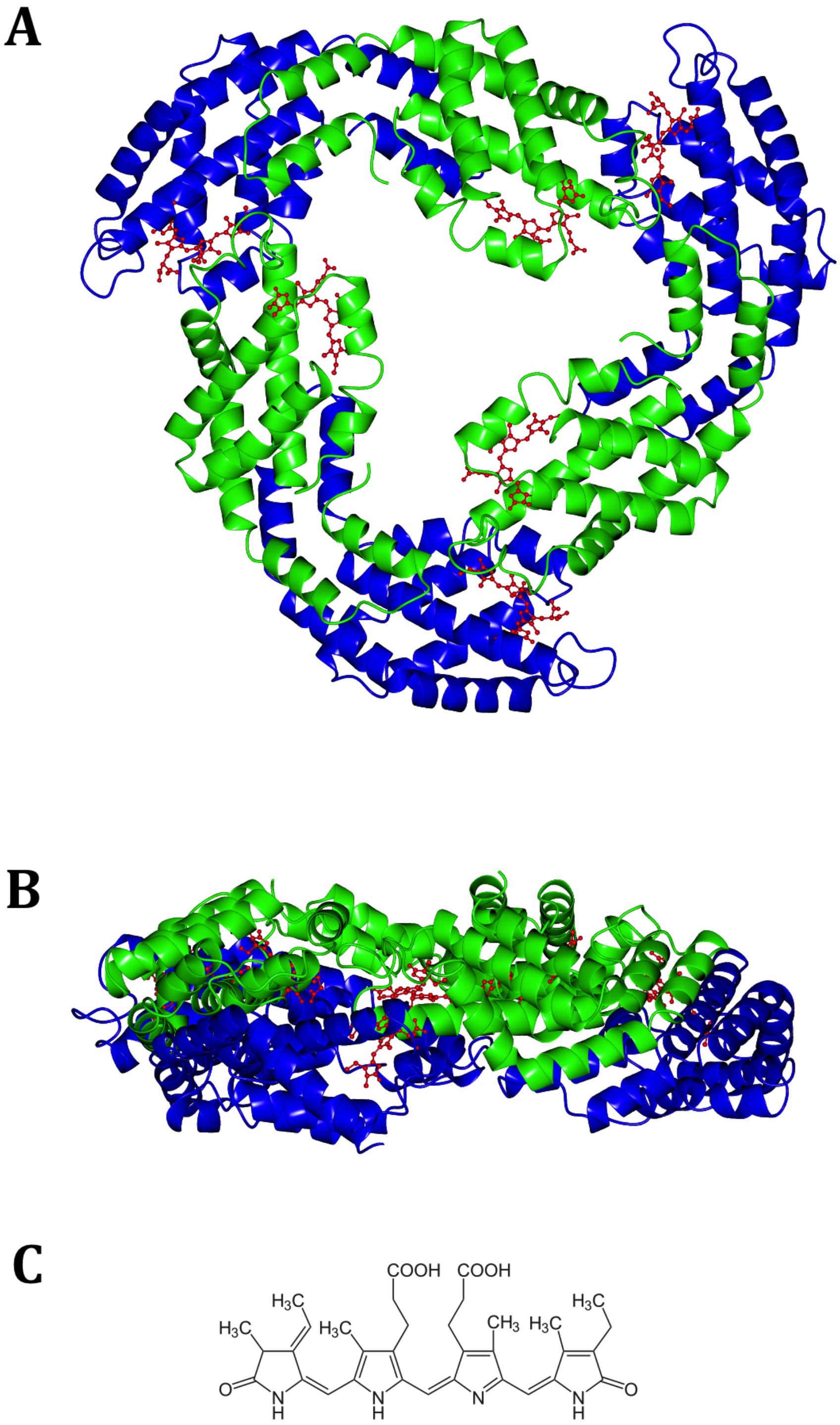

Figure 1.6: (Panels A and B) Model representation of the crystal structure of allophycocyanin B from *Synechocystis* PCC 6803 (PDBe ID 4po5, [27]). The phycocyanobilin prosthetic groups are shown in red. Generated using CCP4 Molecular graphics program (University of York), [22]. (Panel C) Structure of the phycocyanobilin prosthetic groups.

The final quaternary structure of the phycobilisome antenna supercomplex represents stacked like formations of individual phycobiliproteins proteins into a final barrel and rod like complex (a simplified representation is shown in Figure 1.7, adapted from reference [24].

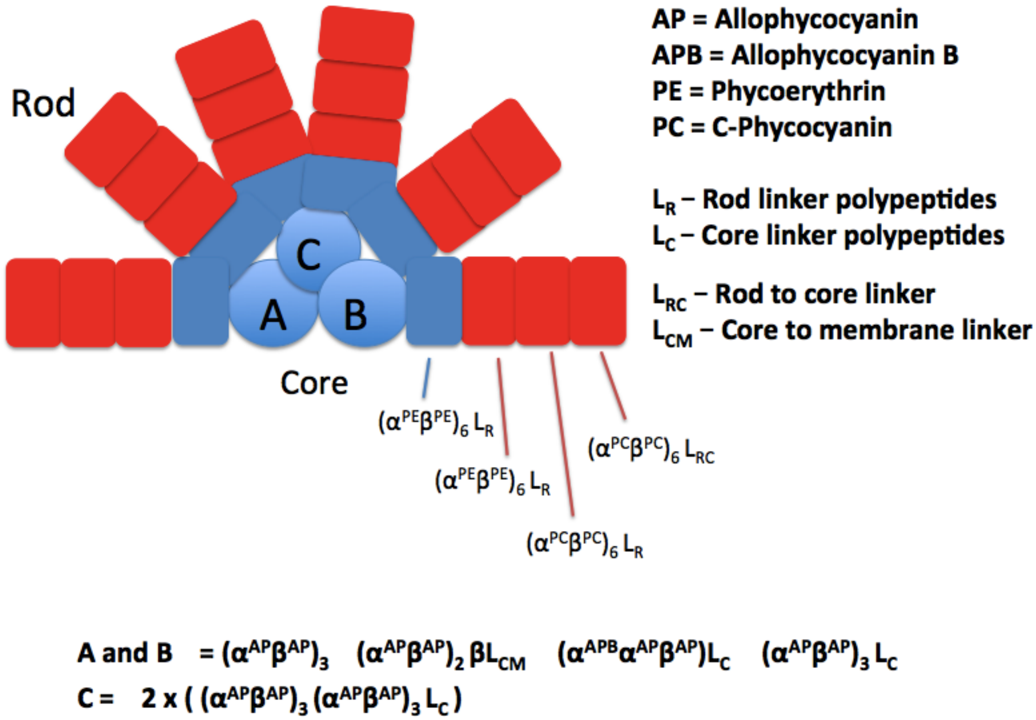

Figure 1.7: Simplified representation of the quaternary structure of the phycobilisome antenna supercomplex from *Synechocystis* 6701, constituting stacked superarrangements of individual phycobiliprotiens. The overall structure represents a central core with attatched rod like stacks of phycobiliproteins. Adapted from Glazer [24].

1.1.7 *Synechocystis* PCC 6803 - a model system for the study of photosynthesis

Cyanobacteria are the phylum of nitrogen fixing bacteria and the simplest oxygen-evolving photosynthetic organisms [5]. Since the identification of the first species of cyanobacteria in 1829 [28] there are currently approximately 2,698 known species [28]. *Synechocystis* PCC6803 is a specific species of unicellular fresh water cyanobacteria capable of oxygenic photosynthesis [29]. As a result of being naturally transformable by exogenous DNA [30], in addition to the ability for it to be grown at the expense of glucose, it remains a widely used model system in the study of proteins, and photosynthesis in general. The complete *Synechocystis* PCC6803 genome was first sequenced in 1996 [31] and was found to contain 3167 individual genes (Table 1.2), of which 131 having being impicated with involvement in photosynthesis and respiration [29].

Table 1.2: The function of the genes of *Synechocystis* PCC 6803. Adapted from Ikeuchi *et. al* [29].

Involvement	Number
Total	3167
Unknown function	1751
Other	255
Amino acid biosynthesis	84
Biosynthesis of cofactors, prosthetic groups and carriers	108
Cell envelope	64
Cellular processes	62
Central intermediary metabolism	31
Energy metabolism	86
Fatty acid, phospholipid and sterol metabolism	35
Photosynthesis and respiration	131
Nucleic acid metabolism	38
General regulatory functions	147
DNA replication, recombination and repair	49
Transcription	24
Translation	144
Transport and binding proteins	158

In current work, the ChlI, ChlD and ChlH subunits of magnesium chelatase from *Synechocystis* PCC 6803 [32] were used as a model system for the study of chelatase complexes.

1.2 The heme and chlorophyll biosynthetic pathways are identical until protoporphyrin-IX

Chlorophyll and heme share the same biosynthetic pathway until protoporphyrin-IX [33, 34].

5-Aminolevulinic acid (ALA) is the precursor of the heme and chlorophyll biosynthetic pathway and has two distinct synthetic routes depending on the organism, the first is a condensation reaction of glycine with Succinyl-Coenzyme A, catalysed by the enzyme 5-aminolevulinic acid synthase and occurs in animals, yeast and some bacteria. A second pathway the C_5 pathway utilises glutamyl- tRNA in a 3 step reaction occuring in higher plants, bryophytes, cyanobacteria, and many eubacteria [33].

The first step on the chlorophyll and heme biosynthetic pathway is the condensation of two ALA molecules catalysed by 5-Aminolevulinic acid dehydratase that results in the formation of porphobilinogen (Figure 1.8). Following this the sequential condensation of four porphobilinogen (PBG) molecules, catalysed by the enzyme porphobilinogen deaminase leads to the formation of 1-hydroxymethylbilane [33].

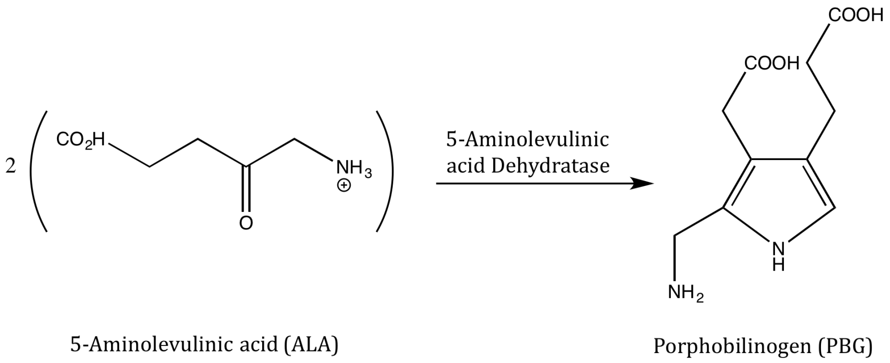

Figure 1.8: The condensation of 5-Aminolaevulinic acid resulting in the formation of porphobilinogen is the first step in the biosynthetic pathways of chlorophyll and heme [33].

The next steps in the pathway (Figure 1.9) involve firstly the ring closure of 1-hydroxymethylbilane, catalysed by uroporphyrinogen III synthase yeilding uroporphyrinogen III. Next uroporphyrinogen III decarboxylase catalyses the shortening of the four acetic acid side chains to methyl groups forming coproporphyrinogen III. Following this the conversion of two of the propionic acid side chains into vinyl groups by coproporphyrinogen III oxidase results in protoporphyrinogen IX. Finally protoporphyrinogen IX oxidase forms the conjugated double-bond system of protoporphyrin IX [33].

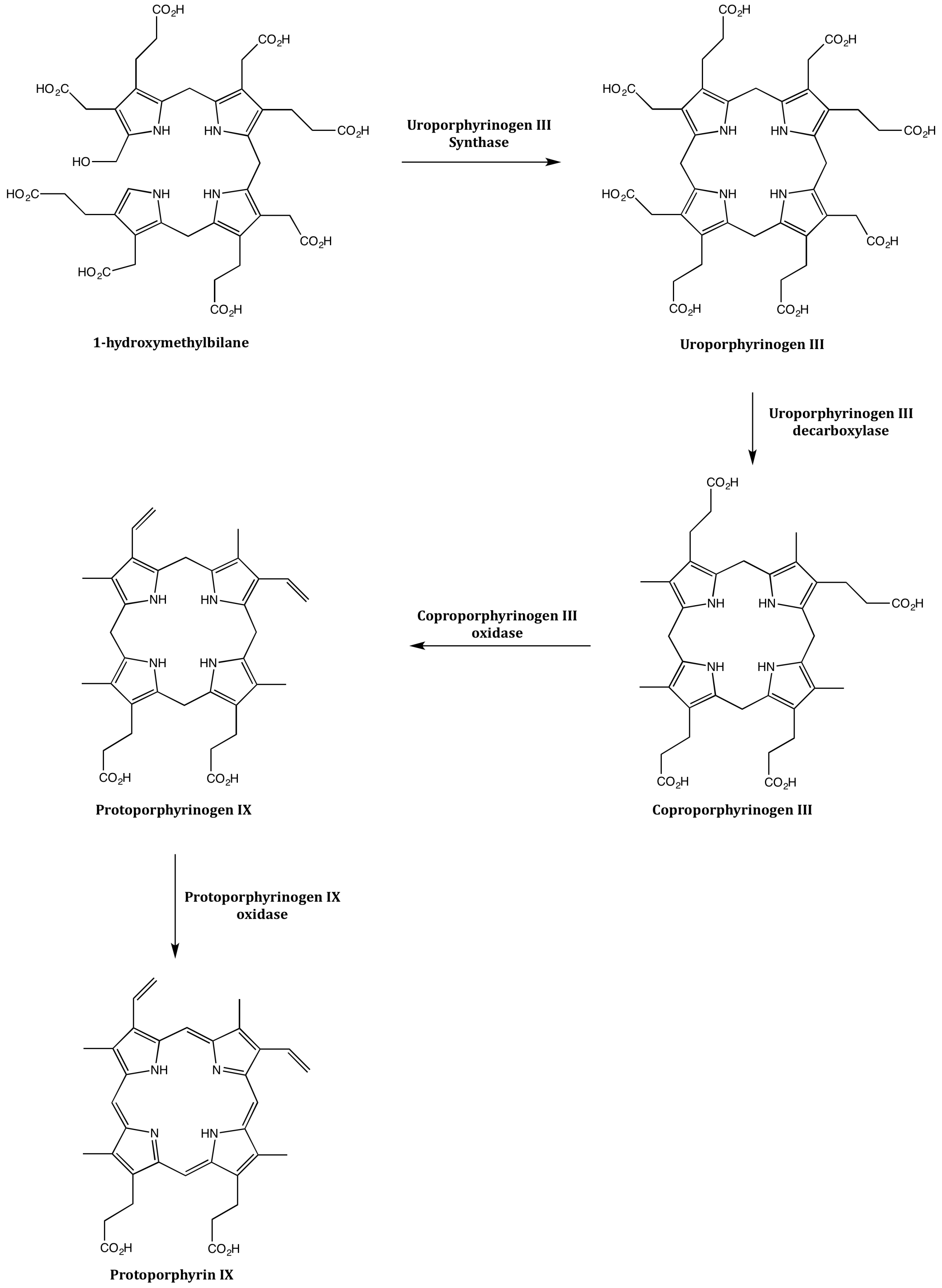

Figure 1.9: The biosynthetic pathways of heme and chlorophyll are identical from 1-hydroxymethylbilane to protoporphyrin IX [33].

1.3 Magnesium insertion into protoporphyrin-IX is the first committed step in chlorophyll biosynthesis

The insertion of the central Mg^{2+} ion into protoporphyrin-IX is the first committed step in chlorophyll biosynthesis, occurring at the branch-point between the biosynthetic pathways of heme and chlorophyll.

Magnesium insertion into protoporphyrin-IX is energetically unfavourable with a $\Delta G^{o\prime}$ of approximately 25-33 $kJ.mol^{-1}$ [35] and requires the complex multi-subunit enzyme system magnesium chelatase. The chelatase hydrolyses $MgATP^{2-}$ to provide the energy required for the reaction [35]. The alternative reaction at this branchpoint, the insertion of iron into protoporphyrin-IX forming heme, requires only the single, homodimeric protein ferrochelatase [36, 37, 38] and no additional requirement for ATP hydrolysis.

As two possible metal ion insertion reactions that can occur here form this branch point in the biosynthetic pathways of chlorophyll and heme, the two enzymes, magnesium chelatase and ferrochelatase, are expected to play a significant regulatory role in the overall downstream levels of chlorophyll and heme produced.

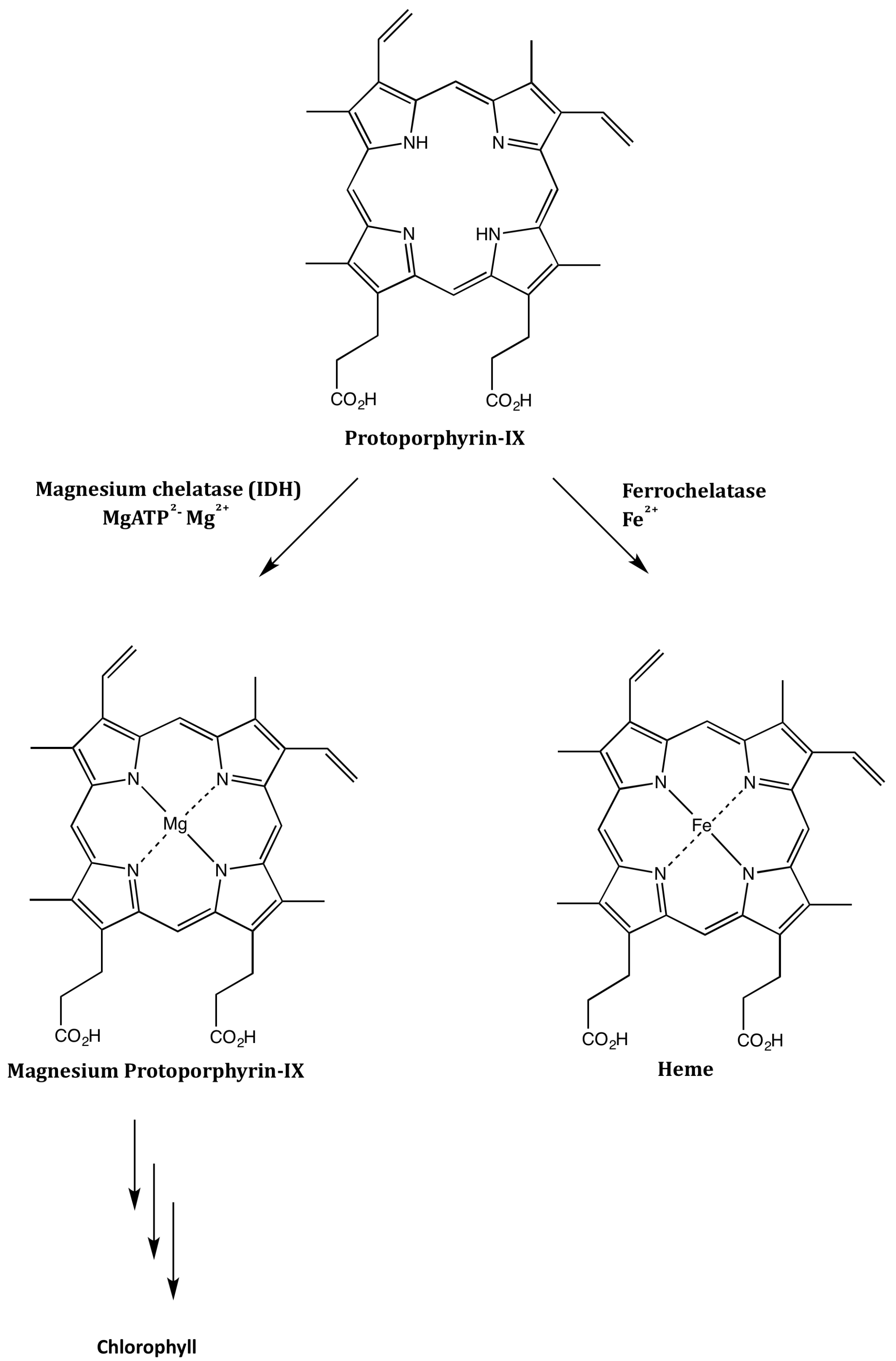

Figure 1.10: Mg^{2+} insertion into protoporphyrin-IX yeilding magnesium protoporphyrin-IX is the first committed step in chlorophylls biosynthetic pathway, occurring at a branch point in the heme and chlorophyll biosynthetic pathways.

1.4 The AAA$^+$ protein family

The AAA$^+$ protein family (ATPases Associated with various cellular Activities) represents a subset of functionally diverse proteins within the larger P-loop NTPase family. [39, 40, 41, 42, 43].

A vast range of AAA$^+$ family members have been studied and are involved in a wide range of processes including DNA replication and repair, membrane fusion, protein unfolding and degradation and intracellular transport [44].

The I and D subunits of magnesium chelatase are AAA$^+$ ATPases [42, 45] .

1.4.1 The AAA$^+$ domain

A distinguishing feature of the AAA$^+$ protein family is a conserved region of approximately 200 — 250 amino acid residues, commonly referred to as the AAA$^+$ domain. The AAA$^+$ domain contains two distinct sub-domains, an N-terminal α/β (Rossman fold) region and a C-terminal α-helical region [40]. The crystal structures of many AAA$^+$ family members have been determined showing a high degree of conservation of this two-domain architecture [44]. The core of the N-terminal subdomain constitutes parallel strands of β-sheets arranged in the form of β5-β1-β4-β3-β2, with the position of β4 being unique to the AAA$^+$ domain when compared to other nucleotide-binding domains. Additionally the structural and functional diversity observed between different AAA$^+$ domains can be attributed to the number and position of the five or more α-helices that connect the strands of this core β-sheet [44]. The C-terminal sub-domain constitutes several α-helices and is another distinguishing feature of the AAA$^+$ family [40].

The Walker A and B motifs, responsible for nucleotide binding and hydrolysis are contained within the AAA$^+$ domain. The Walker A motif (GXXXXGK[T/S], where X denotes any amino acid) is responsible for nucleotide binding. Within the Walker A motif, conserved lysine and threonine/serine residues bind the β- and γ-phosphates of bound ATP substrate and Mg^{2+} ions [46]. The lysine residue has also been suggested to be involved in maintaining the correct conformation of the P-loop [40]. The Walker B motif, involved in nucleotide binding and hydrolysis (hhhhDE, where h denotes any hydrophobic amino acid) contains acidic residues critical for ATPase activity. Within this motif the aspartate residue is suggested to coordinate Mg^{2+} during ATP hydrolysis, whilst the glutamate residue activates water for hydrolysis [44].

Another region, the second region of homology (SRH), contains additional conserved regions seen throughout the AAA$^+$ family, the sensor-I region and arginine finger [44, 43]. The sensor-I lies in close proximity to the Walker A and B motifs and contains a conserved polar residue involved in nucleotide hydrolysis [47]. The second conserved region within the SRH, the Arginine finger has been implicated in processes including nucleotide hydrolysis and intersubunit communication [48].

The AMPPNP-Mg^{2+} bound crystal structure of the D2 domain of the N-ethylmaleimide sensitive factor (D2-NSF) has been determined [49] and provides an illustrative representation of the AAA$^+$ domain (Figure 1.11). The relative position of the Walker A, Walker B, sensor-I regions and the position of bound nucleotide (AMPPNP-Mg^{2+}) are highlighted.

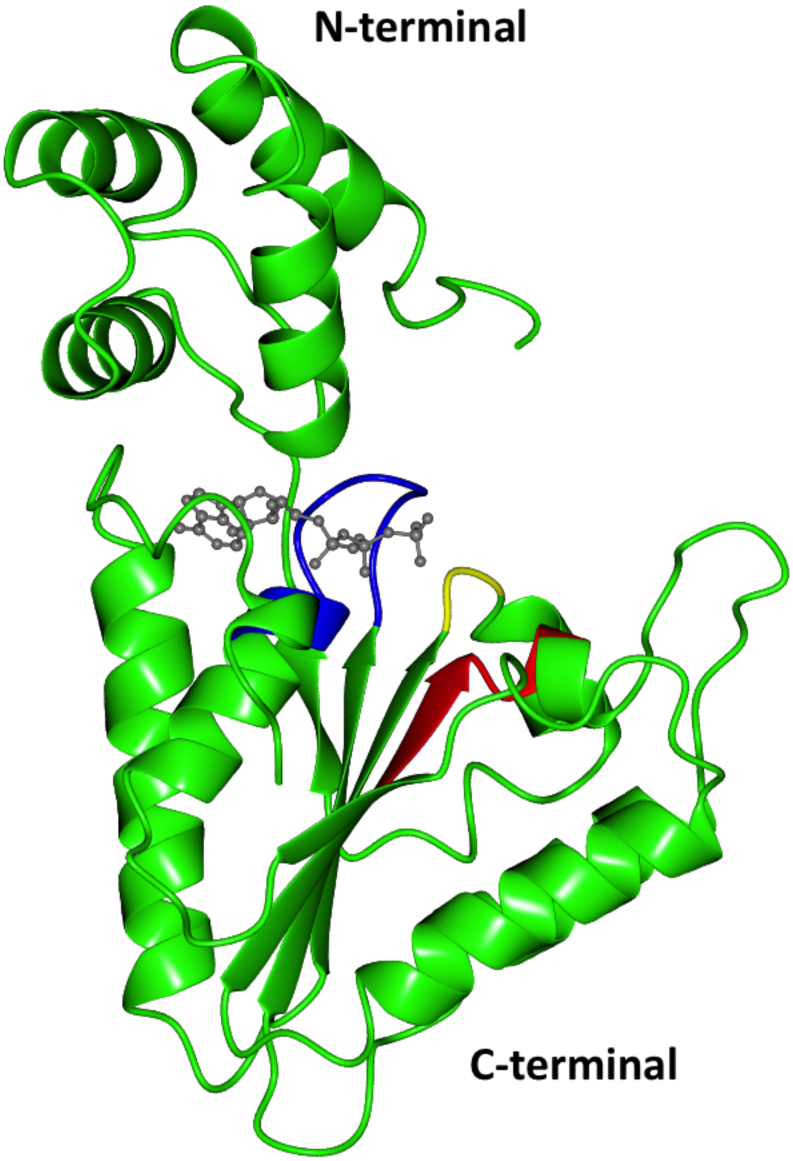

Figure 1.11: The AAA$^+$ N-ethylmaleimide sensitive factor (NSF) D2 domain (PDB-ID 1D2N, [49]) provides an illustrative example of the AAA$^+$ domain. The positions of the Walker A (blue), Walker B (red) and sensor-I (yellow) motifs are highlighted, bound nucleotide is Mg^{2+}-AMPPNP. Generated using CCP4 Molecular graphics program (University of York) [22].

1.4.2 Structural features of AAA$^+$ proteins

A widely observed structural feature of AAA$^+$ proteins is the formation of rings of their individual subunits — commonly hexamers although other types have been demonstrated — with these rings often representing the active form of the enzyme. Within these rings, the central pore often serves a functional role, with the threading of AAA$^+$ protein substrates through this central pore often occurring, and being essential during the catalytic roles of AAA$^+$ proteins [50, 41]. Examples of the arrangements formed by an array of AAA$^+$ proteins are summarised in Table 1.3.

Table 1.3: Examples of the active arrangements of AAA$^+$ proteins.

AAA$^+$ member	Involvement	Active arrangement	References
VPS4	Membrane protein sorting	Homohexamer	[51, 52]
ClpX	Protein degradation	Homohexamer	[53, 54]
ClpP	Peptide cleavage	Homoheptamer	[55, 56]
NSF	Membrane fusion processes	Homohexamer	[57]
Pex1 / Pex6	Peroxisomal transport	Heterohexamer	[58]
Dynein	Intracellular transport	Heterohexamer	[59]
RuvB	DNA recombination	Homohexamer	[60]
Replication factor C	DNA replication	Heteropentamer	[61]

Although the formation of single rings is common, two-tiered arrangements of AAA$^+$ protein subunits can also occur, such as those formed by ClpP and ClpX yielding ClpXP [53] and P97 [62].

A model representation of an ATP-dependent hexameric assembly of the N-ethylmaleimide sensitive factor, based on single particle cryoelectron microscopy data [63], provides a illustrative example of these hexameric assemblies (Figure 1.12).

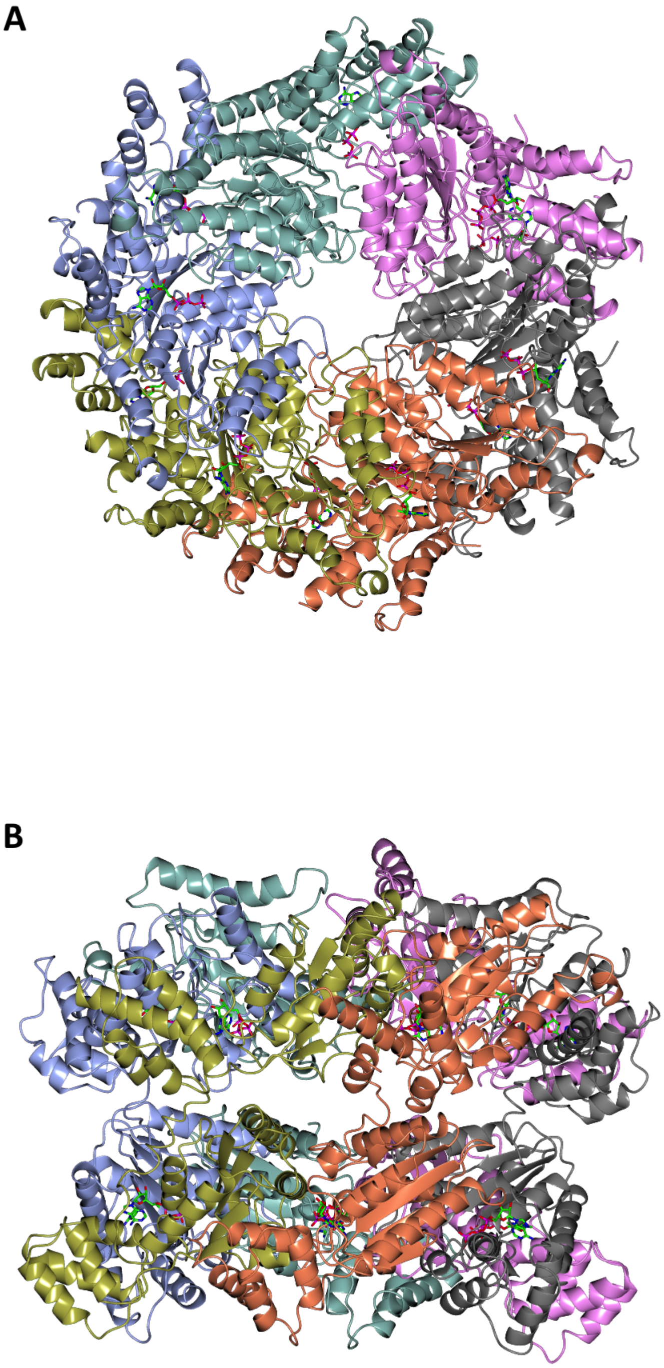

Figure 1.12: The AAA$^+$ N-ethylmaleimide sensitive factor (NSF) provides a model example of hexameric rings formed by AAA$^+$ proteins. Top (A) and side (B) views of a model representation of hexameric rings formed by NSF in the presence of ATP based on single particle cryoelectron microscopy data (PDBe ID 3j94 [63]). Generated using CCP4 Molecular graphics program (University of York) [22].

Within rings formed by AAA$^+$ proteins, nucleotide binding and hydrolysis occurs at the interface between subunits [41]. At this interface, or active site, inter subunit communication is facilitated by sensors which detect the presence of the γ-phosphate and relay this information via conformational changes throughout the ring [64, 48].

There are multiple models describing the ATP hydrolysis occurring within hexameric rings of AAA $^+$ proteins, including synchronised, rotational and sequential [64]. Within a synchronised model, ATP hydrolysis is performed by all 6 subunits simultaneously, conserving the overall symmetry of the ring. Within rotational models, every other subunit within the ring is active and at a different ATP hydrolysis state. Whilst in a sequential model, all subunits are active, with the subunits directly opposite each other in phase (Figure 1.13).

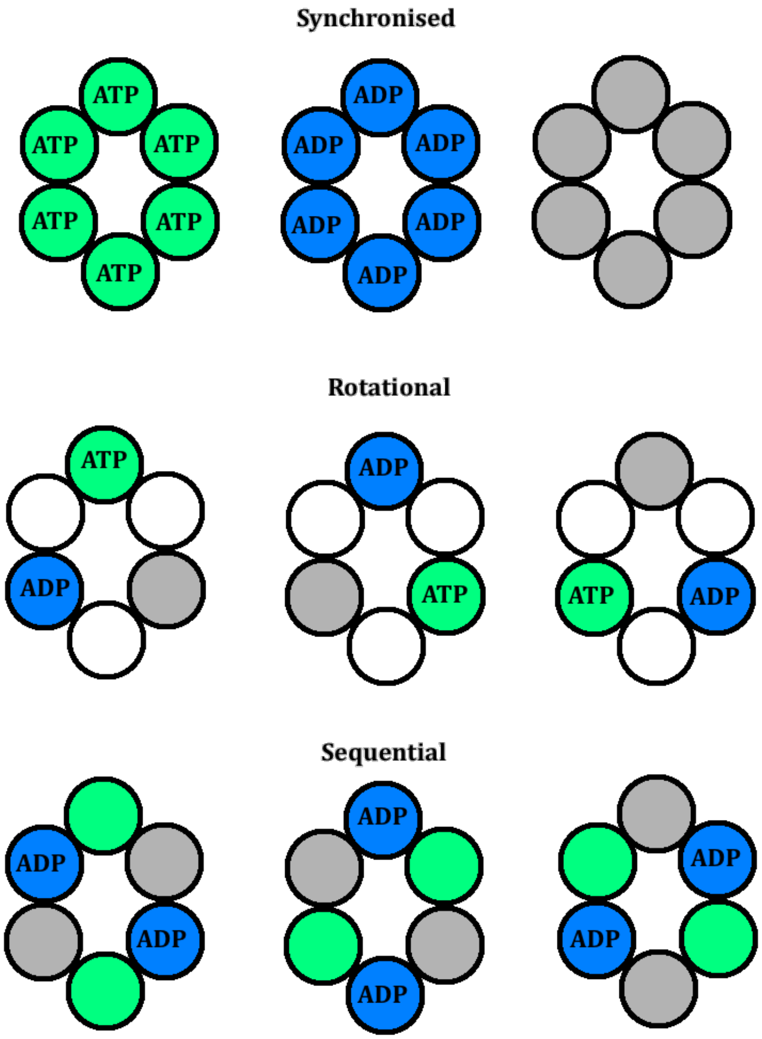

Figure 1.13: Synchronised, rotational and sequential models for ATP hydrolysis within AAA$^+$ hexamers. Green is ATP-bound, Blue is ADP- and Pi- bound, and grey is nucleotide free. Adapted from [64].

The complexes formed by AAA$^+$ proteins are structurally dynamic, exhibiting a high degree of structural rearrangment between specific nucleotide states. The exact nature of such conformational changes varies between different AAA$^+$ proteins, however changes in relation to the relative positions of the N and C sub-domains, in addition to opening or closing of a central pore are commonly observed [41, 50].

Specific examples include the conformational asymmetry observed in VPS4 following ATP hydrolysis, with the ADP bound form having one high-affinity and five-low affinity binding sites [65], whilst within ClpX, nucleotide binding results in a taller and more narrow hexamer with constriction of its central pore [54]. Within the protein transporting Pex1/6 complex, the hetero-hexameric rings formed by a trimer of Pex1/6 dimers undergo a high degree of conformation variation between nucleotide states, demonstrated by single particle electron microscopy reconstructions of the Pex1/6 complex in the presence of ADP, ATP and ATPγS [58]. With the ATPγS bound showing a constricted central pore and overall taller structure, in comparison to the ADP bound form having a much larger pore and an overall shorter structure (Figure 1.14).

Such nucleotide dependent conformational changes are thought to allow AAA$^+$ proteins to couple ATP hydrolysis with mechanic work on their substrates [44, 50].

Although these AAA $^+$ complexes are likely to undergo a high degree of comformational change when hydrolysing nucleotide, the complexes often remain fully assembled throughout multiple ATP hydrolysis cycles, especially those that thread their substrates through a central pore [44, 64]. However the exchange of subunits within complexes of AAA$^+$ proteins can occur and has been demonstrated in some AAA$^+$ proteins including ClpB [66] and magnesium chelatase [67].

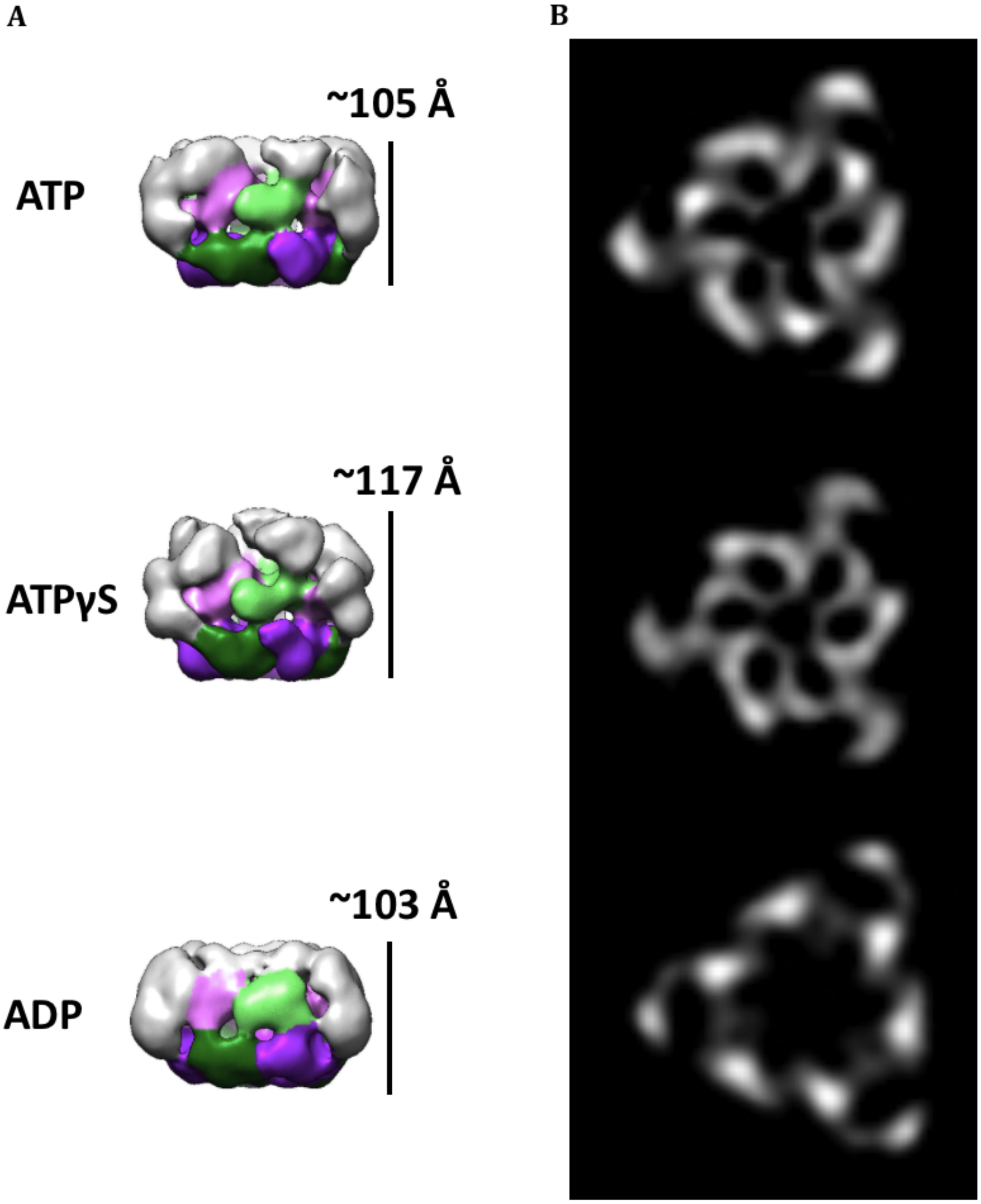

Figure 1.14: The overall conformation of the AAA$^+$ Pex1/6 complex is highly dependent on nucleotide state. (A) Electron microscopy reconstructions for the ATP bound (EMD-2585), ADP bound (EMD-2582) and ATPγS bound (EMD-2583) *S. cerevisiae* Pex1/6 wild type complex [58]. (B) Slice views of the corrosponding electron microscopy reconstitutions, produced using the PDBe volume slicer at www.rcsb.org [68]. EMD codes correspond to EM entries in Protein Data Bank in Europe [58].

1.5 Magnesium chelatase contains three essential protein subunits - I, D and H

The magnesium chelatase enzyme system contains three essential protein subunits, I (38-42 kDa), D (60-74 kDa) and H (140-150 kDa). The gene isolation and subsequent over-expression systems of the individual subunits of magnesium chelatase is well established and has led to in depth studies of the subunits from numerous species including bacteria *Rhodobacter sphaeroides* [69, 70], *Rhodobacter capsulatus* [71], *Synechocystis* PCC6083 [72] and *Thermosynechococcus elongatus* [73], in addition to plants including rice (*Oryza sativa*) [74], barley [75] and pea [76].

Magnesium insertion into protoporphyrin-IX is an energetically unfavourable and complex process. The reaction requires both ATP in the form of $MgATP^{2-}$ and free Mg^{2+} ions. The enzyme is also activated by Mg^{2+} ions [35]. Studies on the *Synechocystis* system have shown that the insertion of a Mg^{2+} ion into protoporphyrin-IX requires the hydrolysis of approximately 15 $MgATP^{2-}$ molecules, resulting in a $\Delta G^{o\prime}$ of approximately -880kJ mol^{-1} [35], whilst approximately 40 $MgATP^{2-}$ molecules are required by the enzyme from *Rhodobacter capsulatus* [77]. Further highlighting the complex behaviour of magnesium chelatase is the species dependent regulatory role played by Mg^{2+}. A cooperative response in free Mg^{2+} is seen for the chelatase within some species including *Synechocystis* [32, 35], while the enzyme from other species such as *Thermosynechococcus elongatus* exhibit no such cooperative response [73]. An additional protein GUN4 also stimulates magnesium chelatase activity, however it is not essential for metal ion chelation in vitro [78, 79, 80].

The overall configuration and orientation of subunits within the active chelatase complex formed by the I, D and H subunits is poorly understood, with an active, intact IDH complex yet to be isolated. However, the active chelatase is thought to contain two distinct components. An ATPase motor complex containing an unknown number of the AAA^{+} I and D subunits providing the energetic driving force and the porphyrin binding catalytic H subunit [81].

1.5.1 The I subunit of magnesium chelatase

The I subunit (38-42 kDa) belongs to the AAA$^+$ protein family [45] and is the only subunit of magnesium chelatase with an ATPase activity [35, 82]. Sequence alignment of the I subunit (Figure 1.15) demonstrates the high degree of sequence similarity between different species, as well as the conservation of the Walker A and B motifs involved in nucleotide binding and hydrolysis.

The crystal structure of *Rhodobacter capsulatus* BchI has been determined [45]. A model representation of the BchI subunit is shown in Figure 1.16.

Overall the BchI subunit is similar to many other AAA$^+$ proteins and contains two distinct N- and C-terminal domains. The N-terminal domain (residues 1-265) contains the Walker A and B motifs involved in nucleotide binding and hydrolysis. The C-terminal domain (residues 266-350) has a unique orientation in relation to the N-terminal domain in comparison to other AAA$^+$ proteins with the C-terminal domain lying directly behind the nucleotide binding site. Additionally the presence of a deep, positivly charged groove is evident within BchI, constituting 10 arginine residues, proposed to be a possible binding site with the BchD subunit [45]. The sensor-I motif, involved in the detection of nucleotide binding and hydrolysis [48], is also present within BchI. Although no crystal structures have yet to be determined for other I subunits, the high sequence similarity that between different species of this subunit would imply a relatively conserved overall structure for the I subunit [45].

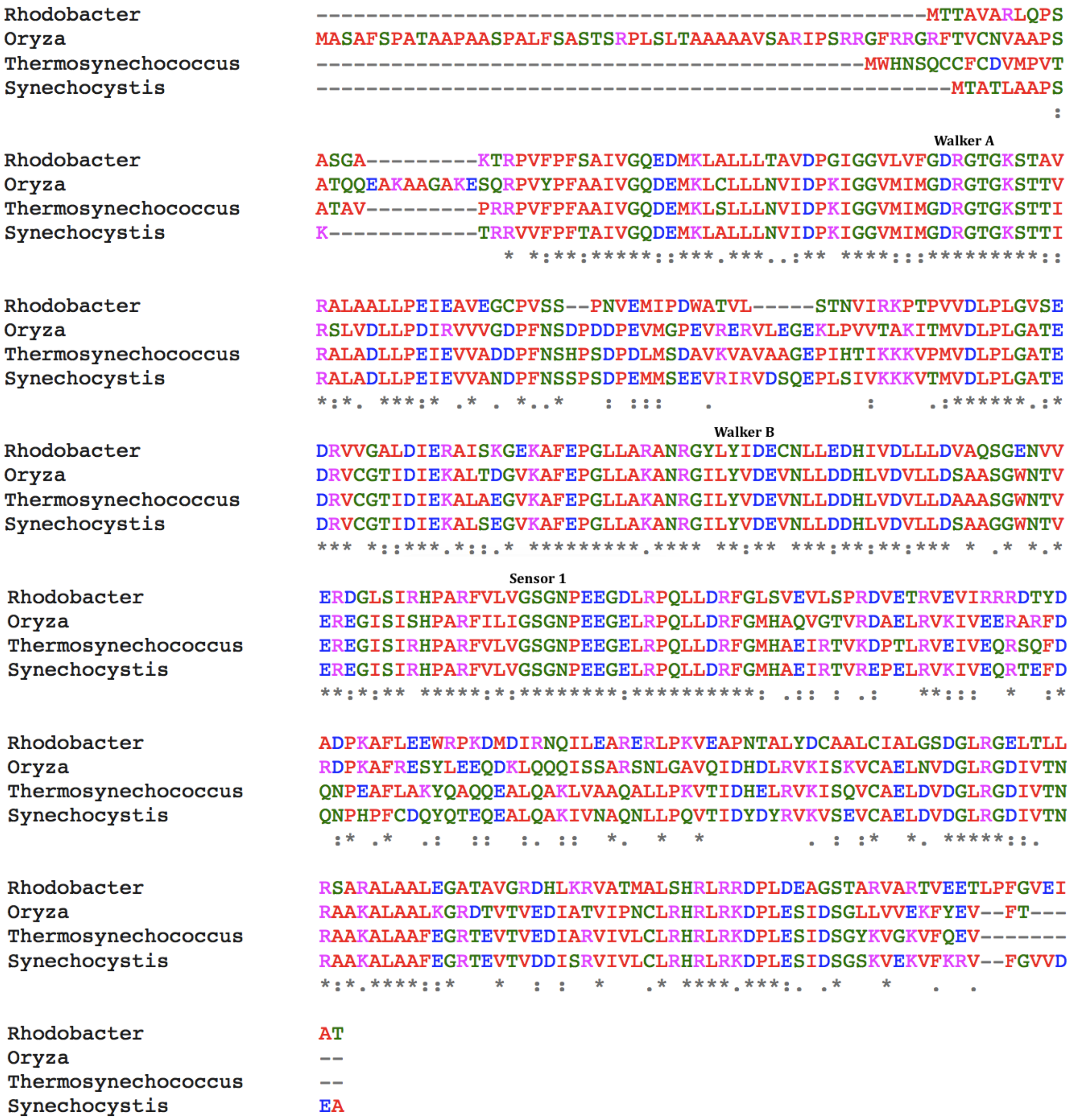

```
Rhodobacter             -------------------------------------------------MTTAVARLQPS
Oryza                   MASAFSPATAAPAASPALFSASTSRPLSLTAAAAAVSARIPSRRGFRRGRFTVCNVAAPS
Thermosynechococcus     --------------------------------------------MWHNSQCCFCDVMPVT
Synechocystis           ---------------------------------------------------MTATLAAPS
                                                                                   :

                                                                 Walker A
Rhodobacter             ASGA---------KTRPVFPFSAIVGQEDMKLALLLTAVDPGIGGVLVFGDRGTGKSTAV
Oryza                   ATQQEAKAAGAKESQRPVYPFAAIVGQDEMKLCLLLNVIDPKIGGVMIMGDRGTGKSTTV
Thermosynechococcus     ATAV---------PRRPVFPFAAIVGQDEMKLSLLLNVIDPKIGGVMIMGDRGTGKSTTI
Synechocystis           K------------TRRVVFPFTAIVGQDEMKLALLLNVIDPKIGGVMIMGDRGTGKSTTI
                                       * *:**:*****::***.***..:** ****:::*********::

Rhodobacter             RALAALLPEIEAVEGCPVSS--PNVEMIPDWATVL-----STNVIRKPTPVVDLPLGVSE
Oryza                   RSLVDLLPDIRVVVGDPFNSDPDDPEVMGPEVRERVLEGEKLPVVTAKITMVDLPLGATE
Thermosynechococcus     RALADLLPEIEVVADDPFNSHPSDPDLMSDAVKVAVAAGEPIHTIKKKVPMVDLPLGATE
Synechocystis           RALADLLPEIEVVANDPFNSSPSDPEMMSEEVRIRVDSQEPLSIVKKKVTMVDLPLGATE
                        *:*. ***:* .* . *..*   : :::   .            :    .:******.:*

                                                        Walker B
Rhodobacter             DRVVGALDIERAISKGEKAFEPGLLARANRGYLYIDECNLLEDHIVDLLLDVAQSGENVV
Oryza                   DRVCGTIDIEKALTDGVKAFEPGLLAKANRGILYVDEVNLLDDHLVDVLLDSAASGWNTV
Thermosynechococcus     DRVCGTIDIEKALAEGVKAFEPGLLAKANRGILYVDEVNLLDDHLVDVLLDAAASGWNTV
Synechocystis           DRVCGTIDIEKALSEGVKAFEPGLLAKANRGILYVDEVNLLDDHLVDVLLDSAAGGWNTV
                        *** *::***.*::.* *********.**** **:** ***:**:**:*** * .* *.*

                                       Sensor 1
Rhodobacter             ERDGLSIRHPARFVLVGSGNPEEGDLRPQLLDRFGLSVEVLSPRDVETRVEVIRRRDTYD
Oryza                   EREGISISHPARFILIGSGNPEEGELRPQLLDRFGMHAQVGTVRDAELRVKIVEERARFD
Thermosynechococcus     EREGISIRHPARFVLVGSGNPEEGELRPQLLDRFGMHAEIRTVKDPTLRVEIVEQRSQFD
Synechocystis           EREGISIRHPARFVLVGSGNPEEGELRPQLLDRFGMHAEIRTVREPELRVKIVEQRTEFD
                        **:*:** *****:*:********:**********: .:: : .:   **:::  *  :*

Rhodobacter             ADPKAFLEEWRPKDMDIRNQILEARERLPKVEAPNTALYDCAALCIALGSDGLRGELTLL
Oryza                   RDPKAFRESYLEEQDKLQQQISSARSNLGAVQIDHDLRVKISKVCAELNVDGLRGDIVTN
Thermosynechococcus     QNPEAFLAKYQAQQEALQAKLVAAQALLPKVTIDHELRVKISQVCAELDVDGLRGDIVTN
Synechocystis           QNPHPFCDQYQTEQEALQAKIVNAQNLLPQVTIDYDYRVKVSEVCAELDVDGLRGDIVTN
                         :* .*  .:  ::  :. ::  *.  *  *        . : :*  *. *****::.

Rhodobacter             RSARALAALEGATAVGRDHLKRVATMALSHRLRRDPLDEAGSTARVARTVEETLPFGVEI
Oryza                   RAAKALAALKGRDTVTVEDIATVIPNCLRHRLRKDPLESIDSGLLVVEKFYEV--FT---
Thermosynechococcus     RAAKALAAFEGRTEVTVEDIARVIVLCLRHRLRKDPLESIDSGYKVGKVFQEV-------
Synechocystis           RAAKALAAFEGRTEVTVDDISRVIVLCLRHRLRKDPLESIDSGSKVEKVFKRV--FGVVD
                        *:*.****::*   *  : :  *   .* ****.***:. .*   *   .  .

Rhodobacter             AT
Oryza                   --
Thermosynechococcus     --
Synechocystis           EA
```

Figure 1.15: Sequence alignment of *Thermosynechococcus elongatus* ChlI (UniProt code Q8DIS0), *Rhodobacter capsulatus* BchI (UniProt code P26239), *Synechocystis* sp. PCC6803 ChlI (UniProt code P51634) and rice ChlI *Oryza sativa* (UniProt Code Q53RM0) show a high degree of sequence similarity. The position of residues within the nucleotide binding Walker A and B motifs and sensor-1 region are highlighted. Sequence alignment was generated using MUltiple Sequence Comparison by Log- Expectation (MUSCLE) sequence alignment tool (EMBL-EBI, UK) [83]. Codes relate to the UniProt [84] accession number.

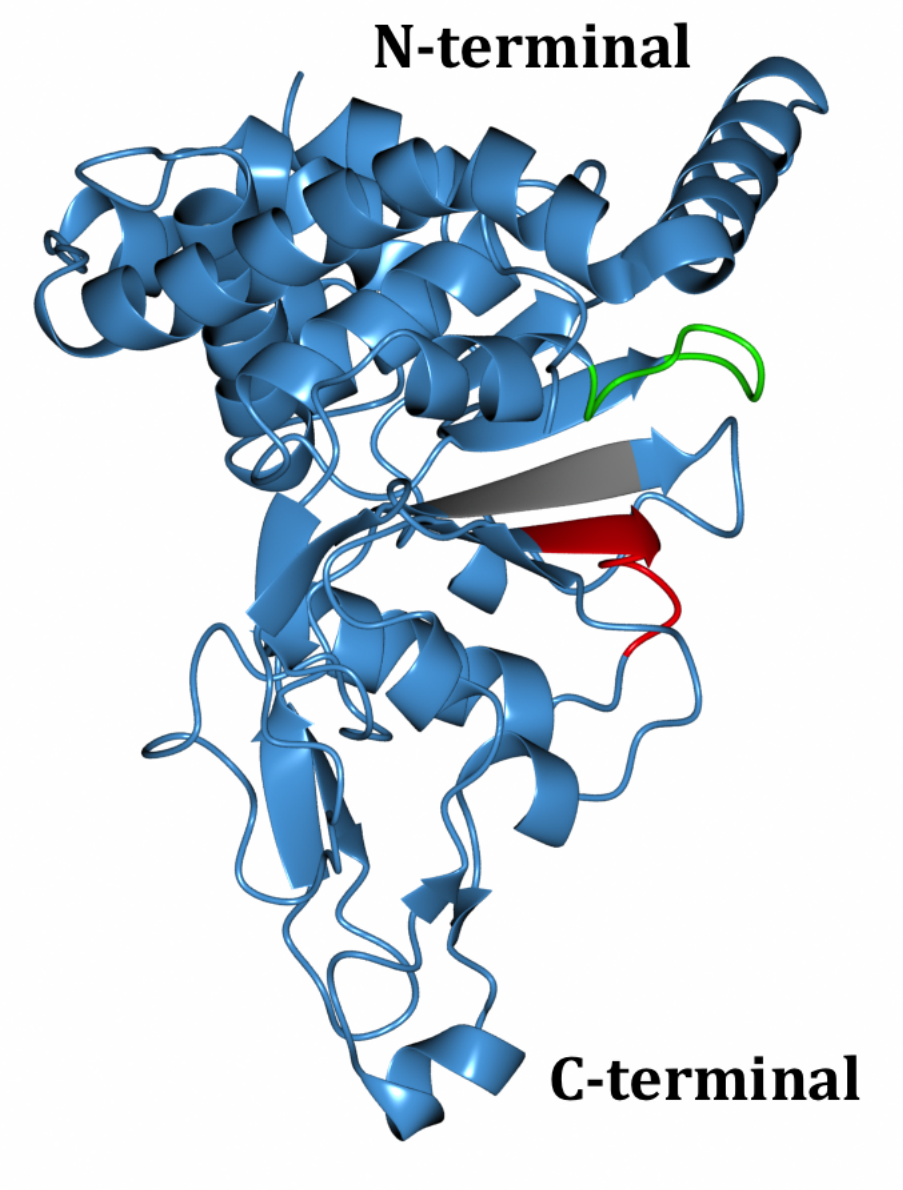

Figure 1.16: The *Rhodobacter capsulatus* BchI subunit (PDB ID 1G8P, [45]). The N-terminal nucleotide binding Walker A and B motifs are highlighted in green and red respectively, the sensor-I region is highlighted in grey. Generated using CCP4 Molecular graphics program [22] (University of York).

An ATPase activity for the I subunit both in isolation and in combination with the D and H subunits has been demonstrated within numerous species including *Synechocystis* ChlI [82, 85] and *Rhodobacter sphaeroides* BchI [86, 87]. Unlike the D and H subunits the I subunit is the only subunit of magnesium chelatase to exhibit an essential ATPase activity. Furthermore the ATPase activity of *Synechocystis* ChlI requires free Mg^{2+} [35], suggesting the presence of at least one magnesium binding site within ChlI.

The I subunit, like numerous other AAA^+ proteins, can form ring like arrangements of subunits in the presence of nucleotide (Figure 1.17). The *Synechocystis* ChlI subunit, in the presence of $MgATP^{2-}$, has been shown to assemble into a range of ring like structures including 6-, 7- and 8-fold arrangements with heptamers being directly observed [85], whilst *Rhodobacter capsulatus* BchI can form hexamers in addition to smaller arrangements in the presence of ATP [45, 88].

Although ring like assemblies of AAA^+ proteins often represent their active form [40, 44], it is currently unknown whether similar such behaviour is shared with the I subunit. Previously it was demonstrated that initiating a chelatase reaction with pre-formed complexes of ChlI — formed by preincubating the ChlI subunit with ATP — resulted in a substantial lag phase prior to steady state metal ion chelation occuring [32]. Such behaviour would indicate that pre-assembled complexes of ChlI formed in the absence of other subunits do not represent active components of the chelatase system, however such experiments cannot rule out the formation of ring like arrangements of the I subunit during the reaction cycle.

Overall, with the I subunit being the only subunit of magnesium chelatase to exhibit an essential ATPase activity, the ATP hydrolysis performed by this subunit is essential for driving the Mg^{2+} insertion reaction.

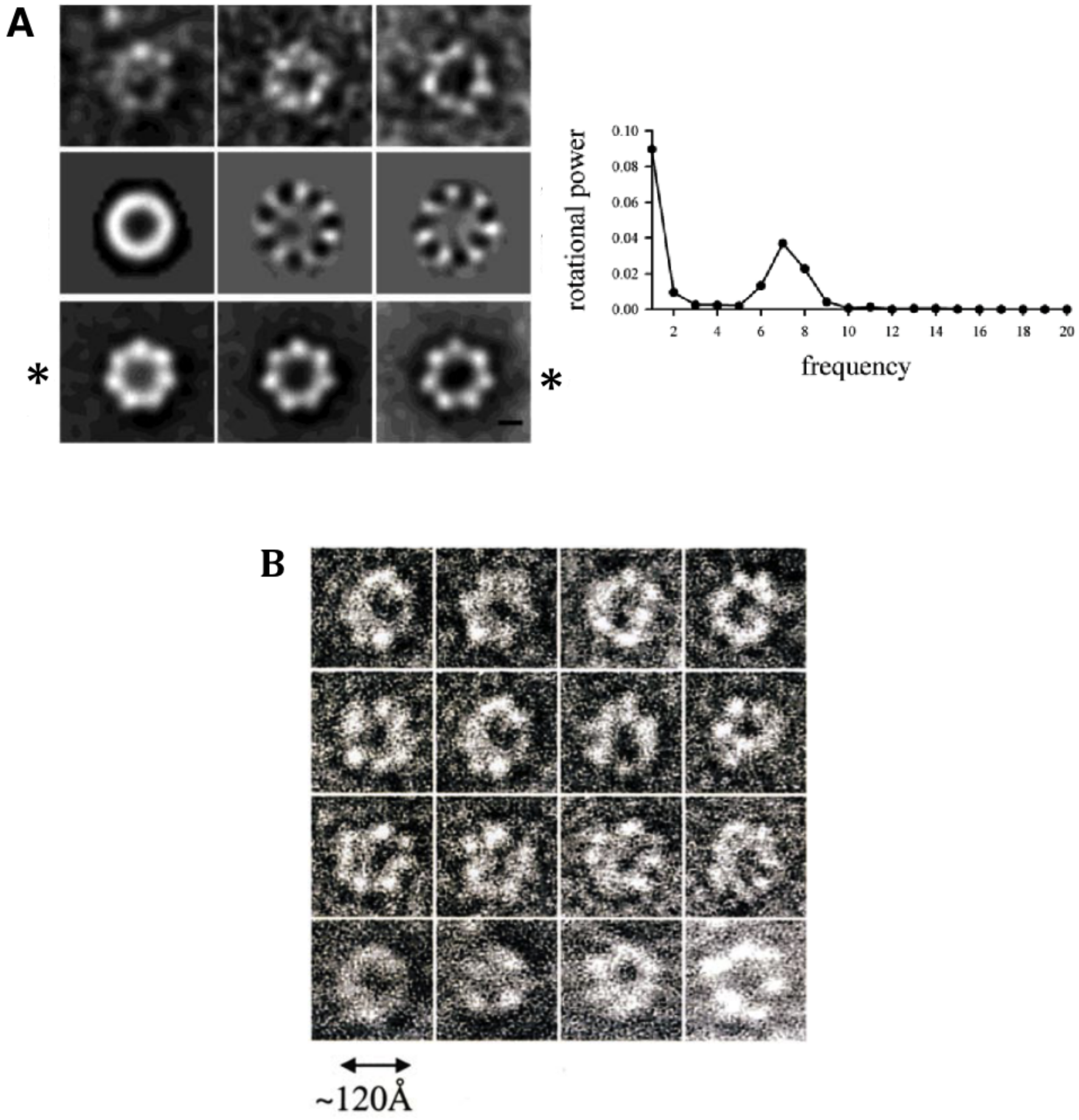

Figure 1.17: The I subunit undergoes the formation of ring-like assemblies in the presence of nucleotide. (Panel A) electron microscopy of *Synechocystis* ChlI shows formation of ring-like assembelies, row * denotes class averages. Figure was adapted with permisson from [85]. (Panel B) Electron microscopy of *Rhodobacter capsulatus* BchI shows formation of ring-like assemblies in the presence of 4mM ATP and 10mM $MgCl_2$, figure was adapted with permission from [45].

1.5.2 The D subunit of magnesium chelatase

The D subunit (60-74kDa) also belongs to the AAA$^+$ protein family [42], however unlike the I subunit lacks ATPase activity. Analysis of site directed mutants suggests a regulatory role by this subunit within the chelatase system [89, 90].

Structurally the D subunit contains 3 distinct regions, an N-terminal AAA$^+$ domain with a high sequence similarity to the I subunit (Figure 1.18), a C-terminal domain containing an integrin-I domain and MIDAS (Metal Ion dependent Adhesion Site) motif [45, 91] and a polyproline rich linker connecting the N- and C-terminals [45]. An overview of the structural features of the D subunit and sequence alignment between different species is shown in Figure 1.19.

The N-terminal AAA$^+$ domain of the D subunit shares a high sequence similarity with the I subunit (Figure 1.18) although some residues of the nucleotide binding Walker A and B motifs are poorly conserved within the D subunit and as a result the D subunit lacks ATPase activity in isolation [82, 86].

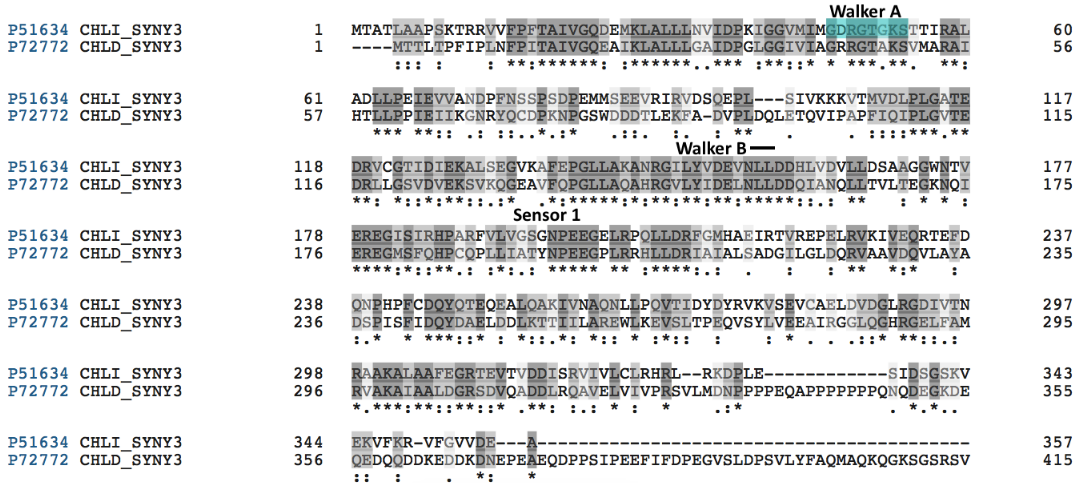

```
P51634 CHLI_SYNY3          1    MTATLAAPSKTRRVVFPFTAIVGQDEMKLALLLNVIDPKIGGVMIMGDRGTGKSTTIRAL    60
P72772 CHLD_SYNY3          1    ----MTTLTPFIPLNFPITAIVGQEAIKLALLLGAIDPGLGGIVIAGRRGTAKSVMARAI    56
                                    ::: :    : **:******: :******..*** :**::* * ***.**.  **:

P51634 CHLI_SYNY3         61    ADLLPEIEVVANDPFNSSPSDPEMMSEEVRIRVDSQEPL---SIVKKKVTMVDLPLGATE   117
P72772 CHLD_SYNY3         57    HTLLPPIEIIKGNRYQCDPKNPGSWDDDTLEKFA-DVPLDQLETQVIPAPFIQIPLGVTE   115
                                  *** **:: .: ::..*.:*   .::.  :.  : **   .     . ::::***.**

P51634 CHLI_SYNY3        118    DRVCGTIDIEKALSEGVKAFEPGLLAKANRGILYVDEVNLLDDHLVDVLLDSAAGGWNTV   177
P72772 CHLD_SYNY3        116    DRLLGSVDVEKSVKQGEAVFQPGLLAQAHRGVLYIDELNLLDDQIANQLLTVLTEGKNQI   175
                                **: *::*:**::.:*  .*:*****:*:**:**:**:*****::.: **   : * * :

P51634 CHLI_SYNY3        178    EREGISIRHPARFVLVGSGNPEEGELRPQLLDRFGMHAEIRTVREPELRVKIVEQRTEFD   237
P72772 CHLD_SYNY3        176    EREGMSFQHPCQPLLIATYNPEEGPLRRHLLDRIAIALSADGILGLDQRVAAVDQVLAYA   235
                                ****:*::**.: :*:.: ***** ** :****:.:  .   :   : **  *:*   :

P51634 CHLI_SYNY3        238    QNPHPFCDQYQTEQEALQAKIVNAQNLLPQVTIDYDYRVKVSEVCAELDVDGLRGDIVTN   297
P72772 CHLD_SYNY3        236    DSPISFIDQYDAELDDLKTTIILAREWLKEVSLTPEQVSYLVEEAIRGGLQGHRGELFAM   295
                                :.*  * ***::* : *::.*: *:: * :*::  :    : * . . .::* **::.:

P51634 CHLI_SYNY3        298    RAAKALAAFEGRTEVTVDDISRVIVLCLRHRL--RKDPLE------------SIDSGSKV   343
P72772 CHLD_SYNY3        296    RVAKAIAALDGRSDVQADDLRQAVELVIVPRSVLMDNPPPPEQAPPPPPPPQNQDEGKDE   355
                                *.***:**::**::* .**: :.: * :  *    .:*              . *.*..

P51634 CHLI_SYNY3        344    EKVFKR-VFGVVDE---A------------------------------------------   357
P72772 CHLD_SYNY3        356    QEDQQDDKEDDKDNEPEAEQDPPSIPEEFIFDPEGVSLDPSVLYFAQMAQKQGKSGSRSV   415
                                ::  :    .  *:   *
```

Figure 1.18: Sequence alignment between the N-terminal of *Synechocystis* ChlD (UniProt code 72772) and ChlI (UniProt code P51634) show a high degree of sequence similarity. Approximate positions of the Walker A, Walker B and Sensor 1 region are highlighted. Sequence alignment was generated using MUltiple Sequence Comparison by Log- Expectation (MUSCLE) sequence alignment tool (EMBL-EBI, UK) [83]. Codes relate to the UniProt [84] accession number.

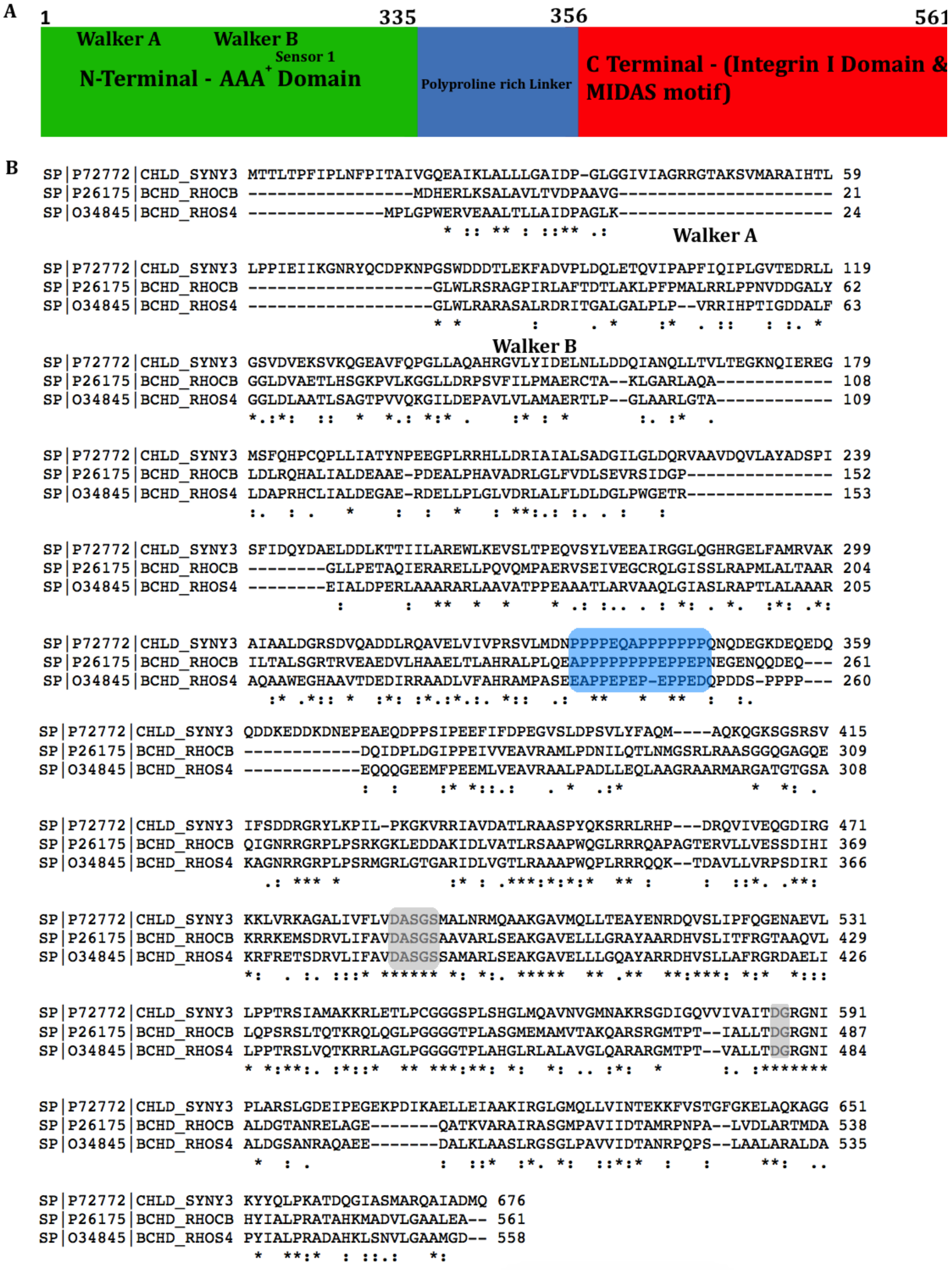

```
SP|P72772|CHLD_SYNY3 MTTLTPFIPLNFPITAIVGQEAIKLALLLGAIDP-GLGGIVIAGRRGTAKSVMARAIHTL 59
SP|P26175|BCHD_RHOCB -----------------MDHERLKSALAVLTVDPAAVG---------------------- 21
SP|O34845|BCHD_RHOS4 --------------MPLGPWERVEAALTLLAIDPAGLK---------------------- 24
                                         * :: ** : ::** .:

SP|P72772|CHLD_SYNY3 LPPIEIIKGNRYQCDPKNPGSWDDDTLEKFADVPLDQLETQVIPAPFIQIPLGVTEDRLL 119
SP|P26175|BCHD_RHOCB -------------------GLWLRSRAGPIRLAFTDTLAKLPFPMALRRLPPNVDDGALY 62
SP|O34845|BCHD_RHOS4 -------------------GLWLRARASALRDRITGALGALPLP--VRRIHPTIGDDALF 63
                                        * *       :     . *    :*  . ::   : :. *

SP|P72772|CHLD_SYNY3 GSVDVEKSVKQGEAVFQPGLLAQAHRGVLYIDELNLLDDQIANQLLTVLTEGKNQIEREG 179
SP|P26175|BCHD_RHOCB GGLDVAETLHSGKPVLKGGLLDRPSVFILPMAERCTA--KLGARLAQA------------ 108
SP|O34845|BCHD_RHOS4 GGLDLAATLSAGTPVVQKGILDEPAVLVLAMAERTLP--GLAARLGTA------------ 109
                     *.:*:  ::  *  *.: *:* .    :* : *       :. :*  .

SP|P72772|CHLD_SYNY3 MSFQHPCQPLLIATYNPEEGPLRRHLLDRIAIALSADGILGLDQRVAAVDQVLAYADSPI 239
SP|P26175|BCHD_RHOCB LDLRQHALIALDEAAE-PDEALPHAVADRLGLFVDLSEVRSIDGP--------------- 152
SP|O34845|BCHD_RHOS4 LDAPRHCLIALDEGAE-RDELLPLGLVDRLALFLDLDGLPWGETR--------------- 153
                     :.  : .   *   :  :  *   :  **:.: :. . :   :

SP|P72772|CHLD_SYNY3 SFIDQYDAELDDLKTTIILAREWLKEVSLTPEQVSYLVEEAIRGGLQGHRGELFAMRVAK 299
SP|P26175|BCHD_RHOCB --------GLLPETAQIERARELLPQVQMPAERVSEIVEGCRQLGISSLRAPMLALTAAR 204
SP|O34845|BCHD_RHOS4 --------EIALDPERLAAARARLAAVATPPEAAATLARVAAQLGIASLRAPTLALAAAR 205
                              :      :  **  *  *    * .: :.. . : *: .  *. :*: .*:

SP|P72772|CHLD_SYNY3 AIAALDGRSDVQADDLRQAVELVIVPRSVLMDNPPPPEQAPPPPPPPQNQDEGKDEQEDQ 359
SP|P26175|BCHD_RHOCB ILTALSGRTRVEAEDVLHAAELTLAHRALPLQEAPPPPPPPPEPPEPNEGENQQDEQ--- 261
SP|O34845|BCHD_RHOS4 AQAAWEGHAAVTDEDIRRAADLVFAHRAMPASEEAPPEPEP-EPPEDQPDDS-PPPP--- 260
                       :* .*:: *  :*: :*.:*.:. *::  .:  **   *  **  :  :.

SP|P72772|CHLD_SYNY3 QDDKEDDKDNEPEAEQDPPSIPEEFIFDPEGVSLDPSVLYFAQM----AQKQGKSGSRSV 415
SP|P26175|BCHD_RHOCB ------------DQIDPLDGIPPEIVVEAVRAMLPDNILQTLNMGSRLRAASGGQGAGQE 309
SP|O34845|BCHD_RHOS4 ------------EQQQGEEMFPEEMLVEAVRAALPADLLEQLAAGRAARMARGATGTGSA 308
                                 :  :    :* *::.:   . *  .:*             *  *: .

SP|P72772|CHLD_SYNY3 IFSDDRGRYLKPIL-PKGKVRRIAVDATLRAASPYQKSRRLRHP---DRQVIVEQGDIRG 471
SP|P26175|BCHD_RHOCB QIGNRRGRPLPSRKGKLEDDAKIDLVATLRSAAPWQGLRRRQAPAGTERVLLVESSDIHI 369
SP|O34845|BCHD_RHOS4 KAGNRRGRPLPSRMGRLGTGARIDLVGTLRAAAPWQPLRRRQQK--TDAVLLVRPSDIRI 366
                       .: *** *           :* : .***:*:*:*  ** :     :  ::*. .**:

SP|P72772|CHLD_SYNY3 KKLVRKAGALIVFLVDASGSMALNRMQAAKGAVMQLLTEAYENRDQVSLIPFQGENAEVL 531
SP|P26175|BCHD_RHOCB KRRKEMSDRVLIFAVDASGSAAVARLSEAKGAVELLLGRAYAARDHVSLITFRGTAAQVL 429
SP|O34845|BCHD_RHOS4 KRFRETSDRVLIFAVDASGSSAMARLSEAKGAVELLLGQAYARRDHVSLLAFRGRDAELI 426
                     *:  . :. :::* ****** *: *:. *****  ** .**  **:***: *:*  *:::

SP|P72772|CHLD_SYNY3 LPPTRSIAMAKKRLETLPCGGGSPLSHGLMQAVNVGMNAKRSGDIGQVVIVAITDGRGNI 591
SP|P26175|BCHD_RHOCB LQPSRSLTQTKRQLQGLPGGGGTPLASGMEMAMVTAKQARSRGMTPT--IALLTDGRGNI 487
SP|O34845|BCHD_RHOS4 LPPTRSLVQTKRRLAGLPGGGGTPLAHGLRLALAVGLQARARGMTPT--VALLTDGRGNI 484
                     * *:**:. :*::*  ** ***:**: *:  *: .. :*:  *      :. :*******

SP|P72772|CHLD_SYNY3 PLARSLGDEIPEGEKPDIKAELLEIAAKIRGLGMQLLVINTEKKFVSTGFGKELAQKAGG 651
SP|P26175|BCHD_RHOCB ALDGTANRELAGE-------QATKVARAIRASGMPAVIIDTAMRPNPA--LVDLARTMDA 538
SP|O34845|BCHD_RHOS4 ALDGSANRAQAEE-------DALKLAASLRGSGLPAVVIDTANRPQPS--LAALARALDA 535
                      *  : .             :  ::*  :*. *:  ::*:*  :   :     **:  ..

SP|P72772|CHLD_SYNY3 KYYQLPKATDQGIASMARQAIADMQ 676
SP|P26175|BCHD_RHOCB HYIALPRATAHKMADVLGAALEA-- 561
SP|O34845|BCHD_RHOS4 PYIALPRADAHKLSNVLGAAMGD-- 558
                      *  **:*  : ::.:   *:
```

Figure 1.19: (A) Domain overview of ChlD showing the positions of the N-terminal AAA$^+$ domain, polyproline rich linker and C-terminal regions. Amino acid residues are numbered according to the *Rhodobacter capsulatus* BchD subunit. (B) Sequence alignment of *Synechocystis* ChlD (UniProt code 72772), *Rhodobacter sphaeroides* (UniProt code O34845) BchD and *Rhodobacter capsulatus* BchD (UniProt code P26175). The approximate positions of the Walker A and Walker B motifs are highlighted. The polyproline linker is highlighted in blue, position of residues within the MIDAS motif are highlighted in gray. Sequence alignment was generated using MUltiple Sequence Comparison by Log- Expectation (MUSCLE) sequence alignment tool (EMBL-EBI, UK) [83]. Codes relate to the UniProt [84] accession number.

Mutagenesis of the AAA$^+$ domain of *Synechocystis* ChlD shows the ChlD subunit plays a regulatory role within the overall chelatase system [89].

Mutations within the Walker A motif of ChlD, which commonly peturb nucleotide binding in other AAA$^+$ proteins [44], completely abolish chelatase activity, this would suggest that nucleotide binding by this subunit is essential during the chelatase reaction. Contrastingly Walker B mutations of ChlD, which inhibit nucleotide hydrolysis but still allow binding within other AAA$^+$ proteins, still allow for a chelatase activity, albeit at a reduced rate in comparison with wild-type subunits.

Overall this implies that nucleotide binding within the AAA$^+$ domain of *Synechocystis* ChlD is critical during metal ion chelation, however ATP hydrolysis and therefore an ATPase activity is not.

The C-terminal domain of the D subunit has been suggested to play a regulatory role by binding Mg^{2+} ions. Mutations within the MIDAS motif of *R. capsulatus* BchD abolish chelatase activity, suggesting that this putative magnesium binding motif is required for the reaction [91]. Furthermore it has been demonstrated that *Synechocystis* ChlD controls the cooperative response towards free Mg^{2+}, control that requires 5 glutamic acid residues within the C terminal domain of ChlD [90]. Studies into the tobacco ChlD subunit found that removal of the C-terminal region does not completly abolish chelatase activity [92], again supporting a regulatory role of this region. This behaviour shows that the D subunit plays an allosteric role within the chelatase system, regulating the chelatase in response to both free Mg^{2+} ions and $MgATP^{2-}$.

1.5.3 The formation of complexes between the I and D subunits

Interactions between the I and D subunits and the formation of an ID complex has been demonstrated previously with pull down assays showing the co-elution of I and D in the presence of either ATP or ADP and free Mg^{2+} [87, 82]. These interactions occur in the absence of the H subunit.

It is also widely established that complexes formed between the I and D subunits can hydrolyse ATP, as demonstrated with the protein in multiple species including *Rhodobacter sphaeroides* [86], *Rhodobacter capsulatus* [77] and *Synechocystis* [82]. Such mixtures of the I and D subunits show a reduced ATPase activity in comparison to the I subunit in isolation, consistent with D subunit inhibiting of the ATPase activity of the I subunit within ID complexes [82]. However, although ID complexes can hydrolyse ATP in the absence of H or porphyrin substrates, the highest overall ATPase activities are observed in the presence of H and deuteroporphyrin-IX [82, 77].

The interaction between *Rhodobacter capsulatus* BchI and BchD subunits is thought to be stablised in part by the polyproline linker region in the BchD subunit [45], in agreement with studies on the tobacco chelatase where domains flanking this polyproline region were found to be essential for an interaction between I and D [92]. Studies on the *Synechocystis* subunits show that an interaction between ChlI and ChlD can also occur directly between the N-terminals of ChlD and ChlI. Removal of the C-terminal of ChlD still allows for an interaction between ChlI and ChlD. It was additionally demonstrated that the presence of the polyproline linker region within ChlD aids in the interaction between ChlI and ChlD [93].

The D subunit from Barley forms relativly ordered assemblies in the absence of ATP [91] (Figure 1.20) and it was proposed that the D subunit may act as a platform for assembly of I subunits during formation of ID complexes. Although no evidence for the formation of similar ring like arrangements by the *Synechocystis* ChlD subunits have been observed in the absence of nucleotide or Mg^{2+}.

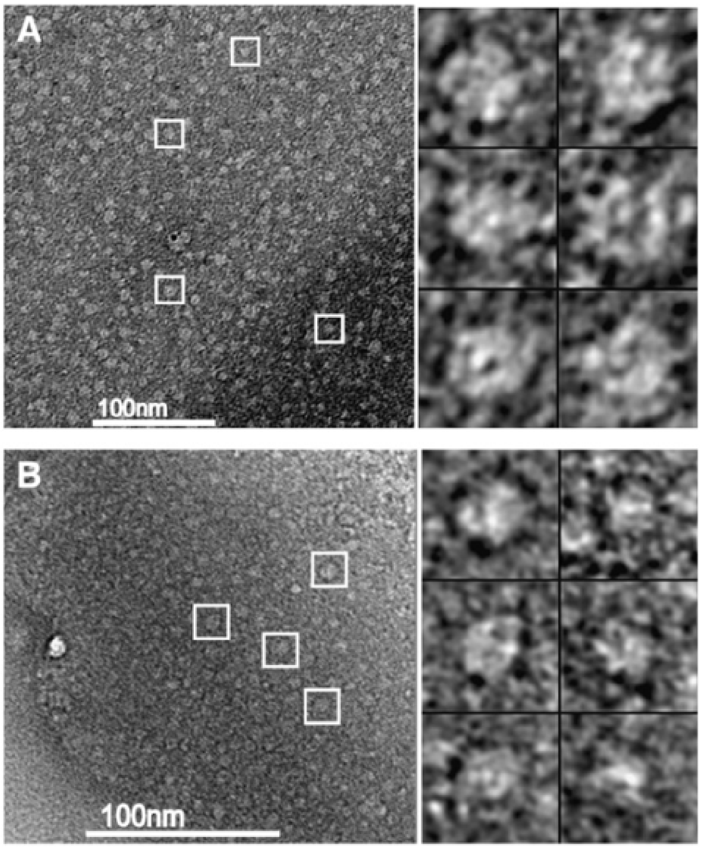

Figure 1.20: Electron microscopy of BchD shows the formation of relativly ordered complexes in the absence of ATP. Adapted with permission from [91]. Experiments also contained 15mM $MgCl_2$.

Cryo-EM and subsequent modelling of a *Rhodobacter capsulatus* BchID complex show evidence for the formation of a two-tiered complex constituting a trimer of dimers of BchI and BchD (Figure 1.21), with the overall conformation of the BchID complex being highly dependent on the nucleotide state [94]. However there is currently no direct evidence for such complexes in other magnesium chelatase species, nor if such complexes represent active components within the overall chelatase system.

Within the overall chelatase system the I and D subunits are the only subunits that belong to the AAA^+ protein family and it will be the ATP hydrolysis catalysed by ID complexes that drives the Mg^{2+} chelation reaction. However the number and arrangement of I and D subunits within complexes involved in ATP hydrolysis, in addition to the involvement of the H subunit remain poorly understood.

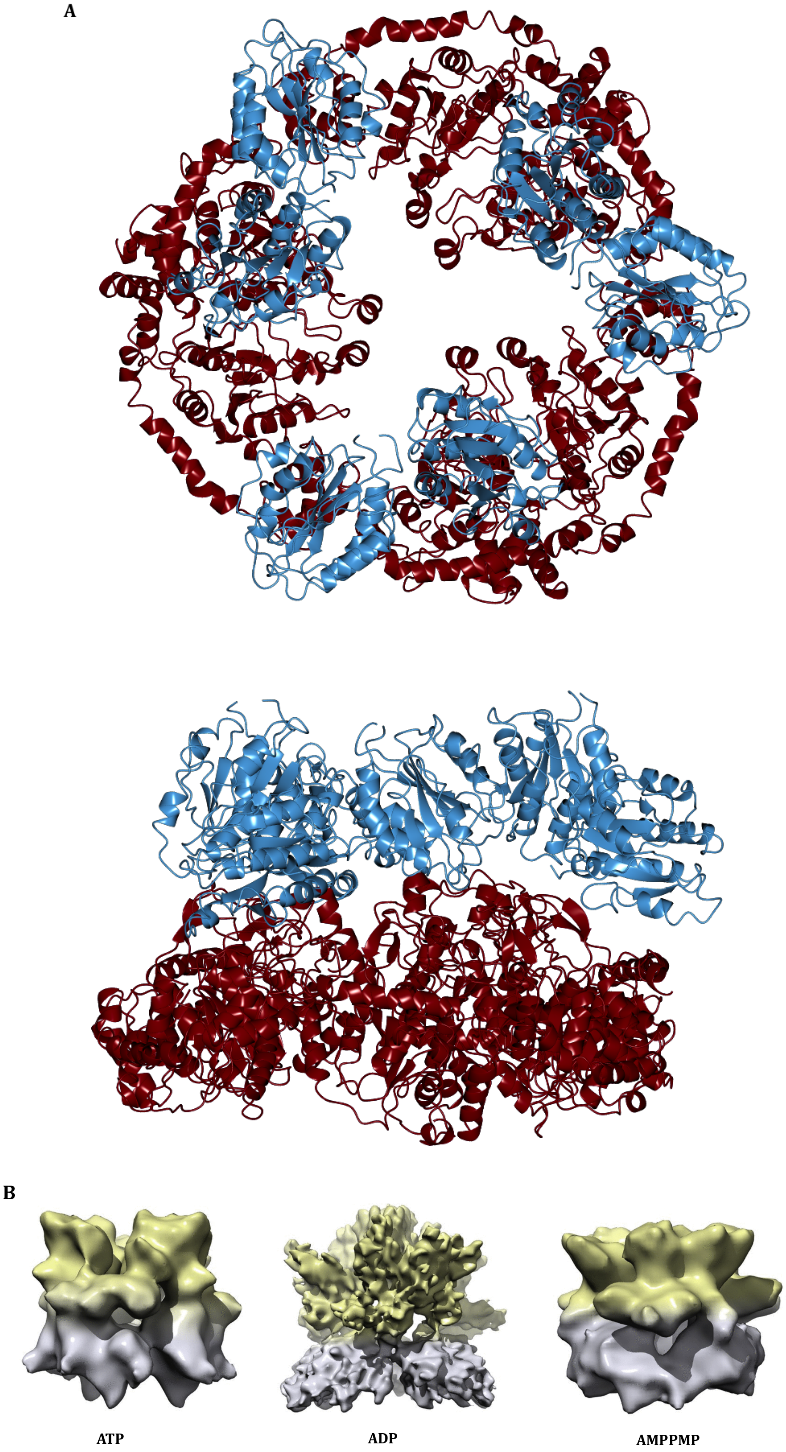

Figure 1.21: (A) Proposed model of a *Rhodobacter capsulatus* two-tiered BchID complex (PDB-ID 2x31, [94]) constituting a trimer of dimers of BchI (red) and BchD (blue). Generated using CCP4 Molecular graphics program (University of York) [22]. (B) Single particle Cryo-EM reconstructions of a *Rhodobacter capsulatus* BchID complex [94] at a resolution of 13Å (ATP, EMDBID-1677), 7.5Å (ADP, EMDBID-1676) and 14Å (AMPPNP, EMDBID-1678) demonstrate a high degree of conformation flexability depending on nucleotide state. EMDB codes correspond to EM entries in EMDataBank.

1.5.4 The H subunit of magnesium chelatase

The H subunit (140-150kDa) binds porphyrin [95], contains the active site for the chelation reaction [96] and is often described at the catalytic subunit. Unlike the I and D subunits of magnesium chelatase the H subunit does not belong to the AAA$^+$ family and lacks ATPase activity [97].

The binding of both the deuteroporphyrin substrate and magnesium deuteroporphyrin product to *Rhodobacter sphaeroides* BchH and *Synechocystis* ChlH has been investigated [95]. BchH was shown to bind deuteroporphyrin with a $K_d = 1.2 \pm 0.4$ μM and magnesium deuteroporphyrin with a $K_d = 0.2 \pm 0.04$ μM. ChlH binds deuteroporphyrin with a $K_d = 0.5 \pm 0.1$ μM and magnesium deuteroporphyrin with $K_d = 2.4 \pm 0.46$ μM. Porphyrin binding to the H subunit does not require the I and D subunits, ATP or Mg^{2+} however the K_d for deuteroporphyrin binding to the ChlH subunit shows an approximate 2-4 fold increase in the presence of ATP and Mg^{2+} while the BchH subunit shows no significant change [95]. Additionally these binding data suggest a single porphyrin binding site on the H subunit, consistent with early studies of BchH [70].

Cryo-EM studies of BchH [98] and small-angle X-ray scattering (SAXS) studies of *Synechocystis* ChlH [99] found the overall structure of the H subunit to constitute a small N-terminal head region in addition to a larger C-terminal main domain. The overall conformation of the H subunit was shown to be highly dependent on the interactions with porphyrin, exhibiting a high degree of conformational change upon binding of porphyrin substrate which resulted in the fusing of the N- and C-terminal domains.

The crystal structure of *Synechocystis* ChlH has been determined to a 2.5Å resolution [96]. ChlH contains six distinct domains (Figure 1.22). Domains I and II are the N-terminal head and neck region, with domains III-IV forming a larger cage-like assembly.

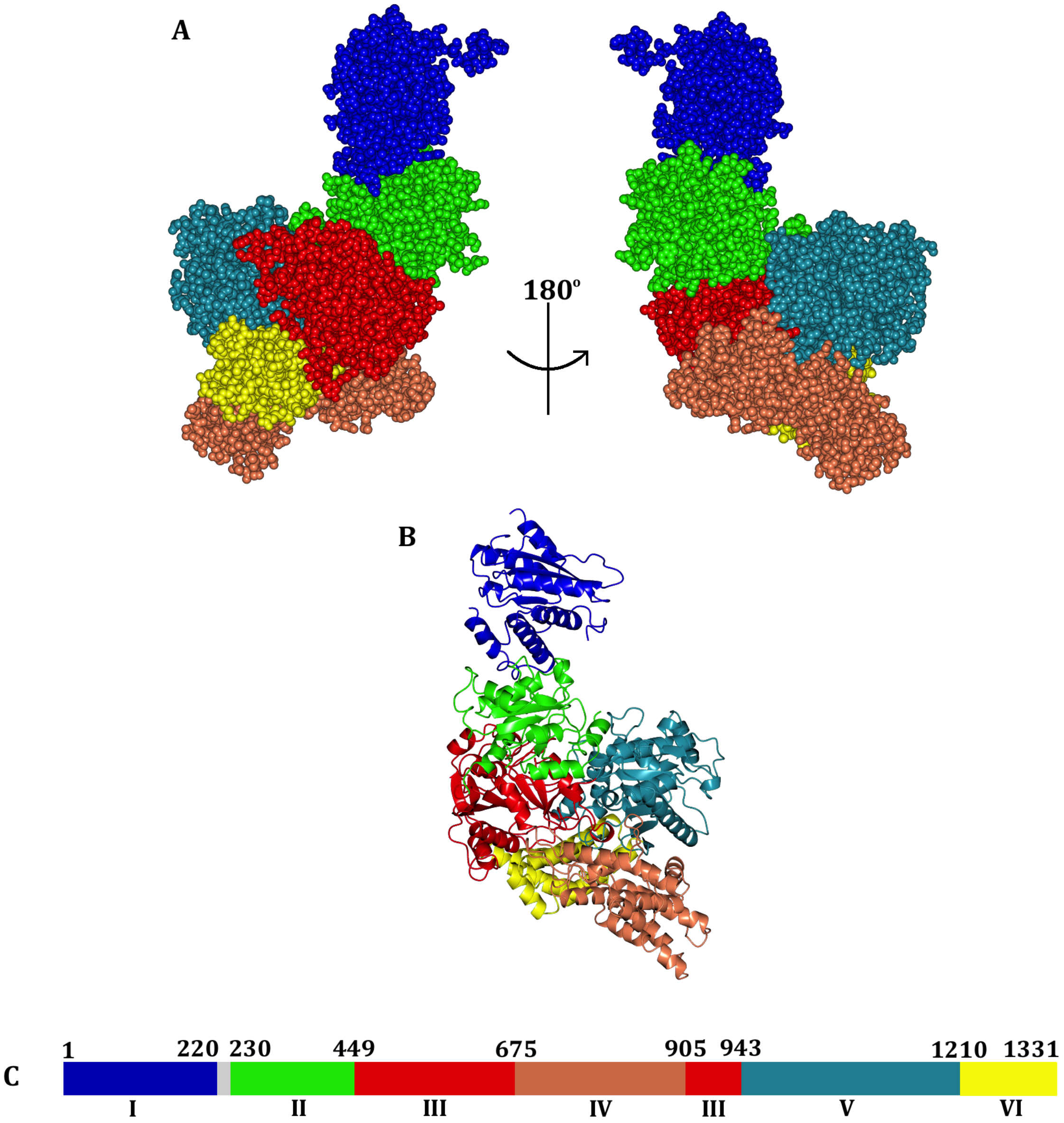

Figure 1.22: The structure of *Synechocystis* ChlH (A) Sphere representation of ChlH based on the crystal structure of the ChlH subunit (PDB-ID 4ZHJ, [96]) showing its six distinct domains. (B) ribbon representation of the ChlH subunit. (C) domain overview of the ChlH subunit. Protein models were generated using CCP4 Molecular graphics program (University of York) [22].

The removal of the N-terminal region (residues 1 - 565) of *Synechocystis* ChlH does not abolish binding of deuteroporphyrin or magnesium deuteroporphyrin, however complete loss of chelatase activity is observed for the truncated ChlH. This loss in activity is not rescued by the addition of GUN4 [99]. As the truncated H subunit binds porphyrin but does not insert magnesium it appears that the N-terminal head region does not contain the active site, but still plays an essential role during Mg^{2+} insertion [99].

The crystal structure of ChlH suggests that the active site for the Mg^{2+} insertion is buried deeply within the protein interior, at the interface between domains III and IV [96]. Residues within this region show a high degree of conservation between different species of the H subunit, indicating similar porphyrin binding mechanisms between different species [96].

Given the direct evidence for a high degree of conformational changes relative to the head and cage regions upon binding substrates [98], evidence for porphyrin binding by the head region [99], and the location of the active within the cage-like assembly [96], it is plausible that the N-terminal head region may be directly involved in the transportation of porphyins to and from the active site during the chelatase cycle.

In conclusion, the H subunit binds porphyrins, contains the active site and is the catalytic subunit. The H subunit does not belong to the AAA^+ protein family, lacks any ATPase activity and therefore requires the ATP hydrolysis performed by motor complexes of the AAA^+ I and D subunits to drive Mg^{2+} insertion into protoporphyrin-IX. The interface between the ID motor complex and the H subunit is unknown. Although an interaction between the ID complexes and the H subunit is required to couple ATP hydrolysis with metal ion chelation, the current lack of an isolated, active IDH complex suggests that any interactions between ID and H are transient.

2 Materials and Methods

Unless stated reagents were purchased from Sigma-Aldrich. All buffers and reagents were made to final volume in Milli-Q H_2O.

2.1 Protein production

2.1.1 Antibiotics

1000x stock solutions of neomycin (30mg/ml) and ampicillin sodium salt (100mg/ml) were made by dissolving the appropriate mass in milli-Q H_2O. Chloramphenicol (34mg/ml) was dissolved in Ethanol. Antibiotic stock solutions were filtered (0.2μM) and stored at -20^{o}C. Fresh stocks were made monthly as required.

2.1.2 Growth media and plates

All growth media was made to final volume with distilled water and sterilised by autoclaving (5psi, 115°C, 15 minutes) prior to use. Appropriate antibiotics were added as required from 1000x stock solutions.

Lysogeny broth (LB) media — Tryptone (10g/L), yeast extract (5g/L) and NaCl (10g/L).

”Super” LB media — Tryptone (20g/L), yeast extract (10g/L) and NaCl (10g/L).

LB-Agar plates — Tryptone (20g/L), yeast extract (10g/L), NaCl (10g/L) and agar (15g/L) containing appropriate antibiotics. Plates were stored at 4^{o}C.

2.1.3 Rosetta competent cell production

Rosetta competent cells (Rosetta2(DE3) pLysS, Novagen) were produced using the calcium chloride method.

Rosetta *E. Coli* cells were streaked onto an LB-Agar plate (no antibiotics) and incubated overnight. The following evening a single colony was incubated overnight (37°C, 250 RPM). The following day 500ml LB was inoculated with 5ml overnight culture and incubated (37°C, 180 RPM) until OD_{600nm} of 0.4 was achieved (approximately 3 - 4 hours) and immediately incubated on ice for 30 minutes.

100ml of culture was harvested by centrifugation (5000 RPM, 10 minutes), the supernatant was discarded and the cells were carefully resuspended into 5ml ice cold 0.1M $CaCl_2$ and incubated for 15 minutes on ice. Cells were harvested by centrifugation (5000 RPM, 10 minutes) the supernatant was discarded and the cells were again carefully resuspended in an additional 5ml ice cold 0.1M $CaCl_2$ and incubated for a further 15 minutes. Following incubation cells were harvested (5000 RPM, 10 minutes), the supernatant discarded and the cells carefully resuspended in 1.5ml 0.1M $CaCl_2$ with 15% (v/v) glycerol.

Cells were alliquoted (35μL) and stored at -80°C.

2.1.4 Transformations of ChlI, ChlD and ChlH

The wild-type *Synechocystis* sp.PCC6803 subunits of I, D and H were produced using expression vectors pET9a-ChlI, pET9a-His6ChlD and pET9a-His6 ChlH [32]. Production of (C244S) ChlI and ChlD to be labelled with Alexa Fluor 488 dye were produced with ChlI and ChlD expression vectors carrying mutations for labelling provided by Dr Nathan Adams (MBB, Sheffield).

Transformations of wild-type and/or mutated ChlI, ChlD and ChlH were as follows. 35μL of competent *E. coli* Rosetta cells were thawed on ice, 1μL plasmid DNA added and incubated on ice for 30 minutes. Cells were heat shocked (42°C, 90 seconds) then rapidly cooled on ice for 2 minutes. 600μL LB-media was added and the cells were incubated (37°C, 250RPM, 1 hour) then harvested via centrifugation (7000 RPM, 2 minutes). Cells were resuspended in 200μL LB and streaked onto LB-Agar plates containing antibiotics neomycin (30μg/μL) and chloramphenicol (34μg/μL) and incubated overnight at 37°C.

2.1.5 Growth and over-expression of wild type magnesium chelatase subunits

A freshly transformed colony was incubated overnight (37°C, 250RPM) in 10ml LB containing antibiotics neomycin (30μg/μL) and chloramphenicol (34μg/μL). 500ml "super" LB containing neomycin (30μg/μL) and chloramphenicol (34μg/μL) was inoculated with 5ml overnight culture and incubated (37°C, 220RPM, 3 - 4 hours) until OD_{600} of 0.6 - 0.8 was reached. Cells were induced with 0.4mM IPTG, incubated overnight (18°C, 180 RPM) and harvested by centrifugation (14000xg, 30 minutes, 4°C). Pellets were stored at -80°C until required.

2.2 Protein purification

Unless stated all columns and purification procedures were performed using an ÄKTA pure chromatography system (GE Healthcare, UK) at 5°C.

2.2.1 Purification buffers

Buffer A (low Salt) — 50mM tricine, 0.3M glycerol, 1mM DTT, pH 7.9 at 5°C.

Buffer B (high Salt) — 50mM tricine, 0.3M glycerol, 1M NaCl, 1mM DTT, pH 7.9 at 5°C.

Tris-HCl binding Buffer — 25mM tris, 5mM imidazole, 0.5M NaCl, 0.3M glycerol, pH 7.4.

Tris-HCl wash Buffer — 25mM tris, 20mM imidazole, 0.5M NaCl, 0.3M glycerol, pH 7.4.

Tris-HCl elution Buffer — 25mM tris, 400mM imidazole, 0.1M NaCl, 0.3M glycerol, pH 7.4.

2.2.2 Purification of ChlI

A ChlI pellet from 4L of culture was resuspended in buffer A containing Pefabloc (AEBSF) protease inhibitor, sonicated on ice (6x15 seconds, 2 minute intervals) and cell debris removed via centrifugation (40000g, 45 minutes, 4°C). ChlI lysate was purified by ionic exchange chromatography (2x5ml Q-Sepharose fast-flow, GE Healthcare, UK) using a linear gradient of NaCl (15 column volumes, 0.2M - 1M) with buffer B (20 - 100 % buffer B), following a wash with 10 - 15 column volumes 0.2M NaCl (20% buffer B). Relevant ChlI fractions were pooled, diluted with an equal volume buffer A and further purified via high resolution anionic exchange chromatography (2ml Source 15Q, GE Healthcare, UK) with a linear NaCl gradient (15 column volumes, 0.2M - 1M NaCl, 20 - 100 % buffer B) following a wash at 0.2M NaCl (10 - 15 column volumes, 20% B).

Relevant, nucleotide free ChlI fractions were pooled, spin concentrated (Vivaspin, 20kDa MWCO, GE Healthcare, UK) to approximately 5ml if required and further purified via gel-filtration (320ml, 26/60, HiLoad, GE Healthcare, UK) using buffer A (0.5ml/min). Monomeric ChlI fractions, eluting at approximately 180ml showing optimum chelatase activity were pooled, aliquoted and stored at -80°C. ChlI was found to maintain full activity for 4 - 6 weeks.

2.2.3 Purification of ChlD and ChlH

A protein pellet from 2 - 4 litres of cell culture was resuspended in Tris-HCl binding buffer containing Pefabloc (AEBSF), sonicated (6x15 seconds, 2 minute intervals) and cell debris removed via centrifugation (40000g, 45 minutes, 4°C).

The initial purification step of ChlD or ChlH was performed at lab temperature. Protein was loaded onto a Ni-Affinity column (5ml His-Trap QFF, GE Healthcare, UK) pre-equilibrated with 10 column volumes Tris-HCl binding buffer. Protein was eluted with Tris-HCl elution buffer, prior to column washing with 20 column volumes Tris-HCl wash buffer. Eluted fractions containing protein were diluted 7 fold into buffer A and further purified via high resolution anionic exchange chromatography (2ml Source 15Q, GE Healthcare, UK), with a linear NaCl gradient (15 column volumes, 0.2M - 1M NaCl, 20 - 100 % buffer B) following a wash at 0.2M NaCl (10 - 15 column volumes, 20% B).

Relevant protein fractions were pooled, aliquoted and stored at -80°C. ChlD and ChlH was found to maintain full activity for 4 - 6 weeks.

2.2.4 Purification of mutant C244S ChlI and ChlD used in AUC experiments

The production of C244S ChlI and ChlD carrying specific mutations to allow labelling with Alexa Fluor 488 were produced and purified exactly according to wild type ChlI and ChlD subunits.

2.2.5 Protein concentration determination

The concentration of unlabelled proteins was determined using a nanodrop 2000 (Thermo Scientific, USA) by taking an average of at least 3 consistent absorbance (280nm) readings using the extinction coefficients below.

Protein	Extinction coefficient ε $M^{-1}cm^{-1}$
ChlI	11290
ChlD	44560
ChlH	163330

Concentrations of ChlI and ChlD labelled with Alexa Fluor-488 were determined by accounting for the contribution of fluorophore absorbance at 494nm.

$$Concentration(M) = \frac{(A_{280}) - (A_{494}.0.11)}{\epsilon} \tag{2.1}$$

2.2.6 SDS-PAGE

SDS-Page gels were produced using the Mini-PROTEAN Electrophoresis System (Bio-Rad, California). Gels were ran at 200V for 45 - 60 minutes.

Stacking gel contained - 0.125M Tris-Hcl, 8% acrylamide, 0.001% (v/v) Tetramethylethylenediamine (TEMED), 10% (w/v) Ammonium persulfate (APS), 0.1 % Sodium dodecyl sulfate (SDS), pH 6.8 in Milli-Q H_2O.

Seperating gel contained - 0.375M Tris-Hcl, 8% acrylamide, 0.001% (v/v) Tetramethylethylenediamine (TEMED), 10% (w/v) Ammonium persulfate (APS), 0.1 % Sodium dodecyl sulfate (SDS) pH 8.8 in Milli-Q H_2O.

APS was added immediately prior to pouring gels.

Running buffer (10X stock) contained - 25 mM Tris, 1.92 M glycine, 1% SDS, pH 8.5.

Sample buffer (2X stock) - 0.25mM Tris-Hcl, 2% SDS, 20% glycerol, 0.01% bromophenol blue, 7% (v/v) 2-Mercaptoethanol, pH6.8 in Milli-Q H_2O.

2.3 Buffer and reagents

2.3.1 MOPS (chelatase) buffer

MOPS buffer contained final concentrations 50mM MOPS (3-(N-morpholino)propanesulfonic acid), 11mM KCl, 0.3M glycerol in Milli-Q H_2O. Buffer was adjusted to the appropriate pH with KOH and HCl. Buffer was generally made as a 4x stock solution, filtered (0.2μM) and stored at 4°C.

2.3.2 Porphyrin stocks

Deuteroporphyrin-IX and magnesium deuteroporphyrin-IX (Frontier Scientific, Utah) stocks were prepared by dissolving the appropriate mass in chelatase (MOPS) buffer.

Once dissolved samples were centrifuged (10000RPM, 2 minutes) to remove any precipitates. A small volume of porphryin stock was diluted into 0.1M HCl to determine accurate concentrations (λ_{max} 398nm, ε 433000 $M^{-1}cm^{-1}$). Porphyrin solutions were made fresh daily as required, protected from light and stored on ice.

2.3.3 ATP / ADP stocks

The appropriate mass of ATP or ADP was dissolved in Milli-Q H_2O, and brought to pH 7.5, following this stock concentration was determined (λ_{max} 259nm, ε 15400 $M^{-1}cm^{-1}$). Solutions were sterile filtered (0.2μM), alliquoted and stored at -20°C.

2.3.4 Magnesium chloride stocks

Magnesium chloride stock solutions produced from solid form were made by dissolving the appropriate mass of $MgCl_2.6H_2O$ in Milli-Q H_2O. Accurate concentration was determined using an EDTA / Eriochrome Black T dye titration.

Magnesium chloride stock solutions (1M ± 0.01 M) in Milli-Q H_2O were alternatively purchased (Sigma Aldrich) and diluted to appropriate concentrations in Milli-Q H_2O.

2.3.5 NADH stocks

Nicotinamide adenine dinucleotide (NADH) stocks were made by dissolving the appropriate mass in milli-Q H_2O and the accurate NADH concentration was determined (λ_{max} 340nm, ε 6300 $M^{-1}cm^{-1}$). Solutions were sterile filtered (0.2μM), alliquoted and stored at -20°C for a maximum of 4 weeks.

2.3.6 PEP Stocks

Phosphoenolpyruvate (PEP) stock solutions (20mM) were made by dissolving the appropriate mass in milli-Q H_2O, alliquoted and stored at -20°C.

2.3.7 PK/LDH enzyme stock

Pyruvate Kinase/Lactic Dehydrogenase enzymes were purchased from Sigma. Solutions contained approximately 600-1,000 units/mL pyruvate kinase and 900-1400 units/mL lactic dehydrogenase in a buffered aqueous glycerol solution. Solutions were alliquoted and stored at -20°C.

2.3.8 DTT stocks

Dithiothreitol stocks were made to a 1M stock (1000x) by dissolving the appropriate mass in milli-Q H_2O. Solutions were sterile filtered ($0.2\mu M$), alliquoted and stored at -20°C.

2.4 Kinetic assays

Measurements were performed using a FLUOstar optima plate reader (BMG Labtech, Germany). Black polystyrene 96 well plates (Greiner bio-one, Germany) with clear bottoms and black sides were used, allowing for fluorescence and absorbance detection through bottom or top optics.

2.4.1 Chelatase assays

Chelatase assays were performed in 50mM MOPS buffer, 10mM free $MgCl_2$, 1mM DTT, $8\mu M$ D_{IX} , pH 7.7, 34°C. Concentrations of protein subunits and $MgATP^{2-}$ was varied depending on the assay. Unless stated, triplicate $MgATP^{2-}$ concentration curves were carried out at each titration point

The required subunits were initially incubated together at 10x final assay concentration in assay buffer (50mM MOPS) then added to the assay mixture containing all components of the chelatase reaction except nucleotide ($MgATP^{2-}$). The assembled assay (absent nucleotide) was pre-incubated at 34°C for 15 minutes in the dark to achieve required temperature. Assays were initiated by the addition of $MgATP^{2-}$ from a 5X stock solution.

Fluorescence excitation and emission was achieved using 420±5 nm and 580±5 nm band pass filters respectively. Throughout the reaction the 96 well plates were sealed to avoid further evaporation. Fluorescence reading were taken at 1 minute intervals with mixing between each measurement cycle.

2.4.2 ATPase assays

ATPase assays were performed in 50mM MOPS buffer, 10mM free $MgCl_2$, 1mM DTT, 400μM NADH, 2mM PEP, 2 units Pyruvate Kinase / Lactic Dehydrogenase (PK/LDH) at pH 7.7, 34°C . Concentrations of protein subunits and $MgATP^{2-}$ were varied depending on the assay.

Absorbance was detected through a 340±5 nm bandpass filter. Throughout the reaction the 96 well plates were sealed to avoid further evaporation. Absorbance reading were taken at 1 minute intervals with mixing between each measurement cycle.

Relevant subunits were pre incubated together at 10x final assay concentration in assay buffer (50mM MOPS) then added to the assay mixture containing all components of the ATPase reaction except nucleotide ($MgATP^{2-}$). The assembled assay (absent nucleotide) was pre-incubated 34°C for 15 minutes in the dark to achieve required temperature. Assays were initiated by the addition of $MgATP^{2-}$ from a 5X stock solution.

2.4.3 Transient state assays for reaction cycle modelling

Enzyme stock was pre-incubated at 20μM ChlH, 10μM ChlI and 5μM ChlD in MOPS buffer at 34°C for exactly 30 minutes prior to assays, demonstrated to reduce lag times prior to chelatase activity [100].

Final D_{IX} and enzyme concentration were varied according to the specific reaction. In addition to enzyme and deuteroporphyrin-IX assays contained 10mM free $MgCl_2$, 5mM $MgATP^{2-}$, 50mM MOPS, 1mM DTT at pH 7.7, 34°C.

Subunit concentrations were held at a 1:2:4 Ratio of D:I:H within assays.

All components of the assays, except the IDH mixture, were pre-incubated together (1X concentration) for approximately 20 minutes at assay temperature in the dark. Assays were initiated by the addition of the required volume of pre-incubated IDH stock.

Assays were performed using a plate reader with simultaneous fluorescence excitation via 295±5 nm and 420±5 nm band pass filters with detection through a 580±5 nm band pass filter. This allows for the detection of both free and enzyme bound deuteroporphyrin-IX [100], as discussed in Section 5.3.2. Readings were taken at 1 minute intervals with mixing between each measurement cycle.

2.5 Analytical Ultra Centrifugation

2.5.1 Labelling of ChlI and ChlD

Mutated C244S ChlI and ChlD subunits for labelling were produced according to wild-type subunits (Section 2.2). The labelling of the subunits with Alexa Fluor 488 dye was performed by Dr Nathan Adams (MBB, Sheffield)

To ensure the removal of protein aggregates and the removal of excess dye following labelling, gel filtration (320ml, HiLoad 26/60, 200 prep grade, GE Healthcare) was performed on all subunits immediately prior to SV-AUC runs.

2.5.2 Experimental setup

All SV-AUC runs were performed in 50mM Tricine, pH 7.9, 1mM DTT, 25°C. Protein, nucleotide and free magnesium concentration was varied depending on the run and is given in the appropriate figure legend. All components of the AUC-experiments were pre-incubated together for approximately 1 hour prior to starting AUC experiments.

Sedimentation velocity experiments were performed on a XL-A analytical Ultra centrifuge (Beckman), Signal was either detected through interference (refractive index) optics to detect unlabelled protein or through absorbance optics (495nm) for detection of protein labelled with Alexa Fluor 488.

2.6 Data analysis and fitting

Plate reader data was collected using Optima software (version 2.2, BMG Labtech, Germany) and viewed in MARS (BMG Labtech, Germany). Production of graphs and fitting was performed in Igor Pro (Wavemetrics, Lake Oswego, OR, USA).

2.6.1 Chelatase assays

The dependence of the observed fluorescence signal from $\mathrm{MgD_{IX}}$ with the concentration of ChlH was established and fitted to a second order polynomial.

$$y = A + BX + CX^2 \tag{2.2}$$

Obtaining parameters A, B and C allows a rearranged form to be used to directly convert observed fluorescence (x) into [$\mathrm{MgD_{IX}}$] within Optima software.

$$[MgDix] = \frac{-b \pm \sqrt{b^2 - 4acx}}{2a} \tag{2.3}$$

Following conversion of fluorescence to $\mathrm{MgD_{IX}}$ concentration, the steady state rate of $\mathrm{MgD_{IX}}$ formation for the reaction was obtained by measuring the slope of the linear region of the reaction.

At each individual titration point (subunit concentration) the $\mathrm{MgATP^{2-}}$ dependent behaviour was plotted in Igor and fitted to either the Michaelis-Menten equation (Equation 2.4) or a modified form accounting for substrate inhibition (Equation 2.6) as required. Additional rearranged forms of the Michaelis-Menten equation were used to determine the errors associated with $\frac{V_{max}}{K_m}$ (Equations 2.5 and 2.7).

$$v_{ss} = \frac{V_{max} \cdot [S]}{K_m + [S]} \tag{2.4}$$

$$v_{ss} = \frac{(\frac{V_{max}}{K_m}).[S]}{1 + (\frac{[S]}{K_m})} \tag{2.5}$$

$$v_{ss} = \frac{V_{max} \cdot [S]}{K_m + (S.(1 + (\frac{S}{K_i})))} \tag{2.6}$$

$$v_{ss} = \frac{\frac{V_{max}}{K_m}.[S]}{1 + (\frac{S}{K_m}).(1 + (\frac{S}{K_i})))} \tag{2.7}$$

Calculation of V_{max} and K_m at each enzyme concentration allows the dependence of V_{max} and $\frac{V_{max}}{K_m}$ with subunit concentration to be determined. The dependence in V_{max} or $\frac{V_{max}}{K_m}$ within performed subunit titrations monitoring chelatase activity were fitted to the single site binding equation (Equation 2.8), with parameters V_{max} (maximum rate), L (ligand or subunit concentration), E (binding site concentration) and K_d.

$$V_{Chelatase} = V_{max} \cdot \frac{(((L + E + K_d) - ((L + E + K_d)^2 - \sqrt{(4LE)})}{2E} \tag{2.8}$$

2.6.2 ATPase assays

To establish the relationship between NADH absorbance and concentration, the dependence of NADH concentration with absorbance (340nm) was characterised within standard curves of known NADH concentrations in 96 well plates and shown to be linear over the measured range of NADH concentrations.

By establishing the dependence of absorbance with NADH concentration the direct conversion to [NADH] within the Optima software can be achieved, using a rearranged form of the straight line equation (Equation 2.10), where x denotes absorbance.

This conversion allows the rate of NADH depletion during ATP hydrolysis to be determined within coupled assays, thus enabling direct calculation of steady state ATP hydrolysis rates within kinetic titrations through coupled assays.

$$y = MX + C \tag{2.9}$$

$$[NADH] = \frac{x - C}{M} \tag{2.10}$$

Following this the $MgATP^{2-}$ dependent behaviour at each individual data point (enzyme concentration) was plotted and fitted to the Michaelis-Menten equation (Equation 2.4). For the ATPase titration of ChlD into ChlI, the variation in levels of the ChlD subunit was fitted to a modified single site binding equation (Equation 2.11).

$$V_{ATPase} = Irate + ((IDrate - Irate).\frac{(((L + E + K_d) - ((L + E + K_d)^2 - \sqrt{(4LE)})}{2E}) \tag{2.11}$$

2.6.3 Analysis of SV-AUC boundary scans

The interpretation of AUC-SV boundary scans and calculation of sedimentation coefficient was performed by Dr Thomas Jowitt (Faculty of Life Sciences, University of Manchester).

2.6.4 Dynafit modelling

Modelling of steady state chelatase data was performed within the Dynafit (BioKin Ltd, USA) software package [101].

3 Kinetic titrations of magnesium chelatase

3.1 Abstract

Kinetic titrations were used to indirectly probe the subunit assembly of magnesium chelatase by monitoring the dependence of metal ion chelation rates and ATP hydrolysis rates with the levels of the individual ChlI, ChlD and ChlH subunits, establishing the relative levels of subunits within complexes involved in these processes. Subunit titrations give strong support to the formation of multiple different chelatase complexes that differ in the relative levels of ChlI and ChlD subunits. During subunit titrations monitoring Mg^{2+} insertion, saturation in the overall chelatase activity can occur at two very different stoichiometries of ChlI and ChlD subunits, with saturation possible at 1:1 levels of ChlI and ChlD, or at much higher levels of ChlI over ChlD depending on the specific titration. Kinetic titrations monitoring ATP hydrolysis suggest a 1:1 interaction between ChlI and ChlD in the absence of ChlH. However, in the presence of ChlH a stimulation in ATPase activity is observed, occurring under conditions where ChlI is at an excess over ChlD. It was proposed based on subunit titration data that the formation of multiple complexes can therefore occur during either Mg^{2+} insertion or ATP hydrolysis that differ in the overall stoichiometries of ChlI and ChlD subunits. Furthermore, the ChlH subunit influences the overall levels of ATP hydrolysis, providing further evidence that interactions of ChlH with the ChlI and ChlD subunits can occur during ATP hydrolysis cycles.

3.2 Introduction

The active complexes of magnesium chelatase that catalyse metal ion chelation and ATP hydrolysis contain a poorly understood number and arrangement of individual I, D and H subunits.

It is well established that the AAA^+ I and D subunits can form stable complexes independently of the H subunit and that the resulting complexes can hydrolyse ATP [82, 86]; ATP hydrolysis is not essential for the formation of complexes between I and D, and complexes can be formed in the presence of ADP or non-hydrolysable nucleotide analogues such as AMP-PNP [82, 86]. The AAA^+ I subunit is the only chelatase subunit to have an essential ATPase activity; this subunit exhibits an ATPase activity in isolation [82, 35]. The D subunit although also belonging to the AAA^+ family, lacks an essential ATPase activity and plays a regulatory role within the chelatase [91, 89]. Ultimately the ATP hydrolysis catalysed by these motor ID complexes drives the chelation reaction.

The H subunit binds porphyrins, contains the active site for the chelation reaction and is often described as the catalytic subunit [96, 95]. Unlike the I and D subunits, the H subunit does not belong to the AAA$^+$ protein family and lacks any resulting ATPase activity in isolation [97], however a high ATPase activity for the overall system is achieved in the presence of H and porphyrin substrate [82]. Although it is well established that ATP hydrolysis within the chelatase is performed exclusively by complexes of the I and D subunits [81], the overall increase in the ATPase activity in the presence of H requires a direct interaction between the ID subunits and H.

There is a vast array of evidence that AAA$^+$ proteins can assemble into ring-like arrangements of their individual subunits, often in a nucleotide dependent manner — of which hexamers are most commonly observed — these ring like arrangements are often the active form of the enzyme [41, 44, 39]. The I and D subunits belong to the AAA$^+$ protein family [42, 45] and these rings of subunits are likely to be formed within the chelatase system. Similiar ring like arrangements have been seen for the I and D subunits in isolation [85, 88, 91]. Additionally it has been proposed that the *Rhodobacter capsulatus* BchI and BchD subunits form a complex in the absence of BchH and this complex was suggested to exist as a two tiered I_6D_6 hexameric arrangement [94], (Figure 1.21). However currently there is no direct evidence for such complexes occurring within the *Synechocystis* system and no evidence to suggest that this is an active component within the overall system.

A widely shared view of magnesium chelatase is that of the system representing two distinct but interacting components [81], an ATPase motor type system containing the AAA$^+$ I and D subunits and the porpyrin binding catalytic H subunit. The overall number and arrangement of subunits and how the ATPase and porphyrin binding systems interact remain unclear, although a direct interaction between the ATPase and catalytic components appears essential to couple ATP hydrolysis and metal ion chelation. However the current lack of an isolated, active IDH complex suggests that the interactions may be transient or short lived, particularly in the case of interactions of the H subunit with the I and D subunits.

During steady state Mg^{2+} insertion reactions a lag period prior to metal ion chelation can be observed, depending on the pre-incubation conditions of the subunits, such as the presence and concentration of nucleotide, or the subunit concentration [100, 32, 102, 70]. If this lag-phase reflects the assembly of the intact, active chelatase than this behaviour suggests that the complete assembly and disassembly of an IDH complex may not occur or be required during each magnesium insertion cycle, with the subunits remaining at least partly within a complex throughout multiple metal ion insertion cycles. In contrast, mutant doping studies involving the *Rhodobacter capsulatus* subunits have suggested that subunit exchange can occur on the same timescale as the catalytic cycle of magnesium chelatase, however it cannot be established if such behaviour is an essential feature of every magnesium chelatase reaction cycle [67].

Although early studies indicated that an approximate molar ratio of 1:2:4, ChlD:ChlI:ChlH is optimal for metal ion insertion within the *Synechocystis* system and that high levels of ChlD results in inhibition [32], the overall number and arrangement of subunits within complexes involved in metal ion chelation and ATP hydrolysis remain poorly understood. Therefore the investigation into the assembly of the subunits into such complexes remains essential to further the overall understanding of the magnesium chelatase system.

3.3 Results and Discussion

3.3.1 Production of the wild-type magnesium chelatase subunits

The study of the subunit assembly of magnesium chelatase requires production of the isolated subunits. Any contaminants, especially nucleotide contaminants, may lead to the formation and detection of biochemically irrelevant species. To ensure this specific problems, such as the presence of contaminating nucleotide in ChlI, need to be overcome during the purification of the individual subunits.

The corresponding over-expression and purification procedures for the *Synechocystis* sp. PCC6803 magnesium chelatase subunits ChlI, ChlD and ChlH are described in detail in Materials and Methods Section 2.2.

3.3.2 Purification of ChlI

The ChlI subunit undergoes nucleotide dependent aggregation — a common characteristic shared with many other AAA$^+$ proteins — resulting in the inhibition of the activity of the subunit due to the formation of inactive complexes or aggregates. The removal of free nucleotide and nucleotide contaminated protein therefore allows the isolation of the fully active, monomeric form of the ChlI subunit.

The removal of a majority of nucleotide contaminated ChlI, free nucleotide and crude material from ChlI is achieved by low resolution anion exchange chromatography. Representative UV elution profiles and the corresponding SDS-PAGE gel are shown in Figure 3.1. The separation of ChlI (Figure 3.1, 6-8) from free nucleotide and nucleotide contaminated ChlI (Figure 3.1, 9) is observed.

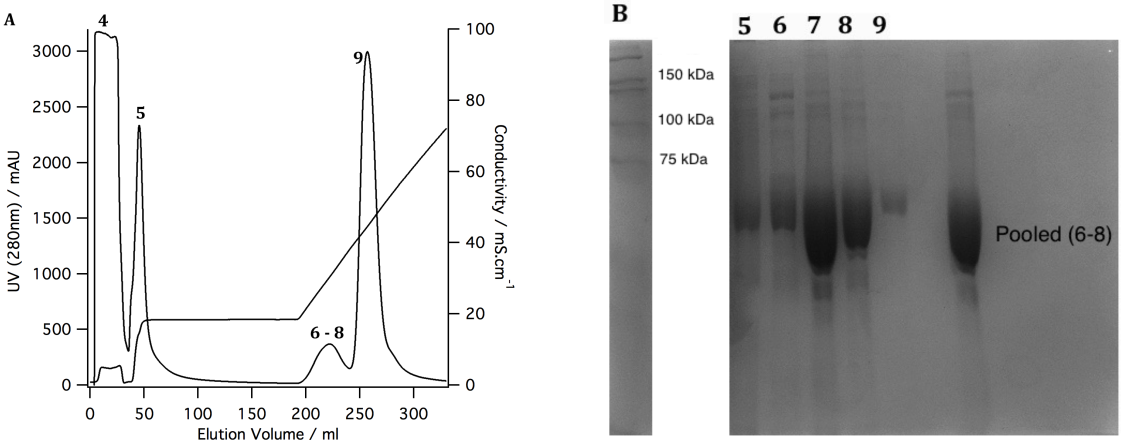

Figure 3.1: The initial low resolution anion exchange purification step of ChlI. (A) UV elution profile of the Q-Sepharose (2x5ml Hi-Trap Q-Sepherose fast-flow (QFF), GE Healthcare) purification step of ChlI showing seperation of free nucleotide and nucleotide contaminated ChlI (9) from ChlI (6-8). Performed at pH 7.9. (B) SDS-PAGE of the initial Q-Sepharose anion exchange purification step of ChlI.

Relevant protein fractions (6-8 in Figure 3.1) are then further purified by high-resolution anion exchange chromatography. Representative UV elution profiles and the corresponding SDS-PAGE are shown in Figure 3.2 demonstrating further separation of ChlI (Figure 3.2, 5 - 7) from nucleotide and nucleotide contaminated ChlI (Figure 3.2, 8 - 9).

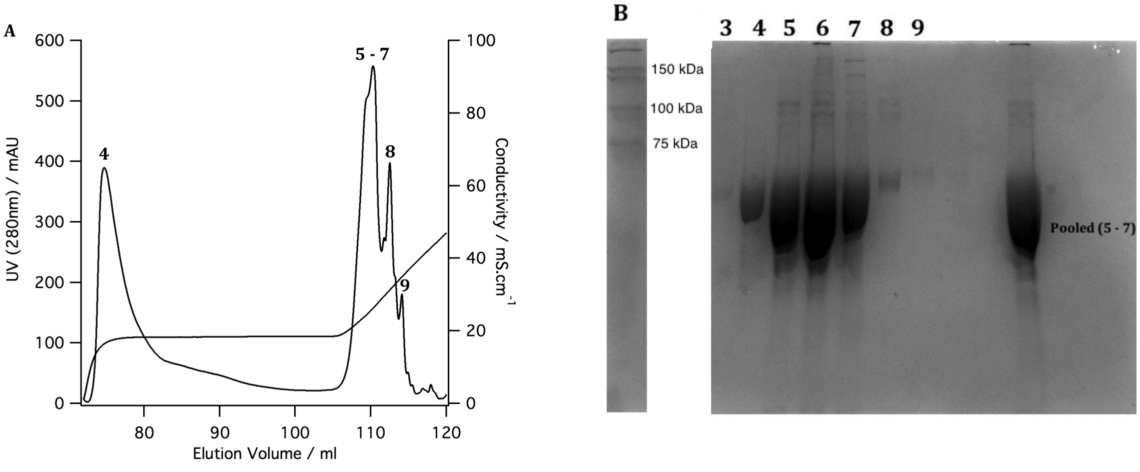

Figure 3.2: The high resolution anion exchange purification step of ChlI. (A) UV elution profile of the high resolution anion exchange (2ml Source 15Q, GE Healthcare) purification step of ChlI showing further seperation of free nucleotide and nucleotide contamined ChlI (8-9) and crude material from ChlI (5-7). Performed at pH 7.9. (B) SDS-PAGE of the high resolution anion exchange purification step of ChlI.

The removal of the majority of nucleotide contamination by the ion exchange steps enables the isolation of the monomeric form of ChlI by gel filtration chromatography. Representative UV elution profiles and the corresponding SDS-PAGE are shown in Figure 3.3, with active monomeric ChlI eluting as a clearly defined peak (Figure 3.3, 6 - 8). ChlI from peaks in the region of 3 - 5 exhibit no chelatase activity when tested.

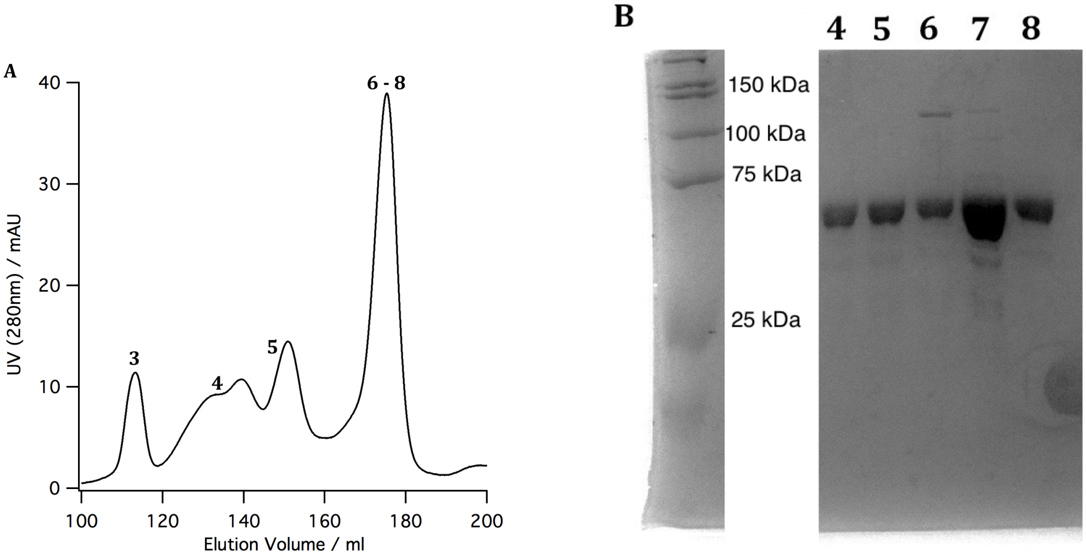

Figure 3.3: The final gel filtration purification step of ChlI. (A) UV elution profile of the gel filtration (320ml, Superdex 200 prep grade, HilLoad 26/60, GE Healthcare) purification of ChlI. Elution of active, monomeric ChlI is denoted by (6-8). Performed at pH 7.9. (B) SDS-PAGE of the gel filtration purification step of ChlI.

3.3.3 Purification of ChlD and ChlH

The inclusion of an N-terminal His_6 tag allows purification of ChlD and ChlH via Ni-affinity chromatography, followed by high resolution anion exchange chromatography. Unlike ChlI, no nucleotide contamination is observed.

Representative UV elution profiles for the high resolution anion exchange purification step of ChlD and ChlH are shown in Figure 3.4. SDS-PAGE gels are shown in Figure 3.5.

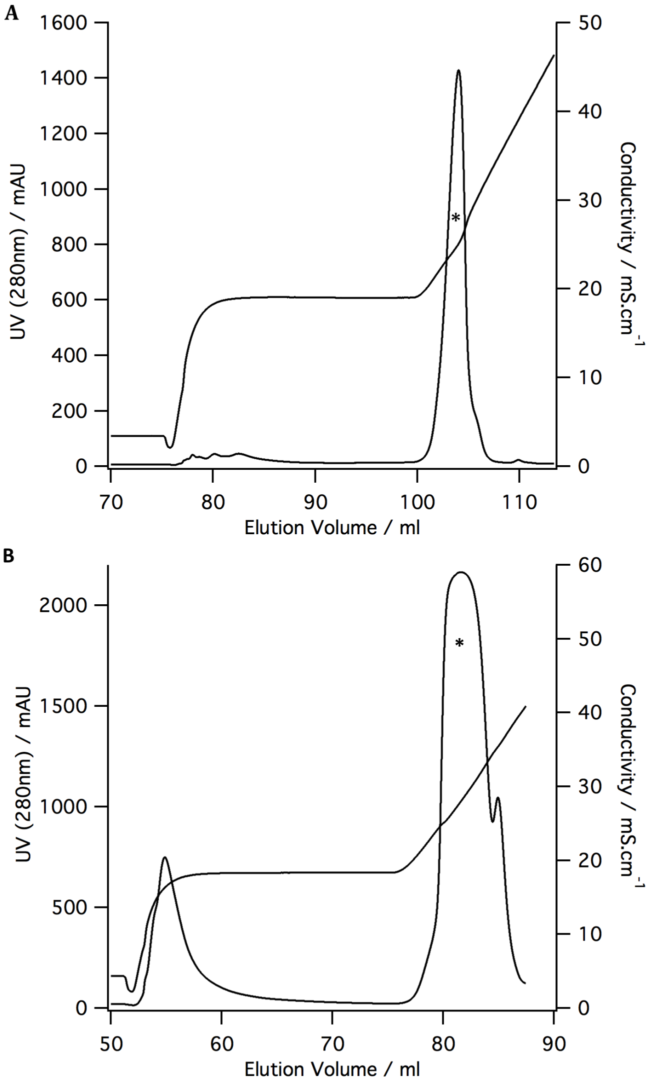

Figure 3.4: Representative elution profiles for the high resolution anion exchange (Source 15Q, GE Healthcare) purification step of ChlD and ChlH. Performed at pH 7.9. (A) ChlD elutes as a clearly defined peak, * denotes elution of ChlD (B) A slight shoulder is observed during purification of ChlH, which is discarded, * denotes elution of ChlH.

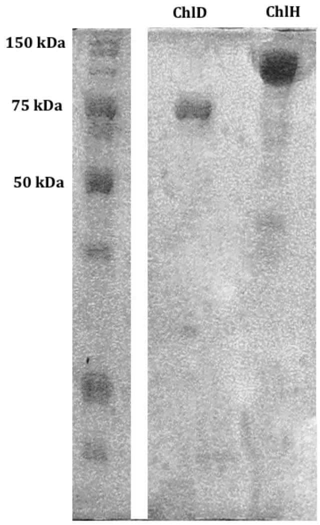

Figure 3.5: SDS-PAGE of ChlD and ChlH following high resolution anion exchange (Source 15Q) purification.

3.3.4 The subunit assembly and activity of magnesium chelatase is nucleotide dependent

The nucleotide dependent assembly of individual protein subunits into ring like arrangements is a common feature of AAA^+ proteins and such arrangements generally represent the biochemically relevant and active forms of the enzyme [39, 41, 50].

To allow for the indepth characterisation of the nucleotide dependent assembly of complexes formed by magnesium chelatase within the subunit titrations, during which the dependence of the chelatase or ATPase activities with the levels of the individual subunits was investigated, full $MgATP^{2-}$ concentration curves were generated at each individual titration point (enzyme concentration). Examples of $MgATP^{2-}$ concentration curves generated during a chelatase assay monitoring Mg^{2+} insertion into deuteroporphyrin-IX are shown in Figure 3.6.

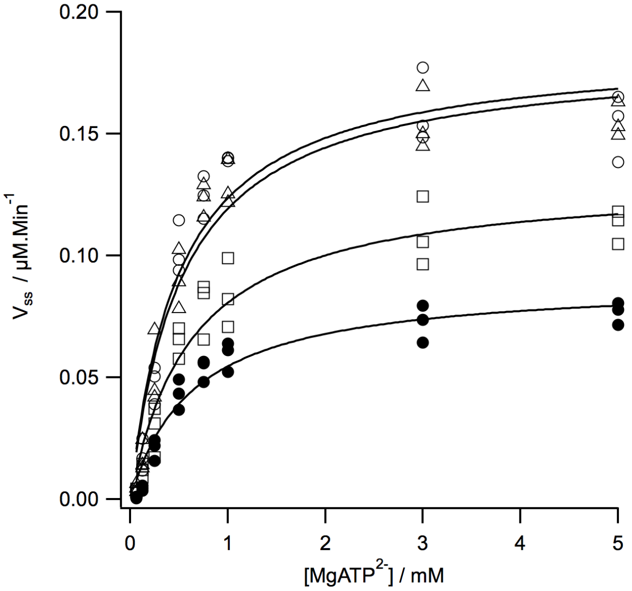

Figure 3.6: Examples of full $MgATP^{2-}$ concentration curves generated from a chelatase reaction. Performed in 0.005μM ChlD (●), 0.01μM ChlD (□), 0.025μM ChlD (△), 0.05μM ChlD (○) measurements also contained 0.1 μM ChlI, 0.4 μM ChlH, 8 μM D_{IX}, 10mM $MgCl_2$, 1mM DTT, 50mM MOPS, 0.3M glycerol, pH 7.7, 34°C. Data were fitted to the Michaelis-Menten equation (Equation 2.4).

By generating full $MgATP^{2-}$ concentration curves and fitting to the appropriate equation such as the Michaelis-Menten equation (Equation 2.4), both V_{max} and $V_{\mathrm{max}}/K_{\mathrm{m}}$ can be established.

The maximal velocity V_{max} is the rate achieved at saturating concentrations of nucleotide and K_{m}, the Michaelis constant, is the nucleotide concentration at half V_{max}.

$V_{\mathrm{max}}/K_{\mathrm{m}}$ overall relates to rate of capture of substrate by free enzyme into complexes that later go on to form products and complete a turnover [103].

3.3.5 Accounting for interactions between ChlH and the chelatase reaction product magnesium deuteroporphyrin-IX during chelatase assays

The insertion of a Mg^{2+} ion into deuteroporphyrin-IX resulting in the formation of magnesium deuteroporphyrin-IX can be directly observed by monitoring the fluorescence emission of magnesium deuteroporphyrin-IX. An example of a time course of a standard chelatase assay detecting the formation of magnesium deuteroporphyrin-IX is shown in Figure 3.7.

As a result of the ChlH subunit binding magnesium deuteroporphyrin-IX, the observed fluorescence signal of magnesium deuteroporphyrin-IX depends on the levels of ChlH. As subunit titrations, monitoring magnesium deuteroporphyrin-IX formation, were performed in varying concentrations of the ChlH subunit, the dependence of the observed fluorescence signal from magnesium deuteroporphryin-IX with the concentration of the ChlH subunit was characterised. This was achieved using standard curves of varying magnesium deuteroporphyrin-IX concentrations in the presence of known amounts of ChlH (Figure 3.8), the relationship can be described by a second order polynomial (Equation 2.2). Fitting methods are discussed in detail in Section 2.6.

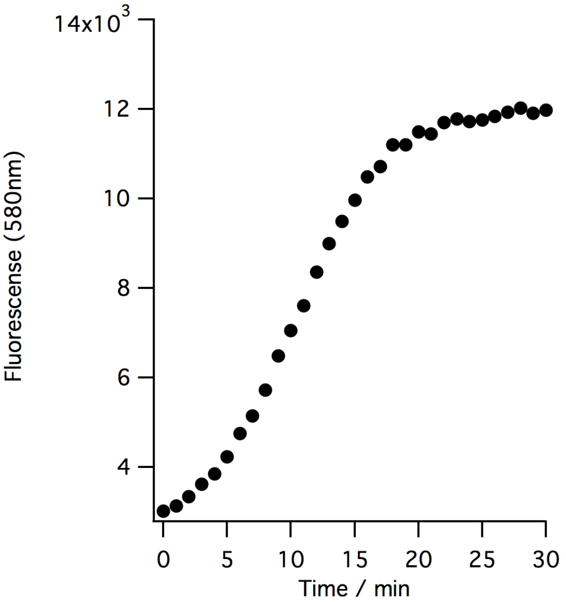

Figure 3.7: The steady state formation of magnesium deuteroporphyrin-IX can be observed via fluorescence spectroscopy (420nm excitation / 580nm emission). Experiments were performed in 0.2μM ChlI, 0.1μM ChlD, 0.4μM ChlH, 5mM MgATP^{2-}, 10mM MgCl$_2$, 8μM D$_{\mathrm{IX}}$, 1mM DTT, 50mM MOPS, 0.3M glycerol, pH 7.7, 34°C.

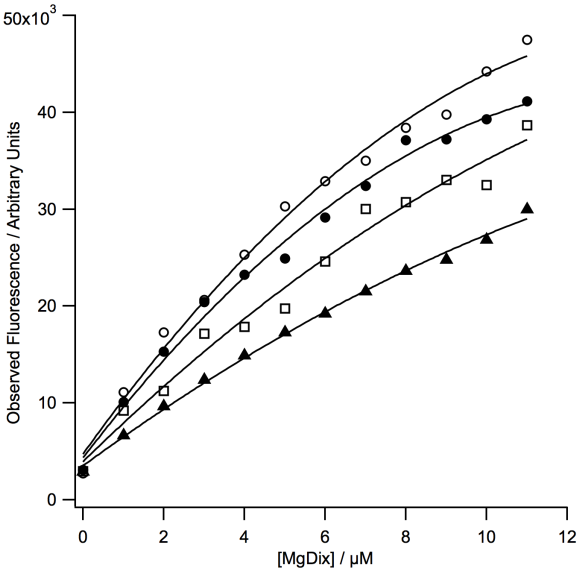

Figure 3.8: The intensity of the observed fluorescence signal (420nm excitation / 580 emission) from magnesium deuteroporphyrin-IX is dependent on the concentration of ChlH. performed in 0.1μM ChlH (▲), 0.4μM ChlH (□), 0.8μM ChlH (●) and 1.2μM ChlH (○), experiments also contained 50mM MOPS, 0.3M glycerol, pH 7.7, 34°C. The dependence of fluorescence with MgD$_{\mathrm{IX}}$ concentration was obtained empirically by fitting to a second order polynomial as described in Materials and Methods Section 2.6.

3.3.6 Investigating the chelatase complexes formed during Mg^{2+} insertion

To probe the overall levels of the individual ChlI, ChlD and ChlH subunits required to form the biochemically relevant complexes during Mg^{2+} insertion, the chelatase activity (i.e. the rate of Mg^{2+} insertion into deuteroporphyrin-IX) was investigated under varying levels of the chelatase subunits.

Both subunit titrations of the ChlI subunit against a fixed level of the ChlD subunit and the contrasting titrations of the ChlD subunit against a fixed level of the ChlI subunit were performed in varying levels of the ChlH subunit. This experimental design allowed investigation of both the complexes formed between ChlI and ChlD and the involvement of the ChlH subunit.

3.3.7 A titration of ChlI against a fixed level of ChlD shows saturation occurs at equimolar levels of ChlI and ChlD

To investigate how the chelatase activity varies in response to the overall levels of the ChlI and ChlD subunits and to probe the interactions and resulting complexes formed between ChlI and ChlD, a titration of varying levels of the ChlI subunit (0.04 - 0.2μM) against fixed levels of ChlD (0.1μM) and ChlH (0.4μM) was performed.

During the titration a linear increase in V_{max} (the chelatase activity observed at saturating concentrations of $MgATP^{2-}$) in response to the addition of increasing amounts of ChlI is observed up to approximately equimolar levels of ChlI and ChlD (0.1μM), followed by a plateau in V_{max}.

Such a plateau in chelatase activity, occurring at equimolar concentrations of ChlI and ChlD would suggest saturation occurring at equimolar levels of ChlI and ChlD. The dependence of V_{max} with ChlI concentration is shown in Figure 3.9, panel A.

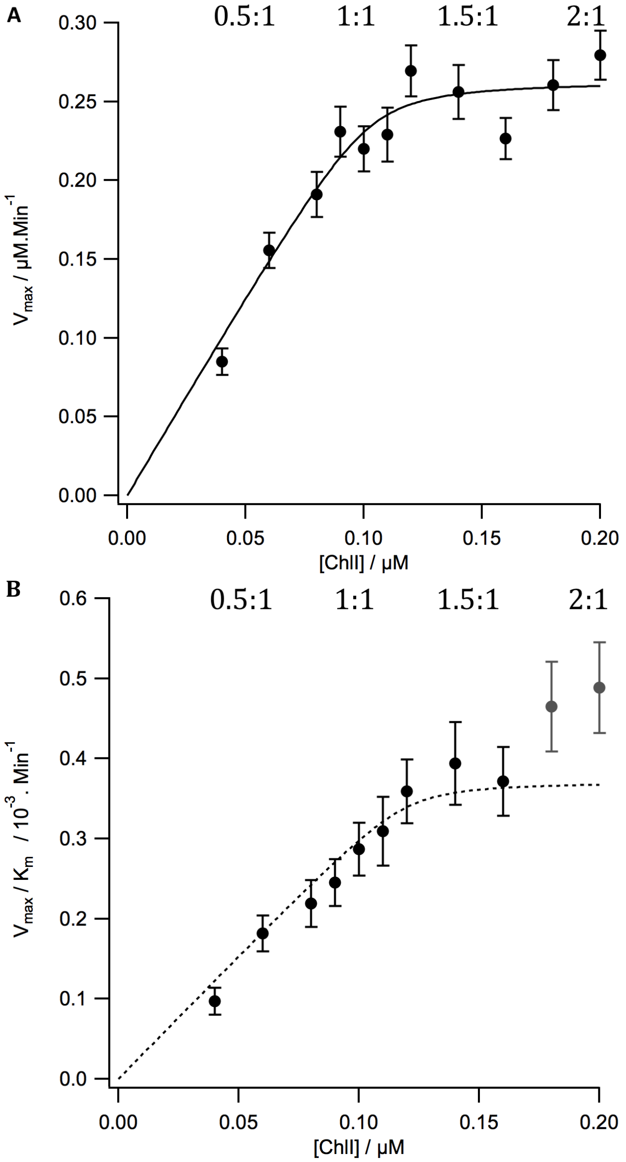

Figure 3.9: Titration of the ChlI subunit (0.04 — 0.2μM) against fixed levels of ChlD (0.1μM) and ChlH (0.4μM) suggest saturation is reached at equimolar levels of ChlI and ChlD. Data was fitted to a single site binding model (Equation 2.8) giving kinetic paramaters (A, V_{max}) E = 0.1 ± 0.01 μM, K$_d$ = 1.4 ± 2.6nM and V_{max} = 0.27 ± 0.02 μM.min^{-1}. (B, $V_{\mathrm{max}}/K_{\mathrm{m}}$) dashed line represents a simulated binding curve with E = 0.12 μM and K$_d$ = 1nm, giving maximal $V_{\mathrm{max}}/K_{\mathrm{m}}$ = 0.38 ± 0.01 x 10^{-3}.min^{-1}. Triplicate MgATP^{2-} curves (0.0625 — 5 mM) were generated at each [ChlI]. Measurements were performed in 0.1μM ChlD, 0.4μM ChlH, 10mM free MgCl$_2$, 8μM D$_{\mathrm{IX}}$, 1mM DTT, 50mM MOPS, 0.3M glycerol, 34°C, pH 7.7. Error bars represents standard deviation. Included ratios are [ChlI] : [ChlD].

A single site binding model (Equation 2.8) was used in fitting the resulting subunit titration curves, providing a way to estimate the binding site concentrations. A representation binding curve showing a 1:1 interaction between two species present at 0.1μM with a low K$_d$ (1nM) is demonstrated in Figure 3.10.

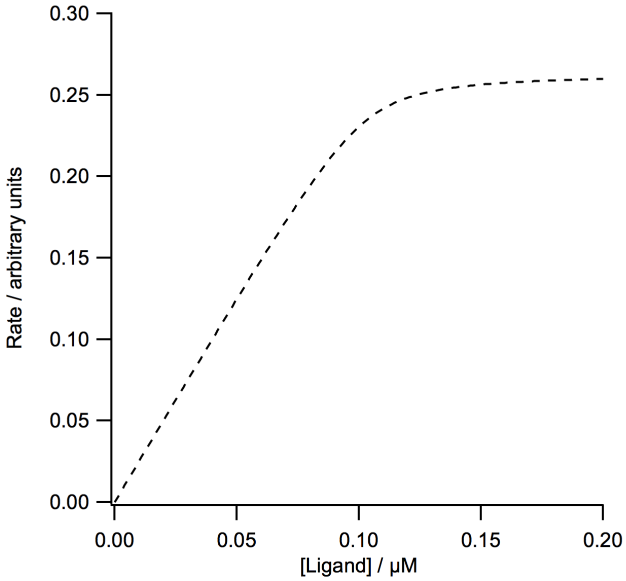

Figure 3.10: Representation of a single site binding curve showing a 1:1 interaction between two species present at 0.1μM with a low K$_d$ (1nM).

Fitting the dependence of V_{max} with ChlI concentration to this single site binding model (Equation 2.8) indicates a binding site concentration of E $= 0.1 \pm 0.01\mu$M (0.1μM ChlI). In comparison to the concentration of the ChlD subunit present during the titration (0.1 μM) this indicates saturation occurs at equimolar levels of ChlI and ChlD.

The estimated K$_d$ for the fitted titration curve is relatively low ($K_d = 1.4 \pm 2.6$nM). As this parameter is below the lowest protein concentration used in these assays (50nM ChlI), this estimate is unlikely to be numerically accurate, however is consistent with a relatively tight interaction occurring between ChlI and ChlD.

In relation to $V_{\mathrm{max}}/K_{\mathrm{m}}$ (Figure 3.9, panel B), which describes the overall conversion of substrate to product by the nucleotide free form of the enzyme, the variation in response to ChlI concentration appears more complex. Modelling the data to an approximate 1:1 binding curve of known binding site concentration (E $= 0.12$ μM) and K_d (1nM) with the assumption that the final two data points (grey) are significant outliers shows the data to be consistent with an increase in $V_{\mathrm{max}}/K_{\mathrm{m}}$ in response to increasing amounts of ChlI up to approximately equimolar levels of ChlI and ChlD which is followed by a plateau in $V_{\mathrm{max}}/K_{\mathrm{m}}$. However, given the assumptions required in fitting, more complex behaviour cannot be ruled out.

The kinetic parameters obtained from fitting to the single site binding model are summarised in Tables 3.1 (V_{max} data) and 3.2 ($V_{\mathrm{max}}/K_{\mathrm{m}}$ data).

Overall the titration of ChlI against fixed levels of ChlD and ChlH indicate saturation in relation to V_{max} occurring when ChlI and ChlD are at equimolar levels and although the variation in $V_{\mathrm{max}}/K_{\mathrm{m}}$ appears somewhat more complex, it may support a similar behaviour.

3.3.8 Titrations of ChlI against a fixed level of ChlD result in saturation at equimolar levels of ChlI and ChlD regardless of ChlH concentration

During a titration of ChlI (0.04 — 0.2 μM) into ChlD (0.1 μM) and ChlH (0.4 μM) saturation in V_{max} occurs when ChlI and ChlD are at equimolar concentrations.

To investigate if the ChlH subunit influences the complexes formed between ChlI and ChlD, the previous titration was repeated at an elevated (0.8μM) and reduced (0.2μM) level of the ChlH.

The titrations of ChlI against fixed levels of ChlD at both elevated (0.8μM) and reduced (0.2μM) concentrations of ChlH are consistent with the previous titration at 0.4μM ChlH. In all three cases, an increase in V_{max} is observed up to approximately equimolar levels of ChlI and ChlD followed by a plateau in V_{max}. The overall change in $V_{\mathrm{max}}/K_{\mathrm{m}}$, although again being more complex, is consistent with a 1:1 interaction. The resulting titrations are shown in Figure 3.11.

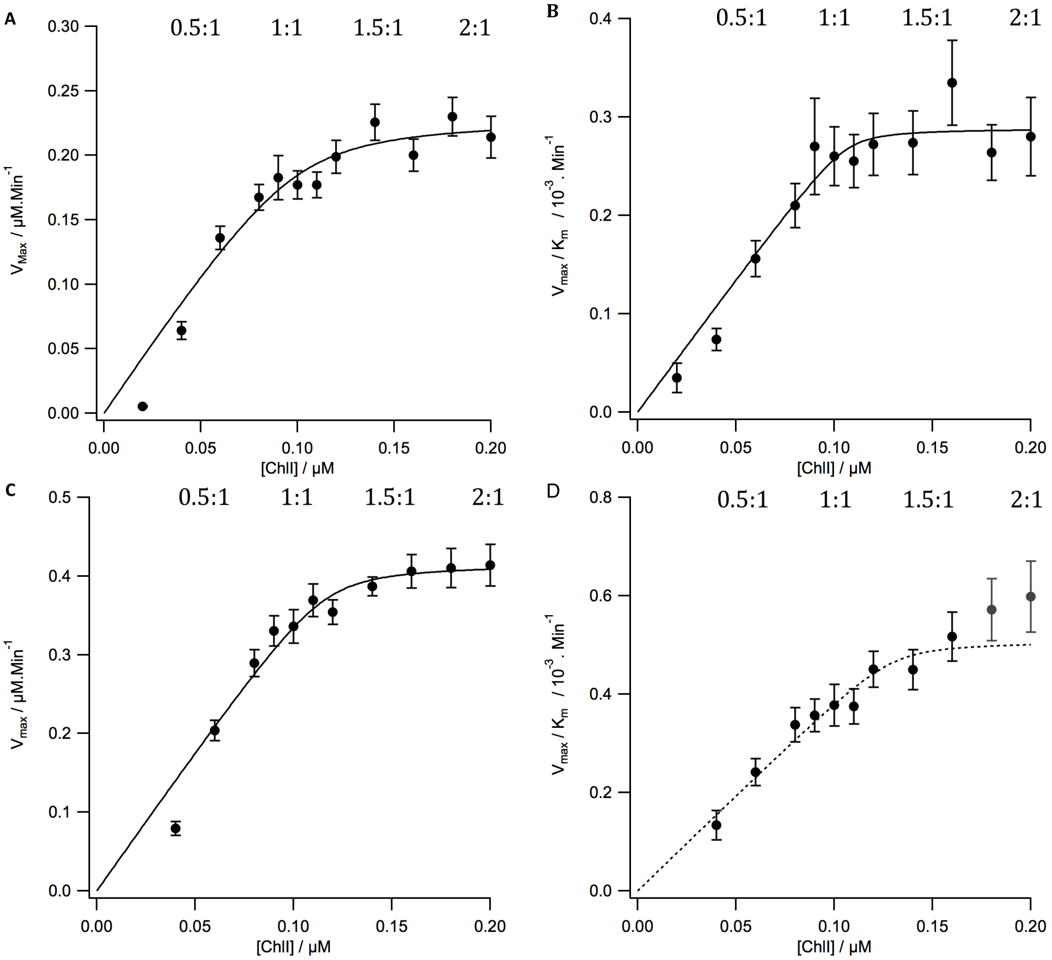

Figure 3.11: Titrations of the ChlI subunit (0.04 — 0.2μM) against fixed levels of ChlD (0.1μM) performed in a reduced (0.2μM) and elevated (0.8μM) level of ChlH suggest saturation occurs at equimolar levels of ChlI and ChlD regardless of ChlH concentration. The variation in V_{max} and $V_{\mathrm{max}}/K_{\mathrm{m}}$ in relation to [ChlI] was fitted to a single site binding model (Equation 2.8) giving kinetic parameters, (A, 0.2 μM ChlH, V_{max}) E = 0.11 ± 0.01 μM, K$_d$ = 2.6 ± 5.1 nM and V_{max} = 0.22 ± 0.02 μM.min^{-1}. (B, 0.2 μM ChlH, $V_{\mathrm{max}}/K_{\mathrm{m}}$) E = 0.11 ± 0.01 μM, K$_d$ = 0.6 ± 2 nM and maximum $V_{\mathrm{max}}/K_{\mathrm{m}}$ = 0.29 ± 0.02 x 10^{-3}.min^{-1}. (C, 0.8 μM ChlH, V_{max}) E = 0.12 ± 0.01 μM, K$_d$ = 1.55 ± 2.9 nM and V_{max} = 0.42 ± 0.03 μM.min^{-1} (D, 0.8 μM ChlH, $V_{\mathrm{max}}/K_{\mathrm{m}}$) dashed line represents a simulation of a 1:1 interaction with K$_d$ (1nM) with exclusion of the last two data points (grey), giving E = 0.13 ± 0.01 μM and maximum $V_{\mathrm{max}}/K_{\mathrm{m}}$ = 0.51 ± 0.02 x 10^{-3}.min^{-1}. Triplicate MgATP^{2-} curves (0.0625 — 5mM) were generated at each [ChlI]. Measurements were performed in 0.1μM ChlD, 10mM free $MgCl_2$, 8μM D_{IX}, 1mM DTT, 50mM MOPS, 0.3M glycerol, 34^{o}C, pH 7.7. Error bars represents standard deviation. Included ratios are [ChlI] : [ChlD].

The titration curves were fitted to a single site model binding model (Equation 2.8) and the resulting kinetic parameters are summarised in Tables 3.1 (V_{max} data) and 3.2 ($V_{\mathrm{max}}/K_{\mathrm{m}}$ data).

Fitting the dependence of $V_{\max}$ with ChlI concentration at both 0.2μM ChlH (Figure 3.11, panel A) and 0.8μM ChlH (Figure 3.11, panel C) gives estimated binding site concentrations of E = 0.11 ± 0.011 μM at 0.2μM ChlH and E = 0.12 ± 0.012 μM at 0.8 μM ChlH and indicates that saturation occurs at approximately equimolar levels of ChlI and ChlD irrespective of ChlH concentration.

The observed K_d values for the interaction between ChlI and ChlD at saturating nucleotide are consistent with those observed previously, with K_d values of 2.6 ± 5.1 nM at 0.2μM ChlH and 1.55 ± 2.9 nM at 0.8μM ChlH, further supporting a tight binding interaction between ChlI and ChlD.

In relation to $V_{\max}/K_{\mathrm{m}}$ (Figure 3.11, panels B and D) fitting the titration at 0.2μM ChlH to the single site binding model results in an observed inflexion at E = 0.11 ± 0.011 μM and supports saturation occurring at equimolar levels of ChlI and ChlD. Simulating the titration at 0.8μM ChlH, under a constrained K_d (1nM) with the exclusion of the last two titration points further supports saturation occurring at equimolar levels of ChlI and ChlD, however due to the constraints used, such behaviour can be treated as a guidance only.

3.3.9 Overall titrations of ChlI against a fixed level of ChlD show saturation at equimolar levels of ChlI and ChlD

The subunit titrations of ChlI (0.04 — 0.2 μM) into ChlD (0.1 μM) show saturation in relation to $V_{\max}$ at equimolar levels of ChlI and ChlD irrespective of ChlH concentration. Overall such behaviour would indicate a 1:1 interaction occurring between ChlI and ChlD. Furthermore although the change in $V_{\max}/K_{\mathrm{m}}$ appears more complex, it does suggest a similar 1:1 interaction.

Estimations for K_d values for the interaction between ChlI and ChlD within the titration are all relatively low (approximately 1 - 3 nM), consistent with a tight binding interaction between the ChlI and ChlD subunits even at low concentrations of ChlH.

At very low levels of ChlI relative to ChlD (i.e the lowest titration points) no chelatase activity is observed, consistent with inhibition at high proportions of ChlD over ChlI. As a result, no titration points were performed at very low levels of ChlI.

Although altering the concentration of ChlH does not noticeably perturb the relative levels of ChlI and ChlD where saturation occurs, the chelatase rate ($V_{\max}$ or $V_{\max}/K_{\mathrm{m}}$) is dependent on the concentration of ChlH, supporting the catalytic role of this subunit.

The kinetic parameters for the subunit titrations of ChlI into ChlD are summarised in Tables 3.1 (V_{max} data) and 3.2 ($V_{\mathrm{max}}/K_{\mathrm{m}}$ data).

Table 3.1: Kinetic parameters for the subunit titration of ChlI (0.04 — 0.2μM) into 0.1μM ChlD performed in varying concentrations of ChlH, as a result of fitting the variation in V_{max} with respect to the concentration of ChlI to the single site binding model. Errors represent standard deviation

Parameter	0.2μM ChlH	0.4μM ChlH	0.8μM ChlH
Binding site concentration E / μM	0.11 ± 0.01	0.1 ± 0.01	0.12 ± 0.01
K_d / nM	2.6 ± 5.1	1.4 ± 2.6	1.55 ± 2.9
V_{max} / μM.min^{-1}	0.22 ± 0.02	0.26 ± 0.02	0.42 ± 0.03

Table 3.2: Kinetic parameters for the subunit titration of ChlI (0.04 - 0.2μM) into 0.1μM ChlD performed in varying concentrations of ChlH, as a result of fitting the variation in $V_{\mathrm{max}}/K_{\mathrm{m}}$ with respect to the concentration of ChlI to the single site binding model. Errors represent standard deviation

Parameter	0.2μM ChlH	0.4μM ChlH	0.8μM ChlH
Binding site concentration E / μM	0.11 ± 0.01	0.12 [a]	0.13 ± 0.01
K_d / nM	0.6 ± 2.4	1 [a]	1 [a]
$V_{\mathrm{max}}/K_{\mathrm{m}}$ / 10^{-3}.min^{-1}	0.23 ± 0.02	0.38 ± 0.01	0.51 ± 0.02

[a] constrained

3.3.10 A 1:1 interaction between ChlI and ChlD cannot account for the change in chelatase activity observed during a titration of ChlD against ChlI

Titrations of ChlI against fixed levels of ChlD show saturation at equimolar levels of ChlI and ChlD, supported by the plateau in the titration curve in relation to $V_{\max}$ at an equimolar concentrations of ChlI and ChlD, furthermore such 1:1 interaction was unperturbed by the concentration of ChlH present.

To further investigate the interactions between ChlI and ChlD a contrasting titration of ChlD (0.02 — 2μM) against fixed ChlI (0.1μM) and ChlH (0.4μM) was performed. In sharp contrast to previous titrations, a 1:1 interaction between ChlI and ChlD is clearly incapable of explaining the observed behaviour (Figure 3.12).

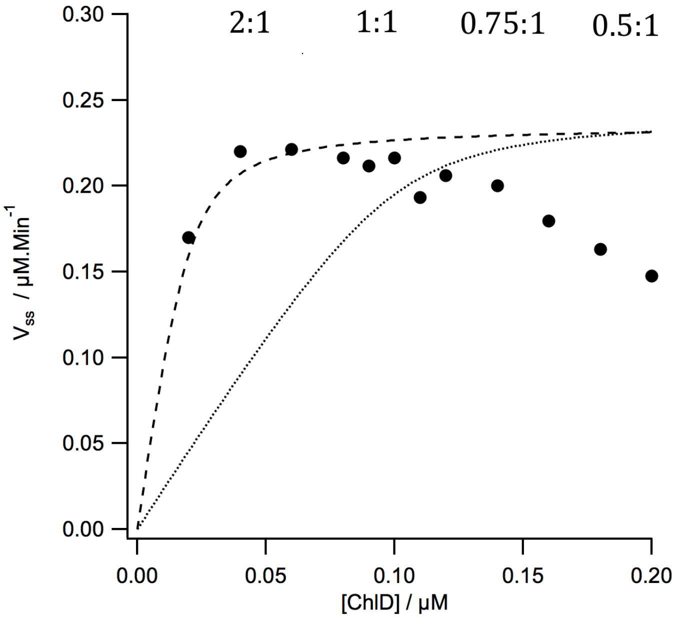

Figure 3.12: A 1:1 interaction between ChlI and ChlD (dotted line) is clearly unable to explain the observed change in chelatase activity during a titration of ChlD (0.02 - 0.2μM) against fixed levels of ChlI (0.1μM) and ChlH (0.4μM) and may suggest a much lower binding site concentration (dashed line, 0.02μM). (●) represents collected titration data. Measurements were performed in 0.1μM ChlI, 0.4μM ChlH, 5mM MgATP^{2-}, 10mM free MgCl$_2$, 8μM D$_{\text{IX}}$, 1mM DTT, 50mM MOPS, 0.3M glycerol, 34°C, pH 7.7. Included ratios are [ChlI] : [ChlD].

A comparison of the experimental data (Figure 3.12, ●) with a predicted binding curve representing a 1:1 interaction between ChlI and ChlD (Figure 3.12, dotted line) shows poor agreement. However a titration curve with a much lower estimated binding site concentration of 0.02μM ChlD (Figure 3.12, dashed line) appears to be a better a representation, at least within early titration points, of the overall change in chelatase activity observed.

The reduction in chelatase activity occuring at elevated levels of ChlD over ChlI is consistent with earlier studies on the system suggesting inhibition by high levels of ChlD [32].

3.3.11 Saturation in chelatase activity is achieved by the addition of very low levels of ChlD to ChlI during a titration of ChlD against fixed levels of ChlI

A simple 1:1 binding model is unable to explain the change in chelatase activity observed during titration of ChlD against ChlI (Figure 3.12). However, a binding curve with a much lower binding site concentration appears to be in better agreement with the initial points of the titration curve and may indicate saturation occurring at a higher ChlI : ChlD ratio.

To investigate if saturation is occurring at high levels of ChlI relative to ChlD, a titration of low amounts of the ChlD subunit (0.0025 — 0.05μM) against fixed levels of ChlI (0.1μM) and ChlH (0.4μM) was performed. In marked contrast to the titrations of ChlI against ChlD that show a 1:1 interaction, the titration of ChlD against ChlI shows saturation is achieved by the addition of very low levels of the ChlD subunit relative to ChlI. The resulting titration of ChlD (0.0025 - 0.05μM) against fixed levels of ChlI (0.1μM) and ChlH (0.4μM) is shown in Figure 3.13.

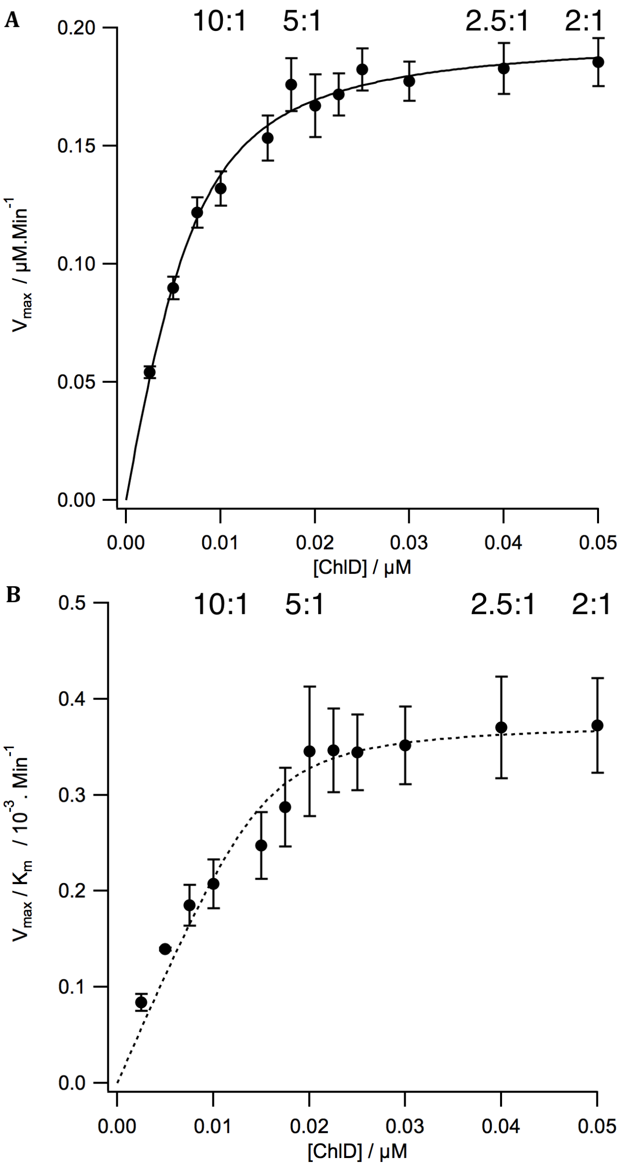

Figure 3.13: Saturation is achieved by the addition of very low levels of ChlD during a titration of the ChlD subunit (0.0025 — 0.05μM) against fixed levels of ChlI (0.1μM) and ChlH (0.4μM). The variation in V_{max} and $V_{\mathrm{max}}/K_{\mathrm{m}}$ in relation to [ChlD] was fitted to a single site binding model (Equation 2.8) giving kinetic parameters (A, V_{max}) E = 6.3 ± 1.5 nM, K$_d$ = 2.5 ± 0.85 nM and V_{max} = 0.2 ± 0.01 μM.min^{-1} (B, $V_{\mathrm{max}}/K_{\mathrm{m}}$), dotted line represent a simulation of a binding curve under a constrained K$_d$ of 1nM giving E = 15 ± 1.5 nM and maximum $V_{\mathrm{max}}/K_{\mathrm{m}}$ = 0.37 ± 0.01 x 10^{-3}.min^{-1}. Triplicate MgATP^{2-} curves (0.0625 — 5mM) were generated at each [ChlD]. Measurements were performed in 0.1μM ChlI, 0.4μM ChlH, 10mM free MgCl$_2$, 8μM D$_{\mathrm{IX}}$, 1mM DTT, 50mM MOPS, 0.3M glycerol, 34°C, pH 7.7. Error bars represents standard deviation. Included ratios are [ChlI] : [ChlD].

The resulting titration curves were fitted to a single site binding model (Equation 2.8) with the resulting kinetic parameters summarised in Tables 3.3 (V_{max} data) and 3.4

($V_{\max}/K_{\mathrm{m}}$ data).

Fitting to a single site binding model results in an estimated binding site concentration of E = 6.3 ± 1.5 nM in relation to $V_{\max}$ (Figure 3.13, Panel A). This estimated binding site concentration is far lower than the concentration of ChlI present (0.1μM) and indicates an approximate concentration ratio of 15 to 1 ChlI to ChlD, indicating saturation occurring at very low levels of ChlD relative to ChlI.

Fitting the $V_{\max}/K_{\mathrm{m}}$ data to the single site binding model requires that K_d is held constant (1nM in fitting shown), however again supports saturation occurring by the addition of low levels of the ChlD subunit, with an estimation of the binding site concentration of E = 15 ± 1.5 nM ChlD.

Overall, the titration of ChlD against ChlI indicates that saturation is reached at very low levels of the ChlD subunit relative to the ChlI and ChlH subunits.

3.3.12 Saturation occurs at very low levels of ChlD relative to ChlI irrespective of ChlH concentration during titrations of ChlD against ChlI

Titration of ChlD against fixed levels of ChlI and ChlH shows saturation at very low levels of the ChlD subunit relative to the ChlI subunit (Figure 3.13). This saturation, at an approximately 15-fold excess of ChlI over ChlD, shows a marked contrast to titrations of ChlI against ChlD, where equimolar (1:1) levels of subunits is required.

To further investigate how the ChlH subunit influences the interactions and complexes between ChlI and ChlD that may give rise to such a low inflexion point within the titration curve, the titration of ChlD against ChlI was repeated in an elevated (0.8μM) and reduced (0.2μM) concentration of ChlH.

The titrations of ChlD (0.0025 — 0.05μM) against ChlI (0.1μM) in an elevated (0.8μM) and reduced (0.2μM) concentration of ChlH both show saturation at very low levels of the ChlD subunit relative to ChlI (Figure 3.14), and are consistent with the titration performed in 0.4μM ChlH.

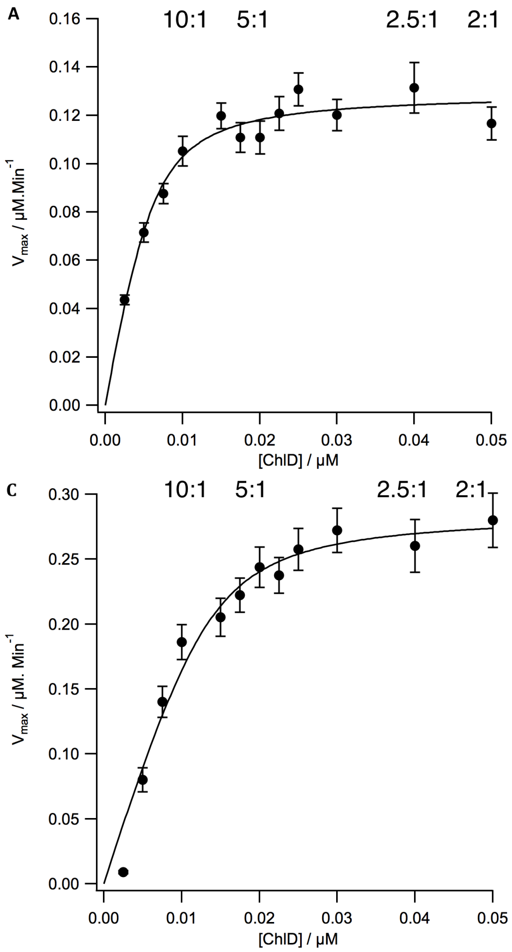

Figure 3.14: Saturation is achieved at very low levels of ChlD during a titration of the ChlD subunit (0.0025 — 0.05μM) against fixed levels of ChlI (0.1μM) at a reduced (Panels A and B, 0.2μM ChlH) and elevated (Panels C and D, 0.8μM ChlH) level of ChlH. The variation in $V_{\max}$ and $V_{\max}/K_{\mathrm{m}}$ in relation to [ChlD] was fitted to a single site binding model (Equation 2.8) giving kinetic parameters (A, 0.2 μM ChlH, $V_{\max}$) E = 5.8 ± 1.8 nM, K_d = 1.4 ± 0.9 nM and $V_{\max}$ = 0.13 ± 0.01 μM.min^{-1} (B, 0.2 μM ChlH, $V_{\max}/K_{\mathrm{m}}$) dotted line represents fitting to the single site binding model under a constrained K_d of 1nM giving E = 13 ± 1.8 nM and maximum $V_{\max}/K_{\mathrm{m}}$ = 0.22 ± 0.01 x 10^{-3}.min^{-1}. (C, 0.8 μM ChlH, $V_{\max}$) E = 14 ± 2.5 nM, K_d = 1.5 ± 1.3 nM and $V_{\max}$ = 0.29 ± 0.02 μM.min^{-1} (D, 0.8 μM ChlH, $V_{\max}/K_{\mathrm{m}}$) dotted line represents fitting to the single site binding model under a constrained K_d of 1nM giving E = 23 ± 3 nM and maximum $V_{\max}/K_{\mathrm{m}}$ = 0.77 ± 0.01 x 10^{-3}.min^{-1}. Triplicate MgATP^{2-} curves (0.0625 — 5mM) were generated at each [ChlD]. Measurements were performed in 0.1μM ChlI, 10mM free $MgCl_2$, 8μM D_{IX}, 1mM DTT, 50mM MOPS, 0.3M glycerol, 34°C, pH 7.7. Error bars represents standard deviation. Included ratios are [ChlI] : [ChlD].

The resulting titration curves were fitted to a single site binding model (Equation 2.8) with resulting kinetic parameters summarised in Tables 3.3 (V_{max} data) and 3.4 ($V_{\mathrm{max}}/K_{\mathrm{m}}$ data).

At saturating nucleotide (V_{max}) fitting the titration at 0.2 μM ChlH to a single site binding model shows good agreement, giving an estimated binding site concentration of 5.8nM. At 0.8μM ChlH the estimate of the binding site concentration increases to 14nM. At each concentration of ChlH, the estimated binding sites concentration is close to K_d (Table 3.3) and therefore will be prone to a large variance, subsequently such values are best viewed as order of magnitude estimates. Nonetheless, the approximately two-fold increase in the binding site concentration (E) from 0.2μM ChlH to 0.8μM ChlH could suggest that high concentrations of ChlH influence the interactions and complexes between ChlI and ChlD occurring here.

Fitting the variation in $V_{\mathrm{max}}/K_{\mathrm{m}}$ to the single site binding model using a constrained low K_d of 1nM, consistent with values observed within other titrations, further agrees with saturation occurring at low levels of ChlD. A change in the estimated binding site concentration is again observed in response to the concentration of ChlH, with values ranging from 13nM at 0.2 μM ChlH to 23nM at 0.8 μM ChlH.

The maximum chelatase activity (V_{max} or $V_{\mathrm{max}}/K_{\mathrm{m}}$, summarised in Tables 3.3 and 3.4) varies in response to the levels of ChlH, with the highest rates observed at highest levels of ChlH and thus further supports the catalytic role of the ChlH subunit.

Table 3.3: Kinetic parameters for the titration of ChlD (0.0025 — 0.05μM) against fixed levels of ChlI (0.1μM) performed in varying concentrations of ChlH, as a result of fitting the variation in V_{max} with respect to the concentration of ChlD to the single site binding model. Errors represent standard deviation.

Parameter	0.2μM ChlH	0.4μM ChlH	0.8μM ChlH
Binding site concentration E / nM	5.8 ± 1.8	6.3 ± 1.5	13.6 ± 2.5
K_d / nM	1.4 ± 0.9	2.5 ± 0.9	1.5 ± 1.3
V_{max} / μM.min^{-1}	0.129 ± 0.01	0.198 ± 0.01	0.285 ± 0.02

Table 3.4: Kinetic parameters for the titration of ChlD (0.0025 - 0.05μM) against fixed levels of ChlI (0.1μM) performed in varying concentrations of ChlH, as a result of fitting the variation in $V_{\mathrm{max}}/K_{\mathrm{m}}$ with respect to the concentration of ChlD to the single site binding model. Errors represent standard deviation.

Parameter	0.2μM ChlH	0.4μM ChlH	0.8μM ChlH
Binding site concentration E / nM	13 ± 1.8	15 ± 1.5	23 ± 3.2
K_d / nM	1[a]	1[a]	1[a]
$V_{\mathrm{max}}/K_{\mathrm{m}}$ / 10^{-3}.min^{-1}	0.22 ± 0.01	0.37 ± 0.01	0.77 ± 0.05

[a] constrained

3.3.13 Summary - subunit titrations suggest at least two widely different arrangements of ChlI and ChlD subunits can within complexes formed during Mg^{2+} insertion

Subunit titrations investigating how chelatase activity (rate of Mg^{2+} insertion into deuteroporphyrin-IX) changes with the concentrations of the subunits supports the formation of multiple chelatase complexes.

Titrations of ChlI against ChlD show saturation — indicated by a plateau in the titration curve — occurring at equimolar levels of ChlI and ChlD, which is unperturbed by the concentration of ChlH. Overall indicating a 1:1 interaction between ChlI and ChlD.

In contrasting titrations of ChlD against ChlI, the addition of only very low levels of ChlD to ChlI results in saturation therefore a 1:1 interaction is clearly unable to explain the observed behaviour. Furthermore, unlike within the titrations of ChlI against ChlD, high concentrations of ChlH appear to influence the relative levels of ChlI and ChlD where this saturation occurs, as seen in the overall change in estimated binding site concentrations at higher levels of ChlH.

With two sharply different ratios of ChlI and ChlD where saturation occurs, multiple different arrangements of subunits occurring within chelatase complexes involved in Mg^{2+} insertion cannot be disregarded. With a 1:1 interaction indicating the formation of complexes containing overall equivalent levels of ChlI and ChlD subunits. Whilst the saturation occurring at very low levels of ChlD may imply the formation of complexes that overall contain higher levels of ChlI relative to ChlD.

Within the overall chelatase, ATP hydrolysis is coupled with Mg^{2+} insertion. However, the complexes involved in Mg^{2+} insertion may not necessarily be the same as those involved in ATP hydrolysis and furthermore this ATP hydrolysis can occur independently of the Mg^{2+} insertion reaction. Therefore, the complexes involved solely in ATP hydrolysis within the chelatase were investigated.

3.3.14 Establishing assays to monitor ATP hydrolysis

The steady state rate of ATP hydrolysis can be monitored using the pyruvate kinase / lactate dehydrogenase (PK/LDH) coupled enzyme system, outlined in Figure 3.15. This system involves coupling the ATP hydrolysis reaction to a secondary reaction, the conversion of pyruvate to lactate during which NADH is oxidised to NAD$^+$. NADH exhibits a strong absorbance at 340nm allowing its depletion to be monitored directly, providing an indirect way to monitor steady state ATP hydrolysis.

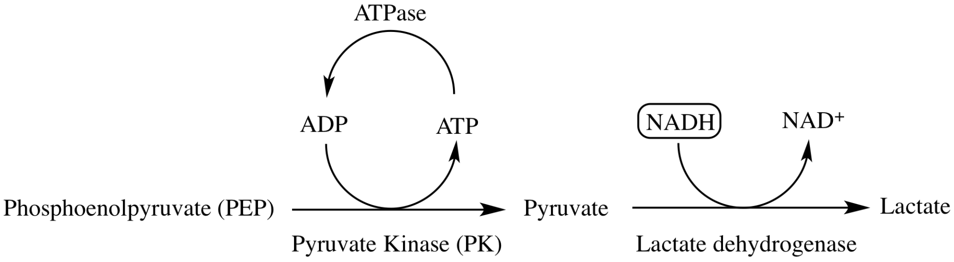

Figure 3.15: The PK/LDH coupled enzyme system allows the indirect detection of ATP hydrolysis by monitoring the depletion of NADH within a secondary coupled reaction.

Standard curves show a linear dependance of NADH concentration with measured absorbance (Figure 3.16, panel C) enabling the dependence of the absorbance signal on NADH concentration to be established during measurements using 96 well plates, providing a convenient system for measuring ATPase activity (Figure 3.16, panels A and B). Fitting procedures and equations are described in Materials and Methods Section 2.6.

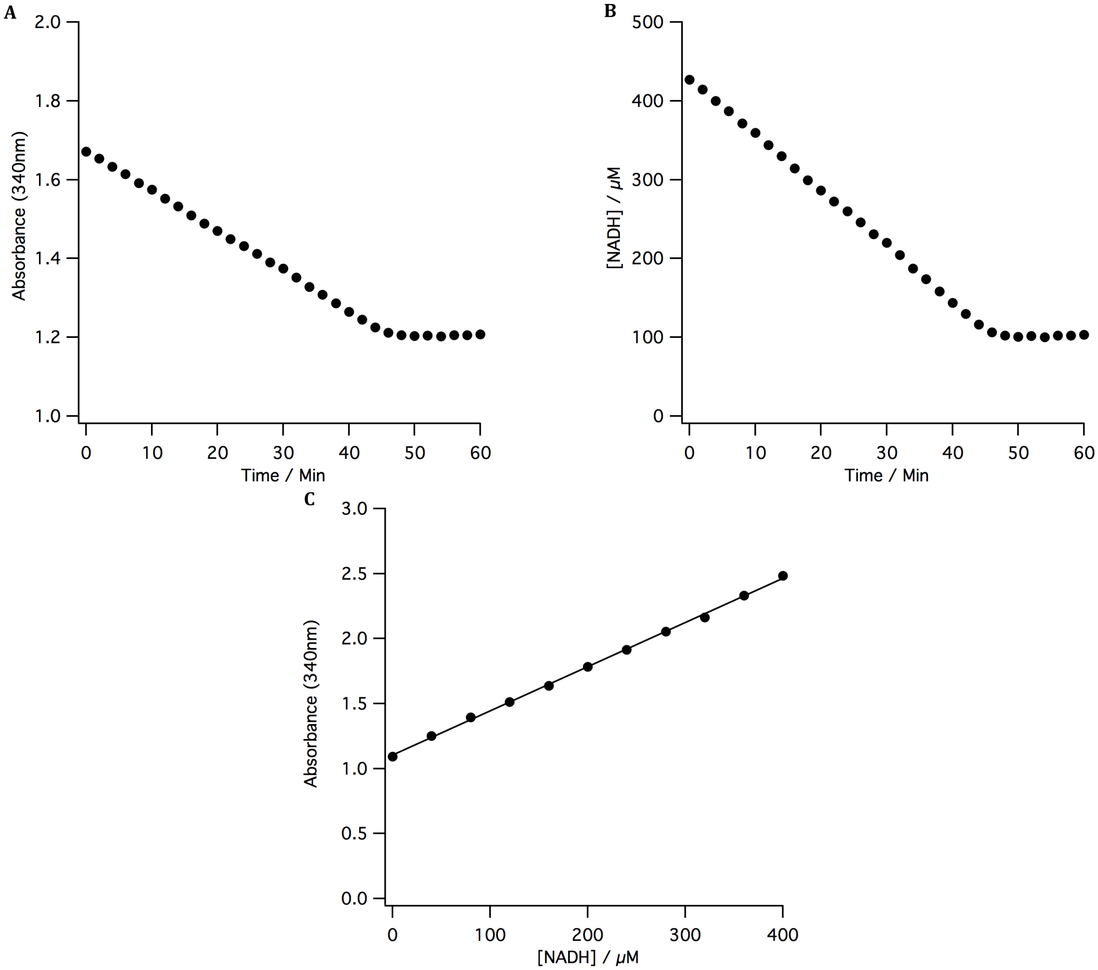

Figure 3.16: The direct conversion between the absorbance signal of NADH and NADH concentration can be achieved using standard curves at known NADH concentrations, enabling the steady-state rate of ATP hydrolysis to be determined. (Panels A and B) example of a steady state ATPase reaction, experiments were performed in 1μM ChlI, 5mM MgATP^{2-}, 10mM $MgCl_2$, 1mM DTT, 400μM NADH, 2mM PEP and 2 units PK/LDH. 50mM MOPS, 0.3M glycerol at 34°C, pH 7.7. (Panel C) a standard curve at known NADH concentrations to establish the dependence of NADH absorbance (340nm) with NADH concentration. Experiments were performed in 50mM MOPS, 0.3M glycerol at 34°C, pH 7.7. The relationship was established empirically by fitting to a straight line (Equation 2.9).

3.3.15 Subunit titrations suggest multiple distinct arrangements of I and D subunits within ATP hydrolysing complexes

The overall chelatase system requires two distinct, but interacting, components, the ATPase motor complex containing the I and D subunits and the catalytic H subunit [81].

Subunit titrations following the chelatase reaction demonstrate saturation can occur at two significantly different overall levels of ChlI and ChlD. Titrations of ChlI against ChlD show saturation at equimolar levels, while the titrations of ChlD against ChlI show saturation occurs when ChlI is in large excess over ChlD. Such behaviour may be as a result of the formation of multiple complexes during Mg^{2+} insertion containing significantly different relative levels of ChlI and ChlD subunits.

However, such experiments give no specific insight into complexes responsible for ATP hydrolysis within the chelatase, therefore to probe the complexes responsible for the ATP hydrolysis, the ATPase activity of the system was investigated via subunit titrations. Titrations of the ChlD subunit into the ChlI subunit, performed in the absence of ChlH or porphyrin reveals the complexes formed between ChlI and ChlD that are involved in ATP hydrolysis. Similar titrations in the presence of ChlH allows the formation of complexes occurring in the presence of ChlH to be investigated.

It was demonstrated that in the absence of ChlH, titration of ChlD against ChlI results in saturation at 1:1 levels of ChlI and ChlD and supports the formation of complexes, although with suppressed activity, capable of ATP hydrolysis that contain equal levels of ChlI and ChlD. In the presence of ChlH, a strikingly different change in ATPase activity is observed, with a stimulation in the overall ATPase activity observed under lower levels of ChlD relative to ChlI and ChlH, giving further support towards complexes containing higher levels of ChlI over ChlD.

3.3.16 Titrations of ChlD against ChlI in the absence of ChlH monitoring ATPase activity give direct support to a 1:1 interaction between ChlI and ChlD

The ChlD subunit (0 — 2μM) was titrated against ChlI (1μM) in the absence of ChlH and deuteroporphyrin-IX. Duplicate full MgATP^{2-} concentration curves were generated at each titration point. The subunit titration was performed according to Materials and Methods Section 2.4 and data analysis was performed according to 2.6.

The ChlI subunit exhibits an ATPase activity in absence of ChlD. Addition of increasing amounts of ChlD to ChlI gradually reduces the ATPase activity until equimolar levels of ChlI and ChlD are reached. Further addition of ChlD results in no change in the ATPase activity, either in V_{max} or $V_{\mathrm{max}}/K_{\mathrm{m}}$. The change in V_{max} and $V_{\mathrm{max}}/K_{\mathrm{m}}$ during the titration of ChlD (0 — 2μM) against fixed levels of ChlI (1μM) is show in Figure 3.17.

The change in V_{max} (Figure 3.17, panel A) during the titration indicates saturation in ATPase activity occurring at approximately 1:1 levels of ChlI to ChlD, although a good fitted to the single site binding model (Equation 2.11) is only possible when the binding site concentration (E) is constrained at E = 1 μM.

An overall curvature in the V_{max} data observed during the initial region (0 — 1 μM) will likely be the cause of this poor fitting. Such a response may be on account of the formation of multiple complexes between ChlI and ChlD of varying ATPase activities occurring within this initial region.

With no significant change in V_{max} occurring in response to the addition of an excess of ChlD over ChlI the formation of complexes containing equivalent levels of ChlI and ChlD subunits is likely with no indication for a complex or complexes containing higher levels of ChlD relative to ChlI.

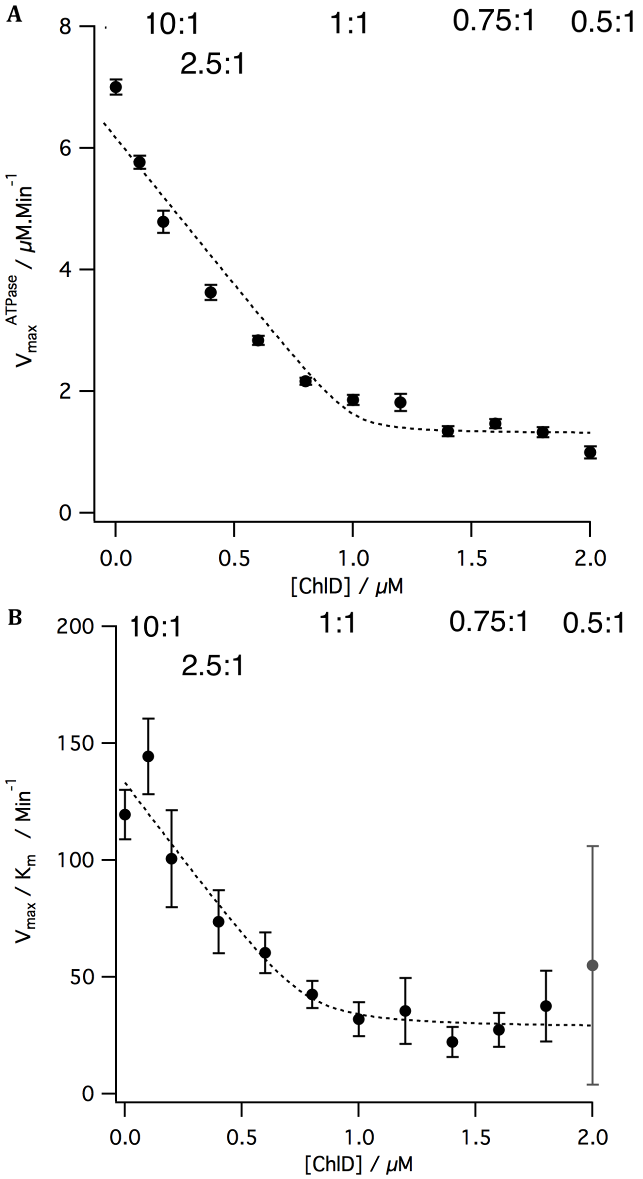

Figure 3.17: Titration of ChlD (0 — 2μM) against fixed levels of ChlI (1μM) in the absence of ChlH and D_{IX} suggests the formation of an ChlID complex containing equal levels of ChlI and ChlD capable of ATP hydrolysis. (A, $V_{\max}$) the dotted line represents modelling of a single site binding curve (Equation 2.11) under a constrained binding site concentration E = 1 μM, with resulting $K_d = 25 \pm 54$ nM. (B, $V_{\max}/K_{\mathrm{m}}$) the dotted line represents fitting of a single site binding curve (Equation 2.11) omitting final titration point (grey), giving E = 0.87 ± 0.09 μM and $K_d = 8.1 \pm 1.9$ nM. Duplicate $MgATP^{2-}$ curves (0.05 - 5 mM) were generated at each [ChlD]. Measurements were performed in 50mM MOPS, 0.3M glycerol, 10mM free $MgCl_2$, 1mM DTT, 400μM NADH, 2mM PEP, 2u PK/LDH, 34°C, pH 7.7. Error bars represents standard deviation. Included ratios are [ChlI] : [ChlD].

The change in $V_{\max}/K_{\mathrm{m}}$ (Figure 3.17, panel B) offers strong support for a 1:1 interaction between ChlI and ChlD, with fitting the variation in $V_{\max}/K_{\mathrm{m}}$ to the single site binding model (although omitting the last titration point due to significant error) showing an estimated binding site concentration of E = 0.87 ± 0.09 μM and K_d = 8.1 ± 1.9 nM.

The observed K_d values for the titration of ChlD into ChlI support a relatively tight interaction between ChlI and ChlD, consistent with that observed in the chelatase titrations, with a K_d of 25 ± 54 nM for the change in $V_{\max}$ and a K_d of 8.1 ± 1.9 nM for the change in $V_{\max}/K_{\mathrm{m}}$ observed. The resulting kinetic parameters and other relevant data are summarised in Tables 3.5 ($V_{\max}$) and 3.6 ($V_{\max}/K_{\mathrm{m}}$).

Table 3.5: Kinetic parameters (inflexion E and K_d) for the subunit titration monitoring the ATPase activity during a titration of ChlD (0 — 2μM) against ChlI (1μM) as a result of fitting the variation in $V_{\max}$ with respect to the concentration of ChlD to the single site binding model. The observed ATPase activities in the absence of ChlD and at saturating ChlD are also included. Errors refer to standard deviation.

Parameter	Value
Binding site concentration E / μM	1[1]
K_d / nM	25 ± 54
$V_{\max}$ (no ChlD) / μM.min^{-1}	7 ± 0.13
$V_{\max}$ (saturating ChlD) / μM.min^{-1}	1.33 ± 0.09

[1] constrained

Table 3.6: Kinetic parameters (inflexion E and K_d) for the subunit titration monitoring the ATPase activity during a titration of ChlD (0 — 2μM) against ChlI (1μM), as a result of fitting the variation in $V_{\max}/K_{\mathrm{m}}$ with respect to the concentration of ChlD to the single site binding model. The observed ATPase activities in the absence of ChlD and at saturating ChlD are also included. Errors refer to standard deviation.

Parameter	Value
Binding site concentration E / μM	0.87 ± 0.09
K_d / nM	8.1 ± 1.9
$V_{\max}/K_{\mathrm{m}}$ (no ChlD) / min^{-1}	120 ± 12
$V_{\max}/K_{\mathrm{m}}$ (saturating ChlD) / min^{-1}	37.6 ± 16.7

3.3.17 In the presence of ChlH a dramatic change in the ATPase activity occurs during titration of ChlD against ChlI

In the absence of ChlH addition of increasing amounts of ChlD to ChlI results in suppression of the overall ATPase activity, consistent with the formation of complexes between ChlI and ChlD with a lower ATPase activity. Following the addition of equimolar levels of ChlD to ChlI, no significant change in the ATPase activity is seen as a result of increasing amounts of ChlD. This suggests the formation of complexes between ChlI and ChlD capable of ATP hydrolysis containing equal levels of the subunits.

To investigate how the ChlH subunit influences the ATP hydrolysis performed by such complexes of ChlI and ChlD, the titration of ChlD (0 — 2μM) against fixed levels of ChlI (1μM) was performed in the presence of ChlH (4μM). The titration of ChlD against ChlI, performed in the presence of ChlH, shows a very different overall response to the ATPase activity to that seen in the absence of ChlH. During the titration, the addition of relatively low amounts of ChlD results in a dramatic increase in the ATPase activity, which is followed by the gradual reduction in the ATPase activity in response to the further addition of ChlD.

Figure 3.18 shows the change ATPase activity observed during the titration of ChlD (0 — 2μM) against fixed levels of ChlI (1μM) and ChlH (4μM) in relation to V_{max} (panel A) and $V_{\mathrm{max}}/K_{\mathrm{m}}$ (panel B). To aid comparison between the titrations performed in the presence and absence of ChlH, a direct comparison of the titrations is shown in Figure 3.19.

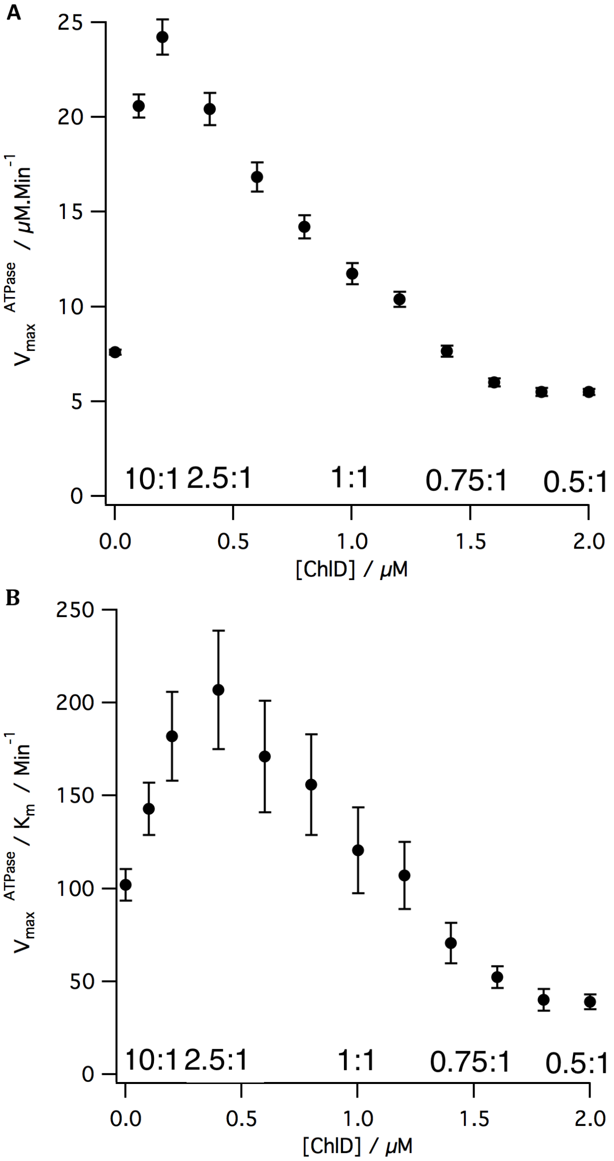

Figure 3.18: The change in ATPase activity observed during a titration of ChlD (0 — 2μM) against fixed levels of ChlI (1μM) shows a significant variation in the presence of ChlH (4μM). (Panel A) V_{max}. (Panel B) $V_{\mathrm{max}}/K_{\mathrm{m}}$. Duplicate MgATP^{2-} curves (0.03 — 5 mM) were generated at each [ChlD]. Measurements were performed in 50mM MOPS, 0.3M glycerol, 10mM free MgCl$_2$, 1mM DTT, 400μM NADH, 2mM PEP, 2u PK/LDH, 34°C, pH 7.7. Error bars represents standard deviation. Included ratios are [ChlI] : [ChlD].

Within the titration, in the absence of ChlD the ChlI and ChlH subunits together exhibit an ATPase activity consistent with that for the ChlI subunit in isolation, with a $V_{\mathrm{max}} = 7 \pm 0.13$ μM.min^{-1} in the absence of ChlH and $V_{\mathrm{max}} = 7.6 \pm 0.14$ μM.min^{-1} in the presence of ChlH. Similar values of $V_{\mathrm{max}}/K_{\mathrm{m}}$ are also observed with $V_{\mathrm{max}}/K_{\mathrm{m}}$ = 120 ± 12 .min^{-1} in the absence of ChlH and $V_{\mathrm{max}}/K_{\mathrm{m}}$ = 102 ± 9 .min^{-1} in the presence of ChlH. Thus, these data provide no evidence for an interaction between ChlI and ChlH in the absence of ChlD.

The addition of low levels of the ChlD subunit (0.1 — 0.4μM) stimulates the ATPase activity in the presence of ChlH, in sharp contrast to the behaviour seen in the absence of ChlH (see Figure 3.19 for direct comparison). An approximate 3-fold increase in the ATPase activity with respect to V_{max} is a seen as a result of the addition of 0.4 μM ChlD to 1μM ChlI and 4μM ChlH. An approximate 2-fold increase in $V_{\mathrm{max}}/K_{\mathrm{m}}$ is observed by the addition of the same concentration of ChlD.

The stimulation of the ATPase activity in the presence of low levels of ChlD relative to ChlI and ChlH, shown here to occur when the ChlD subunit concentration is approximately 10- to 2.5- fold less than ChlI concentration, may be due to the formation of a complex or complexes capable of ATP hydrolysis that overall contain low levels of ChlD relative to ChlI and ChlH.

The further addition of ChlD after the initial spike in the observed ATPase activity results in the gradual reduction and then plateau of ATPase activity in relation to both V_{max} and $V_{\mathrm{max}}/K_{\mathrm{m}}$. Demonstrating a suppression of the overall ATPase activity by high levels of the ChlD subunit.

The ATPase activity seen at high levels of ChlD also depends on the ChlH subunit. With $V_{\mathrm{max}} = 5.5 \pm 0.2$ μM.min^{-1} at high ChlD in the presence of ChlH, this is approximately 4 fold greater than observed in the absence of ChlH (V_{max} 1.33 $\pm$ 0.09 μM.min^{-1}). This difference can be seen in when comparing the titrations in the absence and presence of ChlH (Figure 3.19). This variation in V_{max} as a result of the presence of the ChlH subunit, occurring at saturating levels of ChlD relative to ChlI, supports the view that the ChlH subunit directly influences the ATPase activity of ChlID complexes. Such dramatic changes in the overall ATPase activity in the presence of ChlH provides further direct evidence not only for the interactions between the ChlH and the ChlID complexes during the ATP hydrolysis cycles, but also the regulation of the overall ATPase activity by ChlH. However no significant variation in $V_{\mathrm{max}}/K_{\mathrm{m}}$ is observed at saturating ChlD.

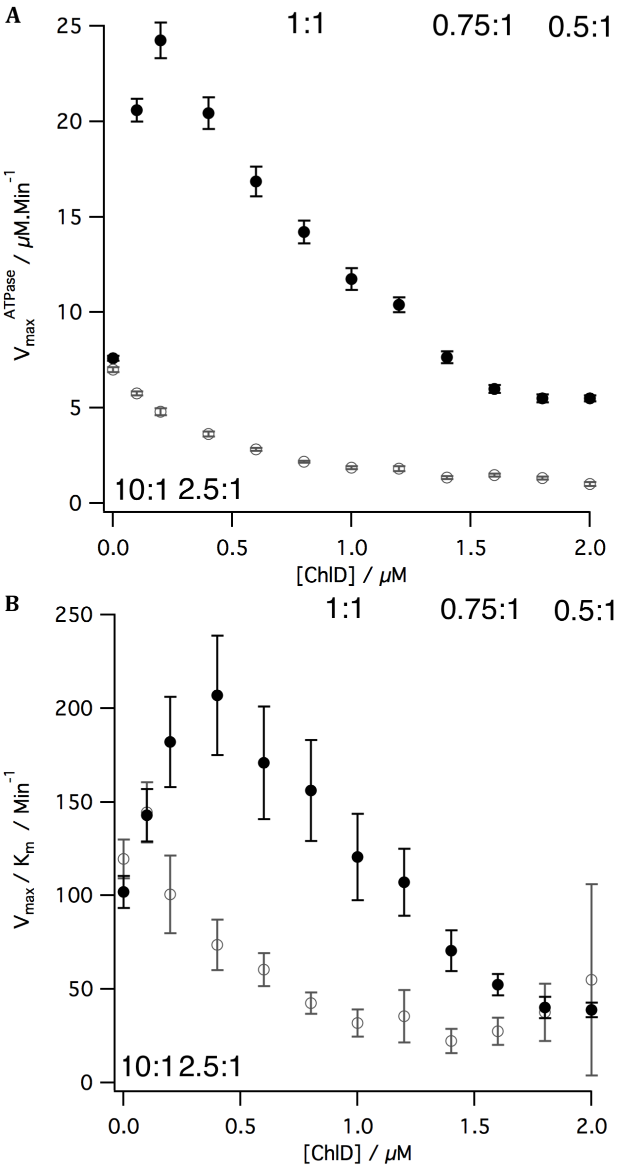

Figure 3.19: Direct comparison of the subunit titrations monitoring ATPase activity during the titration of ChlD (0 — 2 μM) against 1μM ChlI, in the absence (○) and presence of 4μM ChlH (●). (A) V_{max} (B) $V_{\mathrm{max}}/K_{\mathrm{m}}$. Included ratios are [ChlI] : [ChlD].

3.3.18 Summary - kinetic titrations monitoring ATPase activity give further support towards the formation of multiple ChlID arrangements

Subunit titrations monitoring the changes in ATPase activity during titrations of ChlD against ChlI (compared in Figure 3.19) would suggest the formation of multiple complexes between ChlI and ChlD that are capable of ATP hydrolysis.

In the absence of ChlH, the addition of ChlD to ChlI results in a gradual reduction in the ATPase activity until equimolar levels of ChlI and ChlD are reached, with further addition of ChlD resulting in no significant change in the ATPase activity. Overall, indicating a 1:1 interaction between ChlI and ChlD and the formation of complexes — at saturating concentrations of ChlD — containing equal levels of ChlI and ChlD subunits.

Within a similar titration, however performed in the presence of ChlH, a strikingly different overall change in the ATPase activity is seen. With the addition of low levels of ChlD relative to ChlI and ChlH resulting in a much stimulated overall ATPase activity. It therefore appears reasonable that ChlID complex(es) that contain overall higher levels of the ChlI subunit over ChlD will be those leading this initial high ATPase activity observed. Furthermore, the ATPase activity observed at saturating levels of ChlD relative to ChlI is also influenced by the ChlH subunit. Based on these kinetic titrations, models and feasible chelatase complexes are discussed in the following sections.

3.4 Conclusions and Models

The previously discussed kinetic titrations give strong support towards the formation of multiple complexes occurring during Mg^{2+} insertion and ATP hydrolysis that differ in their levels of ChlI and ChlD subunits.

Given the vast array of evidence (Table 1.3) that AAA^+ proteins often assemble, in a nucleotide dependent manner, into ring-like arrangements of their individual subunits — hexamers are most commonly observed — and that these ring-like arrangements often represent the active enzyme form [41, 44, 39], similar behaviour is expected by the AAA^+ I and D subunits of magnesium chelatase.

The formation of rings of subunits can occur by the I and D subunits in isolation [85, 88, 91] and it has been demonstrated that the *Rhodobacter capsulatus* BchI and BchD subunits form a two tiered I_6D_6 hexameric arrangement [94] in the absence of BchH. Currently there is no direct evidence for the formation of this specific complex occurring within the *Synechocystis* system.

Based on the previously described kinetic titrations, reasonable models for subunit assembly can be proposed. Due to numerous individual assembly pathways and the resulting vast range of possible subunit combinations [104], certain simplifications are made when discussing the building of higher order assemblies of subunits.

3.4.1 Subunit titrations observing Mg^{2+} insertion support multiple arrangements of ChlI and ChlD subunits occurring within active complexes

Kinetic titrations monitoring Mg^{2+} insertion, demonstrated saturation can occur at 1:1 levels of ChlI and ChlD, or at a much higher ChlI to ChlD ratio depending on the specific titrations performed. These observations strongly suggest that multiple arrangements of ChlI and ChlD subunits within active complexes is possible.

Titrations of ChlI against ChlD result in saturation at equimolar levels of ChlI and ChlD indicating a 1:1 interaction between ChlI and ChlD. This ratio supports a range of ChlID complexes containing equivalent levels of subunits (Figure 3.20, for clarity the ChlH subunit is omitted). With rings of subunits generally being the active form of AAA^+ proteins, it is reasonable to assume that the active arrangement of ChlI and ChlD subunits would be a ring of subunits, such as I_6D_6. However, there is no direct evidence for the formation of this subunit arrangement within the *Synechocystis* system.

The alternative titrations, again monitoring Mg^{2+} insertion, however with titration ChlD against ChlI results in saturation at a much higher ChlI to ChlD concentration ratio, approximately 15-fold based on estimations of binding site concentrations during titrations. This saturation occurring under these conditions gives strong support towards formation of complexes containing much higher levels of ChlI subunits over ChlD subunits. Figure 3.21 gives examples of feasible higher order ChlID arrangements.

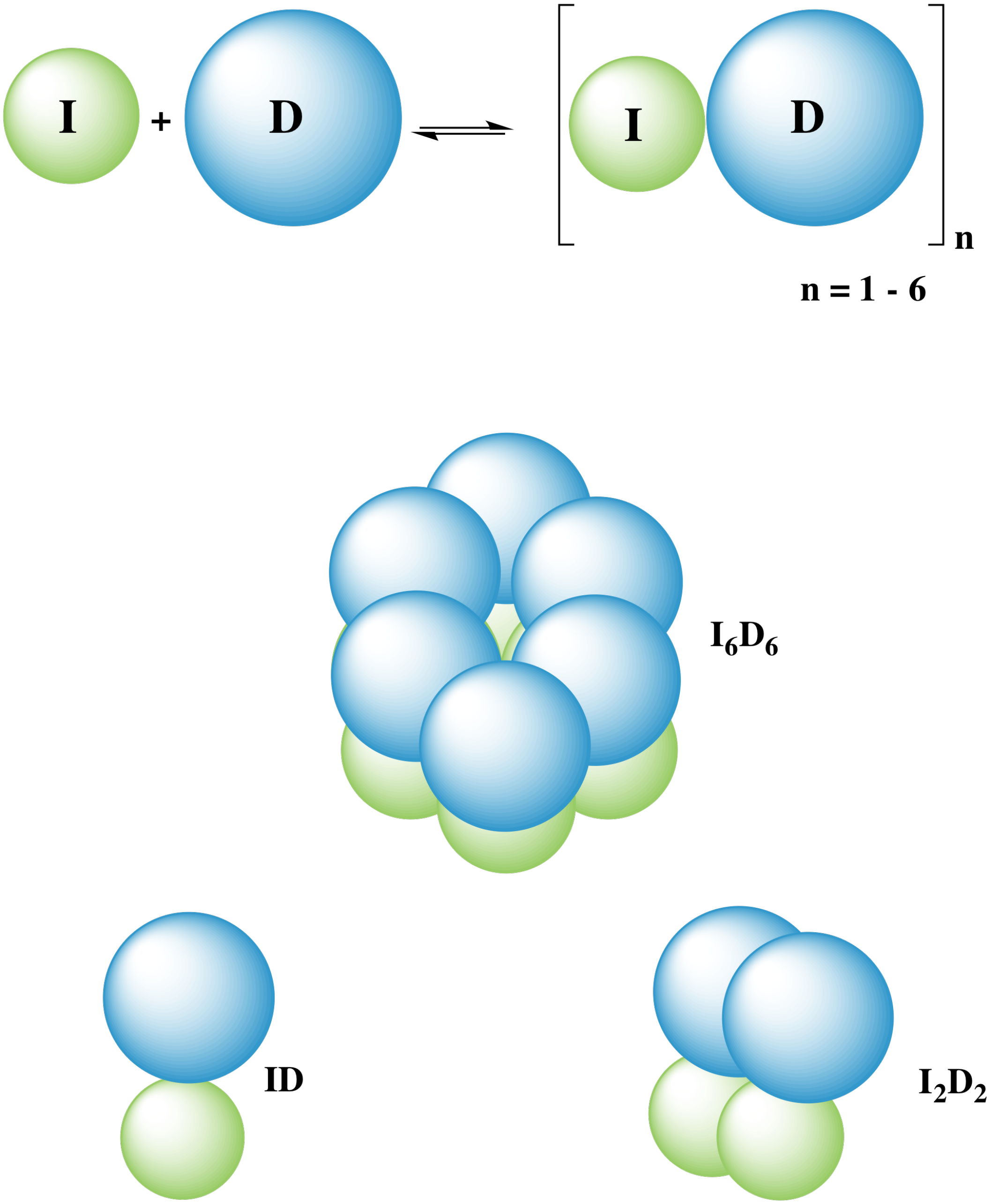

Figure 3.20: Examples of ChlID complexes that support the 1:1 interaction between ChlI and ChlD seen within kinetic titrations of ChlI against ChlD monitoring Mg^{2+} chelation. ChlH is omitted for clarity.

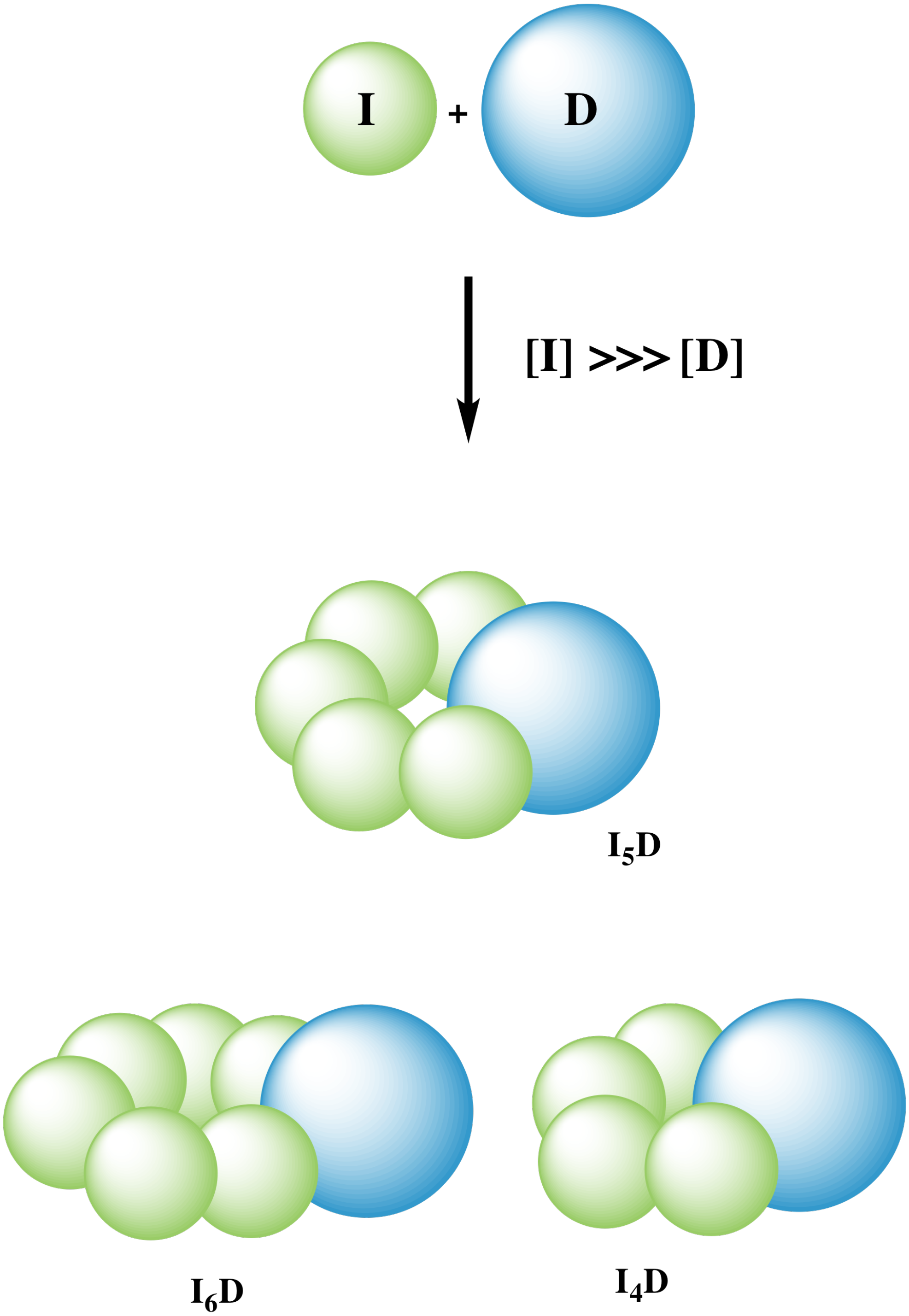

Figure 3.21: Examples of ChlID complexes that can account for the saturation observed at much higher levels of ChlI over ChlD seen within kinetic titrations of ChlD against ChlI monitoring Mg^{2+} chelation. ChlH is omitted for clarity.

Within these complexes, formed when ChlI is in excess over ChlD, high levels of ChlH appears to perturb the relative levels of ChlI and ChlD where saturation occurs, indicated by changes in estimated binding site concentrations within kinetic titrations

(Tables 3.3 and 3.4). This change would suggest that the ChlH subunit influences these higher order ChlI to ChlD arrangements. Although the exact nature of these interactions cannot be established from kinetic titrations, biophysical evidence for a ChlDH interaction (Dr Nathan Adams, unpublished work) would suggest that any reorganisation of the complex is mediated through the ChlD subunit.

Higher levels of ChlD over ChlI leads to inhibition of chelatase activity within titrations of ChlD against ChlI (Figure 3.12), thus complexes containing higher levels of ChlD subunits over ChlI subunits are unlikely to represent any active components of the system.

Overall, these kinetic titrations monitoring Mg^{2+} insertion support at least two distinct arrangements of ChlI and ChlD subunits occurring within active chelatase complexes. With complexes having equimolar levels of subunits, in addition to complexes that contain excess of ChlI over ChlD.

3.4.2 Kinetic titrations monitoring ATPase activity in the absence of ChlH support a 1:1 interaction between ChlI and ChlD

Within kinetic titrations monitoring ATPase activity in the absence of ChlH, the addition of increasing amounts of ChlD to ChlI leads to gradual suppression of the overall ATPase activity, which occurs up to equimolar levels of subunits. This reduction in ATPase activity likely results from suppression of ATPase activity of ChlI by ChlD within formed complexes.

Elevated levels of ChlD over ChlI show no significant change in ATPase activity. Therefore, a 1:1 interaction between ChlI and ChlD and the formation of complexes containing equivalent levels of these subunits are directly supported within this titration. These 1:1 complexes are likely to represent those shown in Figure 3.20, however, these complexes are capable of hydrolysing ATP and can occur in the absence of ChlH.

Within the initial region of the ATPase titration of ChlD against ChlI, a gradual reduction in ATPase activity results from the addition of increasing levels of ChlD. This may be on account of the formation of multiple ChlID complexes within this region of varying ATPase activity. Any number of complexes are plausible and it is not unreasonable to assume — especially when considering the strong evidence for complexes containing higher levels of ChlI over ChlD within kinetic titrations monitoring Mg^{2+} insertion — that the formation of a complex within this region containing higher levels of ChlI over ChlD occurs, analogous to those demonstrated in Figure 3.21. However on the lone basis of this ATPase titration performed in the absence of ChlH, the direct support towards the formation of such complexes is unwarranted. With only direct evidence for a 1:1 interaction between ChlI and ChlD.

3.4.3 Kinetic titrations monitoring ATPase activity in the presence of ChlH support formation of multiple ChlID arrangements and an interaction of ChlH with ChlID complexes

During kinetic titrations of ChlD against ChlI, in the presence of ChlH, an elevated ATPase activity is observed at low levels of ChlD relative to ChlI and ChlH. The further addition of ChlD then leads to the gradual reduction in ATPase activity (Figure 3.19).

This overall change in the ATPase activity observed within the titration may be explained by the formation of multiple ChlID arrangements.

At low levels of ChlD relative to ChlI, the formation of complexes containing a single ChlD subunit and multiple ChlI subunits will be more probable (Figure 3.22). If ChlD-H interactions are those that lead to activation in ATPase activity, then within this complex a single ChlD subunit leads to the formation of a complex of stimulated ATPase activity.

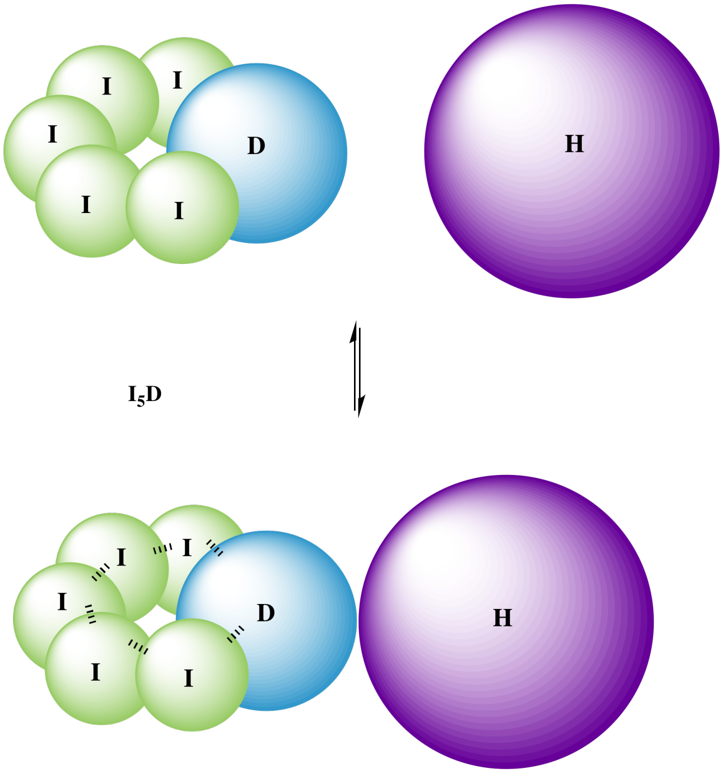

Figure 3.22: Example of a higher order ChlID complex containing higher levels of ChlI over ChlD. Interactions of ChlH likely result in stimulation of the ATPase activity of this complex.

In contrast, in the latter part of the titration where ChlD is present at higher levels, complexes containing more ChlD, for example 1:1 ID complexes such as I_6D_6 would appear more likely. Within these larger arrangements (Figure 3.23), multiple ChlD subunits will be present at close proximity. For example, in the case of an I_6D_6 complex, this active ATPase contains 6 ChlD subunits. As more ChlD subunits are present within one active complex under these conditions, a single ChlD subunit is no longer able to result in the formation of an active complex. Therefore, the overall numbers of active arrangements occurring will be lower which would explain this overall reduction in ATPase activity at increasing levels of ChlD.

Therefore at low levels of ChlD, every ChlD subunit will lead to a fully active complex and the maximum number of active complexes within the titration is achieved. Whilst at higher levels of ChlD, formed complexes will contain more ChlD subunits, reducing the overall numbers of active arrangements.

A alternative explanation for such reduction in ATPase activity, is that high levels of ChlD simply lead to the overall inhibition of ATPase activity of formed complexes.

Nonetheless, these titrations would indicate multiple arrangements of ChlI and ChlD subunits can occur within active complexes.

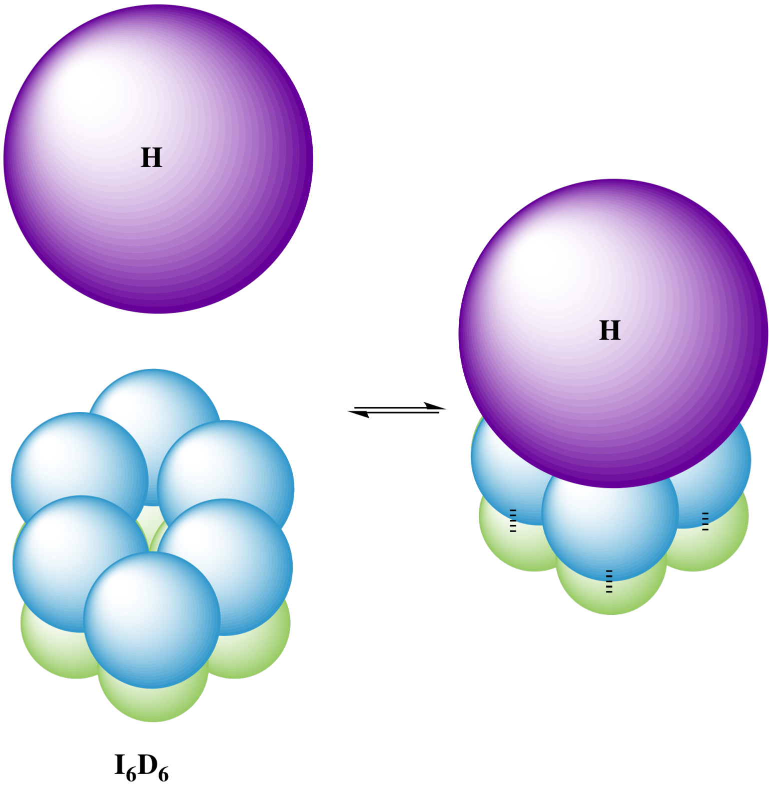

Figure 3.23: Example of a 1:1 ChlID complex containing multiple ChlI and ChlD subunits. Interactions of ChlH likely result in stimulation of the ATPase activity of this complex.

3.4.4 Summary - kinetic titrations support multiple ChlID arrangements within active complexes

These kinetic titrations give strong support towards the formation of multiple complexes involved in Mg^{2+} insertion and ATP hydrolysis. A 1:1 interaction between subunits supports a range of complexes, including a I_6D_6 arrangement. In addition, there is evidence for the formation of higher order ChlID arrangements. The formation of multiple different ChlID arrangements can explain the overall change in ATPase activity observed. Furthermore, if only one ChlD subunit is required within an active complex, this may explain the saturation in chelatase activity observed at very low levels of ChlD relative to ChlI. The ChlH subunit appears to influence these ChlID complexes. There is evidence that ChlH influences the ATPase activity of ChlID complexes. A possible reorganisation of higher order ChlI to ChlD complexes due to high concentrations of ChlH is demonstrated within chelatase titrations. The exact nature of these interactions of ChlH remain unknown, although ChlD-H interactions appears plausible.

Although giving strong support to at least two distinct active arrangements of ChlI and ChlD subunits, these kinetic titrations give no insight towards the formation of any specific complex. To investigate the formation of these complexes further, sedimentation velocity analytical ultra centrifugation (SV-AUC) was used to probe the complexes formed by magnesium chelatase (Chapter 4).

4 SV-AUC of magnesium chelatase complexes

4.1 Abstract

SV-AUC shows ChlI and ChlH are monomeric whilst ChlD is dimeric in the absence of nucleotide or Mg^{2+}. SV-AUC of equimolar mixtures of ChlI and ChlD in the presence of ADP and Mg^{2+} shows a wide range of complexes with apparent sedimentation coefficients of 5 - 14S, consistent with ChlID complexes approximately 40 - 300 kDa in size. SV-AUC performed in a five fold excess of ChlI over ChlD favours a specific complex at 9.1S. SV-AUC performed in the presence of ChlH leads to an overall reduction in the range of complexes observed between ChlI and ChlD, with ChlH appearing to drive the formation of smaller ChlID assemblies into a complex at 9.1S. As this species is also favoured at high levels of ChlI over ChlD it is proposed that this complex represents an I_5D or similar type arrangement. Although ChlH directly influences the assembly of ChlID complexes, no ChlIDH species is observed during SV-AUC, providing further evidence towards transient interactions of ChlH. Ultimately SV-AUC provides no evidence for the formation of a large I_6D_6 type complex within the *Synechocystis* enzyme in the presence of ADP and Mg^{2+}.

4.2 Introduction

4.2.1 Basis for the SV-AUC experiments performed

Kinetic titrations (Chapter 3) demonstrated that multiple magnesium chelatase complexes may be involved in either Mg^{2+} insertion or ATP hydrolysis. There is kinetic evidence for the formation of a complex or complexes containing equal levels of ChlI and ChlD (Figure 3.9) as well as complexes that contain higher levels of ChlI relative to ChlD (Figure 3.13). ChlH interacts with the complexes formed between ChlI and ChlD, demonstrated by ChlH influencing the overall level of ATPase hydrolysis performed by ChlID complexes (Figure 3.19), in addition to a possible reorganisation of higher order ChlID complexes by ChlH.

However, these experiments give no insight into the number of the individual subunits present within chelatase complexes. Given the interest in establishing such numbers, complexes formed by magnesium chelatase were characterised using sedimentation velocity analytical ultra centrifugation (SV-AUC).

4.2.2 Determination of molecular weights of protein complexes based on their apparent sedimentation coefficient

Analytical ultra centrifugation (AUC) is a method used for the direct characterisation of proteins and protein complexes in solution under biologically relevant conditions [105, 106, 107, 108, 109, 110]. In an AUC experiment movement of proteins within a cell is observed with detection of proteins achieved using interference, absorbance or fluorescence based detectors, furthermore the detection of specific proteins within complexes can be achieved using fluorescently labelled proteins.

Sedimentation velocity analytical ultra centrifugation (SV-AUC) involves the use of multiple successive scans of a protein solution within a cell to observe the migration of a protein concentration boundary formed by protein molecules during continuous high speed centrifugation. Examples of these successive interference scans performed during an SV-AUC experiment are demonstrated in Figure 4.1.

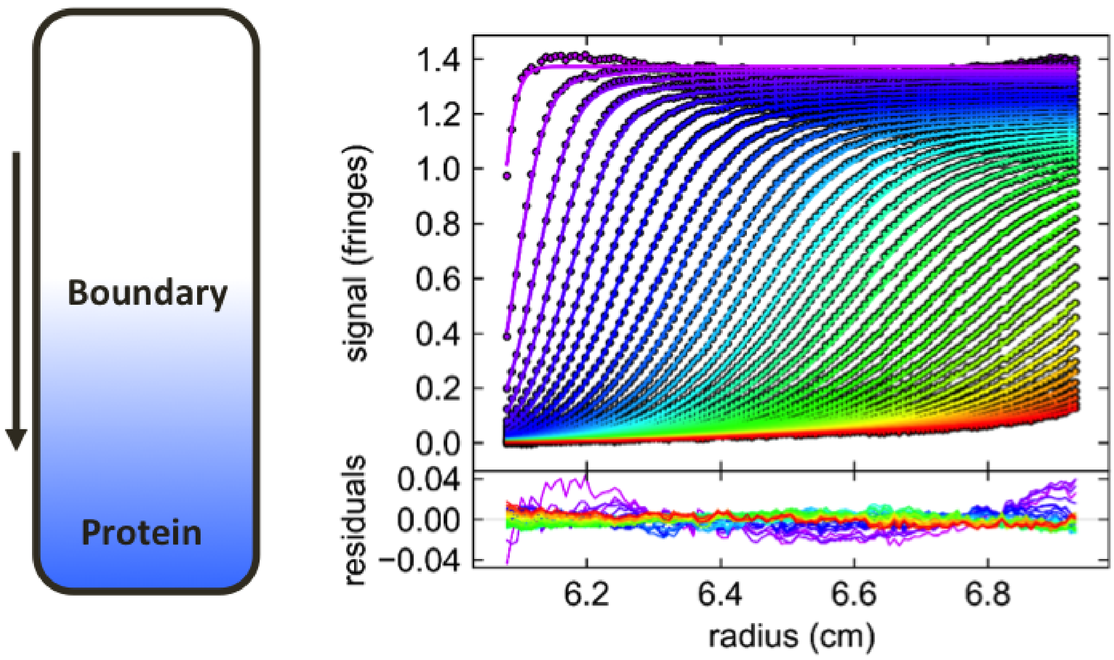

Figure 4.1: (Left) During SV-AUC the continuous high speed centrifugation of a protein solution results in the formation and migration of a protein concentration boundary. (Right) Example of successive interference scans (refractive index optics) of a cell containing a protein solution during an SV-AUC experiment.

The overall behaviour and migration of the protein boundary is influenced by numerous factors including the size, shape and charge of protein molecules, protein concentration and the varying degrees of interaction between individual protein molecules. As a result interpretation of boundary movement provides a powerful way to characterise the proteins being studied. Although boundary shape, and the time dependent change in boundary shape can be complex, recent developments in the computational analysis of AUC data have greatly helped in the interpretation of AUC data. In general two equations the Lamm and Svedberg equations, serve as the starting point for analysis of AUC data.

The Lamm equation describes the radial movement (r) over time (t) of a dilute solution of monodisperse particles χ(r,t) as a result of a centrifugal field, $\omega^2 r$ [105, 111].

$$\frac{d\chi}{dt} = \frac{1}{r}\frac{d}{dr}[rD(M)\frac{d\chi}{dr} - s(M)\omega^2 r^2 \chi] \tag{4.1}$$

The sedimentation s(M) and diffusion coefficients D(M) depend on the molar mass of the protein and are related by the Svedberg equation with parameters ρ (solvent density), $\bar{v}_M$ (solute partial specific volume), temperature (T), gas constant (R) and molecular mass (M).

$$s(M) = D(M)\frac{M - (1 - \bar{v}_M \rho)}{RT} \tag{4.2}$$

During SV-AUC the sedimentation coefficient relates to the overall migration of the sedimentation boundary with time, whilst the diffusion coefficient relates to the spread of the sedimentation boundary with time [112]. The interpretation of the boundary movement (χ(r,t)) with time, such as the boundaries demonstrated in Figure 4.1, is aided by the use of appropriate software (such as SEDFIT) which allow for the direct analysis of boundary movement to the appropriate models, such as Lamm equation modelling, providing a direct way to obtain the sedimentation coefficient of protein complexes observed.

The sedimentation coefficient (s) which is commonly measured in units of Svedberg (S) with 1S = 10^{-13} seconds, of a particle is governed by factors including its overall shape, surface area, charge and molecular weight. Figure 4.2 provides an approximate guideline of how molecular weight relates to the apparent sedimentation coefficients, based on a range of published examples from other AAA$^+$ proteins [113, 114]. Such values are approximations and serve as rough guidelines only.

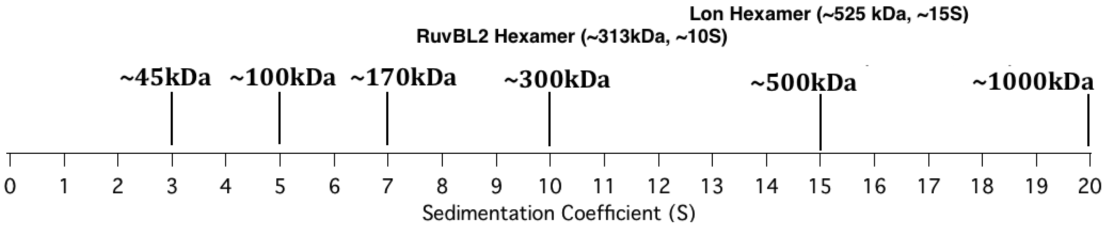

Figure 4.2: Estimations of the molecular weight of protein complexes based on their observed sedementation coefficient. Values are approximations adapted from published data of other AAA$^+$ proteins [113, 114].

4.3 Results and Discussion

4.3.1 SV-AUC experiments were performed in the presence of ADP

Although previous kinetic titrations monitoring Mg^{2+} insertion or ATP hydrolysis were performed in the presence of ATP, due to the longer time course of SV-AUC measurements (approx 4 — 6 hours) and to avoid additional further complexities as a result of ATP hydrolysis by either individual subunits or formed complexes, SV-AUC experiments that contained nucleotide were performed in the presence of ADP.

Immediately prior to SV-AUC, gel filtration (320ml, Hi-Load 26/60, 200 prep grade, GE Healthcare) was performed on wild-type or fluorescently labelled subunits to ensure the removal of protein aggregates or unbound dye. The experimental setup and data analysis are discussed in Materials and Methods Sections 2.5 and 2.6.3. The analysis of SV-AUC data was performed by Dr Thomas Jowitt (University of Manchester). Labelling of C244S ChlI and ChlD was performed Dr Nathan Adams (MBB, Sheffield).

4.3.2 SV-AUC of ChlI, ChlD and ChlH in isolation

To establish the behaviour of the individual subunits, SV-AUC was performed on ChlI, ChlD and ChlH in isolation, in the absence of nucleotide and Mg^{2+}. ChlI and ChlH in the absence of nucleotide and Mg^{2+} are monomeric, in contrast ChlD is dimeric. The sedimentation coefficient distribution for ChlI shows a defined peak at approximately 2.9S (Figure 4.3, panel A). The corresponding molecular weight, calculated as 39.5kDa, is consistent with the molecular weight for the monomeric form of ChlI.

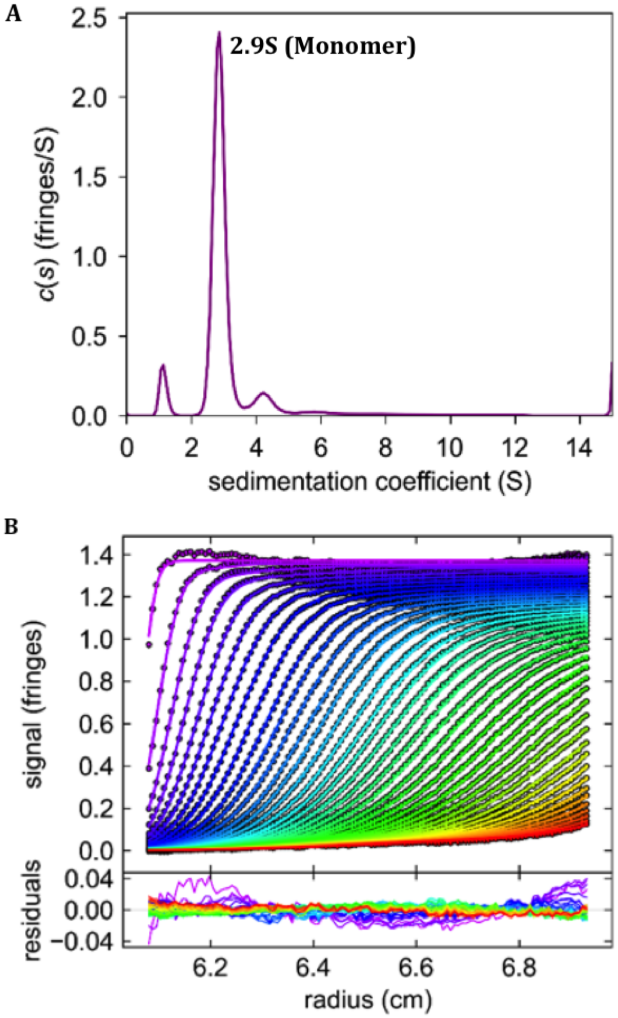

Figure 4.3: SV-AUC of ChlI in the absence of nucleotide and Mg^{2+} shows ChlI to be monomeric. (Panel A) sedimentation coefficient distribution. (Panel B) raw interference scan data. Experiments were performed in 12.5μM ChlI, 50mM Tricine, 1mM DTT, pH 7.9, 20°C.

The sedimentation coefficient distribution for the ChlH subunit shows a defined peak at approximately 5.9S (Figure 4.4, panel A), with a calculated molecular weight of 150kDa, consistent with the weight of the monomeric form of ChlH.

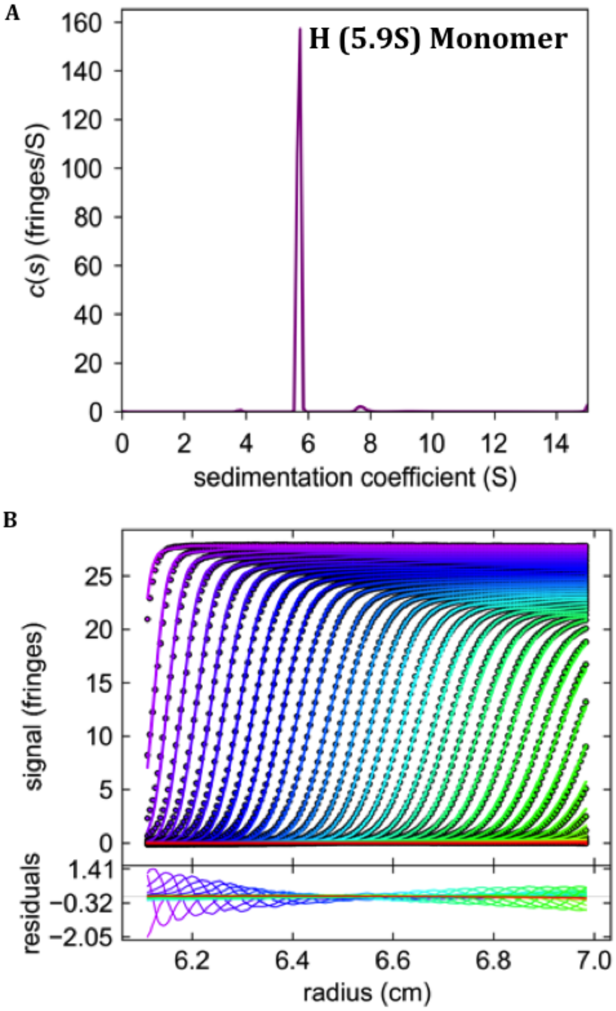

Figure 4.4: SV-AUC of ChlH in the absence of nucleotide and Mg^{2+} shows ChlH to be monomeric. (Panel A) sedimentation coefficient distributions. (Panel B) raw interference scan data. Experiments were performed in 62.5μM ChlH, 50mM Tricine, 1mM DTT, pH 7.9, 20°C.

The sedimentation coefficient distribution for the ChlD subunit shows a defined peak at approximately 5.85S (Figure 4.5, panel A). The calculated molecular weight (152kDa) is twice that expected for the ChlD subunit (approximately 75 kDa), indicating that ChlD is dimeric. Changes in concentration of ChlD during SV-AUC do not noticeably perturb this behaviour.

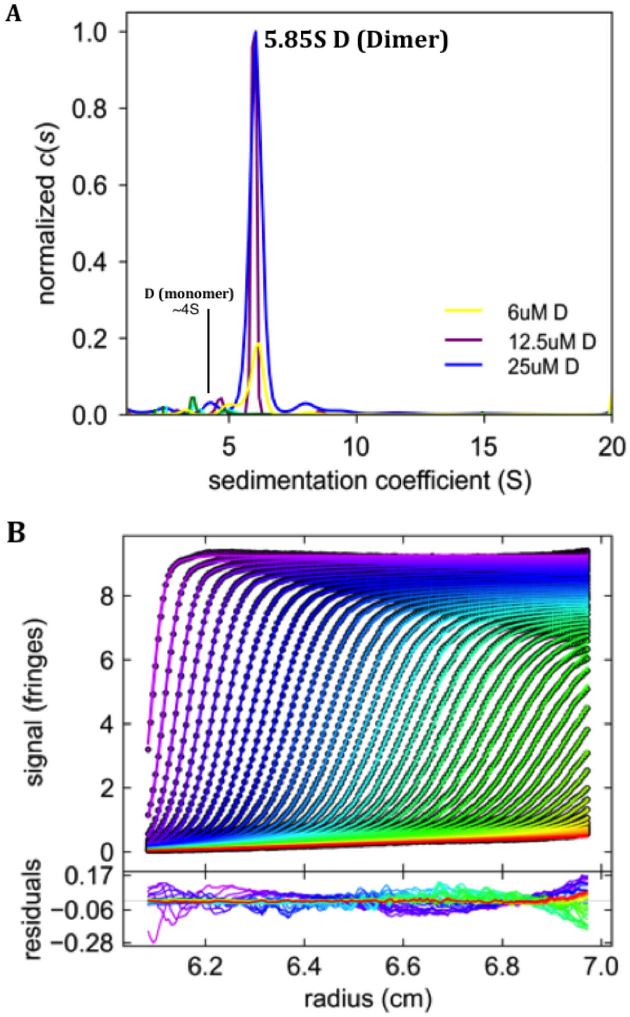

Figure 4.5: SV-AUC of ChlD in the absence of nucleotide and Mg^{2+} shows ChlD to be dimeric. (Panel A) sedimentation coefficient distribution. (Panel B) raw interference scan data. Experiments were performed in 6.25μM, 12.5μM and 25μM ChlD, 50mM Tricine, 1mM DTT, pH 7.9, 20°C.

In the presence of MgADP and Mg^{2+} both ChlI and ChlD form a complex mixture of aggregates, as a result the analysis and characterisation of individual species could not be performed in the presence of nucleotide or Mg^{2+} for either ChlI or ChlD in isolation.

4.3.3 SV-AUC of mixtures of ChlI and ChlD in the absence of ChlH

The formation of ring like arrangements — most commonly hexameric although other arrangements including heptameric have been demonstrated — is a common structural feature of AAA^+ proteins [64, 39, 44] and similiar arrangements can be formed by the AAA^+ I and D subunits in isolation [85, 88, 45, 91]. An I_6D_6 complex occuring between *Rhodobacter capsulatus* BchI and BchD subunits has been demonstrated via cryo-EM [94] in a range of nucleotide states, including ADP bound, in the absence of the H subunit.

The activity titrations (Chapter 3) indicate that the formation of multiple chelatase complexes is possible that differ in the overall levels of ChlI and ChlD subunits present. Both complexes containing equal levels of ChlI and ChlD, and complexes that contain higher levels of ChlI over ChlD are supported by kinetic titrations. However, such experiments give no indication towards the specific numbers of subunits within these complexes formed between ChlI and ChlD.

To investigate the numbers of subunits within complexes formed between ChlI and ChlD, SV-AUC was performed on mixtures of ChlI and ChlD in the presence of MgADP and free Mg^{2+}. SV-AUC was performed in equimolar concentrations of ChlI and ChlD in addition to at a 5-fold excess of ChlI over ChlD.

4.3.4 SV-AUC of equimolar mixtures of ChlI and ChlD shows multiple low molecular weight complexes

SV-AUC performed on equimolar mixtures of ChlI and ChlD in the presence of MgADP and free Mg^{2+} shows multiple distinct complexes with calculated sedimentation coefficients between 0 - 12S.

Estimations of the molecular weight of these observed complexes based on the calculated sedimentation coefficients indicate the complexes are all low molecular weight (40 to 300kDa).

The sedimentation coefficient distributions and raw interference scans obtained from SV-AUC of equimolar mixtures of ChlI and ChlD are shown in Figure 4.6.

For reference, estimations of the expected molecular weights that relate to the observed sedimentation coefficients of other AAA$^+$ proteins, based on previously published data is shown in Figure 4.7. However, such values are very broad approximations and can only be used as rough guidelines only.

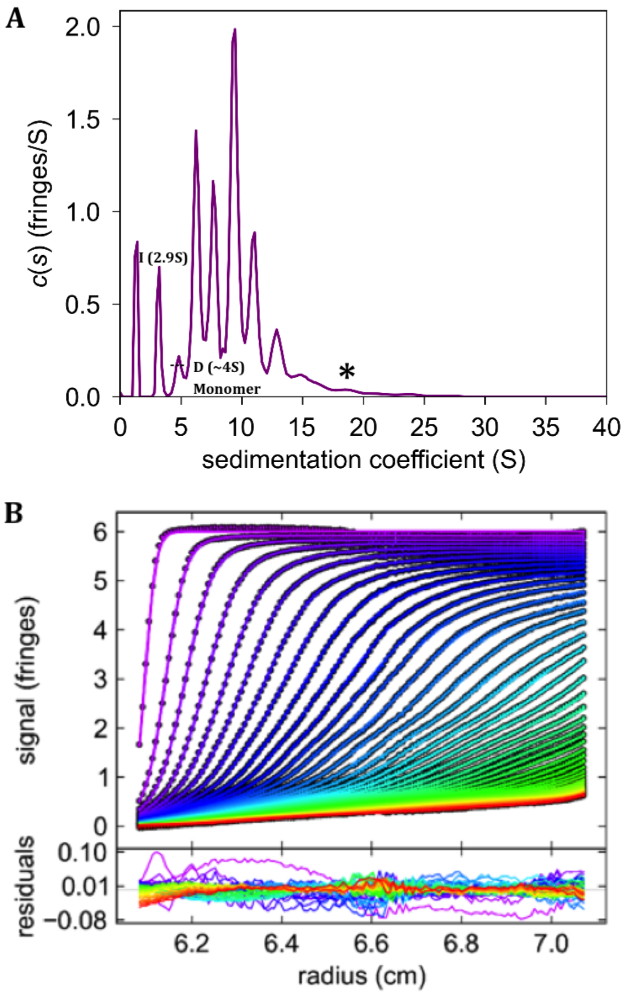

Figure 4.6: SV-AUC of equimolar concentrations of ChlI and ChlD in the presence of nucleotide (MgADP) and free Mg^{2+} indicate the formation of multiple low molecular weight complexes. (Panel A) sedimentation coefficient distributions. (Panel B) raw interference scan data. An estimation of the expected position of an I_6D_6 complex is denoted by (*). Experiments were performed with 12.5μM ChlI, 12.5μM ChlD, 1mM ADP, 3mM $MgCl_2$, 50mM Tricine, 1mM DTT, pH 7.9, 20°C.

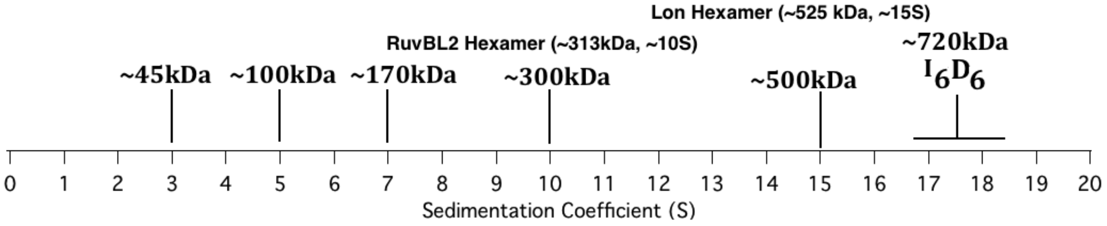

Figure 4.7: Estimations of molecular weight based on the observed sedementation coefficient of protein complexes. Values are approximations adapted from published data on other AAA^+ proteins [113, 114].

A range of complexes are observed during SV-AUC of equimolar mixtures of ChlI and ChlD, these all have a lower sedimentation coefficient than predicted for an I_6D_6 complex (Figure 4.6). Estimations of the molecular weights of complexes with sedimentation coefficients between 5 - 11S (approximately 100 - 300kDa) supports complexes including ID, I_2D, I_2D_2 and I_5D.

However as these SV-AUC experiments use interference optics to detect proteins there is no way to distinguish between ChlI and ChlD subunits, therefore signal can arise from both self assembly and complex assembly.

To establish if both ChlI and ChlD contribute to the formation of complexes observed within the region of 5 - 11S, SV-AUC was performed using ChlI or ChlD labelled with Alexa Fluor 488, allowing for the specific detection of either ChlI or ChlD.

4.3.5 The observation of fluorescently labelled ChlI (C244S) within complexes formed between ChlI and ChlD

To establish that ChlI is present within the complexes between 5 - 12S, SV-AUC was performed on mixtures of fluorescently labelled ChlI (C244S) and unlabelled ChlD allowing for the specific detection of ChlI within formed complexes (Figure 4.8, panel A).

A sharp peak observed at approximately 6S containing negligible levels of labelled ChlI (C244S) indicates a D_2 complex (150kDa). A broad distribution of sedimentation coefficients occurs between 6 - 18S. Throughout this region, a signal from labelled ChlI is observed indicating that complexes formed within this range of sedimentation coefficients contain labelled ChlI.

The overall reduction in resolution of the sedimentation coefficient distribution and the presence of larger species with sedimentation coefficients greater than 15S is likely as a result of non specific aggregation due to fluorescent labelling and prevents isolation of specific complexes.

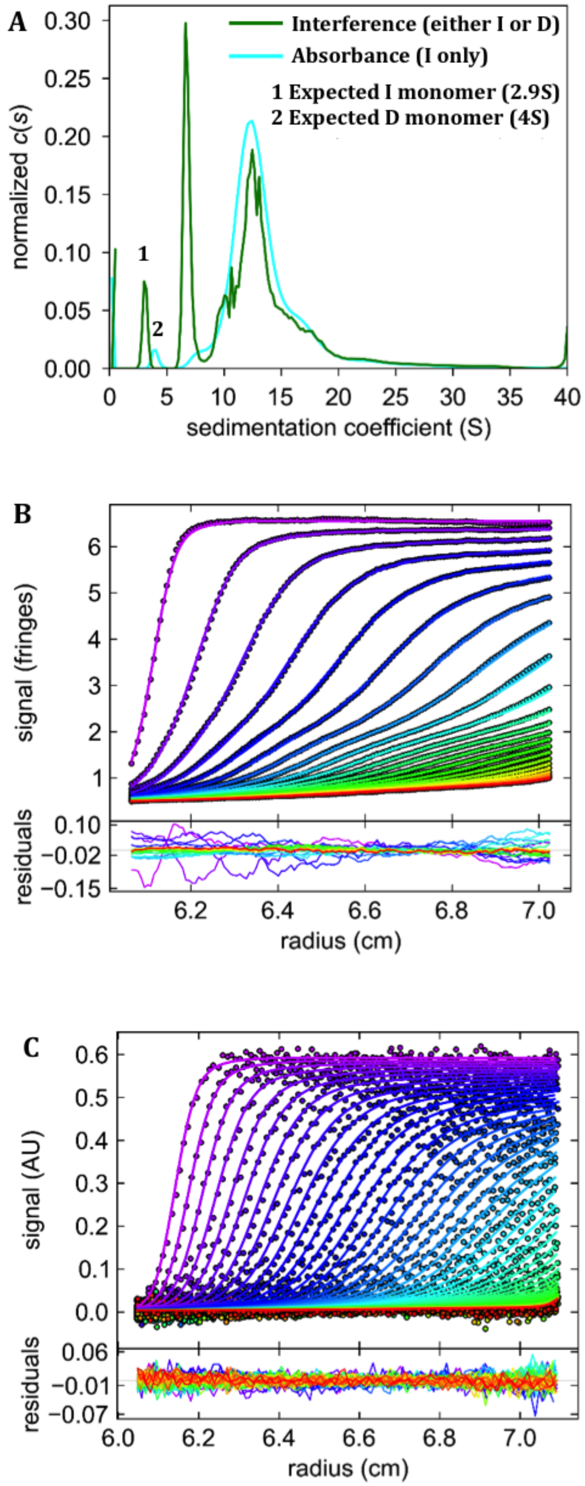

Figure 4.8: SV-AUC of equimolar mixtures of fluorescently labelled ChlI and unlabelled ChlD shows ChlI to be present within all complexes between 6 - 20S. (Panel A) sedimentation coefficient distributions. (Panel B) raw interference scan data. (Panel C) raw absorbance scan data. Experiments were performed with 12.5μM labelled ChlI, 12.5μM ChlD, 2mM ADP, 5mM $MgCl_2$, 50mM Tricine, 1mM DTT, pH 7.9, 20^{o}C.

4.3.6 The detection of fluorescently labelled ChlD within complexes formed between ChlI and ChlD

The analogous SV-AUC experiment on equimolar mixtures of fluorescently labelled ChlD and unlabelled ChlI shows a signal from labelled ChlD being observed from all complexes with sedimentation coefficients of 1 - 12S, in particular within the complexes formed at approximately 5S and 9S, indicating that the ChlD subunit also contributes to all complexes formed within this region (Figure 4.9, panel A).

The overall reduction in the resolution and the observation of larger species (S greater than 20) is likely to again be as a result of non specific aggregation due to fluorescent labelling. Evidence of such aggregation is seen in the raw interference and absorbance scans performed during SV-AUC (Figure 4.9, panels B and C).

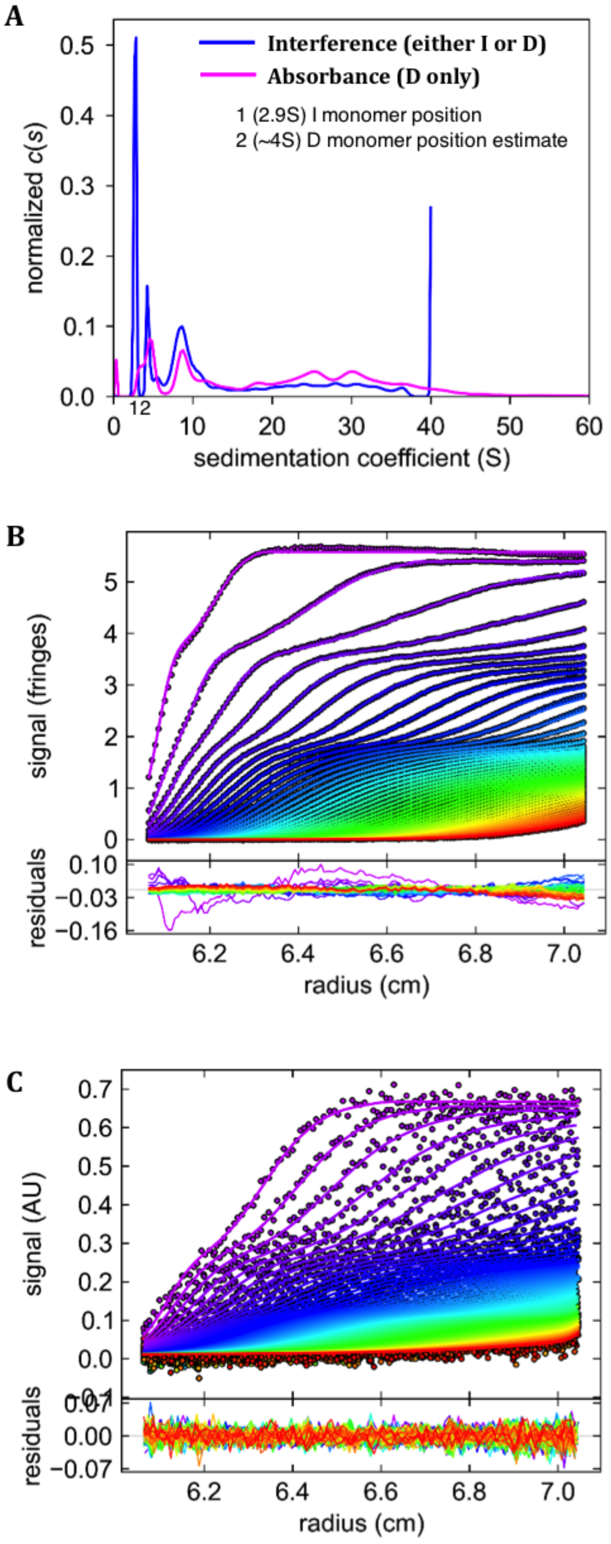

Figure 4.9: SV-AUC on equimolar mixtures of fluorescently labelled ChlD and unlabelled ChlI. (Panel A) sedimentation coefficient distributions. (Panel B) raw interference scan data. (Panel C) raw absorbance scan data. Experiments were performed with 12.5μM fluorescently labelled ChlD, 12.5μM ChlI, 2mM ADP, 5mM $MgCl_2$, 50mM Tricine, 1mM DTT, pH 7.9, 20°C.

4.3.7 SV-AUC of fluorescently labelled subunits demonstrates that both ChlI and ChlD contribute to observed complexes

Fluorescently labelled ChlI and ChlD subunits are observed within all complexes having sedimentation coefficients between 6 - 15S, strongly suggesting that all complexes formed within this region contain both ChlI and ChlD subunits.

Thus, the multiple complexes observed between 6 - 11S during SV-AUC of equimolar mixtures of unlabelled ChlI and ChlD will likely contain both ChlI and ChlD subunits (Figure 4.6).

Feasible complexes, with approximate molecular masses (40 - 300kDa) that would account for sedimentation coefficients between 0 - 11S, containing both ChlI and ChlD are numerous (Table 4.13) and includes ID, I_2D, I_2D_2 and I_5D. No larger arrangements of subunits, such as I_6D_6, having much larger sedimentation coefficients are observed or supported by these data.

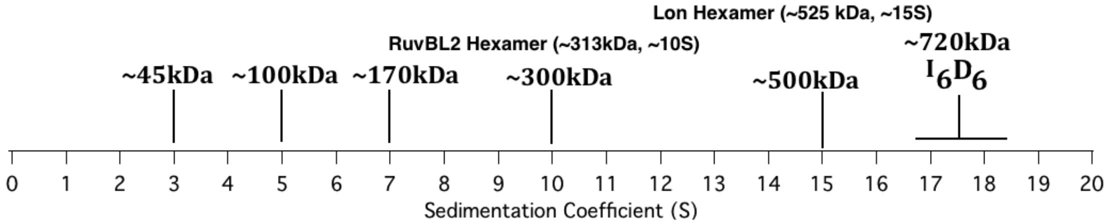

Figure 4.10: Estimations of molecular weight based on the observed sedementation coefficient of protein complexes. Values are rough approximations adapted from published data on other AAA$^+$ proteins [113, 114].

4.3.8 SV-AUC demonstrated a 5-fold excess of ChlI over ChlD favours a specific arrangement of subunits

With kinetic titrations suggesting multiple arrangements of ChlI and ChlD subunits within the ID complexes are possible, SV-AUC was performed in a five fold excess of ChlI relative to ChlD to investigate how the overall levels of ChlI and ChlD present influence the complexes observed. SV-AUC performed in a five fold excess of ChlI (32.5μM ChlI) over ChlD (6.25μM ChlD) appears to favour the formation of a complex with a sedimentation coefficient of 9.1S (Figure 4.11, Panel A). Estimations of the corresponding molecular weight of a complex with a sedimentation coefficient of approximately 9.1S suggest a complex of approximately 200 to 300kDa in size (Figure 4.12).

SV-AUC performed with labelled ChlD shows complexes formed at approximately 9S contain ChlD. As this complex at 9.1S is populated at higher levels of ChlI (five fold) relative to ChlD it appears likely that this complex contains higher numbers of ChlI subunits relative to ChlD, with feasible examples including I_5D or I_6D . However, with no direct evidence for any one specific arrangement, other complexes of similar weight (e.g. I_2D_2) cannot be immediately disregarded.

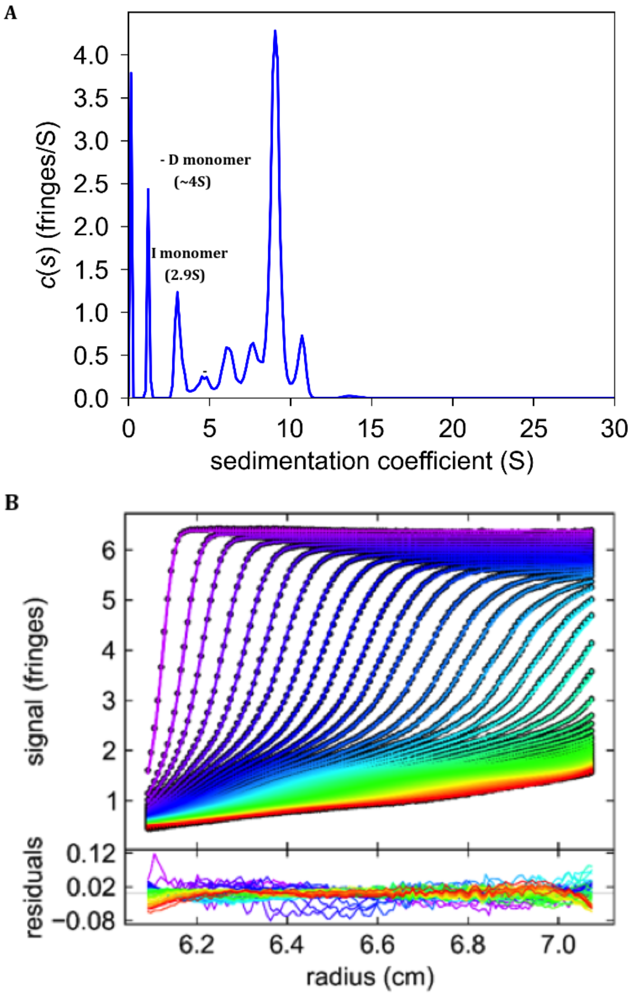

Figure 4.11: SV-AUC performed with a five fold excess of ChlI over ChlD in the presence of nucleotide (MgADP) and free Mg^{2+} favours a complex at 9.1S. (Panel A) sedimentation coefficient distributions. (Panel B) raw interference scan data. Experiments were performed with 32.5μM ChlI, 6.25μM ChlD, 1mM ADP, 3mM $MgCl_2$, 50mM Tricine, 1mM DTT, pH 7.9, 20°C.

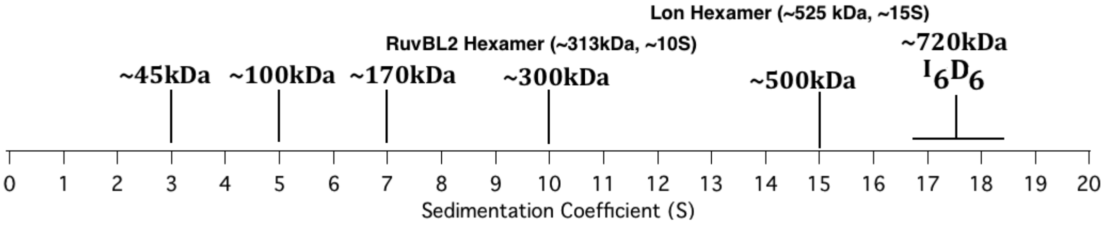

Figure 4.12: Estimations of molecular weight based on observed sedementation coefficient of protein complexes. Values are rough approximations adapted from published data of other AAA^{+}proteins[113, 114].

4.3.9 Summary - SV-AUC of mixtures of ChlI and ChlD show multiple low molecular weight ChlID arrangements occurring in the absence of ChlH

In the absence of ChlH, SV-AUC performed on mixtures of ChlI and ChlD shows a range of complexes occurring between 5 - 11S containing both ChlI and ChlD subunits. A direct comparison of the SV-AUC performed on mixtures of ChlI and ChlD is shown in Figure 4.13.

Estimations of the molecular masses of these complexes within this range of sedimentation coefficients indicate the formation of complexes of approximately 100-300 kDa, which supports a range of complexes, examples of which are summarised in Table 4.1.

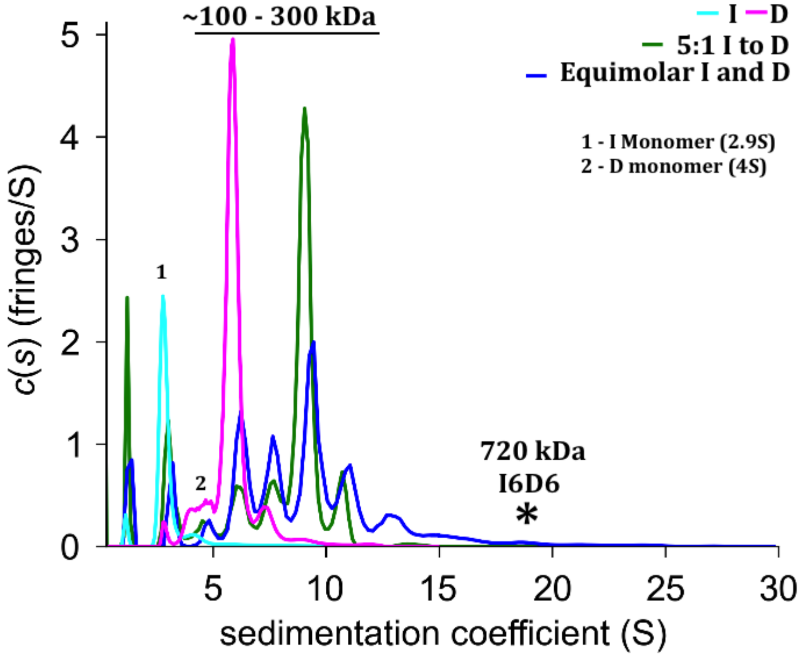

Figure 4.13: Summary of the complexes observed during SV-AUC of ChlI and ChlD in the absence of ChlH in the presence of ADP and Mg^{2+}.

Table 4.1: Molecular masses of I and D complexes

Complex	Molecular weight / kDa
I	40 kDa
D	75 kDa
ID	115 kDa
I_2D	155 kDa
I_2D_2	230 kDa
I_3D	195 kDa
I_4D	225 kDa
I_5D	275 kDa
I_6D	315 kDa

4.3.10 SV-AUC of mixtures of ChlI, ChlD and ChlH

The interaction between ChlH and ChlID complexes is essential to couple the Mg^{2+} insertion reaction on ChlH, with ATP hydrolysis performed by ChlID motor complexes.

Kinetic titrations monitoring ATPase activity demonstrate a marked change in the overall ATPase activity in the presence of ChlH (Figure 3.19), demonstrating that the ChlH subunit interacts with ChlID complexes during ATP hydrolysis. These experiments, performed in the absence of porphyrin, also show that interactions between ChlID complexes and ChlH can occur independently of the Mg^{2+} insertion reaction.

In the absence of ChlH, SV-AUC performed on mixtures of ChlI and ChlD in the presence of ADP and Mg^{2+} show a range of low molecular weight complexes. Although there is no direct evidence for a large complex between ChlI and ChlD such as I_6D_6, a five-fold excess of ChlI over ChlD results in a complex at 9.1S being favoured and it appears reasonable that this complex is one containing higher levels of ChlI subunits over ChlD subunits, for example I_5D or I_6D.

To investigate whether the formation of larger assemblies of chelatase subunits requires the presence of ChlH, and to investigate the interactions and complexes occurring between ChlI, ChlD and ChlH, SV-AUC was performed in the presence of all three subunits.

SV-AUC performed in equimolar levels of ChlI and ChlD (12.5 μM) at high levels of ChlH (63μM) in the presence of ADP and Mg^{2+} does not lead to the detection of larger complexes, nor indicate the presence of a complex containing all three chelatase subunits (Figure 4.14).

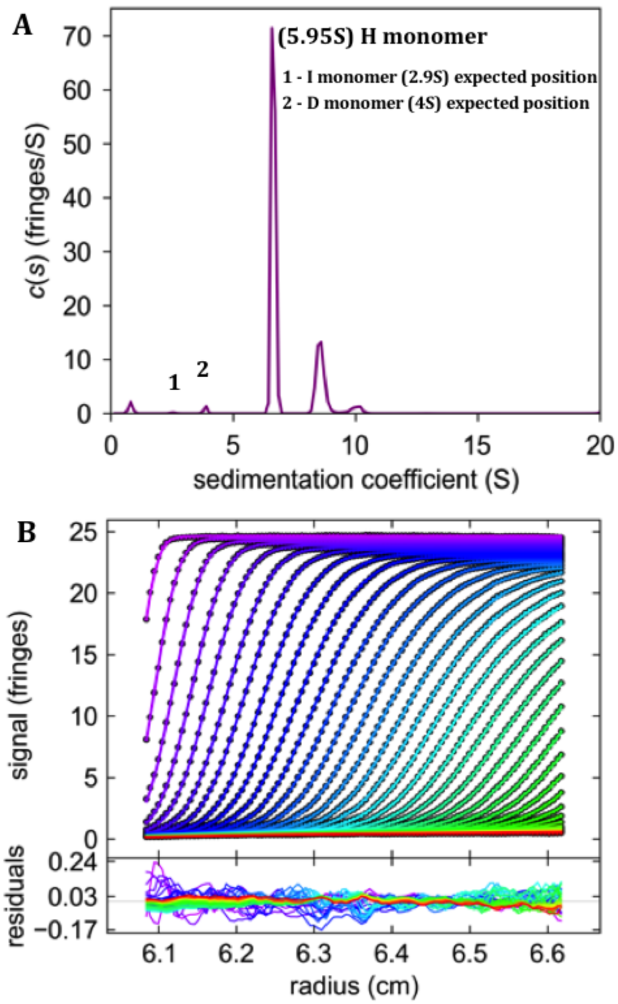

Figure 4.14: SV-AUC performed in equimolar concentrations of ChlI and ChlD at high levels of ChlH in the presence of nucleotide (MgADP) and free Mg^{2+} does not show a larger ChlID arrangement or a ChlIDH complex. (Panel A) sedimentation coefficient distributions. (Panel B) raw interference scans. Experiments were performed with 12.5μM ChlI, 12.5μM ChlD, 63μM ChlH, 1mM ADP, 3mM $MgCl_2$, 50mM Tricine, 1mM DTT, pH 7.9, 20°C.

The ChlH subunit is the predominant species, occurring as a monomer at approximately 6S. Additionally, a complex is observed at approximately 9.1S, this complex at 9.1S is also favoured by high levels of ChlI over ChlD, in the absence of ChlH. Although the presence of ChlH does not lead to the observation of any larger complexes, or a complex containing all three subunits, a significant reduction in the overall range of complexes is seen in the presence of ChlH, with only two major species observed, monomeric ChlH and a complex at 9.1S containing ChlI and ChlD. With no indication of a complex containing the ChlH subunit, even under conditions here which contain a five-fold excess of ChlH over ChlI or ChlD, a transient interaction between ChlH and ChlID appears likely.

To investigate if elevated levels of ChlI over ChlD results in a significant change to the complexes observed in the presence of ChlH, SV-AUC was performed in a 5 fold excess of ChlI (31.5μM) over ChlD (6.25μM) in the presence of high levels of ChlH (63μM) (Figure 4.15). Under these conditions ChlH again is the predominant species, in addition to the complex at approximately 9.1S. This observation suggests that changing the relative levels of ChlI and ChlD does not influence the size of the complexes formed between ChlI and ChlD in the presence of ChlH.

Despite the relatively high levels of ChlI present during SV-AUC, very little ChlI monomer is observed (approximately 3S), lending further support that all ChlI present is contained within a complex with ChlD. Furthermore, this lack of ChlI monomer also makes the presence of a ChlDH arrangement unlikely, as the formation of such arrangement should require the presence of increasing levels of free ChlI monomer being observed as the amount of ChlD in a complex with ChlH increases.

In the absence of ChlH, SV-AUC performed in a five fold excess of ChlI over ChlD favours the formation of a complex at 9.1S (Figure 4.11) and it appears reasonable that this represents a complex containing higher levels of ChlI subunits, such as I_5D. With a similar complex at 9.1S being the only significant species occurring between ChlI and ChlD in the presence of ChlH regardless of the relative levels of ChlI and ChlD, it would indicate that the presence of ChlH also favours such arrangement of subunits.

If smaller complexes having much lower sedimentation coefficients than 9S which are only observed at significant levels in the absence of ChlH represent fragments of larger ID arrangements, it may be that the ChlH subunit is driving the assembly of these fragments into a larger complex observed at 9.1S.

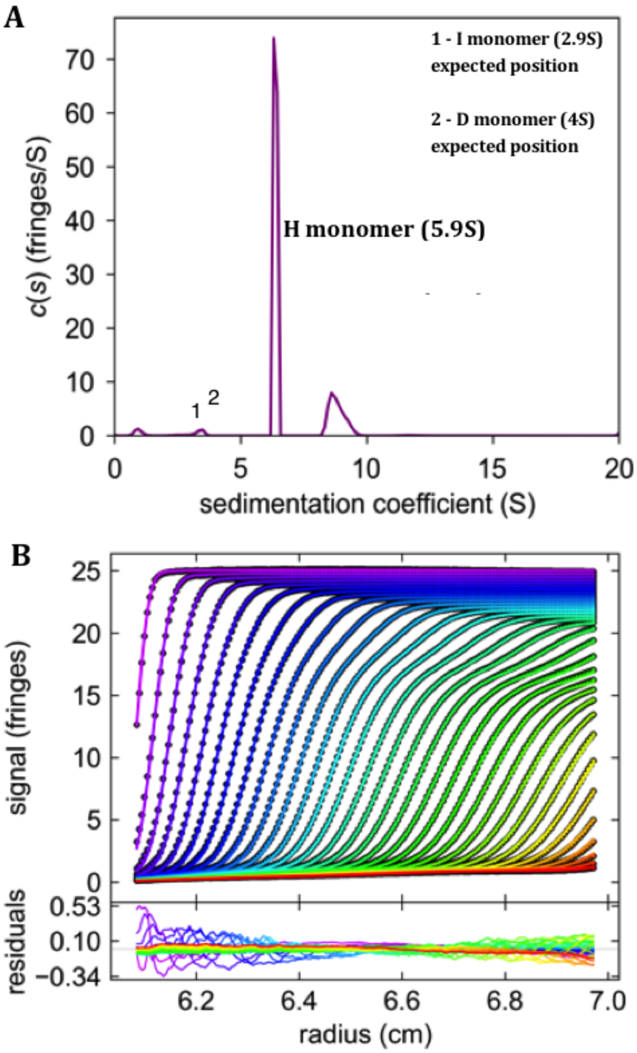

Figure 4.15: SV-AUC performed in elevated levels of ChlI over ChlD at high levels of ChlH in the presence of nucleotide (MgADP) and free Mg^{2+} does not show a larger ChlID arrangement or a ChlIDH complex. (Panel B) raw interference scans. Experiments were performed with 31.5μM ChlI, 6.25μM ChlD, 63μM ChlH, 1mM ADP, 3mM $MgCl_2$ 50mM Tricine, 1mM DTT, pH 7.9, 20°C.

A similar SV-AUC experiment performed in a five fold excess of ChlI (31.5μM) over ChlD (6.25μM), however at a much reduced concentration of ChlH (6.25μM), shown in Figure 4.16, leads to the species at 9.1S predominating, with ChlH appearing as a monomer at approximately 6S. This would suggest that low levels of ChlH (1:1 relative to ChlD) can still drive formation of the 9.1S complex.

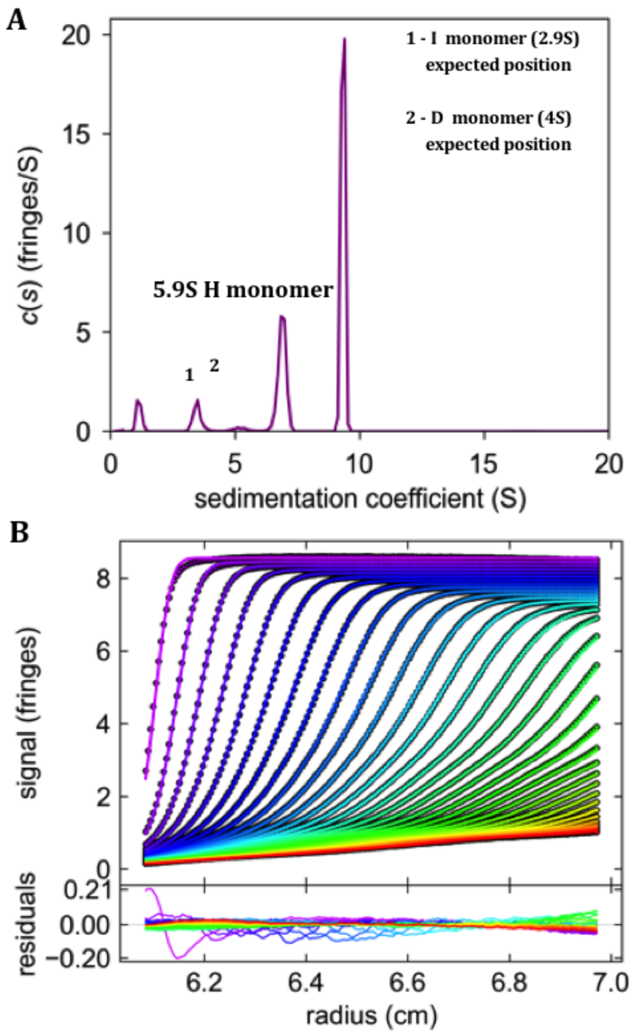

Figure 4.16: AUC sediment velocity experiment performed in elevated levels of ChlI over ChlD at low levels of ChlH in the presence of nucleotide (MgADP) and free Mg^{2+}. (Panel A) sedimentation coefficient distribution. (Panel B) raw interference scans. Experiments were performed with 31.5μM ChlI, 6.25μM ChlD, 6.25μM ChlH, 1mM ADP, 3mM $MgCl_2$ 50mM Tricine, 1mM DTT, pH 7.9, 20°C.

4.4 Conclusions and Models

SV-AUC, performed in the presence of ADP and Mg^{2+} lends no support to an I_6D_6 complex, or a complex containing all three chelatase subunits.

SV-AUC on equimolar mixtures of ChlI and ChlD in the absence of ChlH leads to a range of complexes between 5 - 12S. Rough approximations of the molecular weights of these complexes (40 - 300kDa) supports numerous complexes, with arrangements such as I_5D or similar size supported (Figure 4.17).

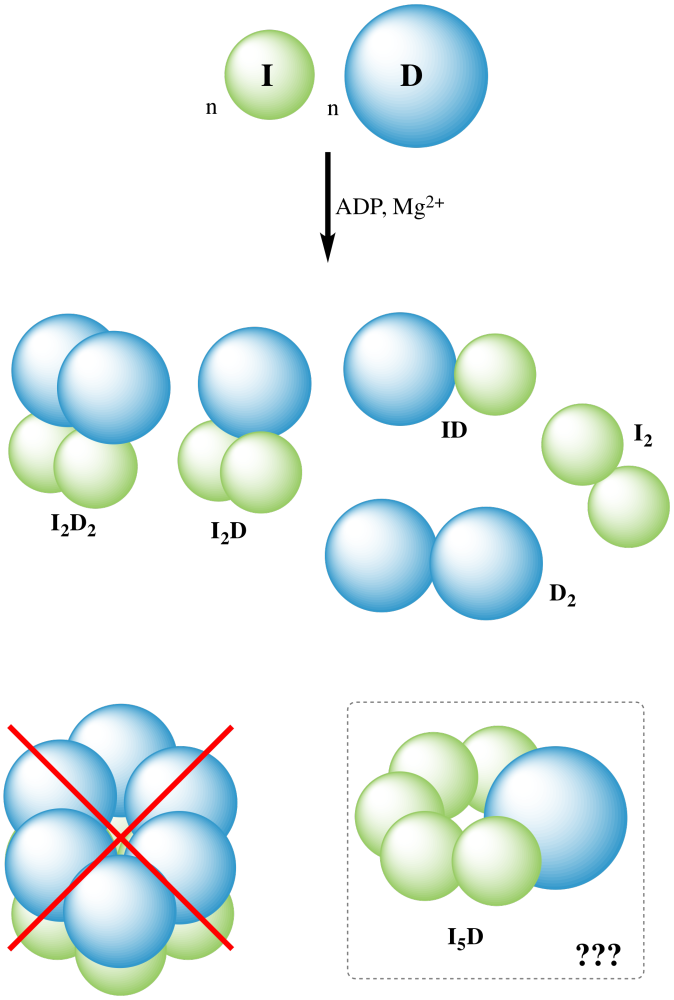

Figure 4.17: SV-AUC on equimolar ChlI and ChlD mixtures shows multiple smaller ChlID arrangements, however provides no evidence for the formation of an I_6D_6 complex.

SV-AUC performed in a five-fold excess of ChlI over ChlD favours the formation of a specific complex at 9.1S (Figure 4.11), this estimated sedimentation coefficient indicates a somewhat larger arrangement (approximately 200 - 300 kDa). With this complex favoured at high concentrations of ChlI, a complex containing higher levels of ChlI subunits would appear likely (such as I_5D), although other complexes of similar size (I_2D_2) can not be immediately disregarded (Figure 4.18).

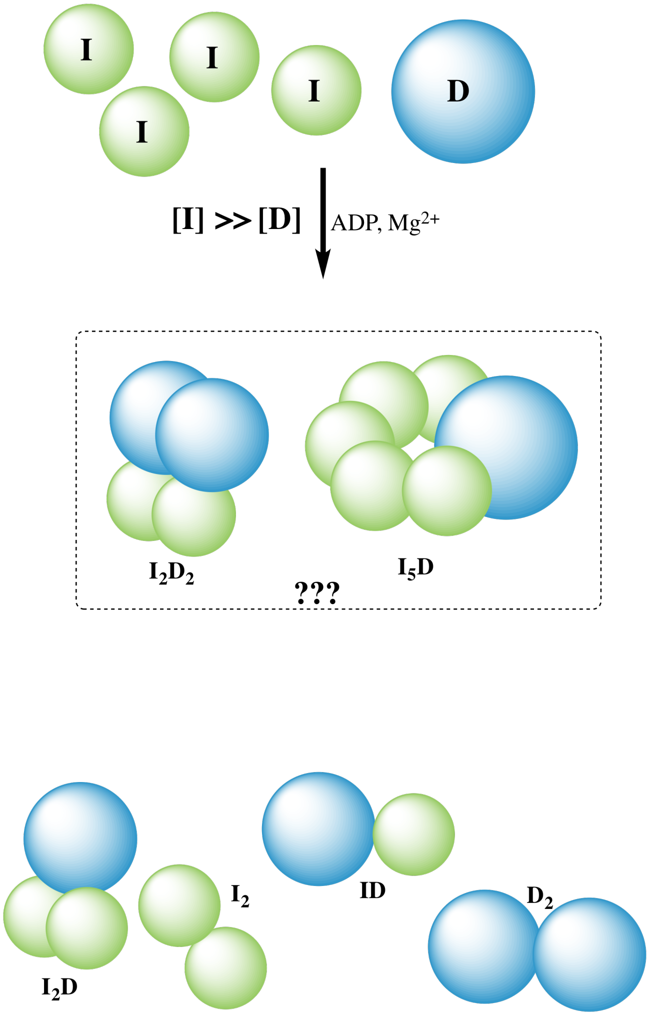

Figure 4.18: SV-AUC at elevated concentrations of ChlI over ChlD favours the formation of a specific and larger arrangement of subunits (9.1S) proposed to be an I_5D or similar size arrangement, however there is no evidence for an I_6D_6 complex.

SV-AUC of all three subunits does not lead to larger ChlID complexes (I_6D_6), or complexes containing all three subunits. This lack of an ChlIDH complex is in support of a transient interaction of ChlH.

Although no ChlIDH complex is observed, the presence of ChlH does lead to a significant reduction in the overall range of complexes occurring, with only two species, ChlH (6S) and a complex at approximately 9S. This apparent reduction in complexes adds further support to reorganisation of ChlID complexes by ChlH, demonstrated in kinetic titrations. Such reduction in the range of complexes may be explained by interactions of the ChlH subunit driving the formation of smaller arrangements of I and D — observed in the absence of ChlH — to this larger arrangement at 9.1S. This larger arrangement, seemingly favoured in the presence of ChlH, would appear to be identical to that also favoured when ChlI is at an excess over ChlD (Figure 4.19).

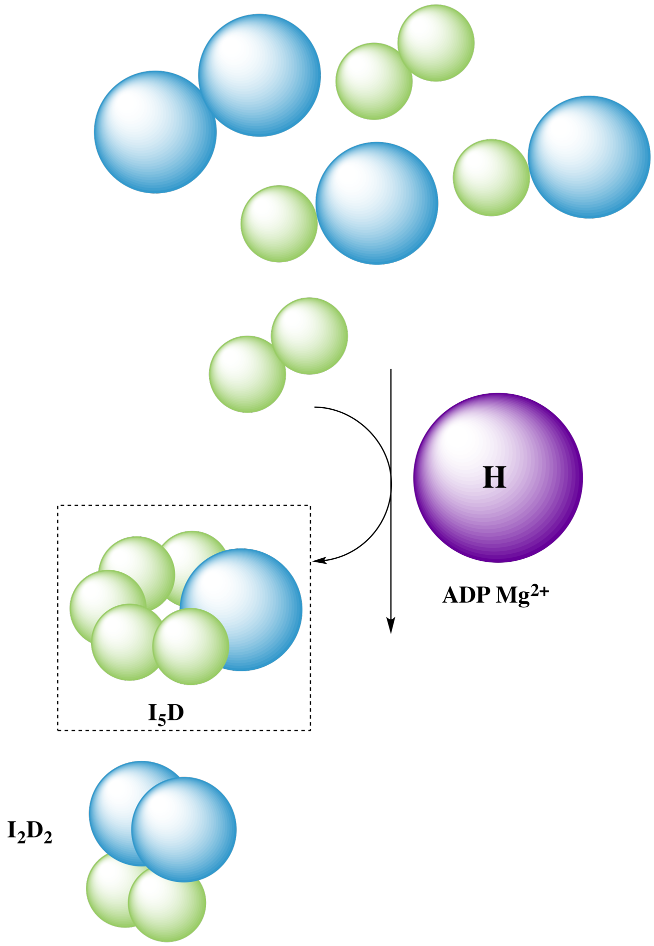

Figure 4.19: ChlH results in an apparent reduction in the range of complexes observed during SV-AUC and favours the formation of a larger complex at 9.1S.

5 The reaction cycle of magnesium chelatase

5.1 Abstract

Modelling of reaction cycle progress curves within Dynafit provides evidence for the isomerisation of ChlH influencing a lag phase occurring prior to metal ion chelation. It was demonstrated that reaction cycle models containing an initial slow step prior to steady state activity can explain chelatase progress curves. The magnitude of the rate constant for this slow step preceding chelatase activity exhibits no significant variation over a range of equimolar ChlH-D_{IX} concentrations. In contrast, under conditions where ChlH is at an excess over D_{IX}, a much slower initial lag phase results. Such behaviour is explained by a slow isomerisation of ChlH preceding the rapid binding of D_{IX} substrate.

5.2 Introduction

The reaction cycle pathway of magnesium chelatase is complex, with numerous individual steps that must include specific processes along the reaction cycle pathway such as nucleotide binding, substrate binding and Mg^{2+} chelation. Furthermore a lag phase is commonly observed prior to steady state chelatase activity, the length of which depends on the preincubation conditions of the enzyme subunits and the reaction conditions. Owing to the complex nature of the reaction cycle and the processes and conditions governing the lag phase, further investigation is required.

5.2.1 A lag phase is commonly observed prior to steady state chelatase activity

Early studies involving pea chloroplast membrane extracts suggested a two step reaction for magnesium chelation, with an ATP dependent activation step requiring either ATP or ATP-γ- S occuring prior to Mg^{2+} insertion [102]. Evidence for an ATP dependent activation has also been demonstrated within the *Rhodobacter sphaeroides* system, with preincubation of BchI, BchD and ATP reducing the lag phase prior to steady state activity [70]. Preincubation of pea cell extracts from *Pisum sativum* with ATP also showed a noticible reduction in the lag phase and required only two of three total cell extracts within the preincubation [76] - analogous to an activation step involving the I and D subunits.

Within the *Synechocystis* system, preincubating ChlI, ChlD, $MgATP^{2-}$ and free Mg^{2+} together reduces the lag phase. This suggests an additional involvement of free Mg^{2+} in combination with $MgATP^{2-}$ during the activation [32]. The requirement for free

Mg^{2+} and $MgATP^{2-}$ was highlighted by the observation of a full length lag phase when preincubating ChlI and ChlD together with only $MgATP^{2-}$ or Mg^{2+}. As only $MgATP^{2-}$ was sufficient to activate the *Rhodobacter sphaeroides* chelatase it is clear that activation varies between species [70].

In addition to this activation step involving the I and D subunits, preincubation of the ChlH subunit with D_{IX} can result in a substantial reduction in the lag phase prior to steady state activity, suggesting a possible activation step involving ChlH independently of ChlI and ChlD [100].

Although such a wide range of evidence suggests that nucleotide and the other substrates are directly involved in the activation step, the preincubation of *Synechocystis* ChlI, ChlD and ChlH subunits at high concentrations under temperatures optimal for the chelatase reaction (34^{o}C) can reduce the observed lag phase without a requirement of $MgATP^{2-}$, Mg^{2+} or D_{IX} [100].

5.2.2 Transient kinetic studies provide evidence for a rate limiting step within the chelatase cycle

The turnover number k_{cat}, for metal ion chelation is likely to be comprised of rate constants from numerous individual steps within the chelatase cycle. This value was estimated using the assumption that the ChlH concentration is the active enzyme concentration at 0.8 min^{-1} [35], in agreement with my current data from subunit titrations suggesting a k_{cat} of approximately 0.5 to 1 min^{-1}.

Transient studies [100] characterising on-enzyme processes occurring during metal ion chelation led to a more detailed insight into the reaction pathway. It was demonstrated that under conditions where enzyme is in excess of porphyrin, the limiting first order rate constant for the formation of an enzyme-product complex was approximately 0.15 min^{-1}, five times smaller than k_{cat} (0.8 min^{-1}). The concentration dependence of k_{obs} demonstrated that the rate determining step of the pathway occurs before nucleotide binding and that binding $MgATP^{2-}$ clamps the system in an enzyme-porphyrin complex.

Under reaction conditions of equimolar ChlH and D_{IX} (8μM ChlH and D_{IX}) kinetic modelling of chelatase reaction progress curves, using numerical integration of the rate law for a simplified model, demonstrated that this observed slow step can be accounted for by a slow first turnover (state 1) that subsequently results in activation of the chelatase system (state 2) [100].

Although a relatively simple two-step model can account for the progress curves under these specific reaction conditions, it is unknown whether such model or similar models are capable of explaining the system under a range of reaction conditions. Therefore further investigation into the behaviour of the system under a wider range of reaction conditions is warranted.

5.3 Results and Discussion

5.3.1 Overview of the transient state chelatase assays performed under two different reaction conditions

A relatively simple two-step model can explain the reaction cycle of magnesium chelatase under specific reaction conditions (8μM ChlH and D_{IX}) in previous data [100].

To investigate whether such models can be used to describe the system under a wider range of reaction conditions, transient state chelatase assays were performed in range of reaction conditions. Transient state chelatase assays were performed in a series of equimolar ChlH-D_{IX} concentrations (0.5, 2, 4 and 8 μM ChlH and D_{IX}, Figure 5.1). In addition to assays containing an excess of ChlH over D_{IX} (2, 4, 6 and 8 μM ChlH at 1μM D_{IX}, Figure 5.2).

During the assays, the detection of reaction product (MgD_{IX}) and an enzyme-product complex (enzyme-MgD_{IX}) is performed simultaneously. Excitation at 420nm allows MgD_{IX} to be observed via fluorescence emission at 580nm. Whilst the specific excitation of protein tryptophan residues at 295nm enables enzyme-metalloporphyrin (enzyme-MgD_{IX}) detection at 580nm (see Section 5.3.2).

An overview of the data collected is outlined in Figure 5.3.

Subunits were preincubated together at 20μM ChlH, 10μM ChlI and 5μM ChlD in MOPS buffer at 34°C for exactly 30 minutes prior to starting the reaction by addition of the appropiate amount of enzyme stock. Such conditions have been demonstrated to overcome a lag phase prior to metal ion insertion in previous work [100]. The levels of the ChlI and ChlD subunits were adjusted accordingly to achieve a final 4:2:1 ratio of ChlH to ChlI to ChlD within the final assay.

Experiments were performed according to Materials and Methods Section 2.4.3. Kinetic modelling of the reaction data to models describing the reaction cycle was performed via the numerical integration of the differential rate laws using the Dynafit software package.

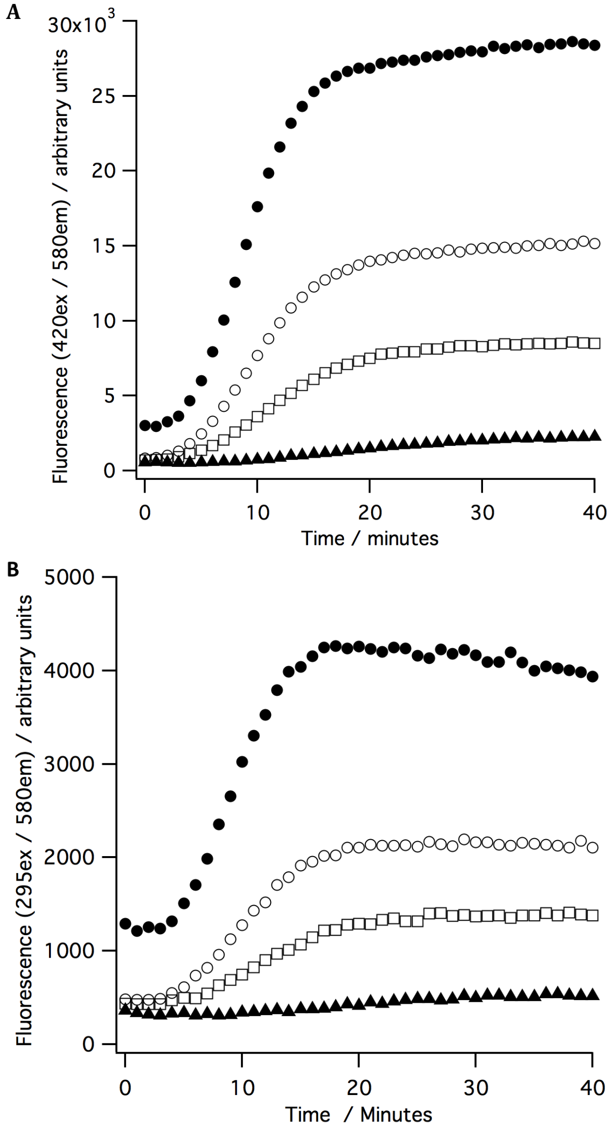

Figure 5.1: Transient state chelatase assays performed in equimolar concentrations of ChlH and D_{IX} of 8μM (●), 4μM (○), 2μM (□) and 0.5μM (▲) ChlH and D_{IX}, with the simultaneous detection of MgD_{IX} (panel A) and enzyme-MgD_{IX} (panel B). Measurements were performed in 5mM $MgATP^{2-}$, 10mM $MgCl_2$, 1mM DTT, 50mM MOPS, 0.3M glycerol, 34°C, pH 7.7. The concentrations of the ChlI and ChlD subunits were adjusted accordingly to achieve a final 4:2:1 ratio of H:I:D.

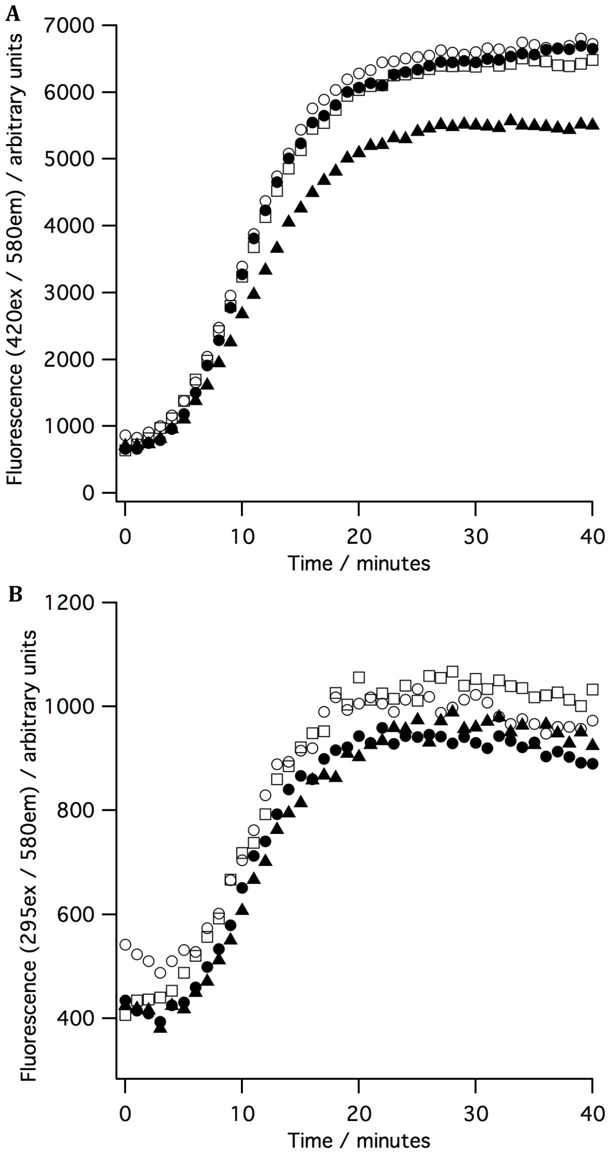

Figure 5.2: Transient state chelatase assays performed in a fixed concentration of D_{IX} (1μM) at 8μM (●), 6μM (○), 4μM (□) and 2μM (▲) ChlH with the simultaneous detection of MgD_{IX} (panel A) and enzyme-MgD_{IX} (panel B). Measurements were performed in 5mM $MgATP^{2-}$, 10mM $MgCl_2$, 1mM DTT, 50mM MOPS, 0.3M glycerol, 34°C, pH 7.7. The concentrations of the ChlI and ChlD subunits were adjusted accordingly to achieve a final 4:2:1 ratio of H:I:D.

Equimolar H-D_{IX} 0.5, 2, 4 and 8µM H-D_{IX} 420ex / 580em **Observing MgD_{IX}**	**Fixed (1µM) D_{IX}** 2, 4, 6 and 8µM H 420ex / 580em **Observing MgD_{IX}**
Equimolar H-D_{IX} 0.5, 2, 4 and 8µM H-D_{IX} 295ex / 580em **Observing Enzyme-MgD_{IX}**	**Fixed (1µM) D_{IX}** 2, 4, 6 and 8µM H 295ex / 580em **Observing Enzyme - MgD_{IX}**

Figure 5.3: Overview of the transient state chelatase assays performed in either equimolar ChlH-D_{IX} or at a fixed D_{IX} concentration with an excess of ChlH, with the simultaneous detection of both MgD_{IX} and enzyme-MgD_{IX}.

5.3.2 Overview of Förster Resonance Energy Transfer (FRET)

The choice of specific excitation wavelengths used during data collection allows the independant detection of either $\mathrm{MgD_{IX}}$ or ChlH bound $\mathrm{MgD_{IX}}$ (Figure 5.4).

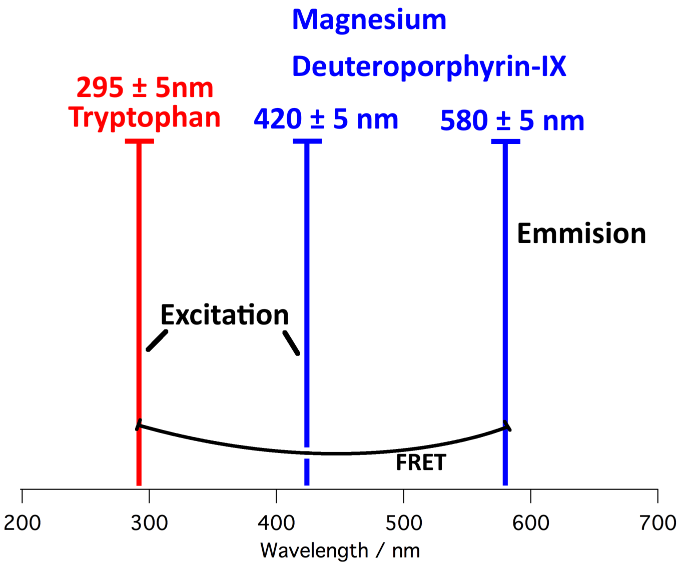

Figure 5.4: Overview of the excitation and emmision wavelengths allowing for specific excitation of either $\mathrm{MgD_{IX}}$ (420nm excitation) or ChlH bound $\mathrm{MgD_{IX}}$, owing to Förster Resonance Energy Transfer (FRET) between donor tryptophan residues of ChlH (295nm excitation) and acceptor ChlH bound $\mathrm{MgD_{IX}}$ (580nm emmision).

The detection of ChlH bound $\mathrm{MgD_{IX}}$ can be achieved as a result of Förster Resonance Energy Transfer (FRET) [115], outlined in Figure 5.5.

Due to the coupled energy transitions between ChlH tryptophan donors and $\mathrm{MgD_{IX}}$ acceptors, following the specific fluorescence excitiation of ChlH tryptophan residues (295nm, [100]) and the following energy transfer (Donor Energy Transfer) to ChlH-bound $\mathrm{MgD_{IX}}$ acceptors, the non-radiative acceptor excitation of ChlH-bound $\mathrm{MgD_{IX}}$ ultimately allows for its fluorescence emmision and detection (580nm).

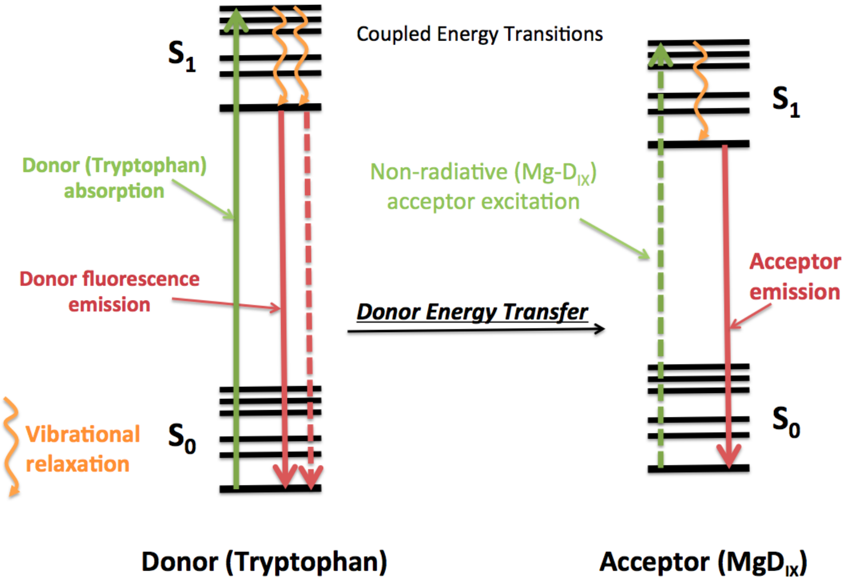

Figure 5.5: Jablonski diagram overview of the Förster Resonance Energy Transfer (FRET) mechanism [116, 115]. Following excitement of ChlH tryptophan residues (295nm), Donor Energy Transfer results in the non-radiative excitation of ChlH bound $\mathrm{MgD_{IX}}$, following this excitation, the resulting fluorescence emmision can be detected (580nm).

5.3.3 Overview of Dynafit

The Dynafit software package [101, 117] was used in fitting reaction progress curves generated from the transient state chelatase assays to a range of models for the reaction cycle.

Within Dynafit, kinetic parameters (such as the microscopic rate constants or thermodynamic equilibrium constants) are obtained from a pre-defined chemical model through the calculation of the concentration dependence with time of the defined molecular species using simultaneous Ordinary Differential Equations (ODE's). A particular advantage of Dynafit is the ability to input fitting models in biochemical notation rather than conventional mathematical notation.

In the case of a simple Michaelis-Menten type scheme (Scheme 5.1) in which enzyme (E) and substrate (S) interact to form an enzyme substrate complex (ES) followed by product release (E + P), the concentration dependence with time of the molecular species (E, S, ES and P) can be fitted to experimental data through the use of ODE's.

The fitting equation used by Dynafit is demonstrated in Equation 5.2 with parameters S(t), the experimental signal observed at time t, S_o, the offset on the signal axis, n number of unique molecular species participating in the reaction mechanism, c_i(t) the concentration of the ith species at time t and r_i, the molar response coefficient of the ith species. An example of ordinary differential equations used to calculate the concentration of species with time, c_i(t), in the simple Michaelis-Menten model are shown in Scheme 5.3.

$$\mathrm{E} + \mathrm{S} \underset{k2}{\overset{k1}{\rightleftharpoons}} \mathrm{ES} \xrightarrow{k3} \mathrm{E} + \mathrm{P} \tag{5.1}$$

$$S(t) = S_o + \sum_{i=1}^{n} r_i \; c_i(t) \tag{5.2}$$

$$
\begin{aligned}
\frac{d[E]}{dt} &= -k_1[E][S] + k_2[ES] + k_3[ES] \\
\frac{d[S]}{dt} &= -k_1[E][S] + k_2[ES] \\
\frac{d[ES]}{dt} &= +k_1[E][S] - k_2[ES] - k_3[ES] \\
\frac{d[P]}{dt} &= +k_3[ES]
\end{aligned}
\tag{5.3}
$$

5.3.4 Accounting for the fluorescence signal from either MgD$_{\mathrm{IX}}$ product or an enzyme-MgD$_{\mathrm{IX}}$ complex within established models

Over the time course of a magnesium chelatase reaction, numerous individual reaction components will be formed and lost over time, including active enzyme (E), substrate (D$_{\mathrm{IX}}$), an enzyme-product complex (enzyme-MgD$_{\mathrm{IX}}$) and reaction product (MgD$_{\mathrm{IX}}$).

Many of the species of the chelatase reaction cycle can be detected fluorometrically. In particular, enzyme-product complexes can be detected via a FRET signal (Section 5.3.2) by specifically exciting protein, in this case the excitation of tryptophan residues at 295nm, and observing enzyme-metalloporphyrin emission (580nm). Some signals will be observed from a combination of species e.g. the direct excitation of metalloporphyrin allows detection of both enzyme-bound and free product.

After the formation of an enzyme-MgD$_{\mathrm{IX}}$ complex no subsequent loss of the enzyme-MgD$_{\mathrm{IX}}$ complex is observed (panel B in Figures 5.1 and 5.2). Such behaviour would suggest that all MgD$_{\mathrm{IX}}$ produced remains either within an enzyme-MgD$_{\mathrm{IX}}$ complex, or at an equilibrium between enzyme (ChlH) and product (MgD$_{\mathrm{IX}}$) over the time course of the reaction.

This observation allows for simplifications in the building of reaction cycle models; we can disregard the enzyme-MgD$_{\mathrm{IX}}$ dissociation. So the formation of a generic reaction product (P) is used instead of explicitly accounting for the formation of MgD$_{\mathrm{IX}}$ or enzyme-MgD$_{\mathrm{IX}}$ during the chelatase reaction. As the fluorescence signal varies depending on the specific reaction conditions — such as the concentrations of enzyme or porphyrin present — the response coefficient for P during the Dynafit fitting process was adjusted for each individual reaction trace.

5.3.5 Overview of the reaction cycle models used to model the progress curves

A series of reaction schemes were used to model the progress curves obtained from transient state chelatase assays within the Dynafit software package.

The interaction of enzyme (E or X) with substrate (S) was assumed to be rapid, with the bimolecular association rate constant (k_1 and/or k_4) for the interaction of enzyme and substrate held at 200 μM^{-1}min^{-1} (approximately 10^6 M^{-1}sec^{-1}). The dissociation rate constants (k_2 and/or k_5) were held high at 200 min^{-1}. With such values, the interactions of E and S (or X and S depending on the model) can be assumed to be at equilibrium. Other parameters were adjusted accordingly during the Dynafit fitting process.

Scheme 5.4 represents an oversimplified model in which the direct conversion of substrate (S) to product (P) occurs via an enzyme-substrate intermediate (ES). Such a scheme is representative of the Michaelis-Menten model under conditions when $k_2 \gg k_3$ with the first step being at an equilibrium.

$$\mathrm{E + S \underset{k2}{\overset{k1}{\rightleftharpoons}} ES \xrightarrow{k3} E + P} \tag{5.4}$$

Scheme 5.5 describes a two-step model, in which the first turnover converts enzyme (E) into a more active form (X) which then undergoes further turnovers. This model is able to account for chelatase reaction progress curves of magnesium chelatase, under a specific reaction condition, within previously published work [100].

$$\begin{aligned} \mathrm{E + S \underset{k2}{\overset{k1}{\rightleftharpoons}} ES \xrightarrow{k3} X + P} \\ \mathrm{X + S \underset{k5}{\overset{k4}{\rightleftharpoons}} XS \xrightarrow{k6} X + P} \end{aligned} \tag{5.5}$$

Scheme 5.6 develops upon the simple model by including an ”activation” step which describes the initial conversion of inactive enzyme (D) to active enzyme (E).

$$\mathrm{D} \xrightarrow{ka} \mathrm{E} \tag{5.6}$$
$$\mathrm{E} + \mathrm{S} \underset{k2}{\overset{k1}{\rightleftharpoons}} \mathrm{ES} \xrightarrow{k3} \mathrm{E} + \mathrm{P}$$

Fitting of chelatase reaction progress curves to these models can be performed either locally or globally. Locally represents the fitting of a single reaction progress curve (i.e. under one specific concentration). Globally involves simultaneously fitting multiple progress curves to a chosen model.

5.3.6 A simple model is unable to explain the magnesium chelatase reaction cycle

A simple model for the reaction cycle pathway, (Scheme 5.7) is unable to describe these data.

$$\mathrm{E} + \mathrm{S} \underset{k2}{\overset{k1}{\rightleftharpoons}} \mathrm{ES} \xrightarrow{k3} \mathrm{E} + \mathrm{P} \tag{5.7}$$

Each of sets of reaction progress curves, generated from assays performed at either in either equimolar ChlH-$\mathrm{D_{IX}}$ or with ChlH in excess over $\mathrm{D_{IX}}$, were fitted to the simple model (Scheme 5.7). During the fitting of each of the data sets, fitting was performed globally, by simultaneously fitting all four progress curves.

The data were fitted to Scheme 5.7 with $k_3 = 0.8\ \mathrm{min}^{-1}$ consistent with previously calculated k_{cat} values [35], under the assumption that the association of enzyme and substrate is at an equilibrium, with $k_1 = 200\ \mu\mathrm{M}^{-1}\ \mathrm{min}^{-1}$ (approximately $10^6\ \mathrm{M}^{-1}\mathrm{sec}^{-1}$) and $k_2 = 200\ \mathrm{min}^{-1}$.

This model fails both quantitatively, as the fitted lines fall far from the data, as well as qualitatively, with the fitted lines being in poor agreement with the overall shape of the data (Figure 5.6).

Variations in k_3 (representative of k_{cat}) do not result in any significant improvement towards the fitted lines and thus under / over estimations of k_3 do not account for the failure of the fitted model. In addition to fitting all four progress curves within each individual data set globally, fitting each individual progress curve independently (locally) to Scheme 5.7 is also unsuccessful.

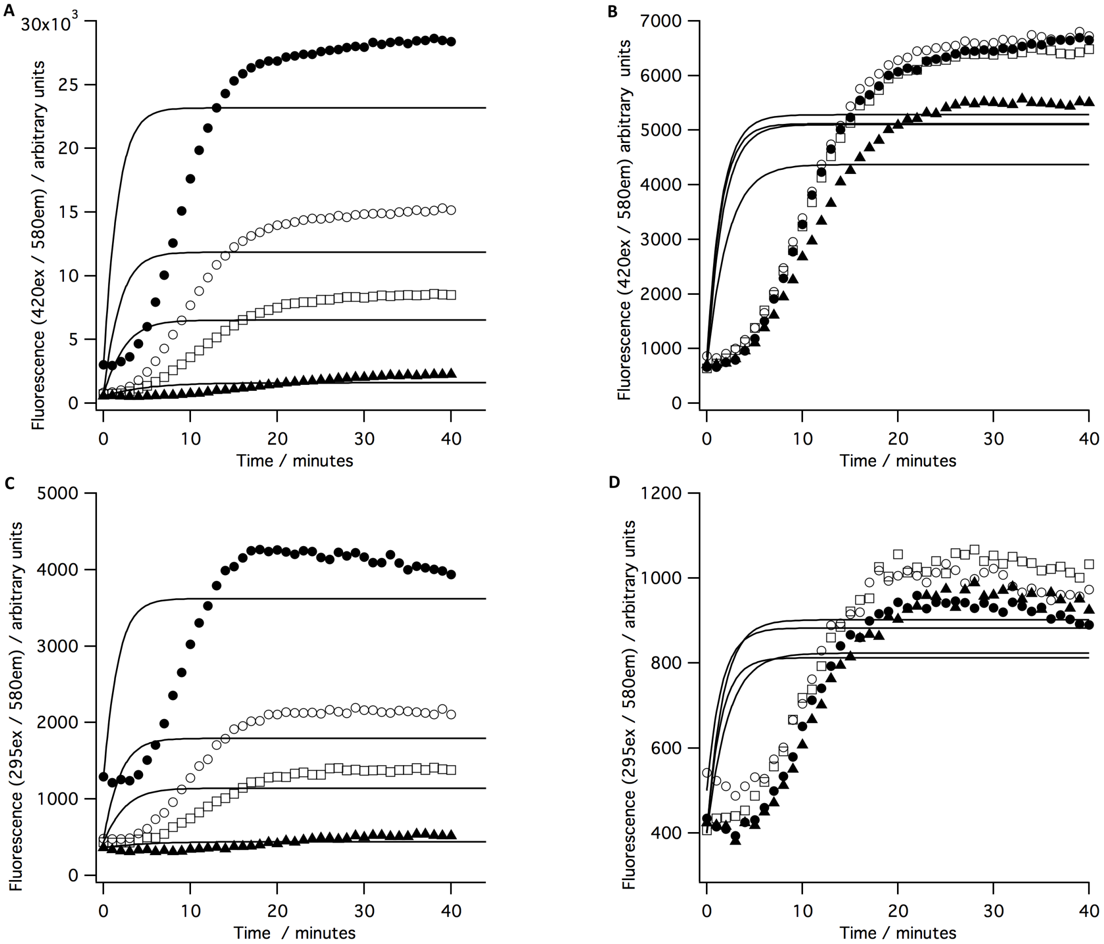

Figure 5.6: A simple model is unable to explain these data. Simultaneously (globally) fitting all four of the transient state progress curves within each of the data sets (panels A, B, C or D) to a simple reaction cycle model (Scheme 5.7) with $k_3 = 0.8$ min^{-1} is unsuccessful.

With simple models clearly unable to explain the data, further models were explored.

5.3.7 A two step model for the reaction cycle of magnesium chelatase can explain previously obtained reaction progress curves

Transient kinetic studies of magnesium chelatase indicated a rate limiting step ($k_{\mathrm{obs}} = 0.15\ \mathrm{min}^{-1}$) [100] approximately 5 slower than k_{cat}, calculated to be 0.8 min^{-1} [35].

It was demonstrated that a two-step model for the reaction cycle of magnesium chelatase could account for such behaviour [100]. Within such model, a slower first turnover results in the conversion of inactive enzyme (E) into active enzyme (X) that then undergoes multiple faster turnovers (Scheme 5.8).

$$\begin{aligned} \mathrm{E} + \mathrm{S} &\underset{k2}{\overset{k1}{\rightleftharpoons}} \mathrm{ES} \xrightarrow{k3} \mathrm{X} + \mathrm{P} \\ \mathrm{X} + \mathrm{S} &\underset{k5}{\overset{k4}{\rightleftharpoons}} \mathrm{XS} \xrightarrow{k6} \mathrm{X} + \mathrm{P} \end{aligned} \tag{5.8}$$

Figure 5.7 shows previously collected data, adapted from reference [100], performed in 8μM ChlH and $\mathrm{D_{IX}}$. It was demonstrated that modelling this progress curve, within Dynafit, to a two-step model (Scheme 5.8) with kinetic parameters $k_3 = 0.15\ \mathrm{min}^{-1}$ which represents an initial first slower turnover that results in conversion of inactive enzyme (E) to active enzyme (X) and $k_6 = 0.8\ \mathrm{min}^{-1}$ representing faster subsequent turnovers performed by active enzyme (X), can account for this reaction progress curve.

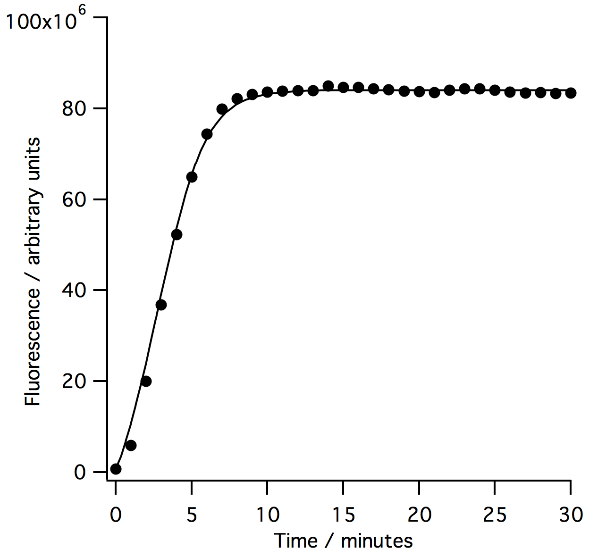

Figure 5.7: Previously collected data for a chelatase reaction performed in 8μM ChlH and D_{IX} adapted from reference [100]. It was demonstrated that modelling such data, within Dynafit, to a two-step model (Scheme 5.8) with kinetic parameters $k_3 = 0.15$ min^{-1} and $k_6 = 0.8$ min^{-1} is able to explain this data [100].

5.3.8 Current progress curves cannot be explained by a two-step model

As this two-step model could explain the behaviour of magnesium chelatase in previous work, although under a more limited series of reaction conditions, current data was explored with this model.

During the Dynafit fitting procedure, the rapid and reversible association of enzyme and substrate was assumed with the bimolecular association rate constants k_1 and k_4 held at 200 μM^{-1}min^{-1} (10^6 M^{-1}sec^{-1}), k_2 and k_5 were held at 200 min^{-1}.

The progress curves, monitoring MgD_{IX} formation in a range of equimolar concentrations of ChlH and D_{IX} were globally fitted to the two step model (Scheme 5.8), with parameters $k_3 = 0.15$ min^{-1} representing an initial first slower turnover that results in the conversion of inactive enzyme (E) to active enzyme (X) and $k_6 = 0.8$ min^{-1} representing the faster subsequent turnovers performed by active enzyme (X).

These data cannot be explained by this two step model, with the model showing clear disagreement with the reaction progress curves performed in equimolar concentrations of ChlH and D_{IX}. As with the simple model, this two step model fails both quantitatively, with the fitted lines falling far from the data, as well as qualitatively, with the fitted lines being in poor agreement with the overall shape of the data (Figure 5.8).

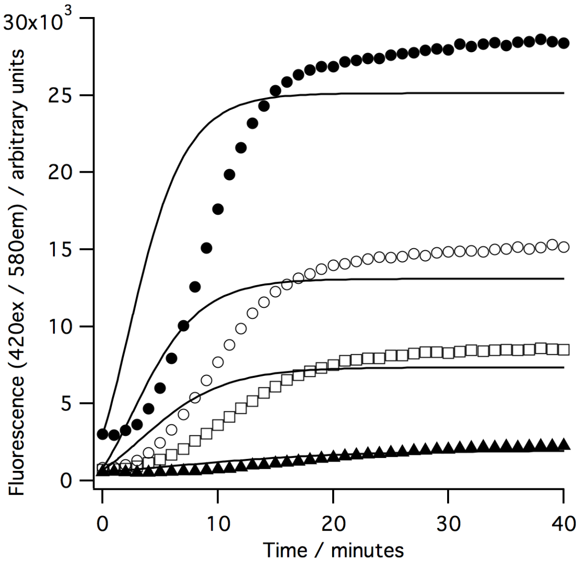

Figure 5.8: A two step model cannot explain these progress curves monitoring $\mathrm{MgD_{IX}}$ formation in 8μM (●), 4μM (○), 2μM (□) and 0.5μM (▲) ChlH and $\mathrm{D_{IX}}$. The overlayed lines are the result of fitting to Scheme 5.8 with $k_3 = 0.15\ \mathrm{min}^{-1}$ and $k_6 = 0.8\ \mathrm{min}^{-1}$.

Locally (individually) fitting each progress curve to this two step model does not lead to a significant improvement in the fitted curves. This indicates that the inability of this model to explain these progress curves is not a result of simultaneously fitting multiple curves at a range of reaction concentrations. Furthermore, allowing for variations in the rate constants for either the slower first turnover (k_3) or the faster subsequent multiple turnovers (k_6) by allowing for k_3 and/or k_6 to be adjustable during the Dynafit fitting procedure does not result in any significant improvement.

Fitting the alternative series of generated progress curves, again monitoring $\mathrm{MgD_{IX}}$ formation, however performed in a fixed $\mathrm{D_{IX}}$ concentration (1μM) at an overall excess of ChlH also shows poor agreement with this two step model. Figure 5.9 shows the result of fitting these data to the two step model (Scheme 5.8) with parameters $k_3 = 0.15\ \mathrm{min}^{-1}$ and $k_6 = 0.8\ \mathrm{min}^{-1}$. Again, fitting these traces individually or allowing for k_3 and/or k_6 to be adjustable during the Dynafit fitting procedure does not result in any significant improvements in fitting.

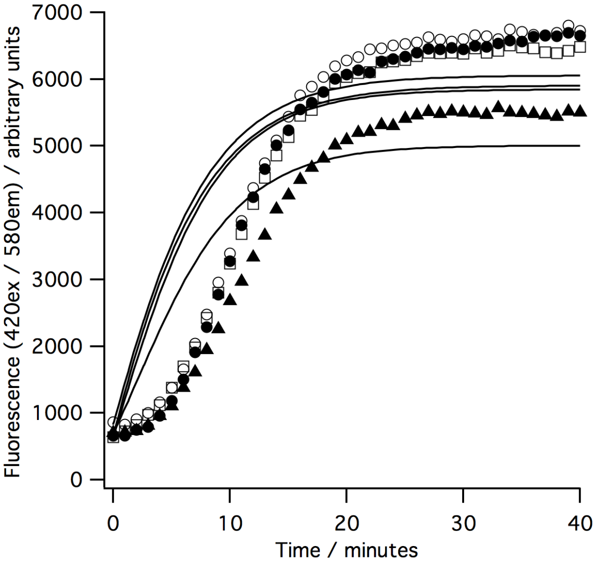

Figure 5.9: A two step model cannot explain these progress curves monitoring $\mathrm{MgD_{IX}}$ formation in a fixed concentration of $\mathrm{D_{IX}}$ (1μM) at 8μM (●), 6μM (○), 4μM (□) and 2μM (▲) ChlH. The overlayed lines are the result of fitting to Scheme 5.8 with $k_3 = 0.15\ \mathrm{min}^{-1}$ and $k_6 = 0.8\ \mathrm{min}^{-1}$.

Simultaneous detection of both MgD_{IX} and enzyme-MgD_{IX} was performed during data collection. To establish whether this model being unable to describe the reaction progress curves is a result of the specific detection method used, the alternative progress observing enzyme-MgD_{IX} formation were investigated. Fitting to the two step model (Scheme 5.8) with $k_3 = 0.15\ \mathrm{min}^{-1}$ and $k_6 = 0.8\ \mathrm{min}^{-1}$ finds the data to be in poor agreement with the fitted model (Figure 5.10). Therefore, the choice of detection method is not the cause of the model failing to explain these data.

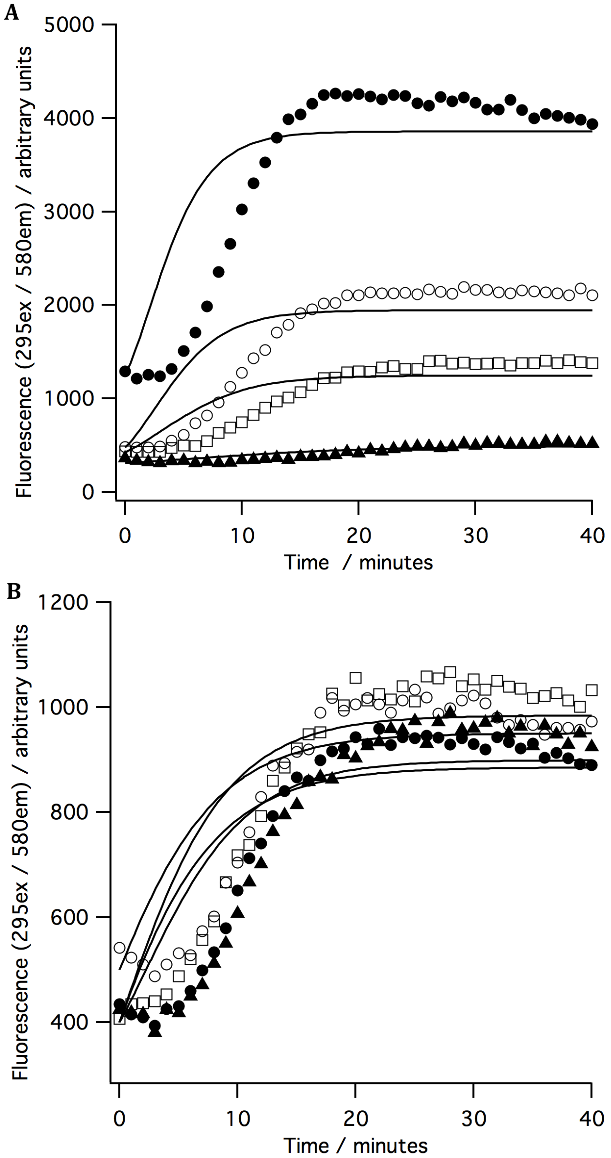

Figure 5.10: A two step model cannot explain these progress curves monitoring enzyme-MgD_{IX} formation. (A) performed in equimolar concentrations of ChlH and D_{IX} of 8μM (●), 4μM (○), 2μM (□) and 0.5μM (▲) ChlH and D_{IX}. (B) performed in a fixed concentration of D_{IX} (1μM) at 8μM (●), 6μM (○), 4μM (□) and 2μM (▲). The overlayed lines are the result of fitting to Scheme 5.8 with $k_3 = 0.15\ \mathrm{min}^{-1}$ and $k_6 = 0.8\ \mathrm{min}^{-1}$.

5.3.9 Summary - A two step model is unable to explain these data

A two step model (Scheme 5.8) is unable to explain these progress curves, generated from assays performed in either equimolar ChlH-D_{IX} concentrations, or under conditions where ChlH is in excess over D_{IX}. Modifications in the fitting parameters (rate constants) does not result in any improvement in fitting. Furthermore, the choice of detection method is not the cause of this failure.

This model fails both quantitatively with the fitted lines falling far from the data sets as well as qualitatively with the fitted lines been in poor agreement with the overall shape of the data. In particular the models show poor agreement with the initial part of the progress curve.

Although subunits were preincubated at conditions identical to those demonstrated to eliminate a lag phase prior to Mg^{2+} insertion [100], a lag phase is evident within these data sets. Therefore, to investigate if such lag phases are responsible for the apparent failures within the previously discussed models, further models were developed that incorporate an additional initial step to account for a lag phase.

5.3.10 An initial slow step is required to explain current data

Building on the previously discussed models, an initial reaction step was added describing the total irreversible conversion of inactive enzyme (D) to an active enzyme (E) prior to the reaction (Scheme 5.9). This was incorporated to account for a lag phase that is likely the cause of the failure of previous fitting models.

It was demonstrated that an additional slow step within the models is required to be able to explain these data, furthermore the overall nature of the step is governed by the specific reaction conditions. It was demonstrated that this model is capable of explaining multiple reaction progress curves simultaneously under conditions of equimolar ChlH-D_{IX}. However, when ChlH is in excess over D_{IX}, it is incapable explaining multiple progress curves simultaneously, indicating that this slow step is influenced by the relative levels of ChlH and D_{IX} present.

$$\begin{aligned} &\mathrm{D} \xrightarrow{ka} \mathrm{E} \\ &\mathrm{E} + \mathrm{S} \underset{k2}{\overset{k1}{\rightleftharpoons}} \mathrm{ES} \xrightarrow{k3} \mathrm{E} + \mathrm{P} \end{aligned} \tag{5.9}$$

5.3.11 Fitting the progress curves generated from assays performed in equimolar ChlH-D_{IX}

The four progress curves generated from assays performed in a series of equimolar ChlH-D_{IX} concentrations can be explained by a simple model with an additional step that describes the initial conversion of inactive enzyme (D) to active enzyme (E).

Globally (simultaneously) fitting the four progress curves monitoring MgD_{IX} formation under equimolar ChlH-D_{IX} concentrations to Scheme 5.9 finds the model capable of explaining these data. Globally fitting all four progress curves, under a fixed k_3 of 0.8 min^{-1} consistent with previously calculated k_{cat} values, results in a rate constant for the conversion of D to E of $k_{\text{a}} = 0.018 \pm 0.0002\ \text{min}^{-1}$ (Figure 5.11, panel A).

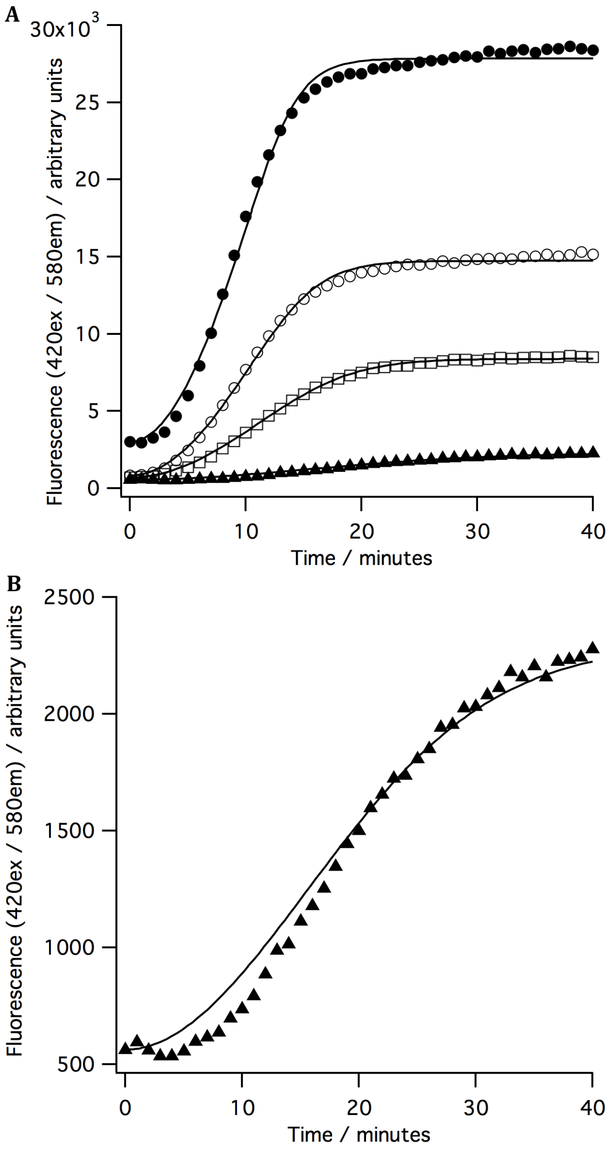

Figure 5.11: A simple model with an initial slow step is capable of explaining multiple progress curves monitoring MgD_{IX} formation under range of equimolar ChlH-D_{IX} concentrations simultaneously. The fitted lines represent fitting to Scheme 5.9 with $k_3 = 0.8$ min^{-1} with a resulting $k_a = 0.018 \pm 0.0002$ min^{-1}. (A) 8μM (●), 4μM (○), 2μM (□) and 0.5μM (▲) ChlH-D_{IX}. (B) Expanded view of the 0.5μM ChlH-D_{IX} data set.

Overall, the shape of the fitted lines are in much better agreement with the data than previous models, however the lowest concentration of ChlH-D_{IX} used does show deviation within the initial region (Figure 5.11, panel B), of which could not be improved through changes in the fitting parameters.

This resulting rate constant for the initial conversion of D to E of $k_a = 0.018 \pm 0.0002$ min^{-1} is much lower than k_3 (0.8 min^{-1}) indicating a very slow initial step within the models is required to explain these data.

During fitting, allowing both k_a and k_3 to be adjustable parameters does not lead to a significant change towards the overall shape of the fitted lines, however results in a change in k_3 and k_a. With $k_3 = 0.48 \pm 0.027\ \mathrm{min}^{-1}$ and $k_\mathrm{a} = 0.034 \pm 0.0024\ \mathrm{min}^{-1}$ resulting. Although being subject to such variance when allowing these parameters to be adjustable during the fitting procedure, these values are not unreasonable, with k_3 still being consistent with k_cat and overall still requiring an very slow initial step (k_a).

Fitting the same equimolar ChlH and $\mathrm{D_{IX}}$ data set, however monitoring the formation of an enzyme-$\mathrm{MgD_{IX}}$ complex, is in similar agreement with Scheme 5.9 (Figure 5.12, panel A). The fitted curves are representative of globally fitting all four progress curves with a fixed $k_3 = 0.8\ \mathrm{min}^{-1}$ with a resulting rate constant k_a for the conversion of D to E of $0.019 \pm 0.0003\ \mathrm{min}^{-1}$. Again the shape of the fitted lines are in close agreement with the data, although the lowest concentration of ChlH-$\mathrm{D_{IX}}$ does show some deviation within the initial region (Figure 5.12, panel B).

Although this model appears capable of explaining multiple progress generated from assays performed in a range of equimolar ChlH-$\mathrm{D_{IX}}$ concentrations simultaneously, to investigate whether the rate constant for this initial step (k_a) changes in response to the concentration of ChlH-$\mathrm{D_{IX}}$, local fitting of progress curves were explored. With no significant variation in the observed k_a values from each of the four data sets seen when fitting under a fixed k_3 of $0.8\ \mathrm{min}^{-1}$ (Figure 5.13).

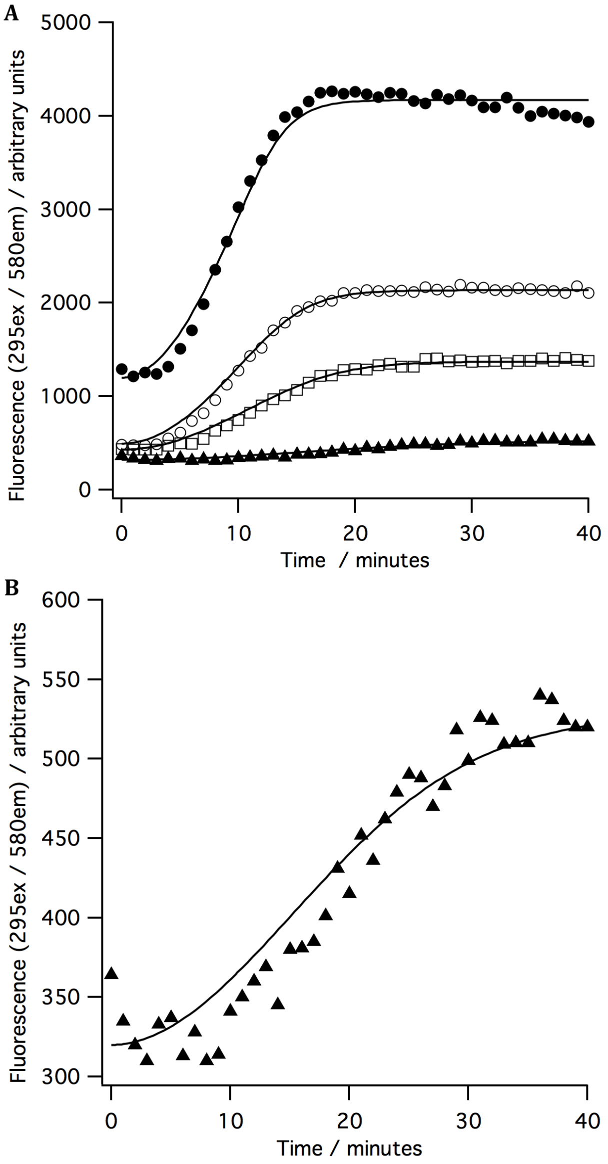

Figure 5.12: A simple model with an initial slow step is capable of explaining multiple progress curves monitoring enzyme-$\mathrm{MgD_{IX}}$ formation under a range of equimolar ChlH-$\mathrm{D_{IX}}$ concentrations simultaneously. The fitted lines represent fitting the data to Scheme 5.9 with $k_3 = 0.8\ \mathrm{min}^{-1}$ with a resulting $k_\mathrm{a} = 0.019 \pm 0.0003\ \mathrm{min}^{-1}$. (A) 8$\mu$M (●), 4$\mu$M (○), 2$\mu$M (□) and 0.5$\mu$M (▲) ChlH-$\mathrm{D_{IX}}$. (B) Expanded view of the 0.5μM ChlH-$\mathrm{D_{IX}}$ data set.

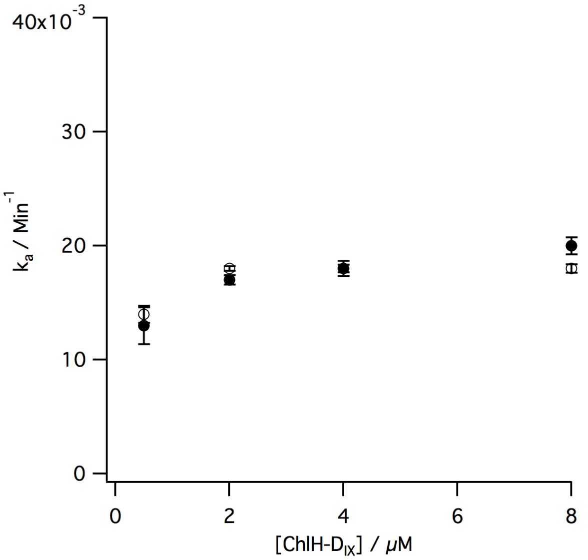

Figure 5.13: The variation on k_a obtained as a result of fitting the progress curves generated from assays performed in equimolar ChlH-D_{IX} detecting either enzyme-MgD_{IX} (○) or MgD_{IX} (●) to Scheme 5.9.

5.3.12 A simple model with an initial slow step can explain multiple reaction progress curves generated from assays performed in a range of equimolar ChlH-D_{IX} concentrations simultaneously

A simple model containing an initial slow step, describing the conversion of inactive enzyme D to active enzyme E of approximately 0.02 - 0.03 min^{-1}, appears capable of explaining multiple progress curves generated from assays performed in a range of equimolar ChlH-D_{IX} concentrations simultaneously. With the rate constant for this slow step (k_a) showing no significant variation with ChlH-D_{IX} concentration.

To investigate this model further, the alternative data sets, performed under a fixed concentration of D_{IX} (1μM) with an excess of ChlH (2, 4, 6 and 8μM ChlH), were explored with this model.

5.3.13 A simple model with an initial slow step fails to simultaneously explain multiple reaction progress curves generated from assays where ChlH is at an excess over D_{IX}

Unlike progress curves generated from assays performed in equimolar ChlH-D_{IX} concentrations, a simple model within an initial slow step is incapable of simultaneously explaining multiple progress curves where the ChlH concentration (2, 4, 6 and 8 μM) is at an overall excess over D_{IX} (μM).

Attempting simultaneously fitting of all four progress curves monitoring MgD_{IX} formation, to this model with k_3 of 0.8 min^{-1}, results in a k_a of approximately 0.007 min^{-1}, however the fitted lines are in clear disagreement with the data (Figure 5.14). Furthermore simultaneously fitting all four progress curves monitoring enzyme-MgD_{IX} formation, to this model with k_3 of 0.8 min^{-1}, results in a k_a of approximately 0.008 min^{-1}, however the fitted lines are again in clear disagreement with the data (Figure 5.15).

To explore this model further, k_3 and/or k_6 were allowed to be adjustable during the fitting procedure, however this does not lead to any significant improvement in the fitted lines. Therefore this model appears incapable of simultaneously explaining these multiple progress curves, where the ChlH concentration (2, 4, 6 and 8 μM) is at an overall excess over D_{IX} (1 μM).

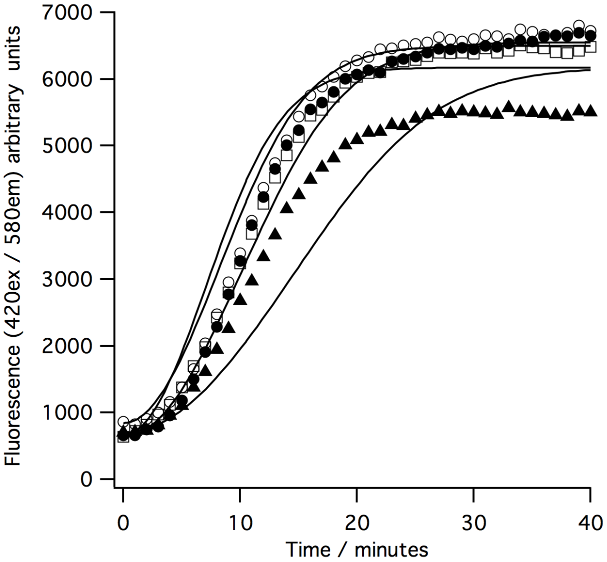

Figure 5.14: A simple model with an initial slow step (Scheme 5.9) is unable to explain these progress curves monitoring MgD_{IX} formation with ChlH in excess over D_{IX} during simultaneous (globally) fitting of all four progress curves. Fitted lines are the result of globally fitting to Scheme 5.9 with $k_3 = 0.8$ min^{-1} with resulting k_a of 0.007 min ± 0.0003 min^{-1}. Performed in 8μM (●), 6μM (○), 4μM (□) and 2μM (▲) ChlH at 1μM D_{IX}.

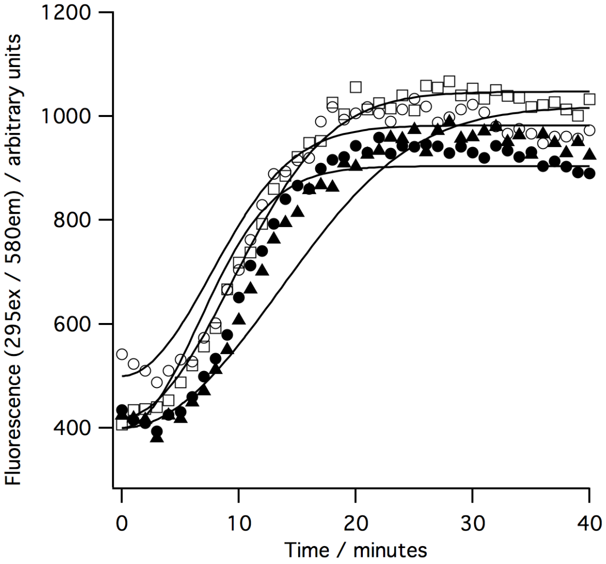

Figure 5.15: A simple model with an initial slow step (Scheme 5.9) is unable to explain these progress curves monitoring enzyme-MgD_{IX} formation with ChlH in excess over D_{IX} during simultaneous (globally) fitting of all four progress curves. Fitted lines are the result of globally fitting to Scheme 5.9 with $k_3 = 0.8$ min^{-1} with resulting k_a of 0.008 min ± 0.0004 min^{-1}. Performed in 8μM (●), 6μM (○), 4μM (□) and 2μM (▲) ChlH at 1μM D_{IX}.

5.3.14 Locally fitting the progress curves generated from assays perfomed in an excess of ChlH over D_{IX}

Attempting simultaneous fitting of multiple progress generated from assays performed with an excess of ChlH over D_{IX}, to this simple model with an initial slow step is unsuccessful. To explore this data further, each of the four progress curves were fitted individually to this model (Scheme 5.9). When fitting the progress curves individually, this model is capable of explaining these data.

Fitting each of the four progress curves, at different ChlH concentrations monitoring MgD_{IX} formation, individually, in turn to Scheme 5.9 finds the data to be agreement with the model, with the progress curves showing very good agreement with the data. Fitting was performed at a known k_3 (0.8 min^{-1}) in agreement with k_{cat}. The result of fitting are shown in Figure 5.16.

Interestingly, the rate constant for the initial step (k_a) appears to show a significant dependence on the ChlH concentration, in stark contrast to the data performed in equimolar concentrations of ChlH-D_{IX}, in which a single k_a of approximately 0.02 min^{-1} within the model is capable of explaining the data under all ChlH-D_{IX} conditions used. A similar response in k_a can be observed whilst holding k_3 at 0.5 or 1.5 min^{-1}.

These data indicate that when ChlH is at a significant (8 fold) excess over porphyrin, a much slower initial step results, as demonstrated by the variation in k_a with ChlH concentration (Figure 5.16, panel B).

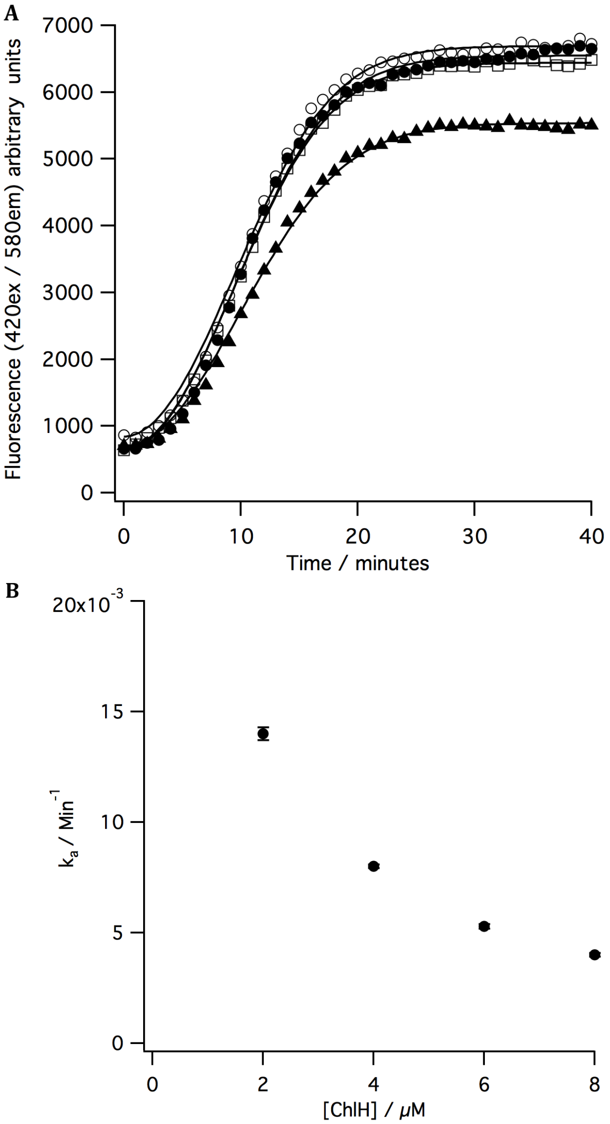

Figure 5.16: The progress curves observing MgD_{IX} formation, with ChlH at an excess over D_{IX}, can only be explained by a simple model containing an initial slow step when fitting each progress curve individually (locally). Performed in $8\mu M$ (●), $6\mu M$ (○), $4\mu M$ (□) and $2\mu M$ (▲) ChlH with $1\mu M$ D_{IX}. (A) Resulting fitted lines from the local fitting of each progress curve. (B) The dependence of k_a with ChlH concentration with $k_3 = 0.8$ min^{-1}.

Fitting these progress curves, performed under these same conditions, however observing enzyme-MgD_{IX} formation, again appear to be in better agreement when fitting each progress curve individually. However, the fitted lines do appear to show some deviation with the data (Figure 5.17), such deviations were not evident in the progress curves observing MgD_{IX} formation. However these data do still show a similar variation in k_a (Figure 5.17). Allowing for adjustments of fitting parameters during local fitting does not lead to a noticeable improvement in fitting.

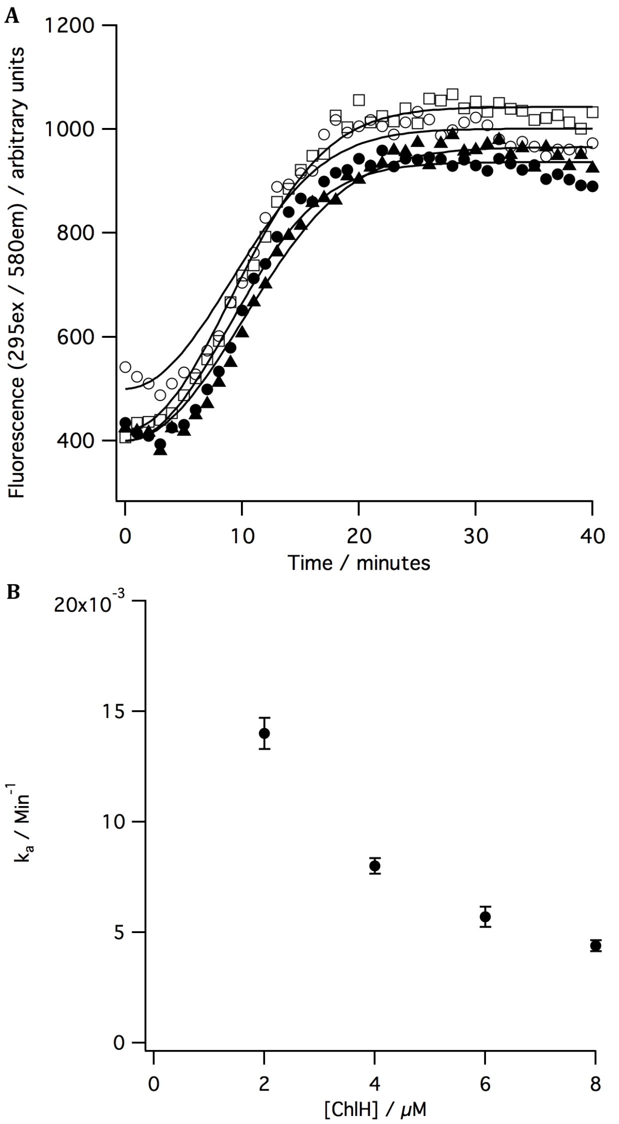

Figure 5.17: The progress curves observing enzyme-MgD$_{\mathrm{IX}}$ formation, with ChlH in an excess over D$_{\mathrm{IX}}$, can only be explained by a simple model containing an initial slow step (Scheme 5.9) with $k_3 = 0.8$ min^{-1} when fitting each progress curve individually (locally). Performed in 8μM (●), 6μM (○), 4μM (□) and 2μM (▲) ChlH with 1μM D$_{\mathrm{IX}}$. (A) Resulting fitted lines from the local fitting of each progress curve. (B) The dependence of k_{a} with ChlH concentration with $k_3 = 0.8$ min^{-1}.

5.3.15 The relative levels of ChlH and $\mathrm{D_{IX}}$ present directly influence this observed slow step

Within progress curves generated from assays performed under a range of equimolar ChlH-$\mathrm{D_{IX}}$ concentrations a slow step is required within reaction cycle models to describe the data. This rate constant (k_a) for this slow step preceding the reaction (within these models describing the total conversion of inactive enzyme D to active enzyme E), exhibits no noticeable variation between progress curves under a range of equimolar ChlH-$\mathrm{D_{IX}}$ concentrations. Thus, such models can explain multiple progress curves performed in varying equimolar ChlH-$\mathrm{D_{IX}}$ concentrations simultaneously, with k_a of 0.019 min^{-1} for this initial step.

In contrast, when modelling progress curves generated from assays performed in a range of ChlH concentrations at an excess over $\mathrm{D_{IX}}$ substrate, a significant variation in k_a for this slow step is seen. Within these data, much higher concentrations of ChlH over $\mathrm{D_{IX}}$ leads to a much lower k_a.

This response is characteristic of slow reversible isomerisation of enzyme and much faster substrate binding, described in Scheme 5.10. Within such a scheme, enzyme (in this case ChlH), exists at slow equilibrium between active (E) and inactive forms (D). Interaction of substrate with the active form leads to the "capture" of this active enzyme form into an ES complex.

$$\mathrm{D} \underset{k2}{\overset{k1}{\rightleftharpoons}} \mathrm{E} \overset{K'}{\rightleftharpoons} \mathrm{ES} \tag{5.10}$$

Under conditions where substrate binding is much faster than enzyme isomerisation, Equation 5.11 can be used to describe Scheme 5.10 and will represent a single exponential. At low levels of substrate relative to enzyme, the rate of this capture of E is low and k_obs will tend to $k_1 + k_2$. At higher levels of substrate relative to enzyme, the first step is essentially irreversible with capture of E dominating and k_obs will tend to k_1 [118, 119].

$$k_{obs} = k_1 + \frac{k_2}{1 + \frac{[S]}{K'}} \tag{5.11}$$

Thus, within these data performed in a range of concentrations of ChlH over $\mathrm{D_{IX}}$, when the levels of $\mathrm{D_{IX}}$ substrate are much lower then ChlH (i.e the highest ChlH concentration) capture of E will be slower and the enzyme isomerisation step will dominate (larger k_2). At lower concentrations of enzyme, the relative levels of D_{IX} available increases, leading to faster capture of E (ChlH) by D_{IX} leading to a reduction in k_2.

Fitting of the observed change in slow step k_a, (determined in Figure 5.16), observed under conditions where enzyme is in excess over substrate to Equation 5.11 was performed. Such equations cannot explicitly be used to explain these data and serve as guidance only, as within these data sets, substrate is held constant and ChlH concentration is varied. Thus, whilst [S] relates to substrate concentration within Equation 5.11, within these data it relates to enzyme concentration that in turn dictates the relative levels of enzyme and substrate present.

Nonetheless, Equation 5.11 does appear capable of explaining the overall variation in this slower step with enzyme concentration, at least quantitatively (Figure 5.18), suggesting that isomerisation of ChlH prior to D_{IX} binding may explain this observed change in k_a.

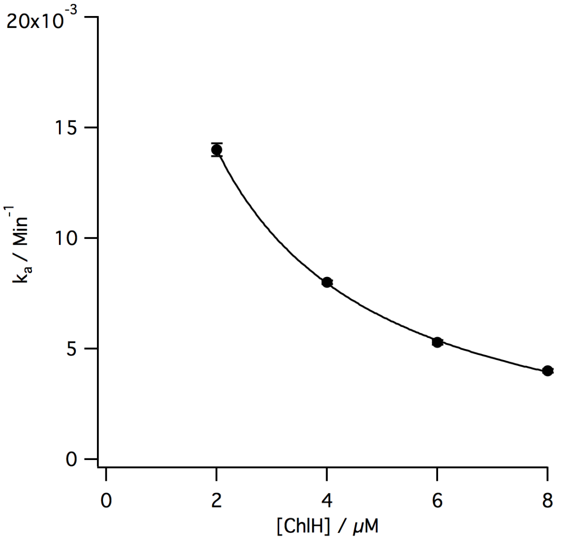

Figure 5.18: Fitting the observed change in k_a obtained in Figure 5.16 to Equation 5.11 may indicate that slow isomerisation of ChlH proceeds D_{IX} binding. With K' = 0.97 ± 0.21 μM, $k_1 = 0.001 \pm 0.0004$ min^{-1} and $k_2 = 0.046 \pm 0.006$ min^{-1}.

5.4 Conclusions

Dynafit modelling of reaction progress curves for the chelatase reaction cycle find a previously established two step model incapable of explaining these data. A lag phase — despite preincubation of subunits under conditions shown to eliminate such lag — is evident. This lag phase is the likely cause of the overall failure of previously established models to explain current data.

However, relatively simple models with the inclusion of an initial step to explicitly account for a lag phase are capable of explaining the reaction cycle progress curves.

Multiple progress curves generated from assays performed under a range of equimolar ChlH-D_{IX} concentrations can be explained by a simple model with an initial slow step, furthermore multiple reaction progress curves under these conditions can be described simultaneously. In contrast, when ChlH concentration is varied over D_{IX}, the behaviour is overall more complex; the magnitude of this initial slow step is influenced by the levels of ChlH relative to D_{IX}. Such behaviour can be explained by slower isomerisation of ChlH preceding fast binding of D_{IX} substrate.

The lag phase commonly observed preceding metal ion chelation is complex with a wide array of studies demonstrating that numerous factors can influence this (Section 5.2.1), thus the overall nature of this lag phase is likely to represent more than one single process. Nonetheless, these data give a strong indication that the isomerisation of ChlH will be involved within the processes governing this lag phase.

6 Concluding remarks and future perspectives

6.1 My work provides no direct evidence for a *Synechocystis* I_6D_6 complex instead supporting a higher order heteromeric ID complex

The quaternary structure of AAA$^+$ protein complexes often resembles ring like assemblies of their respective subunits, the assembly of such arrangements is dynamic and complex [44, 40], exhibiting conformational changes and rearrangements in a nucleotide dependant fashion; Intersubunit communication throughout these rings is often essential to mediate such changes [41, 50, 39]. These complexes formed by AAA$^+$ proteins can contain assemblies of the same type of subunit (homomeric) or mixtures of different subunit types (heteromeric) — examples of these are outlined in Table 1.3. Although single ring type arrangements are common, two-tiered stacked rings of subunits can also occur, such as those occurring between the AAA$^+$ ClpP and ClpX yielding ClpXP [53] or P97 [62]. In relation to magnesium chelatase, single-particle cryo-EM experiments have found evidence for a similiar two-tiered I_6D_6 complex of *Rhodobacter capsulatus* subunits [94], present in a range of nucleotide states of which include MgADP and $MgCl_2$. Furthermore, the I and D subunits of the chelatase can form rings in isolation [45, 85, 91]. On such basis an I_6D_6 arrangement is thought to occur within the magnesium chelatase sytem.

My kinetic titrations demonstrate saturation in chelatase activity at two distinct ChlID concentration ratios dependant on how subunits are titrated — 1:1 when ChlI is titrated against ChlD, in addition to saturation in chelatase activity at a significant excess of ChlI over ChlD occurring during the contrasting titrations of ChlD against ChlI. Feasible complexes that support a 1:1 interaction include I_6D_6 and subsequently such arrangement cannot be ruled out on the basis of kinetic titrations. The contrasting titrations in which saturation occurs at much higher levels of ChlI over ChlD would appear to support different types of ChlID complexes, of which contain a higher overall proportion of ChlI subunits over ChlD. Feasible arrangements include heteromeric ChlID complexes such as I_5D or I_6D. Furthermore, kinetic titrations monitoring the ATPase activity of the enzyme system demonstrate that whilst saturation in ATPase activity is apparent at 1:1 levels of ChlI and ChlD in the absence of ChlH, in the presence of ChlH, much higher ATPase activity is observed under conditions where ChlI is in excess over ChlD. Such conditions would also appear to suggest higher order ChlID arrangements. Additionally, this stimulation in ATPase activity provides direct evidence that ChlH interacts with and influences the ATP hydrolysis performed by ChlID motor complexes.

Although kinetic titrations provide compelling evidence towards the possibility for multiple active chelatase complexes, such experiments do not allow for the direct observation and characterisation of any one specific complex, thus SV-AUC was used to probe subunit assembly of the *Synechocystis* system further. Ultimately SV-AUC provides no evidence for an I_6D_6 complex or a intact chelatase complex containing all three subunits in the presence of ADP and $MgCl_2$. Thus, despite kinetic titrations supporting a 1:1 type complex, the presence of a *Synechocystis* I_6D_6 arrangement remains inconclusive.

However, SV-AUC shows a range of smaller ChlID assemblies in the presence of ADP and $MgCl_2$. Interestingly a particular complex at 9.1S (approximately 300kDa) appears to be favoured under two specific experimental conditions during SV-AUC, a five fold excess of ChlI over ChlD, or the presence of ChlH. On this basis, such complex of appropiate mass is proposed to be that representing a higher order heteromeric ring of I and D subunits such as I_5D. Finally, the ChlH subunit appears to transiently interact with and influence the assembly of ChlID arrangements during SV-AUC, in agreement with chelatase titrations of ChlD against ChlI, in which high levels of ChlH also appear to influence the relative levels of ChlI and ChlD within active complexes.

In summary, my work gives strong support for a higher order heteromeric ID complex containing higher levels of ChlI over ChlD, such as I_5D type complex, and no direct evidence for I_6D_6 or a long lived IDH complex in the presence of MgADP and $MgCl_2$ (Figure 6.1). Within this proposed higher order ChlID arrangement, transient interactions of ChlH appear to influence the overall levels of ATPase activity and its assembly.

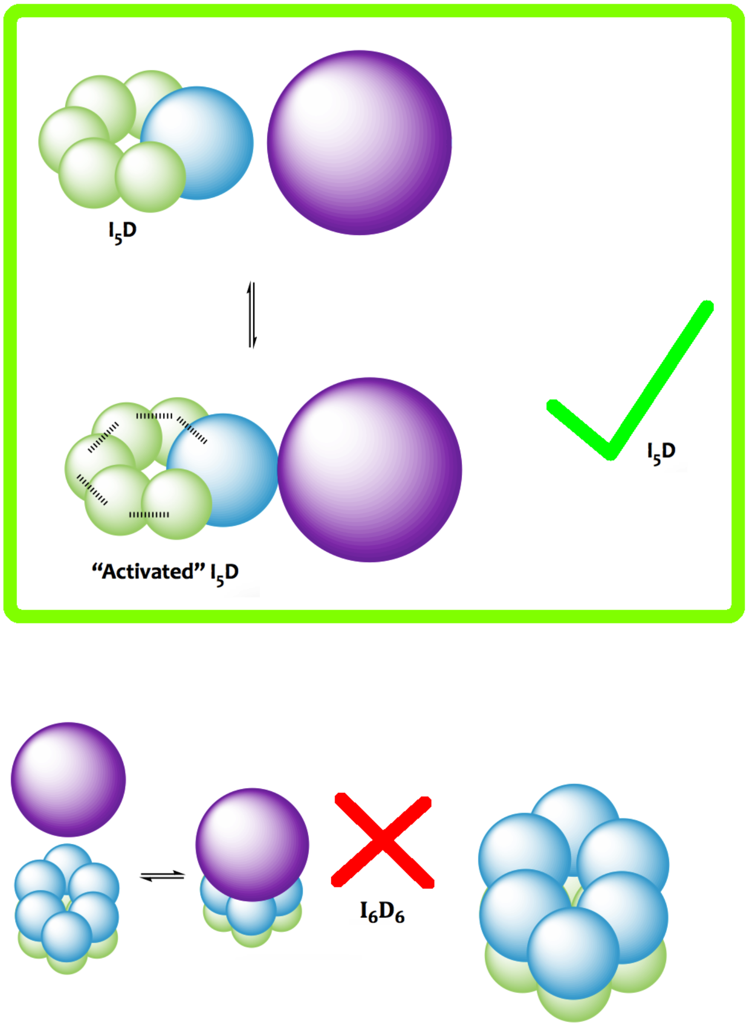

Figure 6.1: My work gives strong support for a heteromeric ID complex containing higher levels of I over D, such as an I_5D type complex. There is no direct evidence for an I_6D_6 or a long lived IDH complex in the presence of MgADP and $MgCl_2$.

6.1.1 Reasons for the lack of a *Synechocystis* I_6D_6 complex

The reasons for the lack of a directly observable *Synechocystis* I_6D_6 complex remain unclear.

Different species of the chelatase show subtle differrences in their assembly behaviour. *Synechocystis* ChlI subunits, in the presence of $MgATP^{2-}$, can assemble into a range of ring like structures including 6-, 7- and 8-fold arrangements with heptamers being directly observed [85], whilst *Rhodobacter capsulatus* BchI forms hexamers in addition to smaller arrangements in the presence of ATP [45, 88]. Consequently, the assembly of ID complexes may exhibit some similiar such dependance, with an I_6D_6 complex being either exclusive to the *Rhodobacter capsulatus* chelatase system, or, if this complex does occur within the *Synechocystis* system, the ADP bound state may represent a much shorter lived complex within the system remaining unobservable on the longer time-scale of SV-AUC. Alternatively, the formation of this I_6D_6 arrangement may be a biochemical artifact observed during cryo-EM.

Alternatively if such larger *Synechocystis* assemblies do constitute an active chelatase component, they may only occur during the Mg^{2+} chelation reaction cycles and thus their formation and detection during SV-AUC will require the presence of D_{IX} during SV-AUC experiments. However, due to additional aggregation as a result of porphyrin being present, in addition to the current limitations of the detection methods used, experiments in the presence of any added porphyin substrates proved unsuccessful.

6.2 Future perspectives - Are structural changes within the ChlID motor complex mediated through the ChlD subunit following interactions of ChlH?

Within the AAA^+ family conformational rearrangments are common in relation to changes in nucleotide state or position along the reaction pathway [44, 50, 41] (See Section 1.4.2 for specific examples). A stimulated ATPase activity of the chelatase is observed in the presence of ChlH and it would appear plausible that transient interactions of ChlH may infer changes in nucleotide hydrolysis states within the ChlID motor complex which will ultimately lead to similiar such conformational rearrangements of ChlID complexes.

ChlD has been implicated as the putative site for interactions of the H subunit (Dr Nathan Adams, unpublished work) and my work gives no direct evidence for an IH complex or interaction. Furthermore, mutagenisis studies have demonstrated that ChlD is an inactive although essential ATPase subunit, having a regulatory role in relation to $MgATP^{2-}$ and Mg^{2+} binding within larger ChlID complexes and the chelatase system in general [89, 90].

If the overall chelatase represents a higher order ChlID arrangement, in theory a single ChlD subunit within active complexes would be acting as both this regulatory subunit and the exclusive interface for interactions of the ChlH subunit.

Following interactions of ChlH with ChlD during the reaction cycle, the D subunit may act as a signalling subunit, triggering switches in nucleotide state and conformational changes throughout the ChlID rings, essentially controlling levels of ATPase activity performed by these motor complexes in relation to the position along the reaction pathway.

Further investigation into methods of directly probing this putative ChlDH interface and how ChlD then signals throughout the ring following interactions of ChlH are therefore of huge interest in the understanding of the chelatase cycle mechanism. Possible routes for this may involve a combination of mutagensis studies of possible residues of ChlD and ChlH involved in this interface and / or signalling mechanism, in combination with establishing new subunit binding techniques to probe the changes in ChlDH binding affinity directly and how this relates to activity of the chelatase.

Finally, the further characterisation of any higher order ChlID complexes is required. This could include attempting to build and isolate specific higher order ChlID arrangements via subunit linking experiments and testing these complexes for activity. Furthermore, with the interactions of subunits being nucleotide dependant, SV-AUC under a wider range of nucleotide states may lead to further insight into the assembly of chelatase complexes and the interactions of ChlH.

6.2.1 Determining the involvement of ChlH in the lag phase prior to steady state metal ion chelation

Dynafit modelling of the reaction cycle pathway demonstrated that an isomerisation step of ChlH may be one of the processes that govern a lag phase commonly observed prior to steady state chelatase activity. In particular, this was proposed to be an isomerisation of the enzyme between active and inactive forms.

This lag phase results from numerous factors and will likely involve processes relating to the ChlI and ChlD subunits in addition to those involving ChlH. Thus, further understanding of the chelatase reaction cycle will ultimately require the identification of characterisation of each of these processes governing it.

Further investigation into the involvement of ChlH could involve preincubation studies of the subunit — examples include the presence of porphyrins in addition to additional ChlH concentration dependent studies — with the subsequent exploration of dynafit models. Furthermore, if this lag phase does constitute an isomerisation step, further direct structural investigations into the ChlH subunit may be required.

References

[1] Tsao, J., Lewis, N., and Crabtree, G. *Solar FAQs.* Tech. rep. 2006, 1–24.

[2] U.S. Energy Information Administration. *International Energy Outlook 2016.* Tech. rep. May 2016. 2016, 1–2.

[3] World Energy Council. “World Energy Resources: 2016 survey”. *World Energy Council*, (2016), 1 –43.

[4] REN21. *Renewables 2016 Global Status Report.* Tech. rep. 2016, 1 –272.

[5] Blankenship, R. E. “Origin and Early Evolution of Photosynthesis”. *Photosynthesis Research*, **33**, (1992), 91–111.

[6] Nealson, K. H. and Conrad, P. G. “Life: past, present and future.” *Philosophical Transactions of the Royal Society of London. Series B, Biological Sciences*, **354**,1392 (1999), 1923–1939.

[7] McKendry, P. “Energy Production from Biomass (Part 1): overview of biomass”. *Bioresource Technology*, **83**,Part 1 (2002), 37–46.

[8] Hall, D. O. and Rao, K. *Photosynthesis.* 6th. Cambridge University Press, 1999, 248.

[9] Barber, J. and Archer, M. “P680, the Primary Electron Donor of Photosystem II”. *Journal of Photochemistry and Photobiology A: Chemistry*, **142**,2 (2001), 97–106.

[10] Stock, D., Leslie, A. G. W., and Walker, J. E. “Molecular Architecture of the Rotary motor in ATP Synthase.” *Science*, **286**,5445 (1999), 1700–1705.

[11] Webber, A. N. and Lubitz, W. “P700: The Primary Electron Donor of Photosystem I”. *Biochimica et Biophysica Acta - Bioenergetics*, **1507**,1-3 (2001), 61–79.

[12] Shiozawa, J. A., Alberte, R. S., and Thornber, J. P. “The P700-chlorophyll a-protein. Isolation and some characteristics of the complex in higher plants”. *Archives of Biochemistry and Biophysics*, **165**,1 (1974), 388–397.

[13] Umena, Y., Kawakami, K., Shen, J.-R., and Kamiya, N. “Crystal Structure of Oxygen-Evolving Photosystem II at a Resolution of 1.9 Å.” *Nature*, **473**,7345 (2011), 55–60.

[14] Suga, M., Akita, F., Hirata, K., Ueno, G., Murakami, H., Nakajima, Y., Shimizu, T., Yamashita, K., Yamamoto, M., Ago, H., and Shen, J.-r. “Native Structure of Photosystem II at 1.95 Å Resolution Viewed by Femtosecond X-ray Pulses”. *Nature*, **517**,7532 (2014), 99–103.

[15] Zouni, A., Witt, H.-T., Kern, J., Fromme, P., Krauss, N., Saenger, W., and Orth, P. “Crystal Structure of Photosystem II from *Synechococcus elongatus* at 3.8 Å resolution”. *Nature*, **409**,6821 (2001), 739–743.

[16] Guskov, A, Kern, J, Gabdulkhakov, A, Broser, M, Zouni, A, and Saenger, W. “Cyanobacterial Photosystem II at 2.9-A Resolution and the Role of Quinones, Lipids, Channels and Chloride”. *Nature Structural & Molecular Biology*, **16**,3 (2009), 334–342.

[17] Fromme, P., Jordan, P., and Krauss, N. “Structure of Photosystem I”. *Biochimica et Biophysica Acta - Bioenergetics*, **1507**,1-3 (2001), 5–31.

[18] Jordan, P, Fromme, P, Witt, H. T., Klukas, O, Saenger, W, and Krauss, N. “Three-dimensional Structure of Cyanobacterial Photosystem I at 2.5 A Resolution.” *Nature*, **411**,6840 (2001), 909–917.

[19] Ben-Shem, A., Frolow, F., and Nelson, N. “Crystal Structure of Plant Photosystem I”. *Nature*, **426**,6967 (2003), 630–635.

[20] Mazor, Y., Borovikova, A., Caspy, I., and Nelson, N. “The Structure of Plant Photosystem I Supercomplex at 2.6Å resolution”. *Nature Plants*, **3**,17014 (2017), 1 –9.

[21] Barber, J. “P680: What is it and where is it?” *Bioelectrochemistry*, **55**,1-2 (2002), 135–138.

[22] Winn, M. D., Ballard, C. C., Cowtan, K. D., Dodson, E. J., Emsley, P., Evans, P. R., Keegan, R. M., Krissinel, E. B., Leslie, A. G. W., McCoy, A., McNicholas, S. J., Murshudov, G. N., Pannu, N. S., Potterton, E. A., Powell, H. R., Read, R. J., Vagin, A., and Wilson, K. S. “Overview of the CCP4 suite and current developments”. *Acta Crystallographica Section D: Biological Crystallography*, **67**,4 (2011), 235–242.

[23] Grossman, A. R., Schaefer, M. R., Chiang, G. G., and Collier, J. L. “The Phycobilisome, a Light-Harvesting Complex Responsive to Environmental Conditions.” *Microbiological Reviews*, **57**,3 (1993), 725–49.

[24] Glazer, A. N. “Light Harvesting by Phycobilisomes”. *Annual Review of Biophysics and Biophysical Chemistry*, **14**,64 (1985), 47–77.

[25] Ghirardi, M. L. and Melis, A. “Photosystem Electron-Transport Capacity and Light-Harvesting Antenna Size in Maize Chloroplasts”. *Plant Physiology*, **74**,4 (1984), 993–998.

[26] Bryant, D. A., Guglielmi, G., Marsac, N. T. de, Castets, A.-M., and Cohen-Bazire, G. “The Structure of Cyanobacterial Phycobilisomes: a Model”. *Archives of Microbiology*, **123**,2 (1979), 113–127.

[27] Peng, P. P., Dong, L. L., Sun, Y. F., Zeng, X. L., Ding, W. L., Scheer, H., Yang, X., and Zhao, K. H. “The structure of allophycocyanin B from *Synechocystis*

PCC 6803 reveals the structural basis for the extreme redshift of the terminal emitter in phycobilisomes". *Acta Crystallographica Section D: Biological Crystallography*, **70**,10 (2014), 2558–2569.

[28] Nabout, J. C., da Silva Rocha, B., Carneiro, F. M., and Sant'Anna, C. L. "How Many Species of Cyanobacteria Are There? Using a discovery curve to predict the species number". *Biodiversity and Conservation*, **22**,12 (2013), 2907–2918.

[29] Ikeuchi, M. and Tabata, S. "*Synechocystis* sp. PCC 6803 - a useful tool in the study of the genetics of cyanobacteria." *Photosynthesis Research*, **70**,1 (2001), 73–83.

[30] Grigorieva, G. and Shestakov, S. "Transformation in the Cyanobacterium *Synechocystis* sp. 6803". *FEMS Microbiology Letters*, **13**,4 (1982), 367–370.

[31] Kaneko, T, Sato, S, Kotani, H, Tanaka, A, Asamizu, E, Nakamura, Y, Miyajima, N, Hirosawa, M, Sugiura, M, Sasamoto, S, Kimura, T, Hosouchi, T, Matsuno, A, Muraki, A, Nakazaki, N, Naruo, K, Okumura, S, Shimpo, S, Takeuchi, C, Wada, T, Watanabe, A, Yamada, M, Yasuda, M, and Tabata, S. "Sequence Analysis of the genome of the Unicellular Cyanobacterium *Synechocystis* sp. strain PCC6803. II. Sequence determination of the entire genome and assignment of potential protein-coding regions." *DNA research*, **3**,3 (1996), 109–136.

[32] Jensen, P. E., Gibson, L. C. D., and Hunter, C. N. "Determinants of catalytic activity with the use of purified I, D and H subunits of the magnesium protoporphyrin IX chelatase from *Synechocystis* PCC6803". *Biochemical Journal*, **334**,Part 2 (1998), 335 –344.

[33] Von Wettstein, D., Gough, S., and Kannangara, C. G. "Chlorophyll Biosynthesis." *The Plant Cell*, **7**,7 (1995), 1039–1057.

[34] Battersby, A. R. "Tetrapyrroles: The Pigments of Life". *Natural Product Reports*, **17**,6 (2000), 507–526.

[35] Reid, J. D. and Hunter, C. N. "Magnesium-dependent ATPase Activity and Cooperativity of Magnesium Chelatase from *Synechocystis* sp. PCC6803." *The Journal of Biological Chemistry*, **279**,26 (2004), 26893–26899.

[36] Hoggins, M, Dailey, H. A., Hunter, C. N., and Reid, J. D. "Direct Measurement of Metal Ion Chelation in the Active Site of Human Ferrochelatase". *Biochemistry*, **46**,27 (2007), 8121–8127.

[37] Davidson, R. E., Chesters, C. J., and Reid, J. D. "Metal Ion Selectivity and Substrate Inhibition in the Metal Ion Chelation Catalyzed by Human Ferrochelatase." *The Journal of Biological Chemistry*, **284**,49 (2009), 33795–33799.

[38] Wu, C.-K., Dailey, H. A., Rose, J. P., Burden, A., Sellers, V. M., and Wang, B.-C. "The 2.0 Å Structure of Human Ferrochelatase, the Terminal enzyme of Heme Biosynthesis". *Nature Structural Biology*, **8**,2 (2001), 156–160.

[39] Snider, J., Thibault, G., and Houry, W. A. “The AAA$^+$ Superfamily of Functionally Diverse Proteins.” *Genome Biology*, **9**,4 (2008), 216 –216.8.

[40] Snider, J. and Houry, W. A. “AAA$^+$ Proteins: diversity in function, similarity in structure.” *Biochemical Society Transactions*, **36**,Part 1 (2008), 72–77.

[41] Erzberger, J. P. and Berger, J. M. “Evolutionary Relationships and Structural Mechanisms of AAA$^+$ proteins.” *Annual Review of Biophysics and Biomolecular Structure*, **35**, (2006), 93–114.

[42] Neuwald, A. F., Aravind, L., Spouge, J. L., and Koonin, E. V. “AAA$^+$: A Class of Chaperone-Like ATPases Associated with the Assembly, Operation, and Disassembly of Protein Complexes”. *Genome Research*, **9**,1 (1999), 27–43.

[43] Iyer, L. M., Leipe, D. D., Koonin, E. V., and Aravind, L. “Evolutionary History and Higher order Classification of AAA$^+$ ATPases”. *Journal of Structural Biology*, **146**,1-2 (2004), 11–31.

[44] Hanson, P. I. and Whiteheart, S. W. “AAA$^+$ Proteins: Have Engine, Will Work.” *Nature Reviews. Molecular Cell Biology*, **6**, (2005), 519–529.

[45] Fodje, M. N., Hansson, A, Hansson, M, Olsen, J. G., Gough, S, Willows, R. D., and Al-Karadaghi, S. “Interplay Between an AAA Module and an Integrin I Domain May Regulate the Function of Magnesium Chelatase.” *Journal of Molecular Biology*, **311**,1 (2001), 111–122.

[46] Saraste, M, Sibbald, P. R., and Wittinghofer, A. “The P-Loop - a mommon motif in ATP-Binding and GTP-binding proteins”. *Trends in Biochemical Sciences*, **15**,11 (1990), 430–434.

[47] Steel, G. J., Harley, C, Boyd, a, and Morgan, a. “A Screen for Dominant Negative Mutants of SEC18 Reveals a Role for the AAA Protein Consensus Sequence in ATP Hydrolysis.” *Molecular biology of the cell*, **11**,4 (2000), 1345–56.

[48] Ogura, T., Whiteheart, S. W., and Wilkinson, A. J. “Conserved Arginine Residues Implicated in ATP hydrolysis, Nucleotide-sensing, and Inter-subunit interactions in AAA and AAA$^+$ ATPases”. *Journal of Structural Biology*, **146**,1-2 (2004), 106–112.

[49] Lenzen, C. U., Steinmann, D., Whiteheart, S. W., and Weis, W. I. “Crystal Structure of the Hexamerization Domain of N-ethylmaleimide Sensitive Fusion Protein”. *Cell*, **94**,4 (1998), 525–536.

[50] Vale, R. D. “AAA proteins: Lords of the ring”. *Journal of Cell Biology*, **150**,1 (2000), F13–19.

[51] Hurley, J. H. “The ESCRT Complexes”. *Critical Reviews in Biochemistry and Molecular Biology*, **45**,6 (2010), 463–487.

[52] Hurley, J. H. and Yang, B. “Making Sense of Vps4”. *Journal of Molecular Biology*, **426**,3 (2014), 503–506.

[53] Baker, T. A. and Sauer, R. T. "ClpXP, an ATP-powered Unfolding and Protein-Degradation Machine". *Biochimica et Biophysica Acta - Molecular Cell Research*, **1823**,1 (2012), 15–28.

[54] Glynn, S. E., Martin, A., Nager, A. R., Baker, T. A., and Sauer, R. T. "Structures of Asymmetric ClpX Hexamers Reveal Nucleotide-Dependent Motions in a AAA$^+$ Protein-Unfolding Machine". *Cell*, **139**,4 (2009), 744–756.

[55] Akoev, V., Gogol, E. P., Barnett, M. E., and Zolkiewski, M. "Nucleotide-induced Switch in Oligomerization of the AAA$^+$ ATPase ClpB." *Protein Science*, **13**,3 (2004), 567–574.

[56] Kim, K., Cheong, G. W., Park, S. C., Ha, J. S., Woos, K. M., Choi, S. J., and Chung, C. H. "Heptameric Ring Structure of the Heat-shock Protein ClpB, a Protein-activated ATPase in *Escherichia* coli". *Journal of Molecular biology*, **303**,5 (2000), 655–666.

[57] Chang, L.-F., Chen, S., Liu, C.-C., Pan, X., Jiang, J., Bai, X.-C., Xie, X., Wang, H.-W., and Sui, S.-F. "Structural characterization of full-length NSF and 20S particles." *Nature Structural & Molecular biology*, **19**,3 (2012), 268–75.

[58] Ciniawsky, S., Grimm, I., Saffian, D., Girzalsky, W., Erdmann, R., and Wendler, P. "Molecular Snapshots of the Pex1/6 AAA+ Complex in Action." *Nature Communications*, **6**, (2015), 7331.

[59] Kon, T., Oyama, T., Shimo-Kon, R., Imamula, K., Shima, T., Sutoh, K., and Kurisu, G. "The 2.8Å Crystal Structure of the Dynein Motor Domain". *Nature*, **484**,7394 (2012), 345–350.

[60] Miyata, T, Yamada, K, Iwasaki, H, Shinagawa, H, Morikawa, K, and Mayanagi, K. "Two different oligomeric states of the RuvB branch migration motor protein as revealed by electron microscopy." *Journal of Structural biology*, **131**,2 (2000), 83–89.

[61] Yao, N. Y. and ODonnell, M. "The RFC clamp loader: Structure and Function." *Subcellular Biochemistry*, **62**, (2012), 259–279.

[62] Zhang, X., Shaw, A., Bates, P. A., Newman, R. H., Gowen, B., Orlova, E., Gorman, M. A., Kondo, H., Dokurno, P., Lally, J., Leonard, G., Meyer, H., Van Heel, M., and Freemont, P. S. "Structure of the AAA ATPase p97". *Molecular Cell*, **6**,6 (2000), 1473–1484.

[63] Zhao, M., Wu, S., Zhou, Q., Vivona, S., Cipriano, D. J., Cheng, Y., and Brunger, A. T. "Mechanistic Insights into the Recycling Machine of the SNARE complex". *Nature*, **518**,7537 (2015), 61–67.

[64] Ogura, T. and Wilkinson, A. J. "AAA+ superfamily ATPases: Common structure-diverse function". *Genes to Cells*, **6**,7 (2001), 575–597.

[65] Caillat, C., Macheboeuf, P., Wu, Y., McCarthy, A. A., Boeri-Erba, E., Effantin, G., Göttlinger, H. G., Weissenhorn, W., and Renesto, P. "Asymmetric Ring Structure of Vps4 Required for ESCRT-III Disassembly." *Nature Communications*, **6**, (2015), 8781.

[66] Werbeck, N. D., Schlee, S., and Reinstein, J. "Coupling and Dynamics of Subunits in the Hexameric AAA$^+$ Chaperone ClpB". *Journal of Molecular Biology*, **378**,1 (2008), 178–190.

[67] Lundqvist, J., Braumann, I., Kurowska, M., Müller, A. H., and Hansson, M. "Catalytic Turnover Triggers Exchange of Subunits of the Magnesium Chelatase AAA$^+$ Motor Unit." *The Journal of Biological Chemistry*, **288**,33 (2013), 24012–24019.

[68] Berman, H. M., Westbrook, J, Feng, Z, Gilliland, G, Bhat, T. N., Weissig, H, Shindyalov, I. N., and Bourne, P. E. "The Protein Data Bank." *Nucleic Acids Research*, **28**,1 (2000), 235–242.

[69] Gibson, L. C. D., Willows, R. D., Kannangara, C. G., Wettstein, D. von, and Hunter, C. N. "Magnesium-protoporphyrin Chelatase of *Rhodobacter sphaeroides*: reconstitution of activity by combining the products of the bchH, -I, and -D genes expressed in Escherichia coli." *Proceedings of the National Academy of Sciences of the United States of America*, **92**, (1995), 1941–1944.

[70] Willows, R. D., Gibson, L. C. D., Kanangard, G. C., Hunter, N. C., and Wettstein, D. von. "Three Separate Proteins Constitute the Magnesium Chelatase of *Rhodobacter sphaeroides*". *European Journal of Biochemistry*, **235**, (1996), 438–443.

[71] Willows, R. D. and Beale, S. I. "Heterologous expression of the *Rhodobacter capsulatus* BchI, -D, and -H Genes That Encode Magnesium Chelatase Subunits and Characterization of the Reconstituted Enzyme". *Journal of Biological Chemistry*, **273**,51 (1998), 34206–34213.

[72] Jensen, P. E., Gibson, L. C. D., Henningsen, K. W., and Hunter, C. N. "Expression of the chlI, chlD, and chlH Genes from the Cyanobacterium *Synechocystis* PCC6803 in Escherichia coli and Demonstration That the Three Cognate Proteins Are Required for Magnesium-protoporphyrin Chelatase Activity." *The Journal of Biological Chemistry*, **271**,28 (1996), 16662–16667.

[73] Adams, N. B. P., Marklew, C. J., Brindley, A. A., Hunter, C. N., and Reid, J. D. "Characterization of the Magnesium Chelatase from *Thermosynechococcus elongatus*." *Biochemical Journal*, **457**,1 (2014), 163–70.

[74] Zhou, S., Sawicki, A., Willows, R. D., and Luo, M. "C-terminal residues of oryza sativa GUN4 are required for the activation of the ChlH subunit of magnesium chelatase in chlorophyll synthesis." *FEBS Letters*, **586**,3 (2012), 205–210.

[75] Jensen, P. E., Willows, R. D., Petersen, B. L., Vothknecht, U. C., Stummann, B. M., Kannangara, C. G., Wettstein, D. von, and Kenningsen, K. W. "Structural Genes for Mg-chelatase Subunits in Barley: *Xantha*-f, -g and -h". *Molecular Genetics and Genomics*, **7**,250 (1996), 383–394.

[76] Guo, R., Luo, M., and Weinstein, J. D. "Magnesium-Chelatase from Developing Pea Leaves. Characterization of a Soluble Extract from Chloroplasts and Resolution into Three Required Protein Fractions". *Plant Physiology*, **116**, (1998), 605–615.

[77] Sawicki, A. and Willows, R. D. "Kinetic Analyses of the Magnesium Chelatase Provide Insights into the Mechanism, Structure, and Formation of the Complex". *Journal of Biological Chemistry*, **283**,46 (2008), 31294–31302.

[78] Verdecia, M. A., Larkin, R. M., Ferrer, J.-L., Riek, R., Chory, J., and Noel, J. P. "Structure of the Mg-Chelatase Cofactor GUN4 Reveals a Novel Hand-Shaped Fold for Porphyrin Binding." *PLoS biology*, **3**,5 (2005), 0777–0789.

[79] Davison, P. A., Schubert, H. L., Reid, J. D., Iorg, C. D., Heroux, A., Hill, C. P., and Hunter, C. N. "Structural and Biochemical Characterization of Gun4 Suggests a Mechanism for Its Role in Chlorophyll Biosynthesis." *Biochemistry*, **44**,21 (2005), 7603–7612.

[80] Larkin, R. M., Alonso, J. M., Ecker, J. R., and Chory, J. "GUN4, A Regulator of Chlorophyll Synthesis and Intracellular Signaling." *Science*, **299**,5608 (2003), 902–906.

[81] Reid, J. D. and Hunter, C. N. "Current Understanding of the Function of Magnesium Chelatase." *Biochemical Society Transactions*, **30**,4 (2002), 643–645.

[82] Jensen, P. E., Gibson, L. C. D., and Hunter, C. N. "ATPase activity associated with the magnesium-protoporphyrin IX chelatase enzyme of *Synechocystis* PCC6803: evidence for ATP hydrolysis during Mg^+ insertion". *Biochemical Journal*, **339**,Part 1 (1999), 127–134.

[83] Edgar, R. C. "MUSCLE: Multiple sequence alignment with high accuracy and high throughput". *Nucleic Acids Research*, **32**,5 (2004), 1792–1797.

[84] The UniProt Consortium. "UniProt: A Hub for Protein Information". *Nucleic Acids Research*, **43**,Database issue (2014), D204–212.

[85] Reid, J. D., Siebert, C. A., Bullough, P. A., and Hunter, C. N. "The ATPase Activity of the ChlI Subunit of Magnesium Chelatase and Formation of a Heptameric AAA^+ ring". *Biochemistry*, **42**,22 (2003), 6912–6920.

[86] Hansson, M and Kannangara, C. G. "ATPases and Phosphate Exchange Activities in mMgnesium Chelatase Subunits of *Rhodobacter sphaeroides*." *Proceedings of the National Academy of Sciences of the United States of America*, **94**,24 (1997), 13351–6.

[87] Gibson, L. C. D., Jensen, P. E., and Hunter, C. N. "Magnesium Chelatase from *Rhodobacter sphaeroides*: initial characterization of the enzyme using purified subunits and evidence for a BchI BchD complex." *Biochemical Journal*, **337**,Part 2 (1999), 243–251.

[88] Willows, R. D., Hansson, A, Birch, D, Al-Karadaghi, S, and Hansson, M. "EM Single Paricle Analysis of the ATP-dependent BchI Complex of Magnesium Chelatase: An AAA$^+$ hexamer". *Journal of Structural Biology*, **146**,1-2 (2004), 227–233.

[89] Adams, N. B. P. and Reid, J. D. "The Allosteric Role of the AAA$^+$ Domain of ChlD Protein from the Magnesium Chelatase of *Synechocystis* Species PCC 6803." *The Journal of Biological Chemistry*, **288**,40 (2013), 28727–28732.

[90] Brindley, A. A., Adams, N. B. P., Hunter, C. N., and Reid, J. D. "Five glutamic acid residues in the C-terminal domain of the ChlD subunit play a major role in conferring Mg $^{2+}$ cooperativity on magnesium chelatase." *Biochemistry*, **54**, (2015), 6659–6662.

[91] Axelsson, E., Lundqvist, J., Sawicki, A., Nilsson, S., Schröder, I., Al-Karadaghi, S., Willows, R. D., and Hansson, M. "Recessiveness and Dominance in Barley Mutants Deficient in Mg-Chelatase Subunit D, an AAA Protein Involved in Chlorophyll Biosynthesis." *The Plant Cell*, **18**,12 (2006), 3606–3616.

[92] Gräfe, S, Saluz, H. P., Grimm, B, and Hänel, F. "Mg-chelatase of Tobacco: the role of the subunit CHLD in the chelation step of protoporphyrin IX." *Proceedings of the National Academy of Sciences of the United States of America*, **96**,March (1999), 1941–1946.

[93] Adams, N. B. P., Vasilev, C., Brindley, A. A., and Hunter, C. N. "Nanomechanical and Thermophoretic Analyses of the Nucleotide-Dependent Interactions between the AAA$^+$ Subunits of Magnesium Chelatase". *Journal of the American Chemical Society*, **138**,20 (2016), 6591–6597.

[94] Lundqvist, J., Elmlund, H., Wulff, R. P., Berglund, L., Elmlund, D., Emanuelsson, C., Hebert, H., Willows, R. D., Hansson, M., Lindahl, M., and Al-Karadaghi, S. "ATP-Induced Conformational Dynamics in the AAA$^+$ Motor Unit of Magnesium Chelatase." *Structure*, **18**,3 (2010), 354–365.

[95] Karger, G. A., Reid, J. D., and Hunter, C. N. "Characterization of the Binding of Deuteroporphyrin IX to the Magnesium Chelatase H Subunit and Spectroscopic Properties of the Complex." *Biochemistry*, **40**,31 (2001), 9291–9299.

[96] Chen, X., Pu, H., Fang, Y., Wang, X., Zhao, S., Lin, Y., Zhang, M., Dai, H.-E., Gong, W., and Liu, L. "Crystal structure of the Catalytic Subunit of Magnesium Chelatase". *Nature Plants*, **1**, (2015), 15125.

[97] Sirijovski, N., Olsson, U., Lundqvist, J., Al-Karadaghi, S., Willows, R. D., and Hansson, M. "ATPase activity associated with the magnesium chelatase H-subunit of the chlorophyll biosynthetic pathway is an artefact." *Biochemical Journal*, **400**,3 (2006), 477–84.

[98] Sirijovski, N., Lundqvist, J., Rosenbäck, M., Elmlund, H., Al-Karadaghi, S., Willows, R. D., and Hansson, M. "Substrate-binding Model of the Chlorophyll Biosynthetic Magnesium Chelatase BchH Subunit". *Journal of Biological Chemistry*, **283**,17 (2008), 11652–11660.

[99] Qian, P., Marklew, C. J., Viney, J., Davison, P. A., Brindley, A. A., Söderberg, C., Al-Karadaghi, S., Bullough, P. A., Grossmann, J. G., and Hunter, C. N. "Structure of the Cyanobacterial Magnesium Chelatase H subunit Determined by Single Particle Reconstruction and Small-angle X-ray Scattering." *The Journal of Biological Chemistry*, **287**,7 (2012), 4946–4956.

[100] Viney, J., Davison, P. A., Hunter, C. N., and Reid, J. D. "Direct measurement of Metal-ion Chelation in the Active Site of the AAA$^+$ ATPase Magnesium Chelatase." *Biochemistry*, **46**,44 (2007), 12788–12794.

[101] Kuzmic, P. "Program DYNAFIT for the analysis of enzyme kinetic data: application to HIV proteinase." *Analytical Biochemistry*, **237**,2 (1996), 260–273.

[102] Walker, C. J. and Weinstein, J. D. "The magnesium-insertion step of chlorophyll biosynthesis is a two-stage reaction." *Biochemical Journal*, **299**,Part 1 (1994), 277–284.

[103] Northrop, D. B. "On the Meaning of Km and V/K in Enzyme Kinetics". *Journal of Chemical Education*, **75**,9 (1998), 1153.

[104] Marsh, J. a. and Teichmann, S. a. "Structure, Dynamics, Assembly, and Evolution of Protein Complexes." *Annual Review of Biochemistry*, **84**, (2014), 551–575.

[105] Schuck, P. "Size-distribution analysis of macromolecules by sedimentation velocity ultracentrifugation and lamm equation modeling." *Biophysical Journal*, **78**,3 (2000), 1606–1619.

[106] Laue, T. M. and Stafford, W. F. "Modern Applications of Analytical Ultracentrifugation." *Annual Review of Biophysics and Biomolecular Structure*, **28**, (1999), 75–100.

[107] Rivas, G, Stafford, W, and Minton, A. P. "Characterization of Heterologous Protein-Protein Interactions Using Analytical Ultracentrifugation". *Methods*, **19**, (1999), 194–212.

[108] Lebowitz, J., Lewis, M. S., and Schuck, P. "Modern analytical ultracentrifugation in protein science: A tutorial review." *Protein Science*, **11**,9 (2002), 2067–2079.

[109] Howlett, G. J., Minton, A. P., and Rivas, G. "Analytical Ultracentrifugation for the Study of Protein Association and Assembly". *Current Opinion in Chemical Biology*, **10**,5 (2006), 430–436.

[110] Cole, J. L., Lary, J. W., Moody, T. P., and Laue, T. M. "Analytical Ultracentrifugation: Sedimentation Velocity and Sedimentation Equilibrium". *Methods in Cell Biology*, **84**, (2008), 143 –179.

[111] Ole, L. *Die differentialgleichung der ultrazentrifugierung.* Almqvistz and Wiksell, 1929.

[112] Balbo, a. and Schuck, P. "Analytical Ultracentrifugation in the Study of Protein Self-association and Heterogeneous Protein-Protein Interactions". *Protein Protein Interactions*, 301 (2005), 253–277.

[113] Niewiarowski, A., Bradley, A. S., Gor, J., McKay, A. R., Perkins, S. J., and Tsaneva, I. R. "Oligomeric Assembly and Interactions within the Human RuvB-like RuvBL1 and RuvBL2 Complexes". *Biochemical Journal*, **429**,1 (2010), 113–125.

[114] Vieux, E. F., Wohlever, M. L., Chen, J. Z., Sauer, R. T., and Baker, T. a. "Distinct Quaternary Structures of the AAA$^+$ Lon Protease Control Substrate Degradation." *Proceedings of the National Academy of Sciences of the United States of America*, **110**,22 (2013), 1–7.

[115] Förster, T. "Zwischenmolekulare Energiewanderung und Fluoreszenz (Intermolecular energy migration and fluorescence, Translated by Knox RS)". *Annalen der Physik*, **437**, (1948), 55–75.

[116] Atkins, P and Paula, J. D. "Atkins' physical chemistry". *Oxford University Press, Oxford, UK*, (2006).

[117] Kuzmic, P. "DynaFit - A Software Package for Enzymology". *Methods in Enzymology*, **467**,C (2009), 247–280.

[118] Shepherd, M. and Hunter, C. N. "Transient Kinetics of the Reaction Catalysed by Magnesium Protoporphyrin IX Methyltransferase". *Biochemical Journal*, **382**,Part 3 (2004), 1009–1013.

[119] Fersht, A. *Structure and Mechanism in protein science: A Guide to Enzyme Catalysis and Protein Folding.* 2nd. W. H. Freeman and Company, 1985, 132 –158.